The Production of Pure Hydrogen with Simultaneous Capture of Carbon Dioxide

A dissertation submitted for the degree of *Doctor of Philosophy*

Christopher D. Bohn
Christ's College
University of Cambridge
June 2010

Preface

This dissertation describes work undertaken in the Department of Chemical Engineering and Biotechnology and the Department of Engineering at the University of Cambridge, between October 2006 and June 2010. It is the original and independent work of the author except where specifically acknowledged in the text. Neither the present thesis, nor any part thereof, has been previously submitted to any other university. This dissertation contains approximately 65,000 words, 20 tables and 80 figures.

Christopher Bohn
Department of Chemical Engineering
University of Cambridge
June 2010

Acknowledgements

I would like to thank my supervisor Dr. John Dennis, who has helped me immeasurably on all aspects of the work. Thanks also go to Dr. Stuart Scott, Prof. John Davidson and Prof. Allan Hayhurst for their excellent teaching and guidance.

I would like to thank Christoph Müller for interesting me in lattice Boltzmann modelling and for his support during the development of the code. Special thanks go to the staff of the Department of Chemical Engineering and Biotechnology, specifically Wei-Yao Ma, John Gannon, Chris Rutt and Surinder Sall as well as Lee Pratt, Andy Hubbard and Gary Chapman. Much help also came from the Department of Engineering staff including Michael Underwood, John Harvey and Sam Taylor. Dr. Mary Vickers and Andrew Moss assisted with the XRD, Simon Griggs with the SEM/ EDS analysis and Zlatko Saracevic with the BET analysis. I also appreciate the support of other lab members: Jason, Roberta, Shin-Young, John, Tamaryn, Chris, Aga, Dan, Saquib, Hassan, Piran, Toyin, Paul, Qilei and Marco.

I would especially like to thank my parents, Sherry and David Bohn, for their support and encouragement, as well as my sisters, Laura and Ruth Ellen. I also appreciate my friends from CUBbC and the Saturday CGS group. Special thanks go to my father, Stuart Lee and Sam Bennett for reading this dissertation.

The use of the Chemical Database Service at Daresbury is gratefully acknowledged as well as financial support from the Gates Cambridge Trust and the EPSRC.

Abstract

The need to stabilise or even reduce the production of anthropogenic CO_2 makes the capture of CO_2 during energy generation from carbonaceous fuels, *e.g.* coal or biomass, necessary for the future. For hydrogen, an environmentally-benign energy vector whose sole combustion product is water, to become a major energy source, it must be produced in an efficient, CO_2-neutral manner. A process, which uses a packed bed of iron and its oxides, *viz.* Fe, $Fe_{0.947}O$, Fe_3O_4 and Fe_2O_3, has been formulated to produce separate, pure streams of H_2 and CO_2. The process is exothermic and has the following stages:

1. Reduction of Fe_2O_3 to $Fe_{0.947}O$ or Fe in syngas (CO + H_2) from gasifying coal or biomass. This stage generates pure CO_2 for sequestration, once the water has been condensed.
2. Subsequent oxidation of Fe or $Fe_{0.947}O$ to Fe_3O_4 using steam. This stage generates H_2 of sufficient purity for use in polymeric membrane fuel cells.
3. Further oxidation of Fe_3O_4 to Fe_2O_3 using air to return the oxide to step (1).

It was shown that reduction to $Fe_{0.947}O$ in step (1) gave stable yields of H_2 in step (2) after 40 cycles, near those predicted from reaction stoichiometry. By contrast, reduction to Fe, rather than $Fe_{0.947}O$, in step (1) gave low levels of H_2 in step (2) after just 10 cycles. This demonstrates that modifying the iron oxide is unnecessary unless reduction to Fe is performed. Wet-impregnation of Fe_2O_3 was performed with salts of Al, Cr and Mg or with tetraethyl orthosilicate for Si to give loadings of 1-30 mol % of the additive element. The addition of Al stabilised the quantity of H_2 produced when the sample was reduced to Fe. Using a sol-gel method, composite particles with different mass ratios of Fe_2O_3 and Al_2O_3 were prepared. For reduction to Fe over 40 cycles, 40 wt. % Al_2O_3 was required to give stable conversions near 75 % of that expected from reaction stoichiometry. Prior to this research, it had been assumed that the alumina acted as an inert support. However, this was shown to be incorrect since the formation of $FeO{\cdot}Al_2O_3$ was quantitatively confirmed using X-ray diffraction. The presence of the compound, $FeO{\cdot}Al_2O_3$, is significant since it reduces the loss in internal surface area but binds reactive iron, two contradictory effects for the production of H_2.

The production of separate streams of pure H_2 and CO_2 from solid fuels, lignite and sub-bituminous coal, was demonstrated. Pure H_2 with $[CO] \lesssim 50$ ppmv and $[SO_2] \approx 0$ ppmv was produced from a low-rank coal, showing that the process is efficacious with an impure fuel. Contaminants found in syngas which are gaseous above 273 K apparently do not adversely affect the iron oxide material or purity of the hydrogen. Subsequent oxidation of the Fe_3O_4 with air, step (3), removed sulphurous and carbonaceous contaminants deposited during reduction, generated useful heat and did not lead to a decrease in the H_2 yield in step (2). It is therefore recommended that step (3) be included in the process.

Rates of reaction are reported for the reduction of iron oxide particles by a mixture of CO, CO_2 and N_2. Importantly, rates were investigated over multiple cycles. Reduction of either Fe_2O_3 to Fe_3O_4 or of Fe_3O_4 to $Fe_{0.947}O$ was found to be first-order in CO. With the particle sizes used, the rates of reduction were controlled by intrinsic chemical kinetics. Activation energies and pre-exponential factors are reported. The rates were used to simulate, satisfactorily, the reduction of a packed bed of iron oxide. The rate of reduction was doubled by the addition of 1 mol. % Ce to the granulated iron oxide. The overall rate was shown to be dependent on the active surface area of the iron oxide.

A lattice Boltzmann model, which incorporates hydrodynamics, mass transport and reaction, was developed. The composition of the solid changed with time. Quantitative agreement between the model and experiments for the reduction of a single particle of Fe_2O_3 to Fe_3O_4 in CO was achieved. Additionally, the model correctly predicted a sharp front in the CO concentration for reduction of a packed bed of Fe_2O_3 to Fe_3O_4.

Contents

Chapter 1

Production of hydrogen

1.1 Global consumption of energy

The shift from fossil fuels to sustainable energy is necessary to mitigate the emission of CO_2, a greenhouse gas with positive radiative forcing. Atmospheric levels of CO_2 have increased from a pre-industrial value of $\sim$ 280 ppmv to $\sim$ 385 ppmv currently (NOAA, 2009). The increase of CO_2 in the atmosphere has been accompanied by a rise in the global average annual temperature by 0.8°C and a rise in global average sea level by 200 mm since 1870 (IPCC, 2007).

The predominant source of anthropogenic carbon dioxide is the combustion of carbonaceous fuels. Currently, the combustion of oil, natural gas and coal accounts for 88 % of the world's supply of primary energy, as seen in Table 1.1. While combustible renewables, such as wood, peat and animal waste, have not been included in Table 1.1, since they are not traded commercially and therefore difficult to quantify (Hayward, 2009), it is estimated that they would increase the figure for total consumption of energy by an additional 10 % (IEA, 2009). Importantly, solar, wind and geothermal renewable sources account for less than 1 % of global consumption (IEA, 2009) and are therefore omitted. The total global consumption of energy is 4.74×10^{20} J and increased by 1.4 % in 2008 (Hayward, 2009). The growth in total energy used between 1998 and 2008 averaged 2.5 % (IEA, 2009) *per annum*.

The estimated reserves of fossil fuels are however limited, as shown in Table 1.1. Oil and natural gas account for less than half of the total reserves of fossil fuels worldwide and are predominantly found in the Middle East. By contrast, coal is more abundant and more widely-distributed with large deposits in the U.S.A., Russia, China and Australia. The ratio of the

Table 1.1: Energy reserves and consumption by fuel in exajoules (10^{18} J) *per annum* derived from Hayward (2009). Reserves are listed for fossil fuels only, *i.e.* oil, natural gas and coal. ^{a} *Per capita* energy consumption is listed in GJ *per* person, with population information obtained from the CIA (2009).

Country	**Oil**		**Natural Gas**		**Coal**		**Nuclear**	**Hydro**	**Total**	**Total**	**Per Capita**^{a}
/Region	**Res.**	**Cons.**	**Res.**	**Cons.**	**Res.**	**Cons.**	**Cons.**	**Cons.**	**Res.**	**Cons.**	**Cons.**
U.S.A.	155	37	254	25	5616	24	8	2	6025	97	314
U.K.	21	3	13	4	4	1	0	0	38	9	145
Russia	454	5	1637	16	3087	4	2	2	5177	29	205
China	88	16	93	3	2436	59	1	6	2617	84	63
India	34	6	41	2	930	10	0	1	1005	18	16
Australia	21	2	95	1	1755	2	0	0	1871	5	234
Middle East	4284	13	2869	12	32	0	0	0	7185	26	74
Total World	7174	165	6994	114	17060	139	26	30	31227	474	70
Percent	23	35	22	24	55	29	5	6	100	100	

capacity of reserves to the current rate of consumption gives a crude indication of the number of years that an energy source can be used at its current level. Worldwide, oil has the shortest expected supply of 43 years; natural gas has an expected supply of 61 years, followed by coal with 123 years.

The consumption of primary energy is also shown in Table 1.1: oil is the principal energy vector with global consumption of 1.65×10^{20} J/y, whilst nuclear and hydro-electric energy account for less than 12 % of overall consumption. From Table 1.1, developed countries consume more energy *per capita* than the developing ones listed, *c.f.* China and India with the United States, which consumes over 4× as much energy as the world average *per capita*. Given the wide distribution of coal and the limited capacity of renewable energy to substitute, currently, for fossil fuels, it seems likely that for many Western countries a short-term solution to meeting the primary demand for energy in an environmentally-sustainable manner will involve the combustion of coal and subsequent capture and storage of the resulting CO_2.

1.2 Methods for the production of hydrogen

Hydrogen is an environmentally-benign energy vector since its combustion yields a single product, water. Hydrogen, H_2, is a colourless, odourless diatomic gas with molecular weight 2 g/mol. Owing to the Earth having an oxidising atmosphere with 21 vol. % O_2, gaseous H_2 is scarce and hydrogen is typically found either as H_2O or fixed *via* a C-H bond in organic material. Hydrogen is therefore classified as a secondary energy vector and must be derived from a primary source such as one of those listed in Table 1.1. It is currently used in industry for, *inter al.*, the synthesis of ammonia, the production of methanol, the conversion of hydrocarbon gases to liquid fuel *via* the Fischer-Tropsch process, hydrodesulphurisation of refined petroleum products such as diesel, hydrocracking and reduction in metallurgy (Isalski, 1989). At present, hydrogen is typically produced in refinery complexes with capacities of ~ 50 kte/y of H_2 (DOE, 2009a); world production in 2008 was 45 Mte/y in total (DOE, 2009b).

The storage and distribution of H_2 remain significant challenges; therefore, methods which enable the production of H_2 at smaller scales are attractive. A summary of methods for the production of hydrogen follows: the first two involve the conversion of a hydrocarbon feedstock into hydrogen. For the production of hydrogen from a carbonaceous fuel to be environmentally benign, however, capture of the resulting CO_2 is necessary. The next three involve supplying energy to split stable molecules of water into H_2 and O_2 using electricity (electrochemical), heat (thermochemical) or sunlight (photochemical). Finally, the production of hydrogen by biological means is discussed.

1. Steam reforming. The reforming of a hydrocarbon, such as methane, with steam is currently the predominant route for producing hydrogen (Rostrup-Nielsen, 2005) and accounts for 80 % of the world's supply of H_2 (Ramage, 2004). Since the reforming reaction (1.1), below, is endothermic, additional O_2 for partial oxidation, reaction (1.2), is introduced. Following reforming, the high and low temperature water-gas shift (WGS) reaction (1.3) is used to reduce the level of CO to ~ 3 vol. % and 0.5 vol. %, respectively (Choudhary and Goodman, 2002; Farrauto *et al.*, 2003). The reactions for the reforming of CH_4 with steam, the partial oxidation of methane, and the subsequent shift are given by:

   $$CH_4 + H_2O \rightleftarrows CO + 3\,H_2 \qquad \Delta H^\circ_{298\,K} = +205\ \mathrm{kJ/mol} \tag{1.1}$$

   $$CH_4 + O_2 \rightleftarrows CO_2 + 2\,H_2 \qquad \Delta H^\circ_{298\,K} = -319\ \mathrm{kJ/mol} \tag{1.2}$$

   $$CO + H_2O \rightleftarrows CO_2 + H_2. \qquad \Delta H^\circ_{298\,K} = -41\ \mathrm{kJ/mol} \tag{1.3}$$

   For steam reforming, reaction (1.1), followed by the WGS reaction (1.3), 4 moles of H_2 *per* mole of CH_4 can be obtained. Including reaction (1.2) for the adiabatic case such that the overall $\Delta H^\circ_{298\,K} = 0$, reduces this value to 3.3 moles of H_2 *per* mole of CH_4. For pure hydrogen, further reduction of the CO contaminant can be obtained by (i) pressure swing adsorption (Isalski, 1989), (ii) separation using *in situ* Pd membranes (Grace *et al.*, 2005; Patil *et al.*, 2007) or (iii) preferential oxidation of the CO to CO_2 (PROX) (Pozdnyakov *et al.*, 2006).

2. Decomposition of hydrocarbons. The thermodynamics of the decomposition of methane to solid carbon (Muradov, 1993) gives $p^2_{H_2}/p_{CH_4} = 1$ and $p^2_{H_2}/p_{CH_4} = 55$ at 10^5 Pa and at 820 K and 1173 K, respectively. The reaction is endothermic:

$$CH_4 \rightleftarrows C_{(s)} + 2\,H_2 \qquad \Delta H^\circ_{298\,K} = +75\ \mathrm{kJ/mol} \tag{1.4}$$

   and, overall, two moles of H_2 are produced *per* mole of CH_4. The endothermic enthalpy of reaction *per* mole of hydrocarbon increases with chain length: $\Delta H^\circ_{298\,K} = +84$ kJ/mol, +105 kJ/mol and +209 kJ/mol for C_2H_6, C_3H_8 and C_8H_{18}, respectively. In passing, the decomposition of hydrocarbons of length C_2 is currently the primary method for the preparation of carbon nanotubes (Awasthi *et al.*, 2005), although this would have little impact on the supply of H_2 for energy.

3. Electrolysis. In electrolysis, the energy required for the splitting of water into H_2 and O_2 is supplied in the form of an electric current. Molecular O_2 is produced at the anode and H_2 is produced at the cathode:

$$2\,H_2O \rightleftarrows O_2 + 4\,H^+ + 4\,e^- \qquad E_{an} = 1.23 - 0.059\,pH \tag{1.5}$$

$$4\,H^+ + 4\,e^- \rightleftarrows 2\,H_2, \qquad E_{cat} = 0.0 - 0.059\,pH \tag{1.6}$$

   where E is the Nernstian potential in V *vs.* the normal hydrogen electrode (NHE). Thus for the production of $n_{H_2} = 4100$ mol or 100 m^3 of H_2 at 298 K and 10^5 Pa, the electrical energy requirement is $n_{H_2}F(E_{an} - E_{cat}) \times (4\ \mathrm{mol}\ e^-)/(2\ \mathrm{mol}\ H_2) \times (1\ \mathrm{h})/(3600\ \mathrm{s}) =$ 270 kWh, where F is Faraday's constant. Recently, a low-temperature, Co-based catalyst for oxygen generation at the anode has been developed which facilitates electrolysis at ambient conditions: pH 7, 298 K and 10^5 Pa (Kanan and Nocera, 2008).

4. Thermochemical. In thermochemical cycles, energy is supplied as heat to decompose water. For the dissociation of H_2O at a reasonable rate, temperatures in excess of 2500 K are required. Therefore, traditional thermochemical cycles have involved chemical intermediates which permit operating temperatures $\leq$ 1123 K and include the hydrogen

iodide process and the chlorine process (Ewan and Allan, 2006). Recently, the supply of heat using solar concentrators has been proposed (Steinfeld and Meier, 2004). Here, metal oxides, *e.g.* ZnO or Fe_3O_4 (Steinfeld, 2005), are thermally dissociated to gaseous oxygen and their reduced form, Zn or FeO, in a highly endothermic reaction. Subsequent reoxidation with steam produces H_2 of high purity.

5. Photochemical. In photochemical cells, photoexcitation is used to generate H_2 directly at the cathode rather than to produce an electric current (Grätzel, 2001). Unlike the case for electricity production where an electrolyte is cycled between reduced and oxidised forms with no net consumption, water is consumed and must be continuously replenished. Photochemical cells for the production of H_2 have primarily focused on nanostructures made of Fe_2O_3 or TiO_2 (Mohapatra *et al.*, 2009) as semiconductor materials for the anode where O_2 is generated.

6. Biological methods. The production of hydrogen by strictly biological means proceeds through pathways such as fermentation. For example, facultative anaerobes, such as *Escherichia coli*, can produce 2 H_2 *per* glucose molecule during glycolysis, whilst obligate anaerobes, such as *Clostridium pasteurianum*, can produce up to 4 H_2 owing to the reduction of 2 NADH to 2 NAD^+ (Turner *et al.*, 2008).

The above methods of production have various advantages and disadvantages. For example, whilst the reforming of methane with steam is the most developed technology, it involves several reactors and therefore is not suitable for implementation on a smaller, distributed scale. While the decomposition of hydrocarbons obviates the need for CO_2 capture since solid carbon is produced, the energy lost from $C + O_2 \rightleftarrows CO_2$ means that, compared to conventional combustion, more hydrocarbon must be consumed for the same yield of energy. Renewable strategies currently suffer from low production rates; for example, fermentation is limited by low yields, 2-4 mol H_2/mol glucose, and overall production limits of $\sim 10^2$-10^3 m^3 H_2/m^3 culture h (Nath and Das, 2004).

1.3 Production of hydrogen with iron

This dissertation focuses on the production of hydrogen with simultaneous capture of CO_2 using the reduction and oxidation of iron oxide. The overall process could be heat-integrated since it is exothermic, could accept either coal or biomass as a primary energy source and could

Table 1.2: Summary of reaction chemistry for the production of H_2 with simultaneous capture of CO_2 using the reduction and oxidation reactions of iron and its oxides. The enthalpy, ΔH°_T, and Gibbs free energy, ΔG°_T, are for the reactions as written and were calculated from standard thermodynamic tables (Barin and Knacke, 1973).

No.	Reaction	$\Delta H^\circ_{298\ \mathrm{K}}$	$\Delta G^\circ_{298\ \mathrm{K}}$	$\Delta H^\circ_{1023\ \mathrm{K}}$	$\Delta G^\circ_{1023\ \mathrm{K}}$	Step	
1.7	$C_{(s)} + H_2O_{(g)} \rightleftarrows CO + H_2$	+131	+91	+136	-11		Gasification
1.8	$C_{(s)} + CO_2 \rightleftarrows 2\,CO$	+172	+120	+170	-9		
1.9	$3\,Fe_2O_3 + CO \rightleftarrows 2\,Fe_3O_4 + CO_2$	-43	-58	-44	-92	1	Reduction
1.10	$1.2\,Fe_3O_4 + CO \rightleftarrows 3.8\,Fe_{0.947}O + CO_2$	+47	+30	+27	-5	1	
1.11	$Fe_{0.947}O + CO \rightleftarrows 0.947\,Fe + CO_2$	-17	-12	-20	+6	1	
1.12	$3\,Fe_2O_3 + H_2 \rightleftarrows 2\,Fe_3O_4 + H_2O_{(g)}$	-3	-30	-10	-90	1	
1.13	$1.2\,Fe_3O_4 + H_2 \rightleftarrows 3.8\,Fe_{0.947}O + H_2O_{(g)}$	+88	+ 58	+61	-4	1	
1.14	$Fe_{0.947}O + H_2 \rightleftarrows 0.947\,Fe + H_2O_{(g)}$	+24	+16	+14	+6	1	
1.15	$0.947\,Fe + H_2O_{(g)} \rightleftarrows Fe_{0.947}O + H_2$	-24	-16	-14	-6	2	Oxidation
1.16	$3.8\,Fe_{0.947}O + H_2O_{(g)} \rightleftarrows 1.2\,Fe_3O_4 + H_2$	-88	-58	-61	+4	2	
1.17	$2\,Fe_3O_4 + 1/2\,O_2 \rightleftarrows 3\,Fe_2O_3$	-240	-200	-238	-102	3	
1.18	$2\,CO \rightleftarrows C_{(s)} + CO_2$	-172	-120	-170	+9		Boudouard
1.19	$C_{(s)} + 1.25\,H_2O_{(g)} + 0.375\,O_2 \rightleftarrows CO_2 + 1.25\,H_2$	-90	-108	-84	-156		$\sum$

be implemented on a distributed scale. The oxides of iron are: haematite, Fe_2O_3, magnetite, Fe_3O_4, and wuestite, $Fe_{0.947}O$. Here, wuestite is written as $Fe_{0.947}O$; generally, wuestite is written (v. Bogdandy and Engell, 1971) as $Fe_{(1-\delta)}O$, where $0.05 < \delta < 0.17$ such that the stoichiometric ratio of $Fe/O = 1$ is never achieved. The oxygen excess can be construed as iron vacancies in the lattice structure, where the appropriate proportion of iron ions must then be trivalent to maintain electrical neutrality.

The cyclic redox process for producing H_2 with simultaneous capture of CO_2 uses the following three basic steps, summarised by the chemical reactions listed in Table 1.2. Starting with a packed bed of Fe_2O_3, maintained at *e.g.* 1023 K:

1. *Production of CO_2 with oxide reduction.* Syngas, a mixture of CO and H_2 from *e.g.* the gasification of coal or biomass with steam or CO_2 *via* reactions (1.7) and (1.8) in Table 1.2, is converted to a stream of CO_2 and H_2O *via* reactions (1.9)-(1.14) in Table 1.2 by passing it through a packed bed of particles of Fe_2O_3. Condensing out the H_2O from the off-gas would leave a pure stream of CO_2 suitable for sequestration. The concentration gradient along the reactor would enable $Fe_{0.947}O$ or even Fe to exist at the gas inlet of the packed bed, while still maintaining Fe_2O_3 in the packed bed towards the gas outlet.

2. *Production of hydrogen with partial reoxidation of metal oxide.* After the partial reduction of the iron oxide in the bed, passing steam through the reactor would generate

hydrogen and reoxidise the reduced iron oxide to Fe_3O_4 *via* reactions (1.15) and (1.16) in Table 1.2.

3. *Complete reoxidation of metal oxide with air.* The reoxidation to Fe_2O_3 in air produces a stream of N_2 with residual O_2, reaction (1.17) in Table 1.2. Once the entire packed bed has been regenerated to Fe_2O_3, the cycle could begin anew at step 1.

Thermodynamic quantities for the relevant reactions, ΔH°_T and ΔG°_T, can be calculated from standard thermodynamic tables (Barin and Knacke, 1973), as outlined in Appendix 1, and are listed in Table 1.2. A phase diagram for the Fe-CO-CO_2 and Fe-H_2-H_2O systems can then be constructed and is shown in Fig. 1.1. The dashed lines are values of the equilibrium constant $K_p = \exp(-\Delta G^\circ/\mathrm{R}T)$, which for reactions (1.9) to (1.11) are equal to the ratio of partial pressures, $p_{\mathrm{CO_2}}/p_{\mathrm{CO}}$ at equilibrium. The solid lines in Fig. 1.1 show equivalent plots for the Fe-H_2-H_2O system, *viz.* reactions (1.12) to (1.16). The equilibrium diagrams for both systems, Fe-CO-CO_2 and Fe-H_2-H_2O, are related by the equilibrium constant for the water-gas shift reaction (1.3), $K_\mathrm{W} = p_{\mathrm{H_2}}/p_{\mathrm{H_2O}} \times p_{\mathrm{CO_2}}/p_{\mathrm{CO}}$; the equilibrium lines intersect one another at 1123 K since at this temperature $K_\mathrm{W} = 1$. Figure 1.1 shows that below the triple point at 848 K, magnetite, Fe_3O_4, is reduced directly to iron, Fe, omitting wuestite, $Fe_{0.947}O$, as the intermediate.

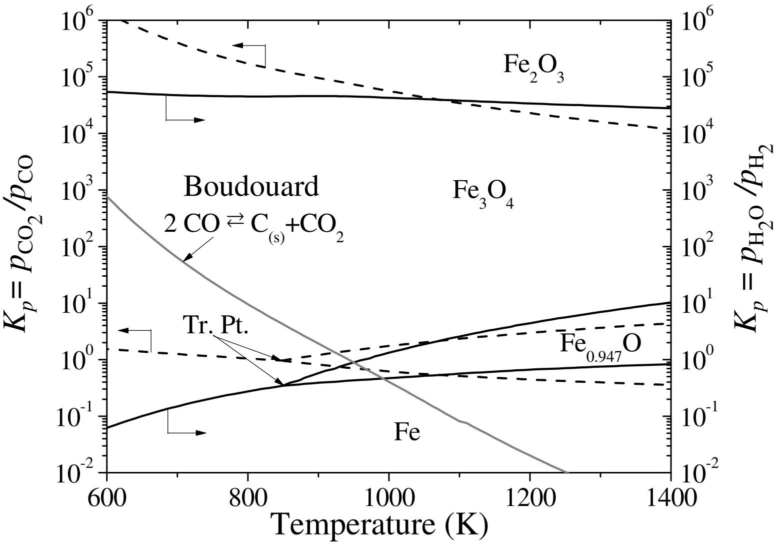

Figure 1.1: Phase diagram showing K_p *versus* temperature for the iron system for reactions with CO_2 and CO (- - -) and H_2O and H_2 (—). The two triple points, where Fe_3O_4, $Fe_{0.947}O$ and Fe coexist, is at 848 K for CO_2/CO or H_2O/H_2. The equilibrium for the Boudouard reaction, $K_p = p_{\mathrm{CO_2}}/p^2_{\mathrm{CO}}$ was converted to the form $K_p = p_{\mathrm{CO_2}}/p_{\mathrm{CO}}$, by assuming a total pressure of $p_{\mathrm{CO}} + p_{\mathrm{CO_2}} = 10^5$ Pa and is shown by the grey line which intersects unity at 940 K.

Considering a typical synthesis gas (Cleeton *et al.*, 2009) from the gasification of coal with steam with a composition of 40 vol. % CO, 40 vol. % H_2, 10 vol. % CO_2, 10 vol. % H_2O and the information presented in Fig. 1.1 and Table 1.2, the following thermodynamic conclusions can be drawn for the packed bed:

- At 1023 K in step 1, the syngas would be fully converted to CO_2 and H_2O provided some Fe_2O_3 existed near the outlet and the residence time in this area was sufficiently long to permit near equilibrium conversion since for reactions (1.9) and (1.12) $p_{CO_2}/p_{CO} = 5 \times 10^4$ and $p_{H_2O}/p_{H_2} = 4 \times 10^4$, respectively, shown by the upper part of Fig. 1.1.

- Reduction to Fe in step 1 would be feasible since the ratios p_{CO_2}/p_{CO} and p_{H_2O}/p_{H_2} in the reducing gas are below the respective equilibrium values of $K_p = 0.6$ and 0.5 at 1023 K, respectively, as shown in Fig. 1.1.

- The deposition of solid carbon during reduction in pure CO (step 1) will be possible up to $\sim$ 1173 K, since at this temperature and 10^5 Pa the equilibrium for the Boudouard reaction (1.18), shown by the grey line in Fig. 1.1, is given by $K_p = p_{CO_2}/p_{CO}^2 \approx p_{CO_2}/p_{CO} = 0.03$. Any deposited carbon could subsequently form carbon oxides, CO and CO_2, upon oxidation of the iron material with steam in step 2 and contaminate the H_2.

- Complete reoxidation of the Fe_3O_4 to Fe_2O_3 using steam in step 2 would be impracticable, since at 1023 K the right hand ordinate of Fig. 1.1 shows that a mole fraction of H_2 as low as 25 ppmv ($p_{H_2O}/p_{H_2} < 4 \times 10^4$) is needed to prevent the transition from Fe_3O_4 to Fe_2O_3. As a result a third step, oxidation with air, would be required to regenerate the original bed of Fe_2O_3.

- At higher temperatures, *e.g.* 1023 K, reduction reactions and reactions involving oxidation with steam are thermally neutral, whilst the oxidation of Fe_3O_4 to Fe_2O_3 in air is exothermic providing the largest source of heat, as shown in Table 1.2.

For the overall process, there is a tradeoff between the amount of H_2 produced and the amount of usable heat generated. Because the iron species are not consumed in the cyclic process, the overall reaction can be expressed as:

$$C_{(s)} + y\,H_2O + (1 - \frac{y}{2})\,O_2 \rightleftarrows CO_2 + y\,H_2, \qquad \Delta H^{\circ}_{1023\,K} = 249y - 395\,\mathrm{kJ/mol} \qquad (1.20)$$

where y is the moles of hydrogen produced *per* mole of $C_{(s)}$ and is limited by the iron transition used:

limits	iron transition	reactions
$0 < y < 2$	$Fe_3O_4 \rightleftarrows Fe_{0.947}O$, $Fe_3O_4 \rightleftarrows Fe$	(1.10,1.16),(1.10,1.11,1.15,1.16)
	$Fe_{0.947}O \rightleftarrows Fe$	(1.11,1.15)
$0 < y < \frac{16}{9}$	$Fe_2O_3 \rightleftarrows Fe$	(1.9-1.11,1.15-1.17)
$0 < y < 1.25$	$Fe_2O_3 \rightleftarrows Fe_{0.947}O$	(1.9,1.10,1.16,1.17)
$y = 0$	$Fe_2O_3 \rightleftarrows Fe_3O_4$	(1.9,1.17)

For example, the exothermic reaction (1.19) in Table 1.2 is reaction (1.20) with $y = 1.25$, *i.e.* a combination of either reaction (1.7) or (1.8) with reactions (1.9),(1.10) and (1.16),(1.17), and interestingly holds whether CO_2 or H_2O is used to gasify the carbon. The overall enthalpy can be decreased by decreasing y in reaction (1.20). Figure 1.2 shows the enthalpy against y, the moles of H_2 produced *per* mole of $C_{(s)}$, at 1023 K and 10^5 Pa. The maximum number of moles of H_2 *per* mole of $C_{(s)}$ that can be obtained while still keeping $\Delta H^\circ_{1023\ K} \leq 0$ is 1.59. The end point $y = 0$ corresponds to $\Delta H^\circ_{1023\ K} = -395$ kJ/mol, which is simply the enthalpy of reaction for $C_{(s)} + O_2 \rightleftarrows CO_2$; the end point $y = 2$ corresponds to $\Delta H^\circ_{1023\ K} = +102$ kJ/mol, which is the enthalpy of reaction for $C_{(s)} + 2\ H_2O \rightleftarrows CO_2 + 2\ H_2$.

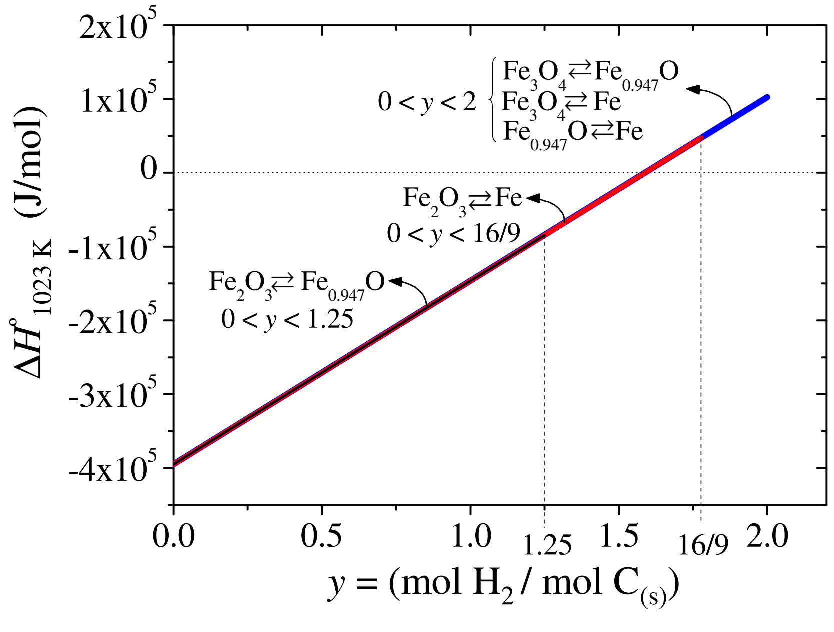

Figure 1.2: The tradeoff between usable heat and H_2 for the overall iron redox reaction, $C_{(s)} + y\ H_2O + (1 - \frac{y}{2})\ O_2 \rightleftarrows CO_2 + y\ H_2$, at 1023 K and 10^5 Pa.

Thus, solid carbon from either biomass or coal can be used to produce separate streams of

CO_2 for sequestration and high purity H_2 for energy consumption, as well as heat. Because the process requires neither an input of heat nor complicated separation units, it is suitable for operation on a distributed scale. However, the coupling of enthalpies between the process steps represents a challenge. While the previous description is specific to a packed bed reactor, other schemes capable of producing a concentration gradient, *e.g.* a counter-current moving bed or a sequence of fluidised beds could be used for the redox reactions (Cleeton *et al.*, 2009).

1.4 Objectives and structure of this dissertation

The principal aim of the work described in this dissertation was to present a fundamental investigation of the production of hydrogen by the reduction and oxidation of iron oxide. In particular, the objectives were as follows:

- to determine the iron oxide species, Fe_2O_3, Fe_3O_4, $Fe_{0.947}O$ or Fe, and operating temperature most suitable for the generation of pure hydrogen,
- to investigate the addition of elements Al, Cr, Mg and Si to enhance the yield of H_2 over repeated redox cycles,
- to describe mathematically the intrinsic kinetics of the reactions involved,
- to investigate the improvement of the reaction rates by the addition of promoters, *e.g.* Ce or Pt,
- to demonstrate the feasibility of producing pure H_2 from representative solid fuels whilst simultaneously capturing CO_2,
- to develop a mathematical model based on kinetic theory, *i.e.* a lattice Boltzmann model, to provide a fundamental, multi-scale description of the process.

This thesis is structured as follows. Chapter 1 outlines the background and presents an introduction to the production of hydrogen. Chapter 2 demonstrates that the production of hydrogen of high purity with simultaneous capture of CO_2 is possible using the redox reactions of iron oxide. In Chapter 3, an attempt to stabilise iron oxide for repeated reduction to Fe *via* the back-addition of Al, Cr, Mg or Si is presented. Chapter 4 investigates iron oxide modified with Al prepared using a sol-gel technique. Next, Chapter 5 presents a fundamental study on the reduction of iron oxide in mixtures of CO, CO_2 and N_2. Pre-exponential factors and activation energies were derived for the transitions from Fe_2O_3 to Fe_3O_4 and Fe_3O_4 to $Fe_{0.947}O$. The effect of chemical promoters on increasing the rate of reduction of Fe_3O_4 to $Fe_{0.947}O$ is studied in Chapter 6. Chapter 7 demonstrates that the production of pure H_2 from solid fuels is feasible. The rate parameters from Chapter 5 are then incorporated into a 3D lattice Boltzmann model of a packed bed in Chapter 8. Finally, conclusions and recommendations for future work are presented in Chapters 9 and 10.

The work presented in this dissertation has been published, or has been accepted for publication, in the following refereed journals (†, corresponding author):

- Bohn, C.D., Müller, C.R., Cleeton, J.P.E., Hayhurst, A.N., Davidson, J.F., Scott†, S.A., Dennis, J.S. Production of very pure hydrogen with simultaneous capture of carbon dioxide using the redox reactions of iron oxides in packed beds. Ind. End. Chem. Res. 2008, 47, 7623-7630.

- Bohn†, C.D.; Cleeton, J.P.E.; Müller, C.R.; Davidson, J.F.; Hayhurst, A.N.; Scott, S.A., Dennis, J.S. The kinetics of the reduction of iron oxide by carbon monoxide mixed with carbon dioxide. AIChE J. 2010, 56, 1016-1029.

- Kierzkowska, A.M; Bohn†, C.D.; Cleeton, J.P.E.; Scott, S.A.; Dennis, J.S; Müller, C.R. Development of iron oxide carriers for chemical looping combustion using sol-gel. Ind. Eng. Chem. Res. 2010, 49, 5383-5391.

- Bohn†, C.D.; Cleeton, J.P.E.; Müller, C.R.; Scott, S.A.; Dennis, J.S. Stabilising iron oxide used in cycles of reduction and oxidation for hydrogen production. Energy Fuels. 2010, 24, 4025-4033.

Further work has been published in the following refereed journals:

- Cleeton†, J.P.E; Bohn, C.D.; Müller, C.R.; Dennis, J.S.; Scott, S.A. Clean hydrogen production and electricity from coal via chemical looping: Identifying as suitable operating regime. Int. J. Hydrogen Energy. 2009, 34, 1-12.

- Müller†, C.R.; Pacciani, R.; Bohn, C.D.; Scott, S.A.; Dennis, J.S. Investigation of the enhanced water gas shift reaction using natural and synthetic sorbents for CO_2 capture. Ind. Eng. Chem. Res. 2009, 48, 10284-10291.

Chapter 2

Production of hydrogen using the reduction and oxidation of iron oxide

2.1 Introduction

Despite the abundance of literature on the redox reactions of iron and its oxides, it is still unclear as to which temperatures and transitions, *viz.* Fe_2O_3 - Fe, Fe_2O_3 - $Fe_{0.947}O$, Fe_3O_4 - Fe or Fe_3O_4 - $Fe_{0.947}O$, are preferable for a cyclic scheme to produce hydrogen. In this Chapter, all four possible transitions are examined at 873, 1023 and 1173 K. The experimental results are then discussed in the light of industrial application, *e.g.* maximising the yield of H_2, maximising the heat output and maintaining the purity of the H_2.

2.2 Experimental

The particles of iron oxide were prepared from Fe_2O_3 powder (Sigma-Aldrich; purity > 99.9 wt. %; size < 5μm). Water, which had been purified by reverse osmosis (Millipore Milli-Q; > 18 MΩ), was sprayed on to the powder to form agglomerates. The resulting mixture was mechanically stirred both during and after spraying, and then the granules were sieved to the desired sieve size fraction of +425,-600 μm. These particles were then sintered in an oven at 1173 K for 3 h, subsequently cooled in air and then re-sieved to a sieve size of +425,-600 μm.

The packed bed reactor was made from 316 stainless steel tubing (I.D. 10.2 mm; total length 430 mm) as shown in Fig. 2.1. A stainless steel plate (1 mm thick) supported the bed: the plate contained 8 evenly-spaced holes on a circular pitch, each with a diameter of

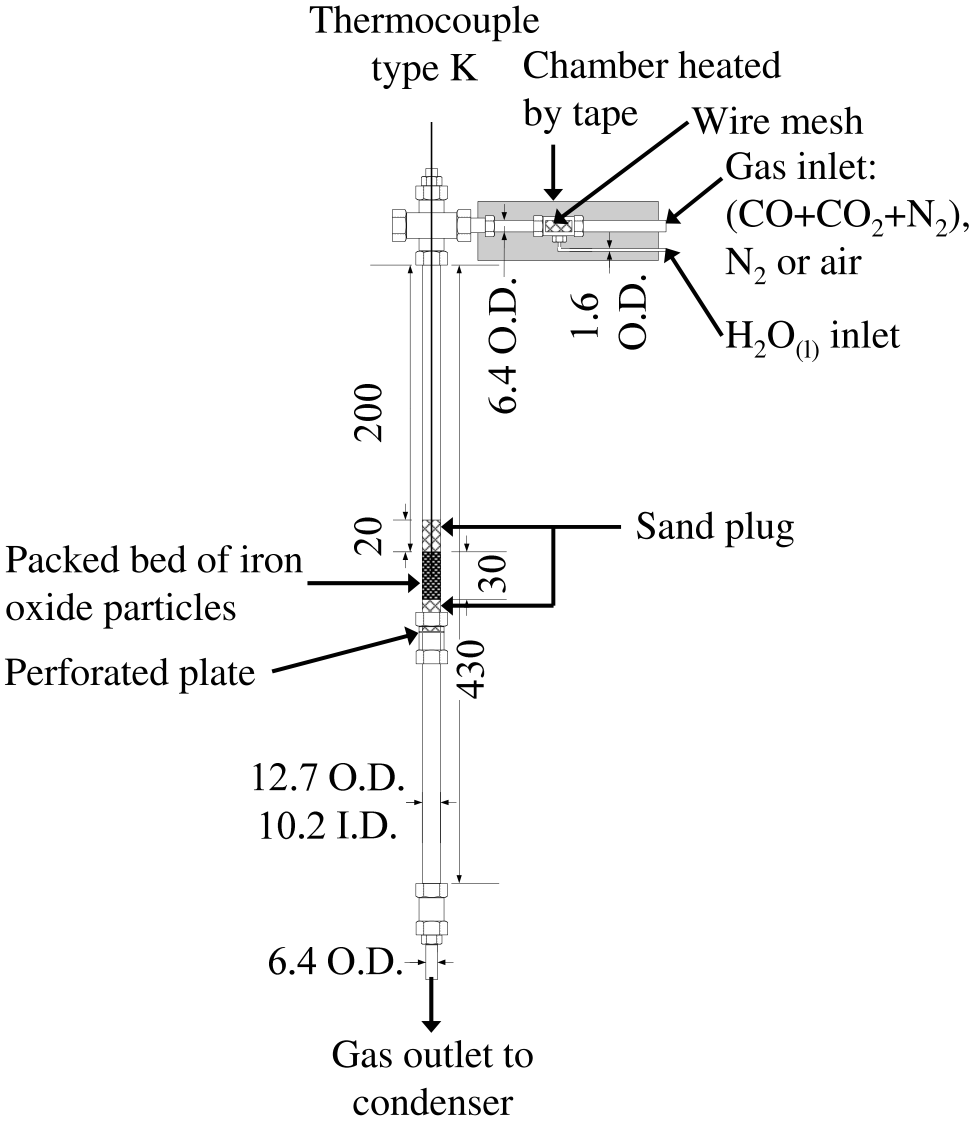

Figure 2.1: Schematic diagram of the reactor containing a packed bed supported on a perforated plate. Resting on the plate was a 4 g plug of sand, supporting the active bed, with another 4 g plug of sand on top. The active bed was either: (i) 20 g Fe_2O_3 particles, see section 2.3.1, or (ii) 1 g of Fe_2O_3 particles mixed with 4 g sand, see sections 2.3.2- 2.3.6. The thermocouple extends to the centre of the active bed. All measurements are in mm.

1 mm. The entire assembly was placed in a tubular furnace and the temperature of the bed was controlled by a K-type thermocouple which had been inserted into the bed.

The reduction of the iron oxide particles was performed using mixtures of: (i) 10 vol. % CO with balance N_2 and (ii) pure CO_2 (BOC plc.; laboratory grade). The flowrates of the gases, except CO_2, were metered into the reactor using mass flow meters (Honeywell AWM5101N) followed by flow control valves. The flowrate of CO_2 was measured with a rotameter. In all cases, the total gas flow was maintained at $\sim 3.3 \times 10^{-5}$ m^3/s, as measured at 10^5 Pa and 298 K. The composition of the reducing gas mixture was chosen, based on Fig. 1.1, to give the desired iron phase at the specified temperature, as seen in Table 2.1. Between each reduction and oxidation stage, the reactor was purged with nitrogen, as shown in Table 2.1.

In order to reoxidise the iron with steam, a syringe pump was used to feed liquid H_2O through a hypodermic tube (0.8 mm I.D.) into an electrically-heated chamber, which was packed with stainless steel mesh to increase the surface area for heat transfer. The water was vaporised and conveyed into the reactor by means of a N_2 sweep gas. Reoxidation to Fe_2O_3 was achieved using air from the laboratory compressed air supply, also metered into the reactor using a mass flow meter (Honeywell AWM5101N) and a control valve. Miniature solenoid valves (Burkert) were used to switch gas streams. A summary of cycle times and gases is presented in Table 2.1 for experiments.

The gas leaving the reactor was cooled to condense most of the water, before being passed through a tube filled with $CaCl_2$ to remove any residual water. The composition of the dried gas was determined by: (1) a non-dispersive infrared (NDIR) analyser measuring $[CO_2]$ and [CO] (ABB Easyline, both 0-20 vol. %); (2) a more sensitive NDIR for [CO] (ABB Easyline, 0-2000 ppmv); (3) a thermal conductivity meter measuring $[H_2]$ (ABB Caldos27, 0-30 vol. %). A description of infrared spectroscopy and other experimental techniques used in this dissertation is presented in Appendix 2. Mass balances on CO and CO_2 confirmed that reduction to a specified oxidation state of the metal had occurred for a given temperature with errors in the closure of the balance being less than 10 %.

Depending on the experiment, the bed was loaded in one of two ways. In each case, particles of Fe_2O_3 were sandwiched between layers of inert quartz sand (David Ball Co.; +425,-500 μm, 4 g), as shown in Fig. 2.1. The upper layer of sand aided in preheating the inlet gas prior to contact with the iron particles; the lower layer prevented iron particles from passing through the holes in the perforated plate. For the experiments described in section 2.3.1, a packed bed of 20.0 g of iron oxide particles ($425 - 600\ \mu$m; $d_p = 513\ \mu$m) was used. The active

Table 2.1: Redox cycling: gas mixtures (vol. %), flowrates (m^3/s) as measured at 298 K and 10^5 Pa and corresponding flow durations (s) for experiments with an initial charge of Fe_2O_3 of 1 g. Reoxidation to Fe_2O_3 required air (a).

	purge	reduction	purge	steam oxidation	purge	(a) air oxidation	(b) purge	Figs.
time (s)	0-60	60-660	660-720	720-960	960-1020	1020-1260	1020-1200	
flow (m^3/s)	3.3×10^{-5}	3.3×10^{-5}	3.3×10^{-5}	3.3×10^{-5} N_2	3.3×10^{-5}	3.3×10^{-5}	3.3×10^{-5}	
flow (m^3/s)				8.33×10^{-9} $H_2O_{(l)}$				
$Fe_2O_3 \rightleftarrows Fe$	N_2	10% CO/90% N_2	N_2	75% N_2/25% steam	N_2	air		2.5a,2.7,2.9
$Fe_2O_3 \rightleftarrows Fe_{0.947}O$	N_2	9% CO/9% CO_2/82% N_2	N_2	75% N_2/25% steam	N_2	air		2.2,2.3,2.5b,2.7
$Fe_3O_4 \rightleftarrows Fe$	N_2	10% CO/90% N_2	N_2	75% N_2/25% steam	N_2		N_2	2.7
$Fe_3O_4 \rightleftarrows Fe_{0.947}O$	N_2	9% CO/9% CO_2 /82% N_2	N_2	75% N_2/25% steam	N_2		N_2	2.4,2.7

bed had a length of $L \sim 200$ mm and an inner diameter of $d_{\text{bed}} \sim 10.2$ mm, giving $L/d_{\text{p}} = 390$ for the bed of iron oxide and $d_{\text{bed}}/d_{\text{p}} = 20$. Here, L = bed length, d_{p} = particle diameter and d_{bed} = bed diameter. The bed length of 200 mm was just shorter than the length (250 mm) of the heated section in the furnace. For experiments described in sections 2.3.2 - 2.3.6, the bed was made by carefully mixing 1.0 g of iron oxide particles with 4.0 g of inert sand. The 1 g of active material was mixed with sand to prevent maldistribution of reactant gas and to ensure near isothermal operation during the reduction and oxidation steps. For experiments with only 1 g of particles of Fe_2O_3, $L/d_{\text{p}} = 137$ and $d_{\text{bed}}/d_{\text{p}} = 20$.

To rule out any reaction of the stainless steel reactor or impurities in the sand, a series of blank experiments were performed with the reactor filled only with sand. The conversion of an equimolar mixture of CO and CO_2 in this case was less than 1 % of the conversion seen in a typical experiment when 1 g of Fe_2O_3 was reduced to $Fe_{0.947}O$ by CO.

2.3 Results

2.3.1 Capture of CO_2 and production of H_2

Figure 2.2 shows the composition of the effluent gas as a function of time for an experiment with 20 g of Fe_2O_3 in a packed bed maintained at 1023 K. The Fe_2O_3 was not mixed with sand; however, 4 g of sand was placed on either end of the plug of Fe_2O_3. Initially, N_2 was flowing through the reactor. From $t = 90$ s to $t = 810$ s, the reducing gas was passed through the bed. Nearly all the entering CO was converted to CO_2 and the mole fraction of CO at the exit remained consistently below 5 ppmv. Once the Fe_2O_3 was exhausted, *i.e.* converted to $Fe_{0.947}O$ or Fe_3O_4, CO broke through between $t = 810$ s and $t = 850$ s. The reducing gas

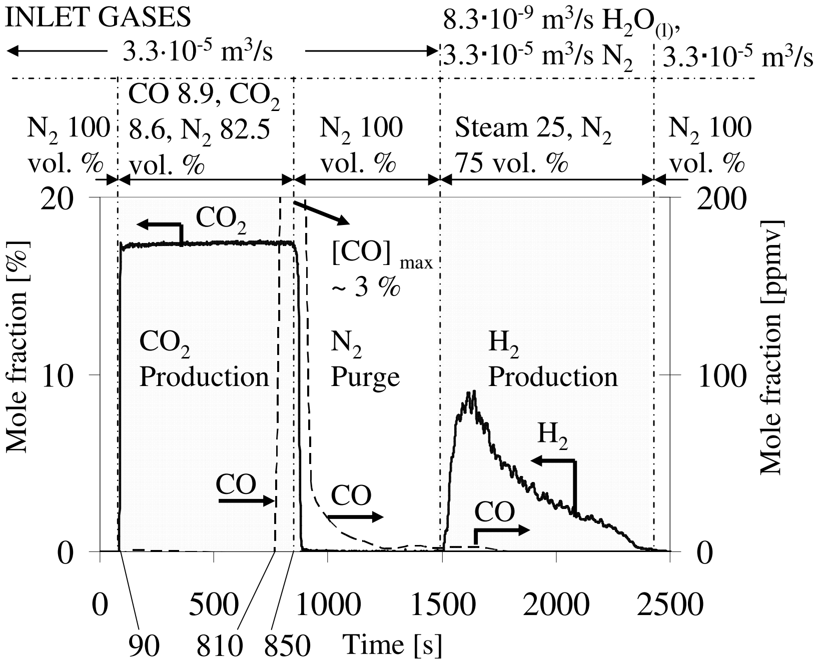

Figure 2.2: Reduction and subsequent oxidation in steam for the transition from Fe_2O_3 to $Fe_{0.947}O$ at 1023 K with a 20 g charge of Fe_2O_3 (no sand). The compositions of the inlet gases are shown; the dashed vertical lines (- · -) indicate the times when the inlet gas to the reactor was changed.

was then turned off, so that minimal CO escaped from the bed. Next, the N_2 purge stream was turned on from $t = 850$ s to $t = 1500$ s. During this time, the trace mole fraction of CO decayed, as shown in Fig. 2.2. Next, from $t = 1500$ s to $t = 2400$ s, steam was supplied and hydrogen of high purity was produced; the concentration of CO did not exceed 5 ppmv during this phase. The purity of this manufactured hydrogen therefore exceeded the constraint required by PEM fuel cells, where CO levels above 50 ppmv are known to poison the Pt anode (Choudhary and Goodman, 2002).

Figure 2.2 demonstrates the feasibility of using the redox reactions (1.9-1.10 and 1.15, respectively, in Table 1.2) of iron oxides to produce both CO_2 suitable for sequestration and H_2 pure enough for use in PEM fuel cells. A mass balance on the effluent stream during reduction ($90 \text{ s} < t < 850 \text{ s}$) shows that more CO_2 is produced than is theoretically obtainable for the transition from Fe_2O_3 to Fe_3O_4 alone. Using the thermodynamically-consistent assumption that the charge of 20 g of Fe_2O_3 reacts sequentially to form Fe_3O_4 and then $Fe_{0.947}O$, the mass balance reveals that ~ 66 % of the Fe_3O_4 formed had been reduced to $Fe_{0.947}O$. In the following sections, a sustained CO_2 effluent gas during the reduction phase was not the primary objective. As such, a shorter, differential packed bed with an initial loading of 1.0 g of Fe_2O_3 mixed with sand was used, and reduction was allowed to proceed to completion, *i.e.* until the composition

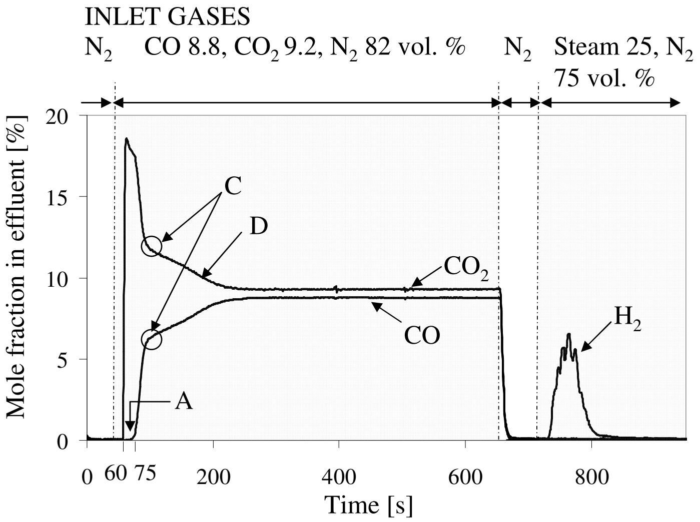

Figure 2.3: Reduction and subsequent steam oxidation for the transition from Fe_2O_3 to $Fe_{0.947}O$ at 1023 K using a 1 g charge of Fe_2O_3. The dashed vertical lines (- · -) indicate the times when the inlet gas to the reactor was changed.

of the outlet gas from the reactor was identical to that at the inlet.

2.3.2 Reduction and oxidation of oxides of iron

One question regarding the redox reactions of iron oxide in a packed bed is whether the transitions between metal oxides occur at sharp fronts or more gradually. Figure 2.3 shows mole fractions in the effluent gas as a function of time for an experiment in which 1 g of Fe_2O_3 was reduced to $Fe_{0.947}O$ at 1023 K. This experiment is identical to that in Fig. 2.2 except that 1 g of Fe_2O_3 mixed with sand, not 20 g of Fe_2O_3 with no sand, was used as the bed and the reducing gas mixture was not switched off at the point of CO slip, *i.e.* the point at which detectable CO occurs in the effluent. Even in this short bed, complete conversion of the inlet CO occurred for 15 s (such that the CO slip was less than 0.05 vol. %) between $t = 60$ s and $t = 75$ s (point A). A simple mass balance shows that the inflow of CO required for the theoretical conversion of 1g of Fe_2O_3 to Fe_3O_4 is nearly identical to the amount entering the bed during this 60-75 s period of time. The kinetics of the transition from Fe_2O_3 to Fe_3O_4, therefore, seem fast enough for the gases to reach equilibrium within the residence time of gas in the bed, which, for the given conditions and an assumed voidage of 0.4, was ~ 0.2 s.

For the transition from Fe_3O_4 to $Fe_{0.947}O$, Fig. 1.1 gives $K_p = p_{CO_2}/p_{CO} = 1.87$ at 1023 K. This equilibrium value corresponds to a kink (point C) in the outlet CO and CO_2 in Fig. 2.3. The ensuing change in slope (point D) demonstrates that the reaction from Fe_3O_4 to $Fe_{0.947}O$

(reaction 1.10 in Table 1.2) is no longer limited by the inlet flow of gas; instead, kinetic or mass transfer effects, or both, come into play. Fig. 2.3 shows that the total time for reaction (1.10) to reach completion is $t = 250 - 75 = 175$ s; significantly longer than the time to reduce Fe_2O_3 to Fe_3O_4. At $t = 250$ s, the effluent gas concentration had reached the inlet condition of 9.2 vol. % CO_2 and 8.8 vol. % CO. A mass balance on the CO consumed shows that if reduction occurs in a stagewise process, Fe_2O_3 to Fe_3O_4 to $Fe_{0.947}O$, 94 mole % of the Fe_3O_4 formed was reduced to $Fe_{0.947}O$. A commensurate mass balance on the H_2 produced shows that if all of the Fe_2O_3 is initially reduced to $Fe_{0.947}O$, 92 mole % of the resulting $Fe_{0.947}O$ is subsequently oxidised by steam to Fe_3O_4, demonstrating that acceptable closure between reduction and oxidation can be achieved.

Besides examining the reaction times for the various metal oxide transitions during reduction, the overall reduction time was also compared to the overall oxidation time. Figure 2.4 shows results when the iron oxide was: (a) reduced to $Fe_{0.947}O$ in a mixture of CO and CO_2 and (b) reoxidised to Fe_3O_4 with steam. In the first cycle, the oxide started as Fe_2O_3; subsequent cycles began with Fe_3O_4. Figure 2.4(a) shows the cumulative amount of CO_2 released during the first five cycles of reduction, calculated by integrating the difference between the outlet and inlet mole fractions of CO_2 with respect to time. The theoretical amount of CO_2 generated in going from Fe_3O_4 to $Fe_{0.947}O$ (reaction 1.10, Table 1.2) can be determined from the mass of iron oxide loaded into the reactor, *viz.* 1 g of Fe_2O_3. Figure 2.4(a) shows that the cumulative amount of CO_2 generated, given by the solid lines (—), was ∼ 90 % of the theoretical value, given by the horizontal dashed line (- - -). Also shown in Fig. 2.4(a) is the amount of CO_2 for the case where all the entering CO is converted to CO_2 (- · · · -). Only for the first cycle is the experimental curve a tangent to this line, again demonstrating that the inflow of reactant gas is rate-limiting for the initial reduction of Fe_2O_3 to Fe_3O_4.

Figure 2.4(b) shows the cumulative amount of H_2 produced when steam was used to oxidise $Fe_{0.947}O$ back to Fe_3O_4 (reaction 1.16, Table 1.2). The time for the reaction with steam to reach completion is noticeably shorter than that for the reduction in the mixture of CO_2 and CO; this difference becomes increasingly apparent after more cycles. Here, it should be noted that the mole fraction of steam was 25 vol. % (5.2 mol/m^3 at 10^5 Pa, 298 K), whereas that of CO had been 9 vol. % (3.7 mol/m^3 at 10^5 Pa, 298 K), so a direct comparison between the rates of reduction and oxidation is not possible.

A comparison between the final molar amounts from the curves in Figs. 2.4(a) and (b) is then given in Fig. 2.4(c). It is clear that the amounts of CO_2 released during the reduction

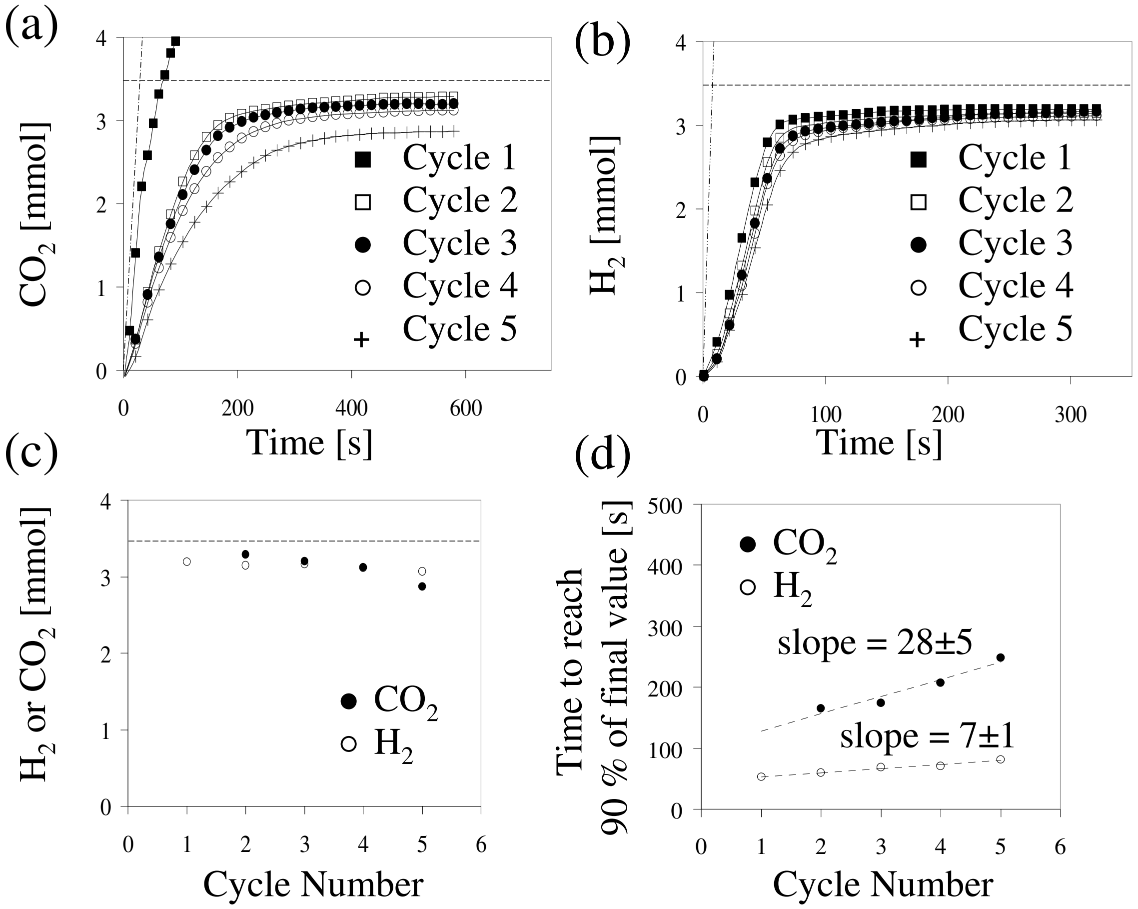

Figure 2.4: Cycles of reduction and oxidation with a 1 g charge of Fe_2O_3 at 1023 K: reduction by inlet gas containing CO 9 vol. %, CO_2 9 vol. %, N_2 82 vol. %, followed by oxidation using steam 25 vol. %, N_2 75 vol. %. The bed was Fe_2O_3 at the start of the first cycle; subsequently the oxide cycled between Fe_3O_4 and $Fe_{0.947}O$. (a) Cumulative integrals of CO_2 produced over five cycles. (b) Corresponding cumulative integrals for H_2. (c) Comparison between the five final values of each graph. (d) Times to reach 90 % of the final values in (a) and (b). In (a) - (c), the dashed horizontal line (- - -) marks the theoretical limit of H_2 or CO_2 for conversion of the original charge between Fe_3O_4 and $Fe_{0.947}O$. The sloped line (- ·· -) in (a) or (b) marks the integral of the inlet flow for reactant (a) CO or (b) steam.

of Fe_3O_4 to $Fe_{0.947}O$ and the H_2 produced during the oxidation of the reduced oxide back to Fe_3O_4 are in good agreement. Thus, it seems that all the metal which is reduced to wuestite is subsequently available for reoxidation with steam. Figure 2.4(d) plots the time to reach 90 % of the final value for the curves in Figs. 2.4(a) and (b). For hydrogen the final value is assumed to be at $t = 320$ s, while for CO_2 the final value is assumed to be at $t = 580$ s. Figure 2.4(d) suggests that, because the time to 90 % conversion increases progressively with increased numbers of cycles, the average rate of reaction falls from one cycle to the next for both reduction and oxidation.

2.3.3 Reduction to $Fe_{0.947}O$ *versus* reduction to Fe

If the iron system is to be used for producing hydrogen, one important consideration is how far to reduce the oxide. Reduction to either $Fe_{0.947}O$ or Fe depends on the composition of the synthesis gas and the constraint imposed by chemical equilibrium at the chosen reaction temperature, as seen in Fig. 1.1. Reduction to Fe would be advantageous, since the capacity for producing hydrogen over the Fe to Fe_3O_4 transition is approximately four times greater than that over the transition from $Fe_{0.947}O$ to Fe_3O_4, based on equal masses of Fe_3O_4.

To examine the difference between reducing Fe_2O_3 to Fe *versus* reducing it to $Fe_{0.947}O$, redox experiments over both transitions were performed at 873, 1023 and 1173 K. In these experiments, the reducing gas was 10 vol. % CO, 90 vol. % N_2 for reduction from Fe_2O_3 to Fe and 9 vol. % CO, 9 vol. % CO_2 and 82 vol. % N_2 for reduction from Fe_2O_3 to $Fe_{0.947}O$; oxidation to Fe_3O_4 used 25 vol. % steam, 75 vol. % N_2; oxidation of the Fe_3O_4 to Fe_2O_3 used air (21 vol. % O_2, 79 vol. % N_2), as shown in Table 2.1. Figure 2.5(a) shows that for the Fe_2O_3 to Fe transition at all three temperatures the amount of H_2 produced decreases rapidly after the first cycle. The most precipitous drops are observed for particles at 1023 K and 1173 K, suggesting that thermal sintering could contribute to the fall in reactivity. At 873 K, the production of H_2 declines less sharply from one cycle to the next; however, after ten cycles, H_2 production at all three temperatures is unsatisfactorily low, having dropped below that achievable with the $Fe_{0.947}O$ to Fe_2O_3 transition. In contrast to Fig. 2.5(a), hydrogen production from $Fe_{0.947}O$ remains more consistent from cycle to cycle in Fig. 2.5(b). Here, the average amount of H_2 produced during the tenth cycle is $\sim$ 80% of that produced during the first cycle. Thus, with the current form of the iron oxide, it is preferable to reduce Fe_2O_3 to $Fe_{0.947}O$ instead of to metallic Fe. It should be noted that the reduction time of 600 s was kept constant

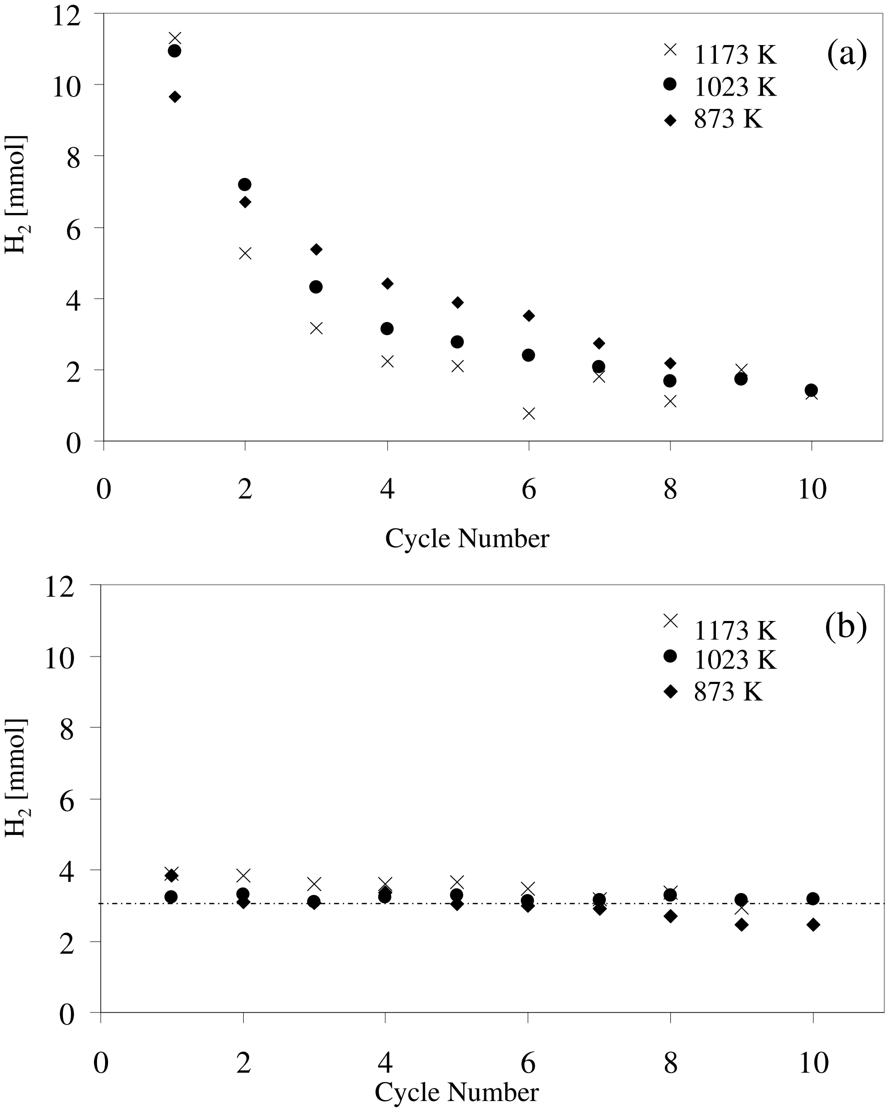

Figure 2.5: Effect of the number of cycles of reduction/oxidation on the production of hydrogen at different temperatures for alternative transitions: (a) Fe_2O_3-Fe (b) Fe_2O_3-$Fe_{0.947}O$; the dashed line gives the theoretical amount of H_2 starting with 1 g of Fe_2O_3. The theoretical amount of H_2 starting with a 1 g charge of Fe_2O_3 in (a) is 16.7 mmol.

for experiments as given in Table 2.1. For the reduction of Fe_2O_3 to Fe the outlet gas had returned to a composition ($\geq$ 9.7 vol. % CO, $\leq$ 0.3 vol. % CO_2, 90 vol. % N_2) before the valve switch compared to the inlet value (10 vol. % CO, 90 vol. % N_2). Thus, for these experiments some of the iron oxide may still have been reacting or, as discussed in section 2.3.5 , carbon was probably being deposited at the end of the reduction cycle.

To determine whether the drop in H_2 produced upon reduction to Fe was a result of incomplete reduction or incomplete oxidation, the quantity of CO consumed during reduction and H_2 produced during oxidation for each cycle at 1023 K was determined and is plotted in Fig. 2.6. The CO consumed in cycle 1 is near that expected from the reduction of a 1 g charge of Fe_2O_3 to Fe, shown by the horizontal solid line, while the H_2 produced upon subsequent oxidation with steam is lower than that expected for the oxidation of Fe to Fe_3O_4, shown by the horizontal dotted line. For reduction in cycle 2, however, the CO consumed is considerably below that expected and also below that expected if only the iron capable of producing H_2 from the previous cycle is considered. Thus, it appears that the loss in reactivity of the solids is a result of both incomplete oxidation in cycle 1 and incomplete reduction in cycle 2. For cycles 3-10, the moles of CO consumed and H_2 produced are very nearly equal and it is difficult to draw firm conclusions. It is noted that while the deposition of solid carbon was possible for experiments in Fig. 2.6, the total moles of CO and CO_2 produced during oxidation with steam and then with air was negligible, < 0.1 mmol in each cycle.

2.3.4 Oxidation to Fe_2O_3 *versus* Fe_3O_4

Besides the issue of how far to reduce the metal oxide, there is also the question of how far to reoxidise it, *i.e.* back to Fe_3O_4 or to Fe_2O_3. For the proposed process, the presence of Fe_2O_3 near the outlet from the reactor is crucial for minimising CO slip during the reduction of the metal oxide as well as for maintaining $\Delta H_T^\circ < 0$ overall. Other processes for the production of hydrogen proposed in the literature (Galvita and Sundmacher, 2007), however, only reoxidise to Fe_3O_4. Final oxidation in air has the potential to oxidise any contaminants, *e.g.* carbon or sulphur, deposited on the particles, but it also causes a large temperature rise in the bed and so could result in thermal sintering.

Experiments were performed with and without additional oxidation of Fe_3O_4 to Fe_2O_3. To ensure that the particles were reacted for the same cycle times, a stream of N_2 replaced the air in experiments without the additional oxidation step. Measurements indicated that the final ox-

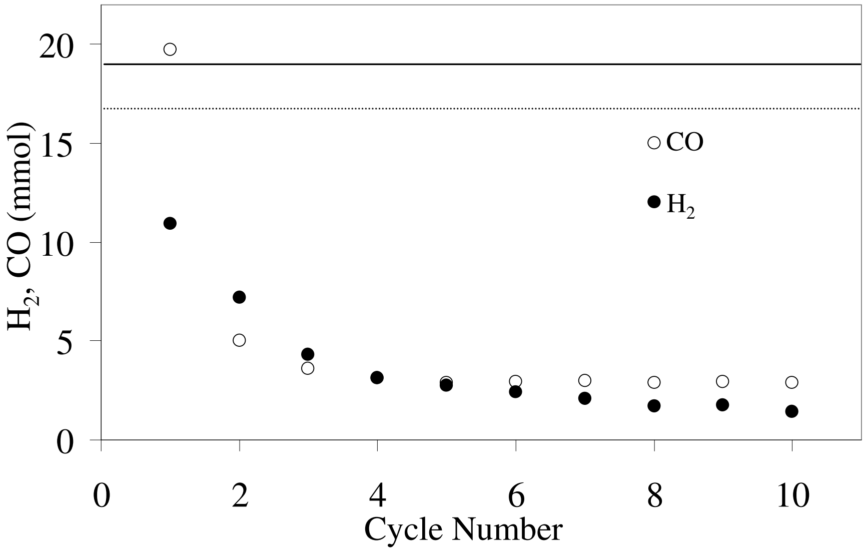

Figure 2.6: Starting with 1 g of Fe_2O_3 mixed with sand at 1023 K, the quantity of CO consumed for $Fe_2O_3 \rightarrow Fe$ and subsequent H_2 produced for $Fe \rightarrow Fe_3O_4$ is shown; further oxidation of $Fe_3O_4 \rightarrow Fe_2O_3$ was performed with air. The solid horizontal line gives the theoretical consumption of CO expected; the dotted horizontal line gives the theoretical production of H_2 expected.

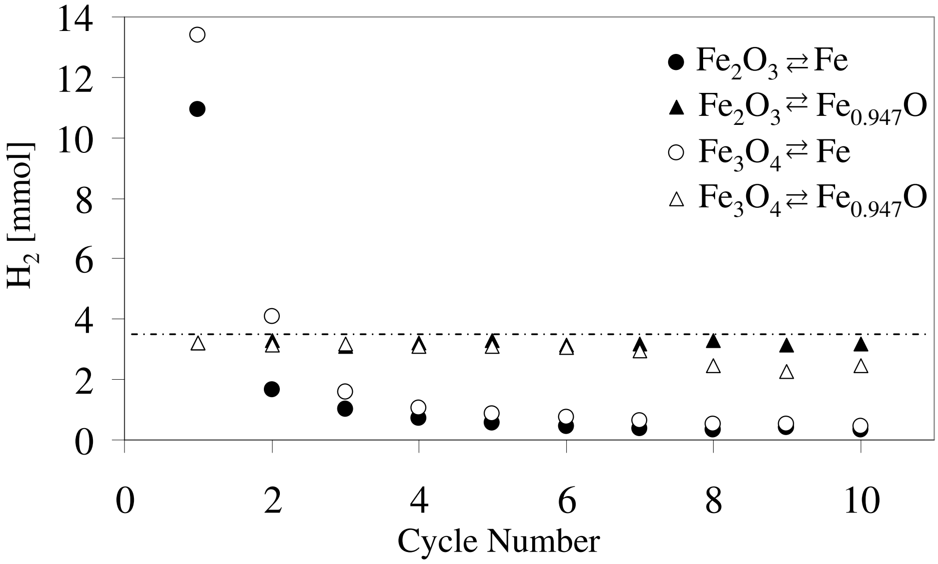

Figure 2.7: Total amounts of hydrogen produced in cycles using the transitions of iron oxide at 1023 K showing the effect of the number of cycles of reduction/oxidation on producing hydrogen. In each case, the basis was a 1 g charge of Fe_2O_3. The dashed line gives the theoretical amount of H_2 for reduction to $Fe_{0.947}O$, 3.5 mmol; the theoretical amount of H_2 for reduction to Fe is 16.7 mmol.

idation in air caused a temperature rise as high as 50 K in a packed bed initially containing 1 g of Fe_2O_3 particles with sand. A simple heat balance confirmed that the theoretical temperature rise when converting Fe_3O_4 to Fe_2O_3 should be just over 50 K, as shown in Appendix 3.

Figure 2.7 shows the total amount of H_2 produced during the transitions from Fe_2O_3 to Fe, Fe_3O_4 to Fe, Fe_2O_3 to $Fe_{0.947}O$ and Fe_3O_4 to $Fe_{0.947}O$ at 1023 K. From Fig. 2.7, the drop in hydrogen production for the Fe_2O_3 to Fe transition follows the same course as that for Fe_3O_4 to Fe. Little difference in the capacity for producing hydrogen is observed between the transitions Fe_2O_3 to $Fe_{0.947}O$ and Fe_3O_4 to $Fe_{0.947}O$ either. Comparing the results for these transitions, Fig. 2.7 demonstrates that the temperature rise during the additional oxidation in air to give Fe_2O_3 seems to have no adverse affect on the amount of hydrogen generated; a slight improvement can even be observed, for later cycles, when the final oxidation is with air. It should be noted that the reducing gas used in these experiments was of laboratory grade. Consequently, any benefits from the additional oxidation of contaminants other than deposited carbon, such as sulphur, which might be present in industrial synthesis gas, would not have been observed.

2.3.5 Deposition of carbon

Thermodynamically it is possible that carbon was deposited on the particles when iron oxide was reduced by CO to Fe at 873 K, 1023 K and 1173 K and also in those experiments involving reduction to $Fe_{0.947}O$ at 873 K. Once deposited, the carbon could be reoxidised to CO or CO_2 during oxidation in steam or in air.

Figure 2.8 shows the mole fractions of CO_2, CO and H_2 as functions of time for the first cycle, oxidising Fe to Fe_3O_4 in steam at 873 K. Reduction to Fe in 10 vol. % CO, balance N_2 at 873 K was the condition most favourable to the deposition of carbon and represented a worst case for producing H_2 of high purity. The mole fraction of CO reached a maximum of 4600 ppmv and exceeded the benchmark of 50 ppmv for the duration of the oxidation stage, as seen in Fig. 2.8. The mole fraction of CO decreased with increasing T for reduction to Fe.

If the particle was reoxidised to Fe_2O_3, any residual solid carbon, not oxidised during the inflow of steam, reacted with oxygen in the air to form CO_2. Figure 2.9 shows the amounts of CO_2 produced during oxidation with air at 873 K. It is notable that cycles 2 and 3 gave more CO_2 in the off-gas than cycle 4, consistent with the fact that Fe catalyzes (Towhidi and Szekely, 1983) the Boudouard reaction (1.18) and that the amount of reactive Fe diminishes

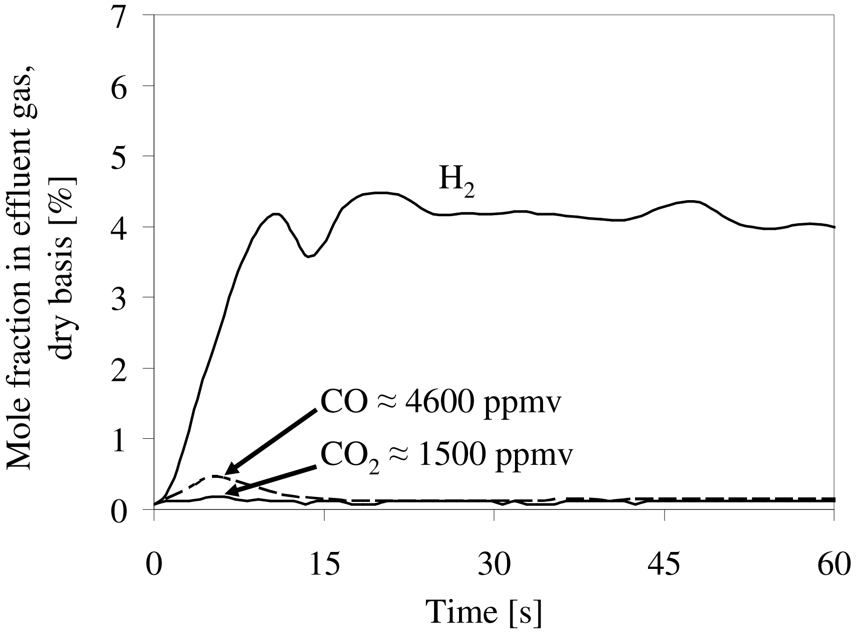

Figure 2.8: The first 60 s of the oxidation of Fe to Fe_3O_4 in steam at 873 K. Prior to the oxidation, 1 g of Fe_2O_3 had been reduced by a the mixture, CO 10, N_2 90 vol. %, depositing carbon on the particles. Contamination of the H_2 by CO and CO_2 is apparent.

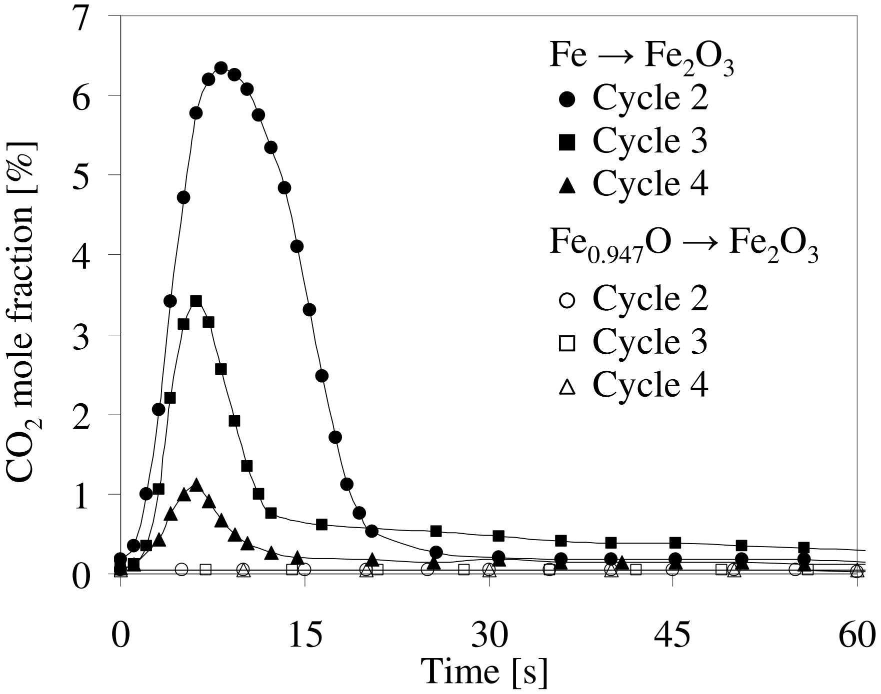

Figure 2.9: Oxidation in air for the Fe → Fe_2O_3 and $Fe_{0.947}O$ → Fe_2O_3 transitions at 873 K for cycles 2,3 and 4. CO_2 is produced by oxidation of residual carbon, which was deposited during reduction of the 1 g charge of Fe_2O_3 in CO and which had not been removed during oxidation with steam. Even though the Boudouard reaction (1.18) is thermodynamically favoured, little CO_2 is produced for the case of $Fe_{0.947}O$.

with increasing numbers of redox cycles, as seen by the fall in the amount of H_2 produced in Fig. 2.5(a). Another interesting finding from Fig. 2.9 is that very little CO_2 was produced during oxidation in air, when $Fe_{0.947}O$ was the lowest form of the oxide used at 873 K. This observation suggests that the rate of the Boudouard reaction (1.18) is sufficiently slower than that of the reduction reactions (1.9-1.10) to prevent significant carbon deposition for reduction to $Fe_{0.947}O$. Here, it should be noted that reduction to Fe occurred in a gas containing 10 vol. % CO, balance N_2 whereas reduction to $Fe_{0.947}O$ occurred in a gas containing 9 vol. % CO, 9 vol. % CO_2, balance N_2 in order to ensure that the $Fe_{0.947}O$ was not reduced further to Fe. The presence of CO_2 in the latter case would also have impeded the kinetics for the deposition of carbon.

2.3.6 Purity of hydrogen

If the hydrogen produced in the packed bed is to be used in low temperature PEM fuel cells, it must contain less than ~ 50 ppmv of CO. It has already been shown for the 20 g bed in Fig. 2.2 that if a sufficiently long period of purging with N_2 is used, H_2 with the necessary purity can be produced. Figure 2.10 shows the mole fraction of CO during the oxidation in steam of $Fe_{0.947}O$ to Fe_3O_4 at 1023 K. Considering this temperature, a pressure of 10^5 Pa and that reduction occurred with $p_{CO_2}/p_{CO} = 1$, the Boudouard reaction (1.18) is not thermodynamically feasible since for these conditions $K_p = p_{CO_2}/p_{CO} = 0.3$, as shown in Fig. 1.1, so carbon should not be deposited during reduction of the metal oxide in a mixture of CO and CO_2. However, some CO was observed during the production of hydrogen and is a result of residual CO from the reduction of Fe_2O_3 to $Fe_{0.947}O$ being swept from the system. In Fig. 2.10, the average mole fraction of CO was determined to be 23 ppmv, demonstrating that a purge of N_2 for 60 s between the reduction cycle and the oxidation with steam is sufficient to produce pure hydrogen. From the decreasing CO curve in Fig. 2.10, it seems that the purity of the hydrogen can be specified to a desired level by adjusting the length of the N_2 purge accordingly, *i.e.* using a longer purge for higher purity H_2 and shorter purge for lower purity H_2.

2.4 Discussion

If fossil fuels are to be used to produce hydrogen, capture of the byproduct CO_2 is essential. Figure 2.2 showed that a process, which both made H_2 of sufficient purity for use in PEM fuel

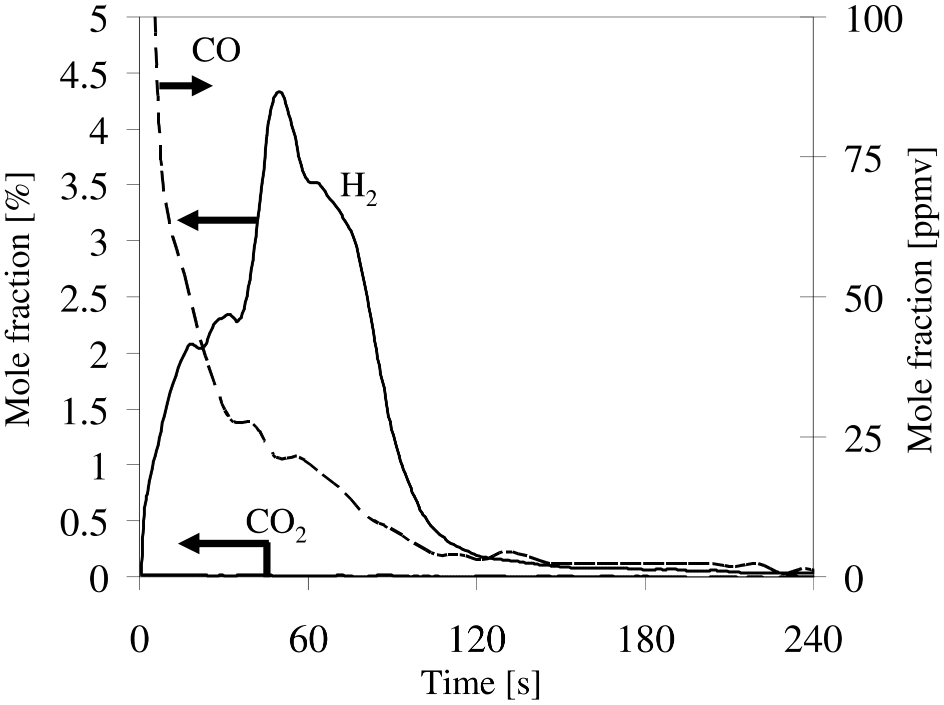

Figure 2.10: Hydrogen production (average CO level < 25 ppmv) of the $Fe_{0.947}O$ to Fe_2O_3 transition at 1023 K. The initial charge of Fe_2O_3 was 1 g.

cells and could separate CO_2 for potential sequestration, is feasible using the redox reactions of iron (1.9-1.11,1.15-1.17) in a packed bed. The CO slip was below the detection limit of the analysers used (< 5 ppmv in the CO_2 stream) during the reduction of the iron oxide and the hydrogen produced in the subsequent reoxidation of the iron oxide with steam had a content of CO < 5 ppmv, as seen in Fig. 2.2.

The results in Fig. 2.3 for the first 200 s suggest the following with regard to the reduction of iron oxides in a packed bed: (a) the total conversion of CO to CO_2 during the time 60 – 75 s suggests rapid reaction, giving a sharp front between Fe_2O_3 and Fe_3O_4 (b) the subsequent reduction of Fe_3O_4 to $Fe_{0.947}O$ during the time 75 – 200 s, is slower, so there is an ill-defined ‘front’ where Fe_3O_4 is converted to $Fe_{0.947}O$. The overall time to reduce the particles is also longer than that to oxidise them for the gas compositions chosen, as seen in Fig. 2.4. A loss in reactivity with increasing cycle number was observed and shown to be more pronounced for reduction than oxidation between Fe_3O_4 and $Fe_{0.947}O$, as shown in Fig. 2.4(d). Therefore, increasing the rate of reduction to $Fe_{0.947}O$ is critical for improving the overall performance of the process.

The experiments summarised in Fig. 2.7 demonstrate that reducing the metal oxide to Fe resulted in an initial H_2 yield $\sim$ 4× that produced when simply reducing to $Fe_{0.947}O$. The additional capacity to produce hydrogen, however, decreased rapidly with increasing cycles. Eliminating such deterioration by using synthetic particles with chemical support will be investigated in Chapters 3 and 4. The drop in H_2 yield for pure Fe_2O_3 reduced to Fe has subsequently been confirmed by Li *et al.* (2009). The decrease in the H_2 produced following reduction to Fe, seems to be a result of both incomplete reduction and incomplete oxidation, as discussed with Fig. 2.6. In contrast to reducing particles to Fe, Fig. 2.5 shows that reducing iron oxide particles to $Fe_{0.947}O$ gave sustained levels of hydrogen for 10 cycles. Again, it should be stressed that the current particles were created from powdered Fe_2O_3, free from other metallic additives.

The difference in the production of H_2 between fully oxidising to Fe_2O_3 *versus* leaving the particle at Fe_3O_4 was marginal, as seen in Fig. 2.7. Since additional oxidation in air did not result in particles being sintered, but improved the overall process by: (i) increasing the heat generated, (ii) burning off carbon impurities and (iii) eliminating CO slip during oxide reduction, it seems that fully oxidising the metal oxide to Fe_2O_3 would be advantageous for producing hydrogen.

One limitation of the above experiments is that a mixture of steam and N_2 was used to reoxidise the metal; this resulted in the produced H_2 being diluted with N_2. Similarly, the reducing gas used was a mixture of CO, CO_2 and N_2. For producing pure CO_2 and H_2, an inlet stream free from any N_2 ballast would be required. For example, synthesis gas from a gasifier operating with inputs of coal and any combination of steam, CO_2 or pure O_2 would suffice. Actual synthesis gas from the gasification of coal or biomass will contain a mixture of CO, CO_2, H_2 and H_2O, as well as hydrocarbons, tars, sulphur compounds and other contaminants. Experiments with synthesis gas are presented in Chapter 7; however, in the current Chapter, for the sake of convenience, only mixtures of CO and CO_2 were considered. Addition of H_2O to the reducing gas has already been shown to improve the purity of the H_2 produced, since the gasification of any solid carbon with H_2O counteracts its deposition (Gupta *et al.*, 2007).

2.5 Conclusions

Starting from synthesis gas, separate streams of very pure hydrogen and carbon dioxide can be produced using cyclical redox reactions with the iron oxides. The preferred cycle for the particles studied here is as follows:

1. Syngas, from coal or biomass, is reacted with Fe_2O_3 particles; the CO in the synthesis

gas reacts with the iron oxides to give CO_2 of sufficient purity for sequestration. The reaction is continued until CO begins to slip from the bed, at which point the iron is in the form of $Fe_{0.947}O$ or Fe_3O_4. Further reduction to metallic iron is not recommended because it gives a loss of reactivity over 10 cycles of reduction and oxidation.

2. The bed of $Fe_{0.947}O$ is then purged with nitrogen to remove CO and CO_2.
3. Steam is then passed through the bed, giving hydrogen ($<$ 25 ppmv CO) suitable for use in fuel cells; the particles are oxidised to Fe_3O_4.
4. The bed is further oxidised in air to Fe_2O_3, giving a usable quantity of heat and burning off any carbon deposited in step (1).

Two critical areas for improving the process involve the iron oxide carrier. Specifically, (i) iron oxide capable of undergoing repeated reduction to Fe and (ii) iron oxide with an increased rate of reduction to $Fe_{0.947}O$, which does not deteriorate with cycling, is desired.

Chapter 3

Stabilising iron oxide used for the production of hydrogen

3.1 Introduction

It is desirable to reduce Fe_2O_3 to Fe, rather than FeO, because the yield of H_2 *per* unit mass of Fe_2O_3 is 4× higher, as shown by comparing the following two reactions:

$$3\,\mathrm{Fe} + 4\,\mathrm{H_2O_{(g)}} \rightleftarrows \mathrm{Fe_3O_4} + 4\,\mathrm{H_2} \qquad \Delta H^{\circ}_{1123\,\mathrm{K}} = -105.3\ \mathrm{kJ/mol} \tag{3.1}$$

$$3\,\mathrm{FeO} + \mathrm{H_2O_{(g)}} \rightleftarrows \mathrm{Fe_3O_4} + \mathrm{H_2}. \qquad \Delta H^{\circ}_{1123\,\mathrm{K}} = -47.4\ \mathrm{kJ/mol} \tag{3.2}$$

Here for simplicity, the Fe^{2+} oxide is written as FeO rather than $Fe_{0.947}O$. It has already been shown in Chapter 2, Figs. 2.5-2.7, that reduction to Fe results in a decrease in the quantity of H_2 produced by reaction (3.1), below that obtained if FeO had been the most reduced species. In sharp contrast to reduction to Fe, reduction to FeO was shown to generate stable quantities of H_2 over repeated cycles, up to 10 in number, as shown in Fig. 2.5(b).

In the present Chapter, to circumvent the limitation posed by reduction to Fe, the addition of a metal oxide support to particles of iron oxide was investigated. Since iron forms chemical intermediates with most supports, *e.g.* $FeO{\cdot}Al_2O_3$ with Al_2O_3, the hypothesis proposed is that choosing an additive which forms an intermediate with a higher melting temperature than that of the iron species could improve the capacity of the oxide carrier to react fully to produce a stoichiometric quantity of H_2 in each cycle. Table 3.1 lists the melting temperature, T_m, for intermediates with Si, Mg, Cr and Al, where Si was specifically chosen to give low-melting silicates for comparison. To reiterate, the iron species are defined as Fe, FeO, Fe_3O_4 and

Table 3.1: Melting points, T_{m}, in kelvin for iron species and intermediates in ascending order from left to right (Barin and Knacke, 1973). Silicates have lower melting points than iron and its oxides. The decomposition point of Fe_2O_3 at p_{O_2} = 0.21 is given [a].

	silicates		**iron species**				**other intermediates**			
species	$FeO{\cdot}SiO_2$	$2FeO{\cdot}SiO_2$	FeO	$Fe_2O_3^{a}$	Fe	Fe_3O_4	$FeO{\cdot}Al_2O_3$	$FeO{\cdot}Cr_2O_3$	$MgO{\cdot}Fe_2O_3$	MgO
T_{m} (K)	1413	1493	1650	1735	1809	1870	2053	2453	2473	3098

Fe_2O_3. The proposed process outlined in Chapter 1, section 1.3 can be summarised by the following three steps:

1. Reduction of Fe_2O_3 or Fe_3O_4 in CO to generate Fe and CO_2.
2. Oxidation of Fe to Fe_3O_4 in steam to produce pure H_2.
3. Oxidation of Fe_3O_4 to Fe_2O_3 in air.

Addition of additives to iron oxide to improve their redox stability is not new. Otsuka *et al.* (2003) investigated the effects of 26 different additives on the redox behaviour of iron oxide prepared by co-precipitation over the temperature interval 523-823 K. The quantity of doped metal was 3 mol. % throughout their study, and cycling between Fe_3O_4 and Fe was performed with 50 vol. % H_2, balance Ar as the reducing gas. They found that oxides of Al, Mo and Ce stabilised the amount of hydrogen produced in each cycle. In similar experiments, Wang *et al.* (2008) confirmed the positive effects of 5 mol. % Mo on the reduction of impregnated Fe_2O_3 powder. Galvita *et al.* (2008a) developed co-precipitated iron oxide particles with a base composition of 80 wt. % Fe_2O_3, 20 wt. % $Ce_{0.5}Zr_{0.5}O$, which when impregnated with 2 wt. % Mo, resisted sintering and gave stable H_2 yields over 100 cycles at a temperature of 873 K.

This work is distinct from previous investigations in three respects. First, previous research has focused on reaction temperatures below 1000 K, while the chosen reaction temperature in this study was 1123 K to accommodate the effluent gas from a typical gasifier. Second, if the redox process is to be used to convert a carbonaceous fuel, such as coal or biomass, into hydrogen, reducing gases with significant CO content must be considered and previous investigations have performed reduction in H_2 only (Otsuka *et al.*, 2003; Wang *et al.*, 2008) or mixtures with ($[CO]/[H_2] \leq 1/2$)(Galvita *et al.*, 2008a). Third, this work investigates the influence that oxidation in air, step 3 in the process, has on the yield of H_2.

In this work, activity is defined as the number of times an overall reaction takes place per active site per unit time. If the effect of adding a second chemical species, which itself lacks significant activity, to the catalyst has a positive effect on activity, it is termed a promoter. If it has a negative effect, it is termed an inhibitor. Promoters can be distinguished based on their effect, either physical or chemical (Satterfield, 1980). Physical promoters, often termed textural promoters, typically maintain active sites by preventing the sintering of crystals. They are effectively chemically inert and so do not alter adsorption isotherms or apparent activation energies; but they can influence the pre-exponential factor. A special case of physical promotion involves using large quantities of inert with a high surface area on which an expensive catalyst is dispersed. The physical promoter is then termed a support, examples of which include alumina, silica, activated carbon or zirconia. In contrast to physical promoters, chemical promoters alter the chemical properties of the catalyst by *e.g.* introducing lattice defects or modifying electronic structure. Chemical promoters will change adsorption isotherms and alter apparent activation energies. Because of the complex nature of interactions between the catalyst and the promoter, it is often difficult to distinguish whether a species has a strictly physical or a chemical effect. In the following Chapter, an additive is defined as a foreign element, *e.g.* Si, Mg, Al or Cr. Since the quantity of additive mixed with the Fe_2O_3 was kept < 30 mol. % and since the measurements were concerned with overall conversion, rather than kinetics, the additive is referred to as a support rather than a promoter. Finally, stability is defined as the ability of a particle to produce a constant quantity of H_2 in each redox cycle.

The objective of this Chapter is to find a support which, with minimal loading, will enable *stable* quantities of H_2 close to those expected from the stoichiometry of reaction (3.1), to be produced over repeated cycles.

3.2 Thermodynamics

The high process temperature, 1123 K, and the switching between reducing and oxidising environments means that the additive, Al, Cr, Mg or Si, is not necessarily inert. The formation of intermediates, *e.g.* aluminates, chromates and silicates, at various partial pressures of CO and CO_2 was investigated using thermodynamic data published by Barin and Knacke (1973) and considering the following groups of compounds: [Al, Al_2O_3, $FeO{\cdot}Al_2O_3$], [Cr, Cr_2O_3, $FeO{\cdot}Cr_2O_3$], [Mg, MgO, $MgO{\cdot}Fe_2O_3$], or [Si, SiO_2, $FeO{\cdot}SiO_2$ and $2FeO{\cdot}SiO_2$]. Minimisation of the Gibbs free energy subject to the constraints of conservation of atomic and molecular species was used to generate a phase diagram, Fig. 3.1(c). Here species CO, CO_2, Fe, FeO, Fe_3O_4 and Fe_2O_3 were considered separately with each group of support compounds. A detailed description of the minimisation of the Gibbs free energy is given in Appendix 1. At 1123 K, the intermediates which thermodynamically occur over the largest range of $y_{CO_2} = (1 - y_{CO})$, are $FeO{\cdot}Al_2O_3 > FeO{\cdot}Cr_2O_3 > 2FeO{\cdot}SiO_2$, as shown in Fig. 3.1(c). The compound $MgO{\cdot}Fe_2O_3$ is only stable in pure CO_2 and readily decomposes to MgO and Fe_3O_4 in the presence of trace amounts of CO at 1123 K. The dashed line in Fig. 3.1(a) and (c) denotes the equilibrium of the Boudouard reaction (1.18), $2CO \rightleftharpoons C_{(s)} + CO_2$, and shows that deposition of solid carbon at 1123 K and 10^5 Pa does not occur if $y_{CO_2} > 0.05$. From the minimisation of Gibbs free energy, it was found that at 1123 K, carbides, *e.g.* Al_4C_3 Fe_3C, and Cr_4C, did not form. The compound $2FeO{\cdot}SiO_2$ was found to exist over a wider range of y_{CO_2} than $FeO{\cdot}SiO_2$; therefore, only $2FeO{\cdot}SiO_2$ is plotted in Fig. 3.1(b) and (c). Based on thermodynamic considerations (McBride *et al.*, 2002), the formation of CrO, CrO_2 and CrO_3, which are gaseous from 800-1400 K, will not occur. A diagram similar to Fig. 3.1, which is based on mixtures of CO_2 and CO, can be produced for the system containing H_2 and steam.

From thermodynamics, oxides of the support elements Al, Cr, Mg and Si each have distinctive characteristics at 1123 K and 10^5 Pa which can be summarised as follows:

$FeO{\cdot}Al_2O_3$ During reduction, $FeO{\cdot}Al_2O_3$ is thermodynamically stable for $1 \geq y_{CO_2} > 0.01$. The $FeO{\cdot}Al_2O_3$ will only reoxidise to Fe_2O_3 and Al_2O_3 in air, not in CO_2 or H_2O. The $FeO{\cdot}Al_2O_3$ can be reduced to Fe and Al_2O_3 in CO or H_2. The melting temperatures of $FeO{\cdot}Al_2O_3$ and Al_2O_3 are higher than those of the iron species.

$FeO{\cdot}Cr_2O_3$ During reduction, $FeO{\cdot}Cr_2O_3$ is thermodynamically stable for $0.98 > y_{CO_2} > 0.14$. The $FeO{\cdot}Cr_2O_3$ can be reoxidised to Fe_3O_4 and Cr_2O_3 by CO_2 or H_2O and to Fe_2O_3 and Cr_2O_3 by air. The $FeO{\cdot}Cr_2O_3$ can be reduced to Fe and Cr_2O_3 in CO or H_2. The melting temperatures of $FeO{\cdot}Cr_2O_3$ and Cr_2O_3 are higher than those of the iron species.

$MgO{\cdot}Fe_2O_3$ During reduction, $MgO{\cdot}Fe_2O_3$ is not stable, but decomposes to MgO and Fe_3O_4 in trace amounts of CO; it cannot be decomposed to Fe_2O_3 and MgO by pure CO_2 or H_2O or air. The melting temperatures of $MgO{\cdot}Fe_2O_3$ and MgO are higher than those of the iron species.

$2FeO{\cdot}SiO_2$ During reduction, $2FeO{\cdot}SiO_2$ is thermodynamically stable for $0.96 > y_{CO_2} > 0.17$;

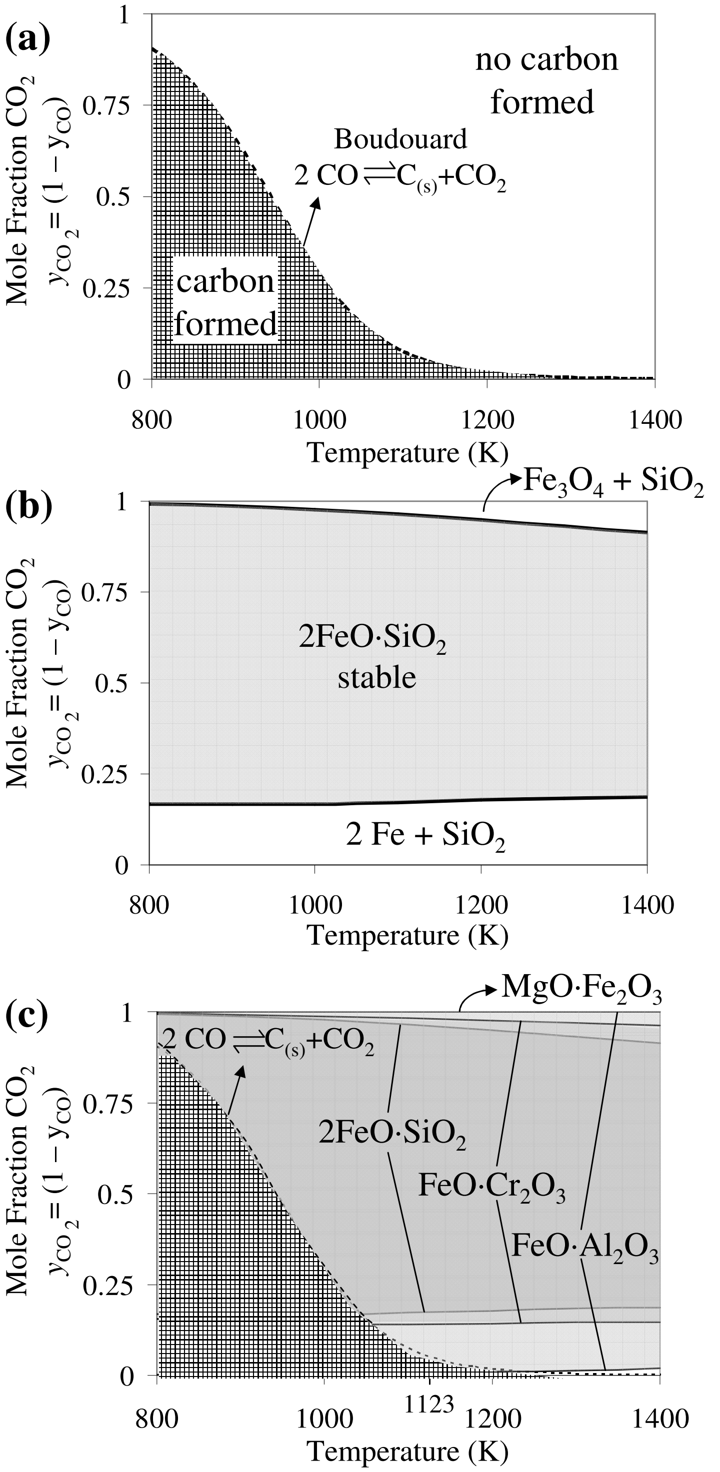

Figure 3.1: (a) The equilibrium for the Boudouard reaction is shown as a dashed line passing through $y_{CO_2} = 0.5$ at 940 K. Below the line, in the shaded region, solid carbon will deposit. Above the line, in the white region, no carbon will form. (b) Thermodynamic stability of $2FeO{\cdot}SiO_2$ in mixtures of CO and CO_2 between 800 and 1400 K at 10^5 Pa. The top line corresponds to the reaction: $3\,(2FeO{\cdot}SiO_2) + 2\,CO_2 \rightleftarrows 2\,Fe_3O_4 + 3\,SiO_2 + 2\,CO$. The bottom line corresponds to the reaction: $2FeO{\cdot}SiO_2 + 2\,CO \rightleftarrows 2\,Fe + SiO_2 + 2\,CO_2$. (c) Thermodynamic stability of $FeO{\cdot}Al_2O_3$, $FeO{\cdot}Cr_2O_3$, $MgO{\cdot}Fe_2O_3$ and $2FeO{\cdot}SiO_2$, in mixtures of CO and CO_2 between 800 and 1400 K at 10^5 Pa. At the experimental temperature of 1123 K, $FeO{\cdot}Al_2O_3$ is stable for $1 \geq y_{CO_2} > 0.01$, $FeO{\cdot}Cr_2O_3$ for $0.98 > y_{CO_2} > 0.14$ and $2\,FeO{\cdot}SiO_2$ for $0.96 > y_{CO_2} > 0.17$. $MgO{\cdot}Fe_2O_3$ is only stable in pure CO_2, and decomposes to MgO and Fe_3O_4 in trace quantities of CO.

$FeO{\cdot}SiO_2$ is stable within a subset of this range. The $2FeO{\cdot}SiO_2$ can be reoxidised to Fe_3O_4 and SiO_2 by CO_2 or H_2O and to Fe_2O_3 and SiO_2 by air. The $2FeO{\cdot}SiO_2$ and $FeO{\cdot}SiO_2$ can be reduced to Fe and SiO_2 in CO or H_2. Both $2FeO{\cdot}SiO_2$ and $FeO{\cdot}SiO_2$ have lower melting temperatures than the iron species.

Thus, only samples with Al should be affected by oxidation with air, which will oxidise any $FeO{\cdot}Al_2O_3$ to Fe_2O_3 and Al_2O_3. The samples with Mg will not form an intermediate species with iron of oxidation state +2, Fe^{2+}, *c.f.* $FeO{\cdot}Al_2O_3$, $FeO{\cdot}Cr_2O_3$ and $2FeO{\cdot}SiO_2$. Only samples with Si should form intermediates ($2FeO{\cdot}SiO_2$ or $FeO{\cdot}SiO_2$) with lower melting points than those of the iron species.

3.3 Experimental

The particles of iron oxide were prepared as in Chapter 2 by spraying water (Millipore Milli-Q; > 18 MΩ) on to Fe_2O_3 powder (Sigma-Aldrich; purity > 99.9 wt. %; size < 5μm) and mechanically mixing. The resulting agglomerates were heated at 1173 K for 3 h and then sieved to $d_\mathrm{p} = +300, -425$ μm. Unlike in traditional catalysis in which an active species is deposited on an inert support, here the support was back-added to the iron oxide by wet impregnation. For the back-addition of Al, Cr, and Mg, the corresponding nitrate, $Al(NO_3)_3 \cdot 9H_2O$ (Fisher; > 98 wt. %), $Mg(NO_3)_2 \cdot 6H_2O$ (Acros; > 99 wt. %) or $Cr(NO_3)_3 \cdot 9H_2O$ (Acros; > 99 wt. %), was dissolved in 300 mL water, purified by reverse osmosis, to give a 0.05 M solution based on the moles of metal, M. The mole fraction of the additive was defined as:

$$x_\mathrm{m} = \frac{\mathrm{mol}\,M}{\mathrm{mol}\,M + \mathrm{mol\,Fe}}. \tag{3.3}$$

For molar loadings of $x_\mathrm{m} = 0.01, 0.1$ and 0.3, 2 g of Fe_2O_3 particles were placed in beakers with 5 mL, 55 mL or 115 mL of the respective 0.05 M solution. The liquid was then evaporated at 353 K (below the boiling point) until dry. All of the nitrate was deposited on the particles for $x_\mathrm{m} = 0.01$ and 0.1; minimal nitrate residue was observed on the beakers for $x_\mathrm{m} = 0.3$. For the addition of Si, 47 mL of ethanol (Fisher; > 98 wt. %) was mixed with 3.3 mL of tetraethyl orthosilicate (TEOS; Acros; > 98 wt. %). This solution was added dropwise over 0.5 h to 250 mL 0.2 M HCl; the resulting mixture was then stirred at 298 K for 5 h to permit the acid-catalysed hydrolysis of the TEOS. Then 2 g of Fe_2O_3 particles were added to beakers of 5 mL, 55 mL and 115 mL of this transparent solution before drying at 333 K, a lower temperature

Table 3.2: Experimental molar loading of support, x_{m} = (mol M)/(mol M + mol Fe), determined gravimetrically. The BET surface area prior to, and after (in parentheses), 10 redox cycles (reactions 1.9, 1.10, 1.11 and 1.15, 1.16 for cycle 1; reactions 1.10, 1.11 and 1.15, 1.16 for cycles 2-10) is listed for selected samples, denoted by *. The surface area for unmodified Fe_2O_3 after 10 redox cycles was below the measurement tolerance of the instrument. The figure number corresponding to the experiment in which each sample was used is listed.

Experimental	**Target Values**			**BET**	
Loading	$\mathbf{x_m = 0.01}$	$\mathbf{x_m = 0.1}$	$\mathbf{x_m = 0.3}$	**(m^2/g)**	**Figure**
	Actual Values				
Unmodified Fe_2O_3 ⇄ Fe				1.50 (∅)	3.2
Unmodified Fe_2O_3 ⇄ FeO				1.50 (0.76)	3.2
Si	0.009	0.043	0.083^*	22.94 (1.77)	3.3
Mg	0.0125	0.100^*	0.288	1.50 (0.02)	3.4
Cr	0.010	0.093^*	0.272	1.24 (0.03)	3.5
Al	0.013	0.097^*	0.293	3.96 (0.43)	3.6

than before to prevent boiling the ethanol. No residue of SiO_2 was observed on the beaker for $x_{\mathrm{m}} = 0.01$ and 0.1; some residue was observed on the beaker for $x_{\mathrm{m}} = 0.3$. After evaporation of the solutions to dryness, the impregnated particles were poured into crucibles and converted to a fully oxidised state by sintering in air at 1173 K for 3 h. This step decomposed any nitrate and converted chlorides to gaseous form for removal.

The experimentally-achieved loading of the support metal oxide was then determined on a mass basis by weighing the resulting particles using a balance (OHaus) with a precision of 10^{-4} g and assuming that the support was present as, Al_2O_3, Cr_2O_3, MgO or SiO_2. Experimental loadings are listed in Table 3.2 and agree with the expected values. The Si sample loadings were below the expected values, demonstrating that not all of the Si added as TEOS was deposited and suggesting that not all of the TEOS underwent hydrolysis.

The reduction and oxidation of the modified iron oxides was performed in a packed bed reactor made from a tube (I.D. = 10 mm) of recrystallised Al_2O_3 (Multi-Lab Ltd.;> 99 wt.% purity), similar to that of stainless steel shown in Fig. 2.1. A frit made from Al_2O_3 containing 4 holes, each 1.5 mm dia., was used to support the bed. The bed was loaded by placing (i) 2 g of +1.4,-1.7 mm Al_2O_3 (Boud Mineral;> 99 wt.% purity), (ii) 2 g of +300,-425 μm Al_2O_3, (iii) modified Fe_2O_3 particles with a mass equivalent of 0.3 g Fe_2O_3 resieved to +300,-425 μm with no sand or Al_2O_3 mixed in (iv) 8 g of +1.4,-1.7 mm Al_2O_3 into the reactor. Thus for unmodified Fe_2O_3, 0.3 g of sample was introduced; for samples with additives, the total mass was greater than 0.3 g because of the presence of the additive metal oxides. A tubular furnace maintained the temperature at 1123 K in all experiments, as measured by a type K thermocouple (O.D.

Table 3.3: Redox cycling: gas mixtures (vol. %), flowrates (m^3/s) as measured at 298 K and 10^5 Pa and corresponding flow durations (s) for experiments with an initial charge of 0.3 g equivalent of Fe_2O_3. Reoxidation to Fe_2O_3 required air which was diluted in N_2. The total cycle time was 1200 s and 960 s for experiments with and without oxidation in air, respectively.

	T	symbol	purge	reduction	purge	steam oxidation	purge	air oxidation	figs.
time (s)			0-120	120-720	720-780	780-960	960-1020	1020-1200	
flow (m^3/s)			3.3×10^{-5}	3.3×10^{-5}	3.3×10^{-5}	3.3×10^{-5} N_2	3.3×10^{-5}	3.3×10^{-5}	
flow (m^3/s)						8.33×10^{-9} $H_2O_{(l)}$			
$Fe_3O_4 \rightleftarrows Fe$	1123 K	▲, ●, ■	N_2	10% CO/90% N_2	N_2	75% N_2/25% steam			3.2-3.6, 3.7
$Fe_3O_4 \rightleftarrows FeO$	1123 K	×	N_2	10% CO/10% CO_2/80% N_2	N_2	75% N_2/25% steam			3.2
$Fe_3O_4 \rightleftarrows Fe$	773 K,1123 K	□, ○	N_2	10% H_2/90% N_2	N_2	75% N_2/25% steam			3.2-3.6
$Fe_2O_3 \rightleftarrows Fe$	1123 K	●	N_2	10% CO/90% N_2	N_2	75% N_2/25% steam	N_2	95% N_2/5% O_2	3.2-3.6, 3.7

1.5 mm) placed within the layer of iron oxide. Gas was supplied to the reactor as in Chapter 2; the flowrates, temperatures and compositions of inlet streams are shown in Table 3.3.

Scanning electron microscopy (SEM, a JSM-5800LV operated at 15 kV with an energy dispersive X-ray spectrometer (EDS), Oxford INCAPentaFET-×3) and X-ray diffraction (XRD, Philips model PW1830/00, Cu K_α, 40 kV and 40 mA, 0.05° per 5 s, in air at 298 K) were used to examine the morphology and composition of the particles. The specific surface area of the samples was calculated from N_2 adsorption isotherms (Micromeritics, Tristar 3000) using the BET model (Brunauer *et al.*, 1938) as outlined in Appendix 2.

3.4 Results

3.4.1 Stability of unmodified Fe_2O_3

Figure 3.2 shows the total quantity of hydrogen produced during cyclic reduction and oxidation of different oxides with unmodified Fe_2O_3 as a control. The quantity of hydrogen produced was determined by integrating the mole fraction of hydrogen in the effluent gas over time and multiplying by the total molar flowrate of the gas. The theoretical quantity of hydrogen from 0.3 g of Fe_2O_3 reduced to Fe can be determined from reaction (3.1) as:

$$\frac{0.3\ \text{g}}{M_{\text{Fe}_2\text{O}_3}} \times \frac{8}{3} = 5\ \text{mmol H}_2, \tag{3.4}$$

where $M_{Fe_2O_3}$ is the molecular weight of Fe_2O_3. This value is indicated by the upper horizontal dashed line in Fig. 3.2.

From Fig. 3.2, the quantity of H_2 produced in each cycle by the unmodified iron oxide, pre-

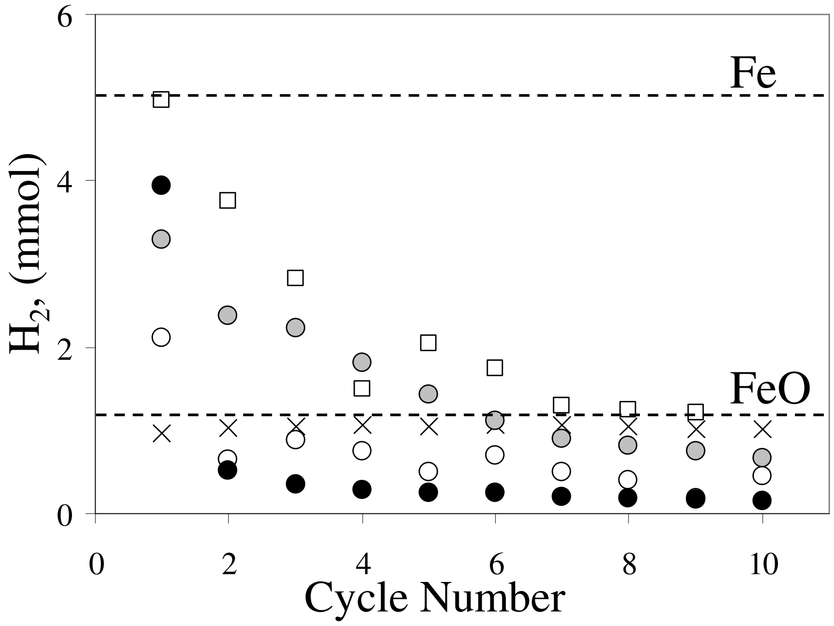

Symbol	Oxidation step	*T* (K)	Reducing gas
●	Fe→Fe_3O_4	1123	CO
○	Fe→Fe_3O_4	1123	H_2
□	Fe→Fe_3O_4	773	H_2
◍	Fe→Fe_2O_3	1123	CO
×	FeO→Fe_3O_4	1123	CO

Figure 3.2: Hydrogen produced *per* cycle over 10 cycles by Fe or FeO from the reduction of 0.3 g of 100 mol. % Fe_2O_3 at 1123 K or 773 K. The upper dashed horizontal line gives the theoretical quantity of H_2 expected, 5.0 mmol, from Fe oxidised to Fe_3O_4. The lower dashed horizontal line gives the theoretical quantity of H_2 expected, 1.25 mmol, from FeO oxidised to Fe_3O_4.

viously reduced by 10 vol. % CO, balance N_2, decreased substantially with increasing cycles. The quantity of hydrogen produced in cycle 10 is less than 5 % of that expected. Figure 3.2 also shows the total quantity of hydrogen produced in each cycle over 10 cycles when reduction proceeds only to FeO and not to Fe. Here, reduction was performed in 10 vol. % CO, 10 vol. % CO_2, balance N_2. The H_2 produced *per* cycle in the experiment is stable over 10 cycles and is near the expected quantity of 1.25 mmol, predicted from stoichiometry assuming FeO was produced from the reduction of a batch of 0.3 g of Fe_2O_3. This limit of 1.25 mmol is shown by the lower horizontal dashed line in Fig. 3.2.

The yield of H_2 for unmodified iron oxide reduced to Fe in 10 vol. % H_2, balance N_2 exhibited a similar decrease to that observed for reduction to Fe in 10 vol. % CO, balance N_2, suggesting that the choice of reducing gas, either H_2 or CO, does not influence the behaviour of the unmodified Fe_2O_3. Decreasing the temperature of reduction from 1123 K to 773 K, however, resulted in a more gradual decrease in the quantity of H_2 produced for the unmodified Fe_2O_3 sample, as seen in Fig. 3.2. The results for reduction in H_2 suggest that a thermal process, *e.g.* sintering, might be one cause of the loss in activity of the metal oxide. Lower temperatures could not be used for reduction in CO owing to the deposition of solid carbon *via* the Boudouard reaction (1.18).

The effect of including oxidation with air on the subsequent yield of hydrogen over 10 cycles is also shown in Fig. 3.2. For these experiments, samples of unmodified Fe_2O_3 were reduced to Fe in 10 vol. % CO, balance N_2 at 1123 K. Next, oxidation in steam and N_2 to produce H_2 and return the Fe to Fe_3O_4 was performed. Finally, the Fe_3O_4 was converted to its initial state, Fe_2O_3, by oxidation in air. The amount of H_2 produced by unmodified Fe_2O_3 decreases less rapidly with number of cycles than before, but is only 15 % of the expected quantity by cycle 10, below that achievable if reduction had only proceeded to FeO.

Thus, the transitions from Fe_2O_3 to Fe_3O_4 and from Fe_3O_4 to FeO do not appear to affect the repeated redox performance of the carrier; rather, the transition from FeO to Fe appears to be the critical step requiring stabilisation. The initial surface area of the unmodified Fe_2O_3, given in Table 3.2 line 1, is 1.5 m^2/g. Table 3.2 line 2 demonstrates that repeated reduction to FeO results in a decrease in surface area of 50 % after 10 cycles; comparatively, all of the active surface area is destroyed, line 1, after repeated reduction to Fe in $CO+N_2$. It is noted that for the surface area measurements the state of the reacted iron oxide was Fe_3O_4 since reoxidation occurred in steam only, while the state of the fresh samples had been Fe_2O_3.

3.4.2 Stability of Fe_2O_3 supported with SiO_2, MgO, Cr_2O_3 and Al_2O_3

Next, modification of the iron oxide through the addition of $x_m = 0.01, 0.04$ or 0.08 Si was investigated. Figure 3.3 shows conversion, X_{H_2}, against cycle number. No correlation between the loading of Si and yield of H_2 is observed and in all cases, the quantity of H_2 produced in each cycle decreased to less 10 % of the expected value by cycle 10. Changing the reducing gas from CO to H_2 did not affect the yield of H_2, nor did oxidation in air. Thus, the addition of Si to Fe_2O_3 did not increase the yield of H_2 over the unmodified Fe_2O_3.

Figure 3.4 shows the quantity of H_2 produced against cycle number for samples of Fe_2O_3 with $x_m = 0.01, 0.1$ or 0.3 Mg. For cycle 1, quantities of H_2 near the theoretical limit are obtained in all cases. At the low loading of $x_m = 0.01$ Mg, the yield of H_2 decreased to less than 4 % of that expected by cycle 10 and offered no improvement over unmodified Fe_2O_3,

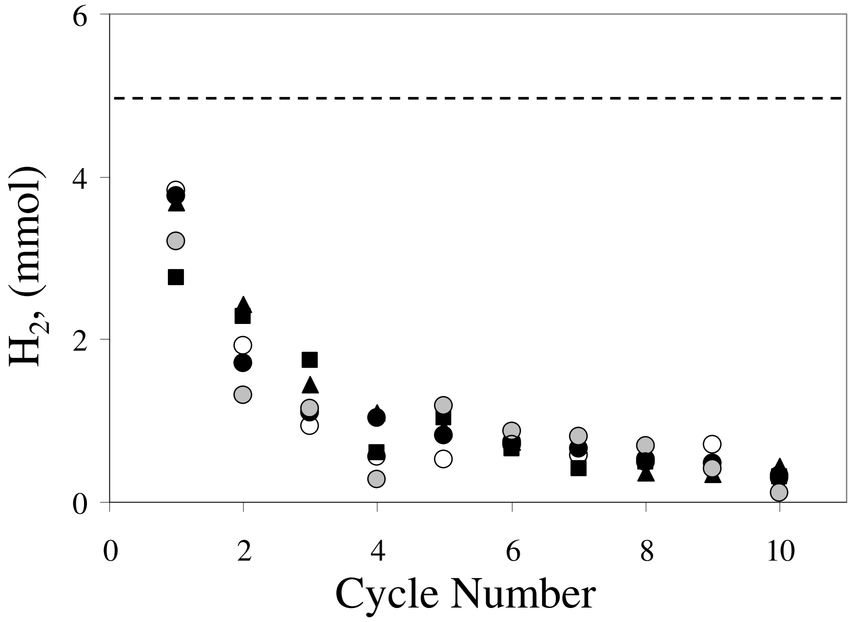

Symbol	Oxidation Step	Additive	x_m	Reducing gas
▲	Fe→Fe_3O_4	Si	0.01	CO
●	Fe→Fe_3O_4	Si	0.1	CO
■	Fe→Fe_3O_4	Si	0.3	CO
○	Fe→Fe_3O_4	Si	0.1	H_2
◍	Fe→Fe_2O_3	Si	0.1	CO

Figure 3.3: Hydrogen produced *per* cycle over 10 cycles by Fe from the reduction of Fe_2O_3 modified with $x_m = 0.01, 0.04$ or 0.08 Si at 1123 K. The dashed horizontal line gives the theoretical quantity of H_2 expected, 5.0 mmol, from Fe oxidised to Fe_3O_4.

c.f. Fig. 3.2. The quantity of H_2 produced increased with the molar loading, however, giving 0.2 mmol, 0.8 mmol and 3.3 mmol H_2 in cycle 10 for $x_m = 0.01, 0.1$ and 0.3, respectively. No difference in yield of H_2 was observed for reduction in CO *versus* H_2. Including oxidation in air, step 3, resulted in a slower decrease in the quantity of H_2 obtained, but by cycle 10 the yield of H_2 was similar to experiments without oxidation in air. The sample containing $x_m = 0.3$ Mg showed the most improvement in yield of H_2 over unmodified Fe_2O_3 and gave an average value of 3.0 mmol H_2 or 60 % of the expected quantity over cycles 5-10.

The quantity of H_2 produced against cycle number is shown in Fig. 3.5 for samples of Fe_2O_3 modified with $x_m = 0.01, 0.1$ or 0.3 Cr. In all cases, values near the theoretical limit were achieved in cycle 1. Increasing the molar loading led to increased quantities of H_2 in subsequent cycles. For a loading of $x_m = 0.01$, 1.7 mmol or 35 % of the expected yield, was obtained over cycles 5-10 and offered no improvement over unmodified Fe_2O_3, *c.f.* Fig. 3.2. The quantity of H_2 produced for the sample with $x_m = 0.1$ Cr decreased over cycles 1-4, but remained stable over cycles 5-10 giving ~ 35 % of the theoretical yield. For reduction in H_2,

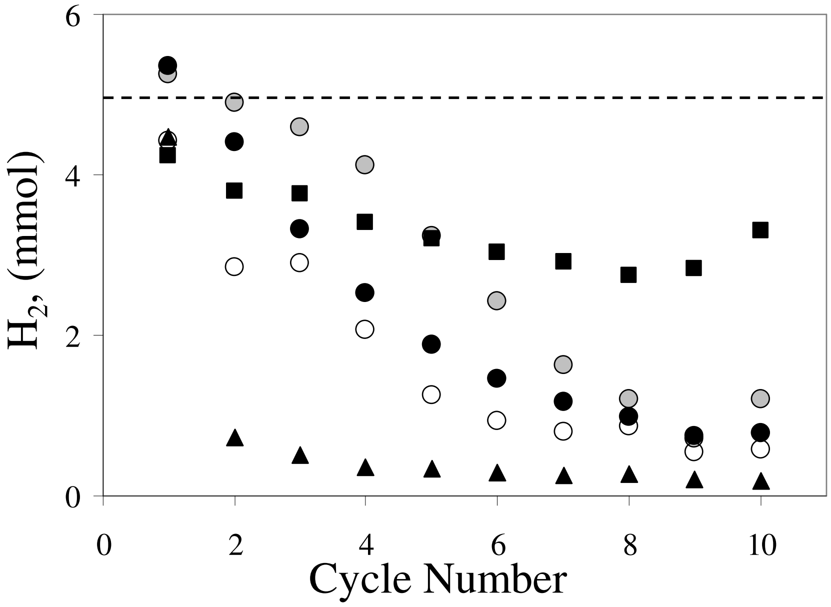

Symbol	Oxidation Step	Additive	x_m	Reducing gas
▲	Fe→Fe_3O_4	Mg	0.01	CO
●	Fe→Fe_3O_4	Mg	0.1	CO
■	Fe→Fe_3O_4	Mg	0.3	CO
○	Fe→Fe_3O_4	Mg	0.1	H_2
◍	Fe→Fe_2O_3	Mg	0.1	CO

Figure 3.4: Hydrogen produced *per* cycle over 10 cycles by Fe from the reduction of Fe_2O_3 modified with x_m = 0.01, 0.1 or 0.3 Mg at 1123 K. The dashed horizontal line gives the theoretical quantity of H_2 expected, 5.0 mmol, from Fe oxidised to Fe_3O_4.

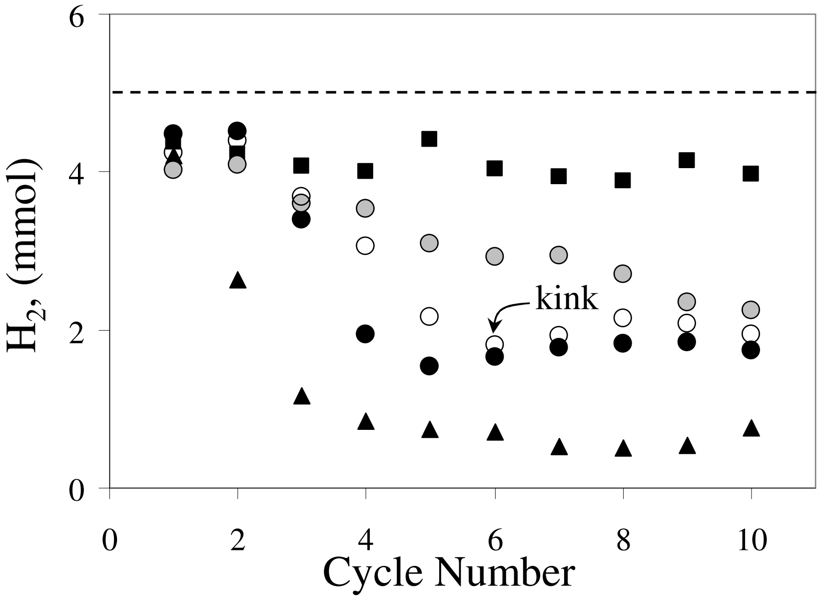

Symbol	Oxidation Step	Additive	x_m	Reducing gas
▲	Fe→Fe_3O_4	Cr	0.01	CO
●	Fe→Fe_3O_4	Cr	0.1	CO
■	Fe→Fe_3O_4	Cr	0.3	CO
○	Fe→Fe_3O_4	Cr	0.1	H_2
◍	Fe→Fe_2O_3	Cr	0.1	CO

Figure 3.5: Hydrogen produced *per* cycle over 10 cycles by Fe from the reduction of Fe_2O_3 modified with $x_m = 0.01, 0.1$ or 0.3 Cr at 1123 K. The dashed horizontal line gives the theoretical quantity of H_2 expected, 5.0 mmol, from Fe oxidised to Fe_3O_4.

this kink at cycle 5 was reproduced and nearly identical yields of H_2 were obtained compared to experiments with reduction in CO, which demonstrates that the choice of reducing gas, either H_2 or CO, has little effect on the performance of the sample. Additional oxidation of the $x_m = 0.1$ Cr sample in air, step 3, slowed the decrease in the yield of H_2 observed for an identical sample oxidised in steam only; however, a prolonged improvement in the yield of H_2 was not maintained. For a loading of $x_m = 0.3$ Cr, however, stable yields of H_2 were obtained over 10 cycles, maintaining 82 % of the expected quantity. Overall, the sample with $x_m = 0.3$ Cr provided the best improvement in the quantity of H_2 produced giving an average of 4.1 mmol over cycles 1-10.

Figure 3.6 shows the quantity of H_2 produced against cycle number for samples of Fe_2O_3 with $x_m = 0.01, 0.1$ or 0.3 Al. Here, the quantity of H_2 produced no longer increases with increased loading of support as was observed for Mg and Cr. Rather, the sample with $x_m = 0.3$ Al generated less H_2 than the sample with $x_m = 0.1$. Similar to previous results, however, a loading of $x_m = 0.01$ Al did not improve the yield of H_2 over that observed with unmodified

Fe_2O_3, and gave 0.2 mmol in cycle 10. For 100 mol. % Fe_2O_3 and the samples modified with Si, Mg and Cr investigated previously, the choice of the reducing gas, either CO or H_2, did not influence the quantity of H_2 produced during subsequent oxidation. Figure 3.6, however, demonstrates that reduction of samples with x_m = 0.1 Al in H_2 resulted in noticably larger quantities of H_2 produced in cycle 10 compared to an identical sample reduced in CO. Also, additional oxidation in air, step 3, improved the yield of H_2 and permitted on average 4.7 mmol or 94 % of the theoretical value to be produced over 10 cycles. Using samples with x_m = 0.1 Al and including additional oxidation in air thus provided, in total, the most H_2 over 10 cycles of any sample tested.

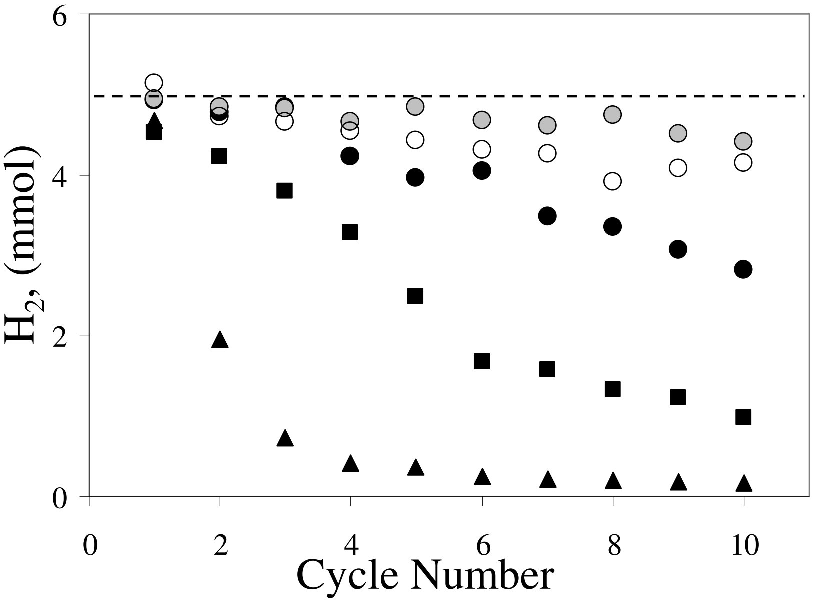

Symbol	Oxidation Step	Additive	x_m	Reducing gas
▲	Fe→Fe_3O_4	Al	0.01	CO
●	Fe→Fe_3O_4	Al	0.1	CO
■	Fe→Fe_3O_4	Al	0.3	CO
○	Fe→Fe_3O_4	Al	0.1	H_2
◉	Fe→Fe_2O_3	Al	0.1	CO

Figure 3.6: Hydrogen produced *per* cycle over 10 cycles by Fe from the reduction of Fe_2O_3 modified with $x_\mathrm{m} = 0.01, 0.1$ or 0.3 Al at 1123 K. The dashed horizontal line gives the theoretical quantity of H_2 expected, 5.0 mmol, from Fe oxidised to Fe_3O_4.

To confirm the effect of oxidation with air on the sample with x_m = 0.1 Al, Fig. 3.7 shows the quantity of H_2 produced over twelve cycles based on a single experiment. For cycles 1-8, oxidation was performed only in steam to return the Fe to Fe_3O_4 *via* step 2; for cycles 9-12 oxidation was performed in steam to return the Fe to Fe_3O_4 *via* step 2, followed by oxidation in a mixture of N_2 and air to return the Fe_3O_4 to Fe_2O_3 *via* step 3. An increase in the H_2

produced by 0.7 mmol is observed following the oxidation with air between cycles 8 and 9. This corresponds to an increase in H_2 of 3× that expected from the release of reactive iron previously bound as $FeO{\cdot}Al_2O_3$ assuming that all of the Al_2O_3 had formed $FeO{\cdot}Al_2O_3$. Further investigation of the formation of $FeO{\cdot}Al_2O_3$ is deferred until Chapter 4.

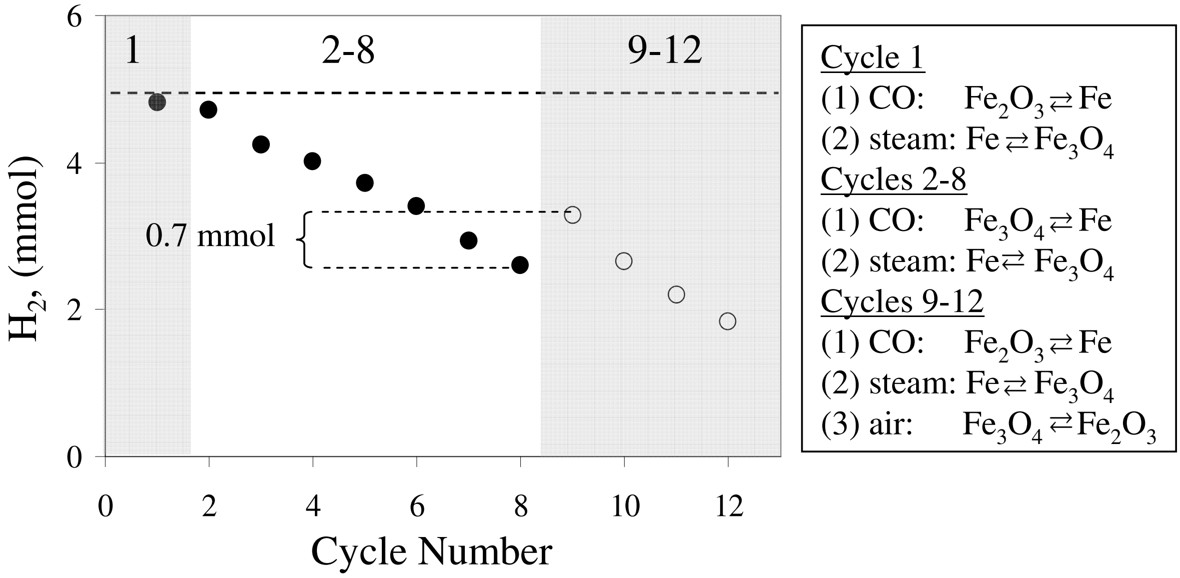

Figure 3.7: Hydrogen produced *per* cycle over 12 cycles by Fe from the reduction of Fe_2O_3 modified with x_m = 0.1 Al at 1123 K. The sample was reduced in 10 vol. % CO, balance N_2 and (•) oxidised in 25 vol. % steam, balance N_2 only for cycles 1-8 and (○) oxidised in 25 vol. % steam, balance N_2, followed by 95 vol. % N_2, 5 vol. % O_2 for cycles 9-12. The dashed horizontal line gives the theoretical quantity of H_2 expected, 5.0 mmol, from Fe oxidised to Fe_3O_4.

The deposition of solid carbon during reduction in 10 vol. % CO, balance N_2 was observed. The Si samples or samples with molar loadings of 0.01 did not produce enough hydrogen to merit a study of CO contamination. For the Fe_2O_3 modified with x_m = 0.1 and 0.3 Al and Mg over cycles 2-10, the average quantity of CO in the effluent stream, obtained by dividing the moles of CO by the sum of the moles of CO and H_2 obtained during oxidation in steam, was 5000 vol. ppm. A higher CO contamination was observed in cycle 1. The average total molar quantity of CO in the effluent stream during oxidation with steam was 25000 vol. ppm for reoxidation of the samples with x_m = 0.1 and 0.3 Cr for cycles 2-10.

Previous work by Otsuka *et al.* (2003) and Wang *et al.* (2008) on the redox reactions of modified iron oxide has focused on iron as a storage medium for hydrogen generation in vehicles. For this application, the US Department of Energy (DOE, 2007) and International Energy Agency (IEA, 2004) list target gravimetric hydrogen storage capacities (g H_2/g storage

Table 3.4: Gravimetric hydrogen storage capacity, (g H_2)/(g Fe + g oxide support)×100 %, for the modified iron oxide samples in this work averaged over cycles 5-10. The figure number from which the H_2 yields were taken is listed.$^a x_m = 0.04$ for Si, $^b x_m = 0.08$ for Si.

	$x_m = 0.01$	$x_m = 0.1^a$	$x_m = 0.3^b$	$x_m = 0.1^a$ in H_2	$x_m = 0.1^a$ air	**Figure**
Si	0.5	0.5	0.4	0.5	0.5	3.3
Mg	0.2	0.9	0.8	0.6	1.2	3.4
Cr	0.5	1.6	**3.4**	1.8	2.3	3.5
Al	0.2	2.7	1.3	**3.4**	**3.7**	3.6

medium) of 6.5 wt. % and 5.0 wt. %, respectively. The theoretical production capacity of H_2 for Fe can be calculated from reaction stoichiometry (3.1) and is 4.8 wt. %, below both targets. Stabilising reaction (3.1) was the objective of the current study, so for comparison with previous work Table 3.4 lists the average hydrogen storage capacity for the modified samples investigated here. The storage capacity was calculated by averaging the quantity of H_2 produced in cycles 6-10 and considering the sample as a composite of Fe together with either Al_2O_3, Cr_2O_3, MgO or SiO_2. The $x_m = 0.3$ Cr and $x_m = 0.1$ Al modified samples provide the best storage capacities of 3.4 wt. % and 3.7 wt. %, respectively, as seen in Table 3.4. These values are smaller than those in other work, *e.g.* Wang *et al.* (2008), which were ~ 4.5 wt. %; however, in the present work, a significantly higher temperature was used, 1123 K *vs.* 873 K, and longer cycling was performed, 10 cycles *vs.* 5 cycles.

3.4.3 SEM-EDS characterisation

The distribution of the additives within the iron oxide matrix will influence the yields of H_2 observed. The introduction of a support should have the most beneficial effect if it can be uniformly distributed throughout the iron oxide matrix. Figure 3.8 (a) shows a SEM cross-section of a particle with $x_m = 0.1$ of Al. The particle has a diameter of 400 μm, within the sieve range of +300,-425 μm. EDS spectra at the eight points shown by black circles give elemental mole fractions of Al = 0.03 ± 0.01, Fe = 0.36 ± 0.07 and O = 0.61 ± 0.06, in good agreement with predicted values for a sample with $x_m = 0.1$ Al, *viz.* Al = 0.04, Fe = 0.36 and O = 0.6, respectively. The EDS linescan in Fig. 3.8 (b) across the portion of the particle shown by the white horizontal line in Fig. 3.8 (a), confirms that the Al is uniformly distributed. In contrast to samples prepared from nitrate solutions, the samples with Si, prepared by the hydrolysis of tetraethyl orthosilicate in HCl solution, displayed an uneven distribution of support. Figures 3.8 (c) and (d) show SEM-EDS results for a particle with $x_m = 0.08$ Si and a diameter of 420 μm after calcination in air at 1173 K. A larger mole fraction of Si near the exterior is observed.

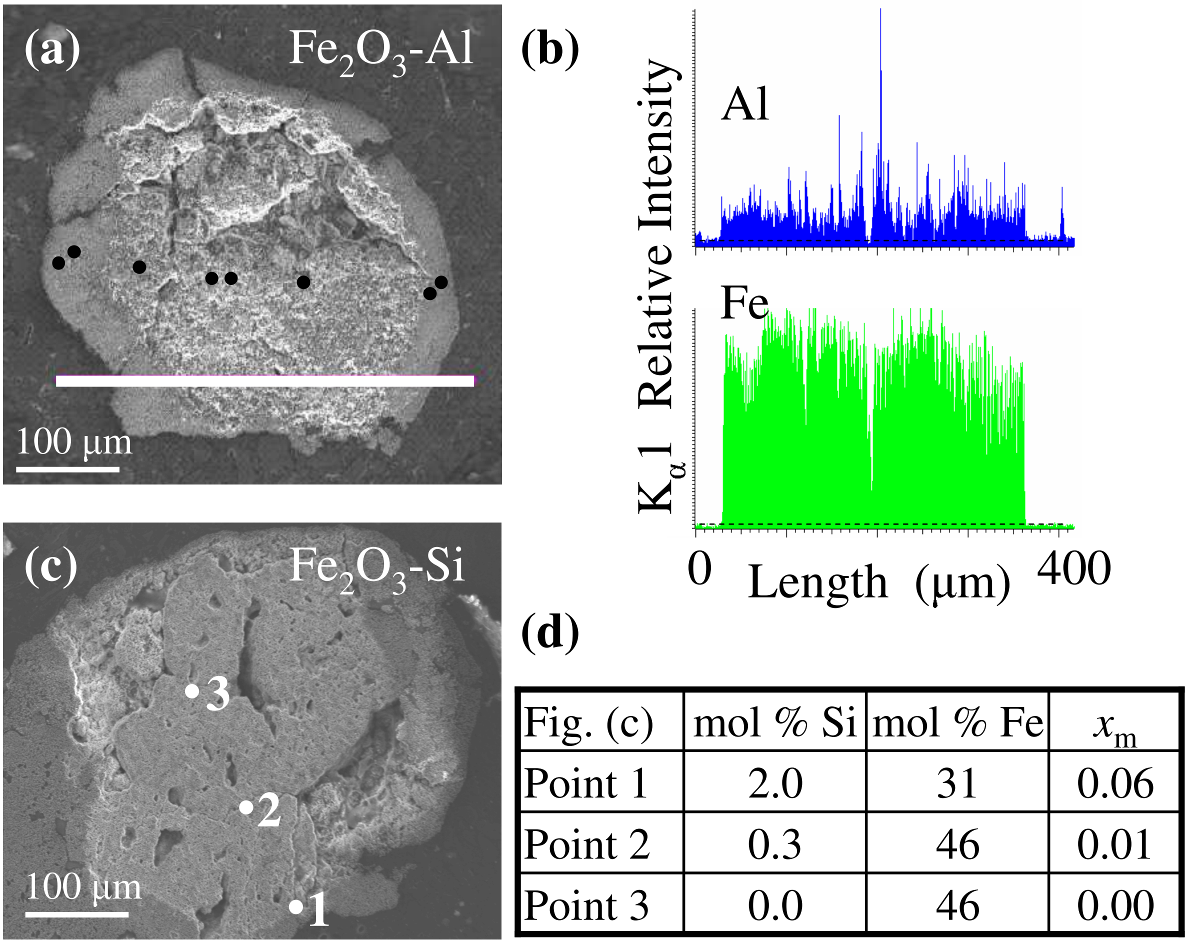

Fig. (c)	mol % Si	mol % Fe	x_m
Point 1	2.0	31	0.06
Point 2	0.3	46	0.01
Point 3	0.0	46	0.00

Figure 3.8: (a) Cross-section of a particle of Fe_2O_3 modified with $x_m = 0.1$ Al prior to reaction. Elemental analysis (EDS) at eight points corresponding to the black circles gave mole fractions of Al, Fe and O of 0.03 ± 0.01, 0.36 ± 0.07 and 0.61 ± 0.06; in agreement with predicted values for $x_m = 0.1$ Al of 0.04, 0.36 and 0.6 respectively. (b) EDS scans corresponding to the white cross-sectional line in (a) confirming the uniform distribution of Al throughout the sample. (c) SEM cross-section of Fe_2O_3 modified with $x_m = 0.08$ Si prior to reaction. (d) EDS analysis of points 1-3 in (c) showing decreasing Si loading towards the interior.

3.4.4 X-ray diffraction

Figure 3.9 shows X-ray diffraction patterns for the Fe_2O_3 modified with Al, Cr, Mg and Si at different stages of the reduction cycle: (a) after reduction in 10 vol. % CO, balance N_2, (b) after reduction in 10 vol. % CO, 10 vol. % CO_2 balance N_2, (c) after reoxidation in 25 vol. % steam, balance N_2, and (d) prior to any reduction or reoxidation. The predicted phase of the iron for each image, (a) Fe, (b) FeO, (c) Fe_3O_4 or (d) Fe_2O_3, is also given and was taken from

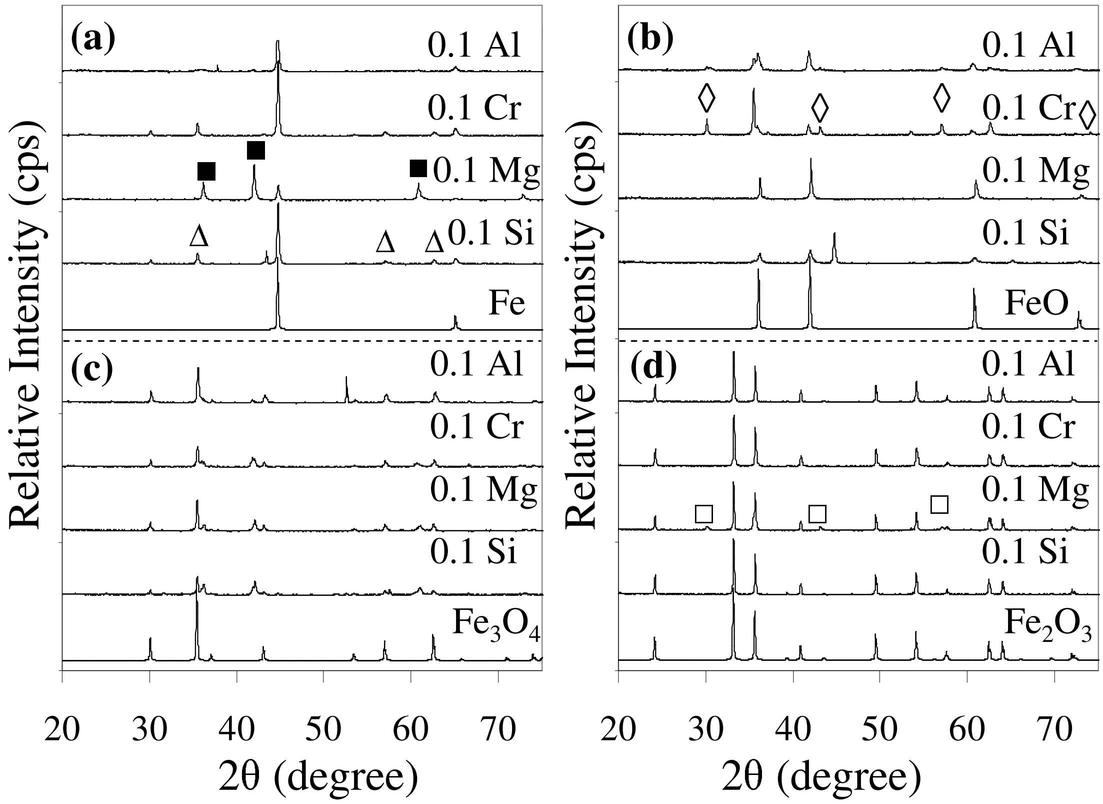

Figure 3.9: X-ray diffraction spectra of samples of Fe_2O_3 modified with $x_m = 0.1$ Al, Cr and Mg and with $x_m = 0.08$ Si (a) after reduction with 10 vol. % CO, balance N_2 with Fe as reference; (b) after reduction with 10 vol. % CO, 10 vol. % CO_2, balance N_2 with FeO as reference; (c) after reoxidation with steam with Fe_3O_4 as reference; (d) prior to experiments after sintering in air at 1173 K with Fe_2O_3 as reference. Peaks corresponding to $2FeO{\cdot}SiO_2$ (△), MgO (■), $FeO{\cdot}Cr_2O_3$ (◊) and $MgO{\cdot}Fe_2O_3$ (□) are identified.

a standard reference (JCPDS, 2005a). The major component in each case is the expected iron species, which is unsurprising considering that the samples contained a molar loading of additive of only $x_m \approx 0.1$. Figure 3.9 (a) shows peaks for Fe_2O_3 modified with Mg at 36.93°, 42.91° and 61.10° indicating the existence of MgO. Figure 3.9 (a) also shows peaks at 36.25°, 57.95° and 63.65° for the Fe_2O_3 modified with Si; these can be attributed to $2FeO{\cdot}SiO_2$. Peaks at 30.15°, 43.45°, 57.07°, 62.67° and 74.15° for the Fe_2O_3 modified with Cr in Fig. 3.9 (b) suggest the presence of $FeO{\cdot}Cr_2O_3$. Figure 3.9 (d) shows minor peaks for the Fe_2O_3 modified with Mg at 30.20°, 43.25° and 57.50°, corresponding to $MgO{\cdot}Fe_2O_3$. Thus, Mg is bound as $MgO{\cdot}Fe_2O_3$ when the sample is fully oxidised (d) and is present as MgO when the bulk of the iron is reduced to Fe (a), in agreement with the thermodynamics discussed in section 3.2. In Fig. 3.9 (a), the expected state of the Si is SiO_2; however experimentally, $2FeO{\cdot}SiO_2$ was detected. If the time of reaction is not sufficiently long, species other than those predicted from equilibrium might arise and could be the reason for the observation of $2FeO{\cdot}SiO_2$. Nevertheless, the formation of $2FeO{\cdot}SiO_2$ is confirmed. The intermediate $FeO{\cdot}Cr_2O_3$ in Fig. 3.9(b) is also in agreement with the thermodynamic predictions of section 3.2. Peak broadening is observed and is most pronounced for Figs. 3.9 (b) and (c). A decrease in the crystallite size below approximately 1 μm or strain in the crystal lattice could cause broadening of the X-ray diffraction peaks. Overall, the XRD analysis confirms that the support additive cannot be considered inert.

3.5 Discussion

Studies of the production of hydrogen using the redox reactions of iron oxide (Otsuka *et al.*, 2003; Wang *et al.*, 2008; Galvita *et al.*, 2008a) have demonstrated that the stability of the iron carrier when reduced fully to Fe, even at temperatures below 1000 K, is an obstacle. Figure 3.2 showed that the capacity of the unmodified Fe_2O_3 to produce H_2 was specifically impaired by the transition from FeO to Fe, since: if FeO was the most reduced form of the oxide, stable yields of H_2 over 10 cycles were obtained; while if Fe was the most reduced form, decreasing yields of H_2 were observed over successive cycles.

The effect of reduction to Fe on decreasing the yield of H_2 can partially be explained by considering molar volumes. The molar density, M_V, for each iron species can be calculated using its mass density (kg/m^3) and molecular weight (kg/kmol) [1], giving 32.6, 22.2, 84.2 and 136.1 kmol/m^3 for Fe_2O_3, Fe_3O_4, FeO and Fe, respectively. Considering molecular formulae, reduction from Fe_2O_3 to Fe_3O_4 will result in no change of the Fe molar density since 1 kmol Fe_2O_3 ($1/32.6 = 0.031$ m^3) gives 2/3 kmol Fe_3O_4 occupying $2/(3 \times 22.2) = 0.030$ m^3; reduction from Fe_3O_4 to FeO will result in a 20 % increase in the Fe molar density; reduction from FeO to Fe will result in a 70 % increase in the molar density. Thus, while the actual particle may not vary in diameter, contraction of the iron lattice as oxygen is removed during reduction will be most severe for the transition between FeO and Fe. The addition of additives would alleviate changes in molar volume. Assuming $FeO{\cdot}Al_2O_3$, $FeO{\cdot}Cr_2O_3$, MgO and $2FeO{\cdot}SiO_2$ form and do not decompose (this assumption only holds over specific y_{CO_2} values and is thermodynamically reasonable), reduction from FeO to Fe with of $x_m = 0.1$ Al, Cr, Mg or Si, will result in a 52, 51, 60 and 43 % increase in the molar density of Fe, respectively, compared to 70 % in the unmodified sample.

---

[1] The specific gravities used are Fe_2O_3, 5.2; Fe_3O_4, 5.15; FeO, 5.8; Fe, 7.6; Al_2O_3, 4.0; Cr_2O_3, 5.21; MgO, 3.58; SiO_2, 2.63; $FeO{\cdot}Al_2O_3$, 3.95; $FeO{\cdot}Cr_2O_3$, 4.79; $2FeO{\cdot}SiO_2$, 4.39.

Considering each additive separately, the samples with Si did not improve the yields of H_2 compared to unmodified Fe_2O_3, as seen from comparing Figs. 3.2 and 3.3. The rapid decrease in the yield of H_2 produced after cycle 1 might be attributable to the formation of the silicates, $FeO\cdot SiO_2$ and $2FeO\cdot SiO_2$, which have melting temperatures ~200 K below that of the iron species or to the uneven coverage of the Si support, which was shown in Fig. 3.8(c)-(d). The presence of $2FeO\cdot SiO_2$ was confirmed by X-ray diffraction, as shown in Fig. 3.9. Low melting silicates would increase lattice mobility (3D) and surface atom mobility (2D), since they have lower Tammann and Hüttig temperatures, given by $0.3\ T_\mathrm{m}$ and $0.5\ T_\mathrm{m}$, respectively (Satterfield, 1980; Ertl *et al.*, 1999). Hence, the rate of morphological changes would be increased in the Fe_2O_3 modified with Si, compared to the unmodified Fe_2O_3, and could lead to a reduction in active surface area. The formation of $2FeO\cdot SiO_2$ is known to occur during reduction and oxidation of mixtures of Fe_2O_3 and SiO_2 (Lund and Dumesic, 1981; Zhang *et al.*, 2006). Additionally, in iron-silicon alloys with loadings between $0.09 < x_\mathrm{m} < 0.33$ Si, oxidation can result in the formation of an external SiO_2 film which considerably inhibits observed rates of reaction (Adachi and Meier, 1986). Overall, experiments demonstrate that Si is not suitable as support for iron oxide undergoing repeated redox cycling.

Figure 3.4 showed that as the MgO content in the sample increased, the amount of H_2 produced increased towards the theoretically expected quantity. However, in the best case shown in Fig. 3.4 with $x_\mathrm{m} = 0.3$ Mg, yields of H_2 equivalent to only 60 % of the theoretical quantity over cycles 5-10 were obtained; Mg is not a suitable support for the proposed process.

Figure 3.5 demonstrated that as the quantity of Cr added to the sample increased, yields of H_2 also increased towards the theoretical limit. If the assumption is made that only the Fe capable of forming the intermediate $FeO\cdot Cr_2O_3$ is stabilised and all the remaining Fe is inactive due to *e.g.* sintering, stoichiometry dictates that for loadings of $x_\mathrm{m} = 0.1$ and 0.3, the expected stable quantity of H_2 produced would be 0.25 and 0.75 mmol H_2, respectively. Instead, from Fig. 3.5, averaging the H_2 produced in cycles 5-10 gives 1.7 mmol and 4.0 mmol, a factor $5 - 7\times$ higher. Hence, the Cr has a much larger effect than simply stabilising the iron sample through the formation of $FeO\cdot Cr_2O_3$. Additional production of H_2 through the reaction of Cr, which itself has several oxides, *e.g.* CrO, CrO_2 and CrO_3, was not found to be possible at 1123 K and 10^5 Pa owing to thermodynamic constraints. Fe_2O_3 and Cr_2O_3 are known to form continuous solid solutions at high temperature (Birks *et al.*, 2006). Also, $FeO\cdot Cr_2O_3$ spinel forms solid solutions with Fe_3O_4. Thus, some mixing of lattice Cr and Fe will occur during the redox cycling and could help prevent sintering. While the addition of Cr increased the yield of H_2, it was not able to offer as significant an improvement as Al.

Results from the samples supported with Al showed that, unlike for those with Mg and Cr, increasing the content of Al did not always improve the yield of H_2. The sample with x_m = 0.3 Al gave lower yields of H_2 than that with x_m = 0.1 Al, as shown in Fig. 3.6. Since the aluminate, $FeO{\cdot}Al_2O_3$, is stable for $y_{CO_2} > 0.01$ (Fig. 3.1), any Al in the sample will bind Fe as $FeO{\cdot}Al_2O_3$ and prevent it from undergoing repeated redox cycles. Increased Al loadings would therefore mean that more iron is bound as aluminate and unavailable for the generation of H_2. The optimum Al loading will therefore be a tradeoff between having enough Al for support and maintaining free Fe for reaction. The current experiments suggest that this value lies in the range $0.01 < x_m < 0.3$ for particles prepared by the back-addition of Al using wet impregnation. The positive effect of Al addition on the yield of H_2 can be explained by considering the Fe-Al-O system. Fe_2O_3 and Al_2O_3 are known to form solid solutions of up to 27 mol % Al_2O_3 in Fe_2O_3 and of up to 9 mol % Fe_2O_3 in Al_2O_3 (Popović *et al.*, 1995). Additionally, at high temperature $FeO{\cdot}Al_2O_3$ spinel readily forms solid solutions with Fe_3O_4. Therefore, some diffusion, *i.e.* mixing, of lattice Al and Fe will occur during redox cycling and could help prevent sintering. From the literature, the addition of Al appears to stabilise iron by the formation of dispersed islands of $FeO{\cdot}Al_2O_3$ (Topsøe *et al.*, 1973); the formation of $FeO{\cdot}Al_2O_3$ will be investigated further in Chapter 4.

Overall, Figs. 3.3-3.6 demonstrated that the choice of reducing gas, either CO or H_2, had little influence on the quantity of H_2 produced for samples of x_m = 0.1 Si, Mg or Cr. Only the sample with x_m = 0.1 Al produced higher yields of H_2 when the reducing gas was H_2. The ratio of measured BET surface area after, and prior to, 10 redox cycles was largest for x_m = 0.1 Al and equal to $0.43/3.96 = 0.11$, as calculated from Table 3.2. Thus, Al maintains active surface area. Comparing results from the tenth cycle in Figs. 3.3-3.6, the additional oxidation in air had the most noticeable effect on the yield of H_2 for the sample containing Al. From thermodynamics, oxidation in air will decompose any $FeO{\cdot}Al_2O_3$ to Fe_2O_3 and Al_2O_3. This release of reactive iron, which has the potential to participate in the subsequent redox cycle, could explain the increased yields of H_2 observed.

3.6 Conclusions

The effect of the addition of Al, Cr, Mg and Si to iron oxide undergoing repeated redox reactions for the generation of H_2 was investigated in a packed bed reactor at 1123 K. Metal additives, which (i) formed an intermediate with a higher melting temperature than the iron species involved and (ii) formed an intermediate which decomposed either during reduction or oxidation to release reactive iron, improved the yield of H_2. Si did not improve yields of H_2 at any loading between 1 and 8 mol %, probably owing to the formation of low melting point silicates and also because SiO_2 was difficult to evenly distribute throughout the particle *via* the hydrolysis of tetraethyl orthosilicate. For Mg, the H_2 yields increased as the loading increased from 1 to 30 mol % Mg. Addition of Cr also increased the amount of H_2 produced, with quantities of H_2 near the theoretical limit for 30 mol % Cr. The presence of Cr facilitated the formation of $FeO{\cdot}Cr_2O_3$, an intermediate with a high melting temperature. Addition of Al up to 10 mol % increased the quantity of H_2 produced; a sample with 30 mol % Al, however, showed lower yields of H_2 compared to one with 10 mol % Al. Unlike for samples with Cr, Mg and Si, oxidation in a mixture of air and N_2 had a marked effect on samples impregnated with Al, presumably owing to the release of reactive iron during decomposition of $FeO{\cdot}Al_2O_3$ to Fe_2O_3 and Al_2O_3. The Fe_2O_3 modified with $x_m = 0.1$ Al and $x_m = 0.3$ Cr investigated in this study can maintain stable yields of H_2 over 10 cycles at a temperature of 1123 K, and are the most promising candidates for H_2 production using the redox reactions of modified iron oxide. Overall, Al provided the best improvement in H_2 yields over unmodified Fe_2O_3 for reduction to Fe at 1123 K. Surprisingly, the back-addition of a small quantity of Al support, 10 mol %, permitted stable quantities of H_2, near the theoretical limit, to be generated over 10 redox cycles.

Chapter 4

Development of iron oxide carriers using the sol-gel process

4.1 Introduction

Conventional methods for preparing mixed metal oxides do not always produce materials with both (i) a high, internal surface area and (ii) homogeneously-mixed components on the molecular scale. For example, co-precipitation does not always favour homogeneity because hydroxides of different metallic cations generally do not precipitate at the same pH. Mechanically-mixed oxides usually do not have high surface areas and suffer from inhomogeneities of the mixed materials (Ward and Ko, 1995). The sol-gel method has received much attention in catalysis (Ertl *et al.*, 1999; Brinker and Scherer, 1989) because it allows the homogenous mixing of components almost at the molecular level as well as the control of pore structure and surface area using a low temperature synthesis. While limited research on Ni-based (Ishida and Jin, 1996; Zhao *et al.*, 2008) oxygen carriers prepared using a sol-gel technique exists, only recently have similar Fe-based (Li *et al.*, 2009) oxygen carriers been investigated for chemical looping combustion.

A complete introduction to sol-gel theory is given in Brinker and Scherer (1989). Briefly, a colloid is defined as a suspension where the dispersed phase is so small ($\sim 1 - 1000$ nm) that gravitational forces are negligible. A sol is defined as a colloidal suspension of solid particles. Sol-gel chemistry relies on two reactions: hydrolysis and condensation.

Starting with a molecule containing a trivalent metal and using M to denote the metal, R an alkyl group, OR an alkoxy group and ROH an alcohol, hydrolysis proceeds according to

$$\mathrm{M(OR)_3 + H_2O \rightleftarrows HO - M(OR)_2 + ROH.} \tag{4.1}$$

Metal alkoxides are preferred precursors for sol-gel chemistry because they readily react with water. If all of the OR groups in the $M(OR)_3$ reacted to form $M(OH)_3$, the metal would be fully hydrolysed. Fully or partially hydrolysed molecules can bond *via* condensation:

$$\mathrm{(OR)_2M - OH + HO - M(OR)_2 \rightleftarrows (OR)_2M - O - M(OR)_2 + H_2O} \tag{4.2}$$

$$\mathrm{(OR)_2M - (OR) + HO - M(OR)_2 \rightleftarrows (OR)_2M - O - M(OR)_2 + ROH.} \tag{4.3}$$

The metallic species on the right hand side of reactions (4.2) and (4.3) are polymers. A gel is defined (Brinker and Scherer, 1989) as a continuous solid chain of polymers encapsulating a continuous liquid phase and is formed when a polymer grows to the dimensions of the solution, *e.g.* the size of the containing beaker. Drying a gel in air will produce a xerogel; supercritical drying, which eliminates capillary pressure and gel shrinkage, will produce an aerogel (Brinker and Scherer, 1989).

The most common support for Fe_2O_3 for chemical looping applications is Al_2O_3 and Chapter 3 has already shown that the addition of Al_2O_3 to iron oxide permits stable quantities of H_2 to be produced over 10 cycles even when the iron oxide is reduced fully to Fe. Table 4.1 gives a summary of some composite particles of Fe_2O_3 and Al_2O_3 used in the literature and the corresponding preparation method and reference. While methods of preparation range from the mechanical mixing of oxide powders (Ishida *et al.*, 2005) to drying aqueous solutions of Fe and Al nitrate precursors (Jin *et al.*, 1999; Ishida *et al.*, 1998), a single weight ratio of 60 wt. % Fe_2O_3 and 40 wt. % Al_2O_3 is typically used. Other supports for Fe_2O_3 include ZrO_2 (Mattisson *et al.*, 2004; Adánez *et al.*, 2004; Galvita *et al.*, 2008b), TiO_2 (Mattisson *et al.*, 2004; Ishida *et al.*, 1998; Jin *et al.*, 1999; Adánez *et al.*, 2004), MgO (Jin *et al.*, 1999), $MgAl_2O_4$ (Mattisson *et al.*, 2004) and yttria-stabilised zirconia (YSZ) (Ishida *et al.*, 1998). Notably, SiO_2 is unsuitable, owing to the formation of unreactive silicates with low melting points, shown in Chapter 3.

The objective of this study is to compare the performance of pure Fe_2O_3 carriers made by mechanical mixing with composite xerogels of Fe_2O_3 and Al_2O_3 made using a sol-gel method, especially with respect to the ability to be reduced completely to Fe over $\sim$ 40 cycles.

Table 4.1: Table summarising Fe_2O_3 and Al_2O_3 composite carriers used in chemical looping combustion. Preparation methods include: mechanical mixing of powders of Fe_2O_3 and Al_2O_3, freeze granulation of mechanically-mixed oxide powders, mixing aqueous solutions of iron and aluminum nitrates, and wet-impregnation of γ-Al_2O_3 support. The final composition of the oxygen carrier is listed as the weight percent of Fe_2O_3 after calcination; the remaining mass fraction is Al_2O_3. The crushing stress is given for the fresh oxygen carrier.

Reference	Preparation	Composition	Calcining		Crushing Stress
		(wt. % Fe_2O_3)	Temp	Time	(MPa)
Li *et al.* (2009)	sol-gel	60 %	1173 K	12 h	10
Ishida *et al.* (2005)	mech. mix	25 %	1073 K	10 h	2
	Fe_2O_3, Al_2O_3		1643 K	10 h	54
Jin *et al.* (1999)	dissolution $Fe(NO_3)_3{\cdot}9H_2O$,	60 %	1573 K	6 h	44.3
Ishida *et al.* (1998)	$Al(NO_3)_3{\cdot}6H_2O$		1573 K	6 h	44.3
Mattisson *et al.* (2004)	mech. mix &	60 %	1373 K	6 h	18
Abad *et.al*, 2007Abad *et al.* (2007)	freeze granulation		1573 K	6 h	167
Mattisson *et al.* (2004)	$Fe(NO_3)_3{\cdot}9H_2O$	22 %	1373 K	6 h	
	impregnated γ-Al_2O_3				
Adánez *et al.* (2004)	mech. mix & 10 wt. %	80 %	1373/1573 K	6 h	6/27
	graphite for pores	60 %	1373/1573 K	6 h	5/25
		40 %	1373/1573 K	6 h	5/29

4.2 Experimental

Oxygen carriers with different mass ratios of Fe_2O_3 and Al_2O_3 (60:40, 80:20, 90:10 wt./wt.) were prepared using the Yoldas sol-gel process (Yoldas, 1975). In a typical synthesis, aluminium isopropoxide (Acros Organics; > 98 wt. % purity) was added to water which had been purified by reverse osmosis and heated to 348 K; the mixture was allowed to hydrolyse slowly for 2 h with constant stirring. The resulting slurry was peptised with nitric acid (Fisher; 70 wt. %, diluted). In all syntheses, the molar ratio between Al^{3+}, water and H^+ was constant and equal to 0.5:50:0.07. The temperature was then raised to 363 K and the sol was refluxed for 12 h. Subsequently, the appropriate amount of $Fe(NO_3)_3 \cdot 9H_2O$ (Acros Organics, > 98 wt. % purity) dissolved in water at 363 K to obtain a $\sim$ 1 M aqueous solution was added. The resulting slurry was refluxed for another 12 h at 363 K, followed by cooling to room temperature. The encapsulated solvents were removed by drying the gel in an oven at 373 K overnight. The resulting xerogel was calcined for 3 h at 1173 K and then sieved to +300,-425 μm.

For comparison, particles of unmodified iron oxide were prepared as in Chapter 2 by spraying water on to Fe_2O_3 powder (Sigma-Aldrich, purity > 99.9 wt. %, size < 5 μm) and mechanically mixing. The resulting agglomerates were sintered for 3 h at 1173 K and then sieved to $d_\mathrm{p} = +300, -425$ μm. Table 4.2 shows results of the BET surface area and mean pore diameter, $\bar{d}_\mathrm{pore}$, for mechanically-mixed Fe_2O_3 particles and particles prepared by the sol-gel

Table 4.2: Measured BET surface area, BJH pore volume, mean pore diameter and crushing stress after calcination and prior to reaction for the 60, 80 and 90 wt. % Fe_2O_3 oxygen carriers prepared using the sol-gel process; 100 wt. % Al_2O_3 prepared using the sol-gel process; and unmodified Fe_2O_3 prepared by mechanical mixing. Determination of the crushing stress involved particles of diameter +1700,-2060 μm; all other characterisations involved particles of diameter +300,-425 μm.

Preparation	Composition	BET (m^2/g)	BJH (cm^3/g)	$\bar{d}_{\mathrm{pore}}$ (nm)	Calcining Temp	Calcining Time	Crushing Stress (MPa)
sol-gel	60 wt. % Fe_2O_3, 40 wt. % Al_2O_3	15.5	0.09	24	1173 K	3 h	0.2
sol-gel	80 wt. % Fe_2O_3, 20 wt. % Al_2O_3	8.5	0.06	27	1173 K	3 h	0.6
sol-gel	90 wt. % Fe_2O_3, 10 wt. % Al_2O_3	10.5	0.06	22	1173 K	3 h	0.3
sol-gel	100 wt. % Al_2O_3	168	0.35	6	1173 K	3 h	
sol-gel	100 wt. % Al_2O_3	299	0.40	4	773 K	3 h	
mech. mix	100 wt. % Fe_2O_3	1.5	0.00	7	1173 K	3 h	3.3

process, both dried in an oven at 373 K, followed by calcination at typically 1173 K.

The reduction and oxidation of the oxygen carrier was performed in the apparatus described in Chapter 3. The temperature of the packed bed was maintained at 1123 K in all experiments, as measured by a type K thermcouple inside the bed. The total mass of particles added to the bed was 0.3 g in all cases. The composition of the effluent gas was measured using identical analysers in the same arrangement as in Chapter 2, section 2.2. The flowrates, compositions of the inlet gases and cycle times for each experiment are listed in Table 4.3.

For a sphere subjected to a force, F_z, on opposite sides of a diameter, the crushing stress was calculated from the empirical relation:

$$\sigma_{\mathrm{T}} = k_{\mathrm{F}} \frac{F_z}{R^2}, \tag{4.4}$$

where σ_{T} is the crushing stress (Pa), F_z is the applied force (N), R is the sphere's external radius (m), and k_{F} is a dimensionless constant with a typical value of $k_{\mathrm{F}} = 0.22$ (Jaeger, 1967; Ishida *et al.*, 2005). The average value of the crushing stress, σ_{T}, was determined (Stable Micro Systems, TA-XT2 Texture Analyser with a 5 kg load cell) using 20 separate particles with $R = 950$ μm, omitting the maximum and minimum value, and is reported in Table 4.2. Since many authors report crushing force (N) rather than stress (N/m^2), some calculations were necessary. For example, the crushing stress for oxygen carriers from Mattisson *et al.* (2004) was calculated using Eq. (4.4) with a particle radius of 112 μm and using their reported breakage forces for particles calcined at 1373 K and 1573 K of 1 N and 9.5 N, respectively, given in Fig. 5 of Mattisson *et al.* (2004). Abad *et al.* (2007) used an identical oxygen carrier

Table 4.3: Redox cycling: gas mixtures (vol. %), flowrates as measured at 298 K and 10^5 Pa, and corresponding flow durations for experiments with an initial charge of 0.3 g of oxygen carrier. Reoxidation to Fe_2O_3 required air. The total cycle time was 20 min and 16 min for experiments with and without oxidation in air.

	purge	reduction	purge	oxidation	purge	oxidation	Figs.	Symbol
time (s)	0-120	120-720	720-780	780-960	960-1020	1020-1200		
flow (m^3/s)	3.3×10^{-5}	3.3×10^{-5}	3.3×10^{-5}	3.3×10^{-5} N_2,	3.3×10^{-5}	3.3×10^{-5}		
flow (m^3/s)				8.33×10^{-9} $H_2O_{(l)}$				
$Fe_3O_4 \rightleftarrows Fe$	N_2	10% CO/90% N_2	N_2	75% N_2/25% steam			4.2	△, ○, □, ◊
$Fe_2O_3 \rightleftarrows FeO$	N_2	10% CO/10% CO_2/80% N_2	N_2	75% N_2/25% steam	N_2	air	4.2, 4.3	+
$Fe_2O_3 \rightleftarrows Fe$	N_2	10% CO/90% N_2	N_2	75% N_2/25% steam	N_2	air	4.2,4.3,4.4	▲, ●, ■, ♦

to that of Mattisson *et al*. (2004), but with slightly different radius; this difference in radius was deemed inconsequential and an identical crushing stress reported. Adánez *et al*. (2004) list the crushing stress for cylindrical extrudates of diameter $d = 2$ mm in units of force *per* unit length extrudate. To convert this value to an estimate for an equivalent spherical crushing stress, Eq. (4.4) was used with the approximation $R = L/2 = d/2 = 1$ mm. Table 4.2 demonstrates that the crushing stresses for the oxygen carriers prepared using the sol-gel process were lower than those for the mechanically-mixed Fe_2O_3. In general, particles with higher surface area gave lower crushing stresses.

A field emission scanning electron microscope (FESEM, JSM-6340F) operated at 5 kV was used to obtain high resolution images of the morphology of the oxygen carriers prior to the redox experiments. X-ray diffraction (XRD, Philips model PW1830/00, Cu K_α, 40 kV and 40 mA, 0.01° s^{-1}, receiving and anti-scatter slits 1°, divergence slit 0.3 mm, in air at 298 K) was used to detect the presence of $FeO{\cdot}Al_2O_3$. The specific surface area of the samples was calculated from N_2 adsorption isotherms (Micromeritics, Tristar 3000) using the BET model (Brunauer *et al.*, 1938); the cumulative pore volume for pores between 1.7 and 200 nm in diameter was estimated using the BJH model (Barrett *et al.*, 1951), as described in Appendix 2.

4.3 Results

4.3.1 SEM characterisation

Prior to any redox experiments, the morphology of the oxygen carriers was investigated using scanning electron microscopy for (a) the unmodified Fe_2O_3 particles prepared by mechanical

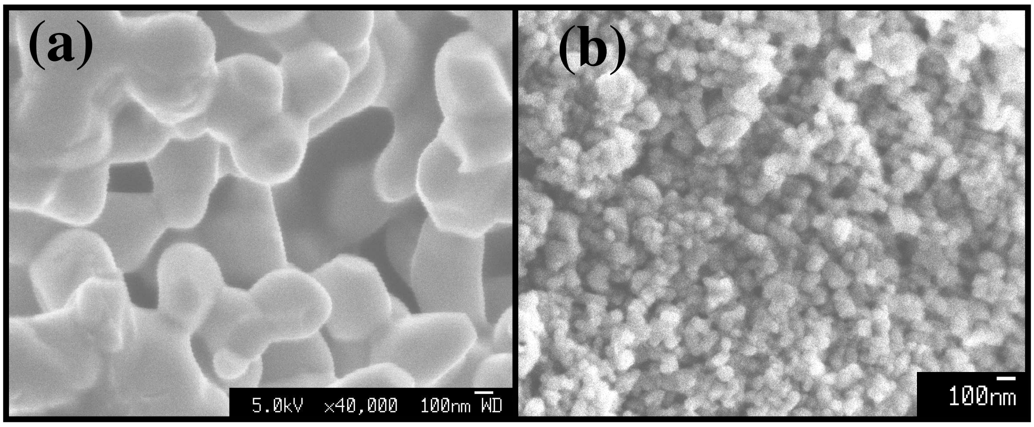

Figure 4.1: Field emission scanning electron microscope (FESEM) images of (a) the unmodified Fe_2O_3 prepared by mechanically mixing and (b) a 60 wt. % Fe_2O_3, 40 wt. % Al_2O_3 carrier prepared using the sol-gel process. The particles are shown in their fully oxidised state after calcining at 1123 K for 3 h and prior to any reaction. A difference in grain size is noticable; the scale bars in each figure are of equal length, 100 nm.

mixing and (b) the 60 wt. % Fe_2O_3, 40 wt. % Al_2O_3 particles prepared using the sol-gel method, as shown in Figure 4.1. The important difference between these images is the disparity in the size of the individual grains. Unmodified Fe_2O_3 has grains with an average diameter of 500 nm, while the sol-gel carrier has grains with an average diameter of 80 nm, nearly one order of magnitude smaller. This difference in grain size translates into a similar order of magnitude difference in specific surface areas, as shown in Table 4.2. The morphological difference between these two samples could contribute towards the difference in conversion discussed later.

4.3.2 Stability of unmodified Fe_2O_3

To quantify the ability of the oxygen carrier to produce H_2 over repeated redox cycles, a conversion was defined as:

$$X_{H_2} = \frac{m_{H_2}}{x_w m_{ox}} \cdot \left(\frac{M_{Fe_2O_3}}{M_{H_2}} \cdot \frac{3}{8} \right) \approx \frac{m_{H_2}}{x_w m_{ox}} \cdot 30, \qquad (4.5)$$

where m_{H_2} is the mass of the H_2 produced, m_{ox} is the mass of the fully oxidised carrier as Fe_2O_3 and Al_2O_3, x_w is the mass fraction of Fe_2O_3 in the fully oxidised carrier and $M_{Fe_2O_3}$ and M_{H_2} are the molecular weights of Fe_2O_3 and H_2, respectively. Here it is noted that the loading of Al_2O_3 is reported as a mass % rather than a mole % as done in Chapter 3; also the quantity of H_2 produced is reported as a conversion, rather than an absolute molar quantity.

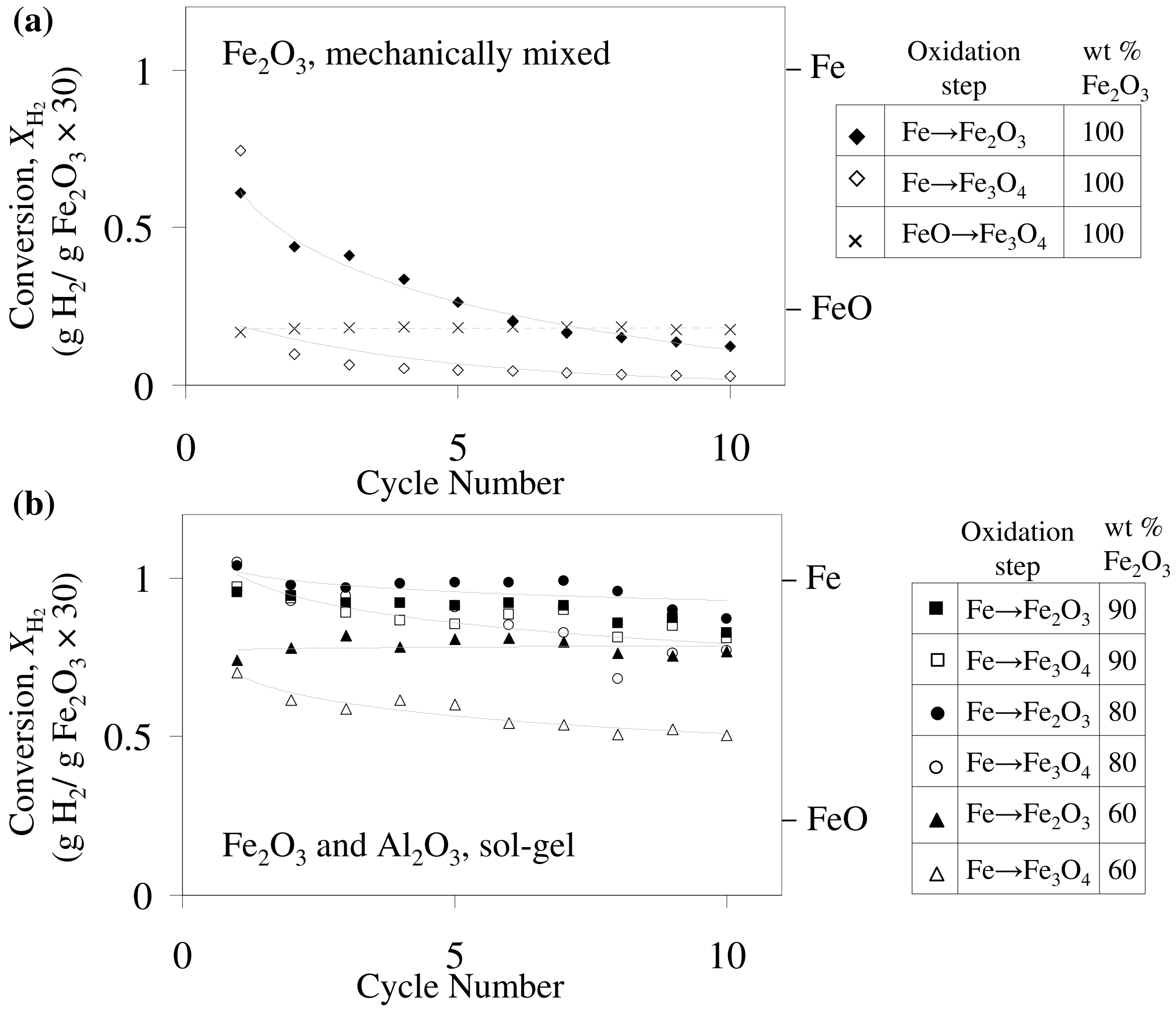

Figure 4.2: (a) Measured conversion, X_{H_2}, as a function of cycle number for the mechanically-mixed oxygen carrier reacted at 1123 K. (b) Measured conversion, X_{H_2}, as a function of cycle number for the oxygen carriers produced by the sol-gel method, reacted at 1123 K. A conversion of $X_{H_2} = 1$ represents the theoretical quantity of H_2 expected from oxidation of Fe to Fe_3O_4 in steam, as shown by the right hand ordinate; the theoretical conversion, X_{H_2}, for oxidation of FeO to Fe_3O_4 is also indicated.

Initially, 10 redox cycles with 0.3 g of the unmodified Fe_2O_3 oxygen carrier were performed at 1123 K. Figure 4.2(a) shows X_{H_2} *versus* cycle number. Reduction to FeO in a mixture of 10 vol. % CO, 10 vol. % CO_2, balance N_2 resulted in stable quantities of H_2, near that predicted from stoichiometry (reaction 1.16), being produced during subsequent oxidation with steam, regardless of whether samples were oxidised in steam or a sequence of steam and air. In contrast to reduction to FeO, for unmodified Fe_2O_3 reduced to Fe, X_{H_2} drops to 0.1 by cycle 2 and 0.03 by cycle 10. If additional oxidation in air, reaction (1.17), is performed to return the oxide to Fe_2O_3, this drop is less precipitous; however, Fig. 4.2 shows that even in this case a low conversion of $X_{H_2} = 0.1$ is obtained by cycle 10. Thus, for repeated production of H_2 it seems preferable to reduce unmodified Fe_2O_3 only to FeO, since by cycle 10, experiments involving reduction to FeO generated higher quantities of H_2 than experiments involving reduction to Fe.

4.3.3 Stability of composites of Fe_2O_3 and Al_2O_3 prepared using the sol-gel process

Next, reduction of the sol-gel oxygen carriers with $x_\mathrm{w} = 0.6, 0.8$ and 0.9 Fe_2O_3, balance Al_2O_3 was performed at 1123 K; the Fe_2O_3 was reduced completely to Fe. Figure 4.2(b) demonstrates that the production of H_2 using the redox of iron oxides is promising for sol-gel derived carriers with 80 and 90 wt. % Fe_2O_3 over 10 cycles, with conversions of $X_{\mathrm{H}_2} \approx 0.9$. Open symbols represent experiments where oxidation was performed with 25 vol. % steam, balance N_2 only, *i.e.*, reaction (3.1); filled symbols represent experiments where oxidation was performed in 25 vol. % steam, balance N_2, reaction (3.1), followed by oxidation in air, reaction (1.17), to Fe_2O_3. In Fig. 4.2(b) for particles with 60 wt. % Fe_2O_3, the observed conversion is lower than the value predicted from stoichiometry in reaction (3.1). Here, an average over 10 cycles gives $X_{\mathrm{H}_2} = 0.78$ and $X_{\mathrm{H}_2} = 0.56$ for experiments with and without additional oxidation in air, respectively. Notably, the filled symbols in Fig. 4.2 consistently give higher values of X_{H_2} than their open symbol counterparts, corroborating the finding in Chapter 3 that oxidation of the Al carrier with air, *via* reaction (1.17), after oxidation in steam, reaction (3.1), has a beneficial effect. An explanation for this observation is provided later, based on the formation of $FeO{\cdot}Al_2O_3$. The volume fraction of CO in the effluent at the end of each reduction cycle in Fig. 4.2 was ≥ 9.7 vol. %; the inlet concentration of CO was 10 vol. %. Therefore, no large discrepancy between the inlet and outlet concentration of CO existed prior to switching off the reducing gas.

Figure 4.2 demonstrated a marked increase in X_{H_2} for composite particles of Fe_2O_3 and Al_2O_3 prepared using the sol-gel process compared to that for unmodified Fe_2O_3 over 10 cycles. However, for chemical looping combustion on an industrial scale, the oxygen carrier must withstand hundreds or even thousands of redox cycles. The sol-gel carriers with $x_\mathrm{w} = 0.6, 0.8$ and 0.9 Fe_2O_3 were therefore tested at 1123 K over 30-40 cycles for reduction on each cycle to Fe. Figure 4.3 shows the conversion of the oxygen carrier, X_{H_2}, calculated using Eq. (4.5), *versus* cycle number. The fraction of CO in the effluent at the end of each reduction cycle in Fig. 4.3 was ≥ 9.7 vol. %; the inlet concentration of CO was 10 vol. %. Therefore, no large discrepancy between the inlet and outlet concentration of CO existed prior to switching off the reducing gas. In all cases, air was introduced after the steam to oxidise the Fe_3O_4 to Fe_2O_3 *via* reaction (1.17). For the 80 and 90 wt. % Fe_2O_3 oxygen carriers, $X_{H_2} > 0.9$ for the initial 7 cycles. From cycle 8 to 25, shown between the dashed vertical lines, however, the conversion decreased to $X_{H_2} = 0.43$ and $X_{H_2} = 0.34$ for the 80 and 90 wt. % Fe_2O_3 carriers, respectively. From cycle 25 to 36 a further reduction of the conversion is observed. In Fig. 4.3, conversions for the 90 wt. % Fe_2O_3 carrier are consistently lower than those for the 80 wt. % Fe_2O_3 carrier. Surprisingly, the 60 wt. % Fe_2O_3 oxygen carrier displayed a nearly constant conversion with an average value of $X_{H_2} = 0.75$ over 40 cycles, as shown in Fig. 4.3. The total moles of H_2 produced *per* unit mass of carrier with 60 wt. % Fe_2O_3, gave 7.5 mmol H_2/ g carrier compared to $\sim$ 4.5 mmol H_2/ g carrier in cycle 35 for the samples with 80 and 90 wt. % Fe_2O_3. Figure 4.3 also shows X_{H_2} for unmodified Fe_2O_3, reduced to FeO only in a mixture of 10 vol. % CO, 10 vol. % CO_2, balance N_2. The conversion is again stable with $X_{H_2} = 0.15$ or 3.0 mmol H_2/ g carrier over 40 cycles. All of the sol-gel carriers, *i.e.* $x_w = 0.6, 0.8$ and 0.9, outperform, for 40 the cycles, the unmodified, mechanically-mixed Fe_2O_3 reduced to FeO.

The point inside the dashed circle at cycle 42 in Fig. 4.3, represents an experiment where the reduction time was increased from 10 min to 20 min for the 90 wt. % Fe_2O_3 carrier. The reducing gas composition was still 10 vol. % CO, balance N_2. Doubling the reduction time increased the conversion from $X_{H_2} = 0.25$ to 0.35, indicating that reduction had not reached completion after the 10 min interval used here. The remaining values in Fig. 4.3, labelled with temperatures of 1013 K and 873 K, were taken from other studies and will be discussed later.

For use in polymeric electrolyte membrane (PEM) fuel cells, the hydrogen must have a contamination of CO < 50 ppmv so as not to poison the Pt on the anode. Other processes, *e.g.* ammonia synthesis or hydrocracking (Isalski, 1989), have less stringent [CO] requirements. The H_2 in this study had an average contamination, calculated from the results in Figs. 4.2 and 4.3 for the 80 and 90 wt. % Fe_2O_3 oxygen carriers, of $[CO]/([H_2]+[CO]) = 1$ vol. % = 10000 ppmv, much in excess of the 50 ppmv limit for PEM fuel cells. For the 60 wt. % Fe_2O_3 oxygen carriers, experiments in Figs. 4.2 and 4.3 gave 0.1 vol. % = 1000 ppmv CO. By contrast, reduction of unmodified, mechanically-mixed oxygen carriers to FeO only at 1123 K, 10^5 Pa and a partial pressure of $p_{CO_2}/p_{CO} = 1$ were shown to give [CO]< 0.005 vol. % = 50 ppmv in Chapter 2, section 2.3.6.

From the experiments shown in Fig. 4.3, the conversion as a function of time for 0.3 g of the (a) 60, (b) 80 and (c) 90 wt. % Fe_2O_3 oxygen carriers reduced in 10 vol. % CO, balance

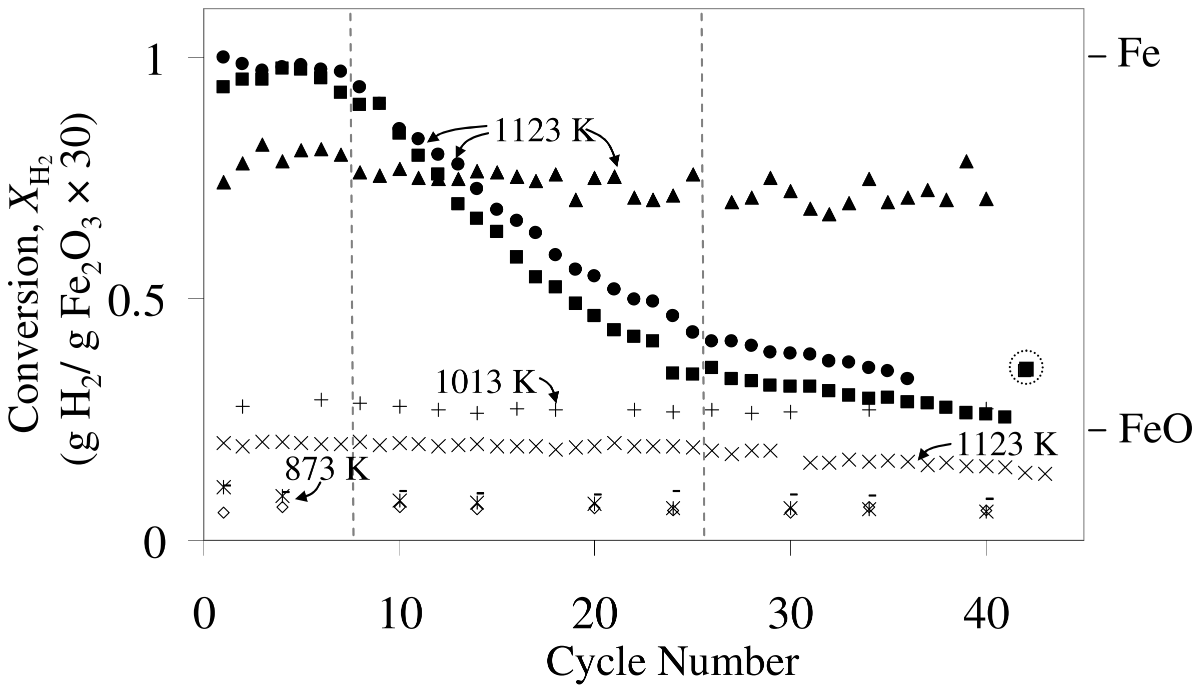

Symbol	Oxidation Step	wt. % Fe_2O_3	Reference
■	Fe→Fe_2O_3	90	this work
●	Fe→Fe_2O_3	80	this work
▲	Fe→Fe_2O_3	60	this work
×	FeO→Fe_2O_3	100	this work
+	Fe→Fe_3O_4	38	Galvita *et al.* 2007
– ◇ ⁎	FeO→Fe_3O_4	76-78	Galvita *et al.* 2008a

Figure 4.3: Measured conversion, X_{H_2}, for 0.3 g of oxygen carrier over 30 to 40 cycles at 1123 K. Results for carriers with 60 (▲), 80 (●) and 90 (■) wt. % Fe_2O_3 prepared using the sol-gel process and reduced to Fe, as well as for unmodified Fe_2O_3 prepared by mechanically mixing and reduced only to FeO (×) are shown. Increasing the reduction time from 1200 to 2400 s with a gas composition of 10 vol. % CO, balance N_2 resulted in a higher conversion for the 90 wt. % Fe_2O_3 particles (■), shown by the point within the dashed circle. Final conversions for modified particles from the literature reacted (Galvita and Sundmacher, 2007) at 1013 K (+) and (Galvita *et al.*, 2008a) at 873 K (-,◇,⁎) are shown for comparison. A conversion of $X_{H_2} = 1$ represents the theoretical quantity of H_2 expected from oxidation of Fe to Fe_3O_4 in steam, as shown by the right hand ordinate; the theoretical conversion, X_{H_2}, for oxidation of FeO to Fe_3O_4 is also indicated.

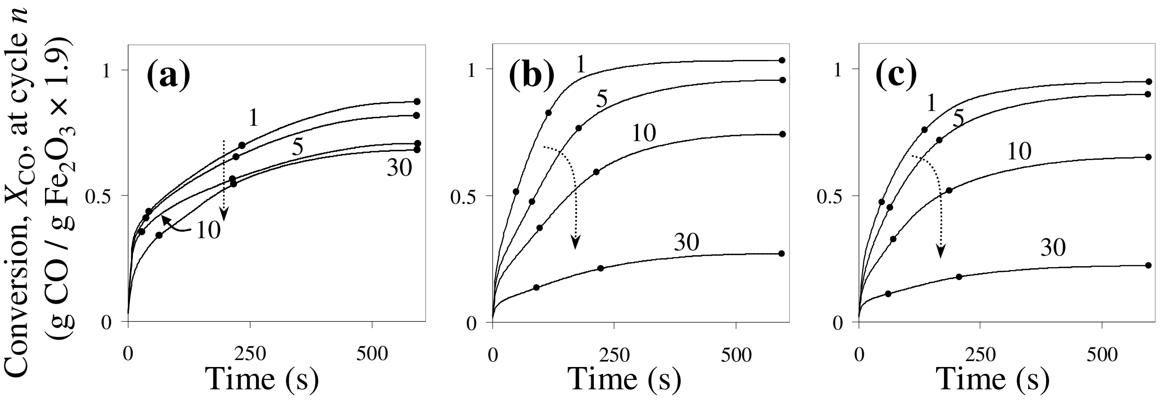

Figure 4.4: Measured conversion, X_{CO}, *versus* time for 0.3 g of (a) 60, (b) 80 and (c) 90 wt. % Fe_2O_3 carrier prepared using the sol-gel process for cycles $n = 1, 5, 10$ and 30 at 1123 K corresponding to experiments in Fig. 4.3. In all cases, reduction was performed in 10 vol. % CO, balance N_2 for 600 s. Black dots represent the time to reach 50 %, 80 % and 100 % of the final conversion at t = 600 s.

N_2 at 1123 K was derived and is displayed in Fig. 4.4. Each line consists of 600 points and corresponds to a specific cycle from Fig. 4.3. The conversion, X_{CO}, was calculated from the amount of CO consumed by:

$$X_{CO} = \frac{m_{CO}}{x_w m_{ox}} \cdot \left(\frac{M_{Fe_2O_3}}{M_{CO}} \cdot \frac{1}{3} \right) \approx \frac{m_{CO}}{x_w m_{ox}} \cdot 1.9, \tag{4.6}$$

where m_{CO} is the mass of the CO consumed, m_{ox} is the mass of the fully oxidised carrier, x_w is the mass fraction of Fe_2O_3 in the fully oxidsed carrier and $M_{Fe_2O_3}$ and M_{CO} are the molecular weights of Fe_2O_3 and CO, respectively. Since the CO reacts to form a commensurate quantity of CO_2, the conversion based on the CO_2 signal, X_{CO_2}, provided a useful check; typically, $X_{CO} = X_{CO_2} \pm 0.05$ where X_{CO} and X_{CO_2} vary between 0 and 1. In Fig. 4.4(a) the final conversion for the 60 wt. % Fe_2O_3 carrier shown by the black dots at t = 600 s decreased from $X_{CO} = 0.87$ in cycle 1 to $X_{CO} = 0.68$ in cycle 30. In Fig. 4.4(b), the final conversion of the 80 wt. % Fe_2O_3 oxygen carrier decreased with cycle number and was $X_{CO} = 1.0$ and 0.27 for cycles 1 and 30, respectively. In Fig. 4.4(c), the final conversion for the 90 wt. % Fe_2O_3 oxygen carrier decreases with cycle number and is given by $X_{CO} = 0.95$ and 0.22 for cycles 1 and 30, respectively. Black dots and dashed arrows indicate that the time to reach 50 % and 80 % of the final conversion, increased with cycle number for oxygen carriers with 80 and 90 wt. % Fe_2O_3, but remained approximately constant for that with 60 wt % Fe_2O_3.

4.3.4 Formation of $FeO \cdot Al_2O_3$

A thermodynamic analysis of the stability of $FeO \cdot Al_2O_3$ at 1123 K and 10^5 Pa was presented in Chapter 3. The formation of $FeO \cdot Al_2O_3$ was found to be favourable for $0.01 < p_{CO_2}/p_{CO} < 1.0$ and $0.01 < p_{H_2O}/p_{H_2} < 1.0$. Thus, $FeO \cdot Al_2O_3$ should be stable over the entire redox cycle for the case without oxidation in air, since during reduction incoming CO is readily oxidised to CO_2 giving $p_{CO_2}/p_{CO} > 0.01$ and during oxidation even trace amounts of H_2 will cause $p_{H_2O}/p_{H_2} < 1.0$. The $FeO \cdot Al_2O_3$ will be oxidised to Fe_2O_3 and Al_2O_3 only if oxidation in air is performed. Considering equilibrium, the preceding experimental observations suggest that (i) increasing the amount of labile Al_2O_3 in the oxygen carrier will result in more atomic Fe being bound as $FeO \cdot Al_2O_3$ and unavailable for reaction and therefore lead to lower initial conversions in oxygen carriers with a higher mass fraction of Al_2O_3, as shown in Fig. 4.2(b); (ii) since $FeO \cdot Al_2O_3$ decomposes to Fe_2O_3 and Al_2O_3 in air, oxidation in air will release reactive iron oxide once *per* cycle and could lead to higher values for X_{H_2}, also shown in Fig. 4.2(b).

To verify the formation of $FeO \cdot Al_2O_3$ experimentally, X-ray diffraction (XRD) was used. Figure 4.5 shows the diffraction pattern for the 60 wt. % Fe_2O_3, 40 wt. % Al_2O_3 carrier which had been reduced in 10 vol. % CO, balance N_2 and oxidised in 25 vol. % steam, balance

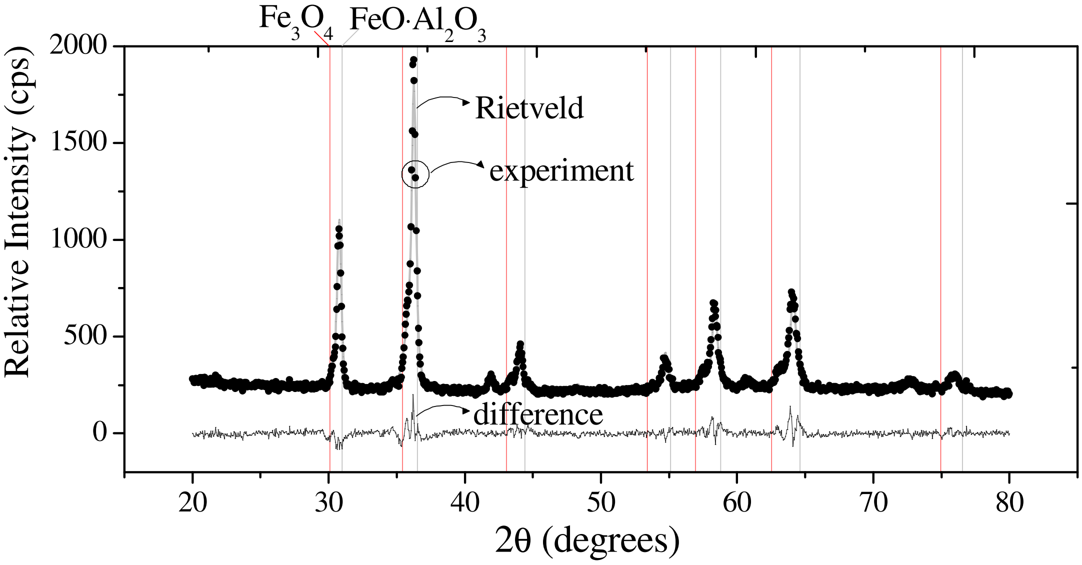

Figure 4.5: Experimental X-ray diffraction pattern (●) and Rietveld fit (—) for a 60 wt. % Fe_2O_3, 40 wt. % Al_2O_3 oxygen carrier which had been reduced in 10 vol. % CO, balance N_2 and oxidised in 25 vol. % H_2O, balance N_2 for 10 cycles. The difference is plotted below the diffraction patterns and is nearly zero. Pairs of vertical lines show diffraction peaks for identical Bragg reflection planes of pure Fe_3O_4 (red, left line in each pair) and $FeO \cdot Al_2O_3$ (grey, right line in each pair). The experimental diffraction peak consistently lies between each line pair indicating a mixture of Fe_3O_4 and $FeO \cdot Al_2O_3$.

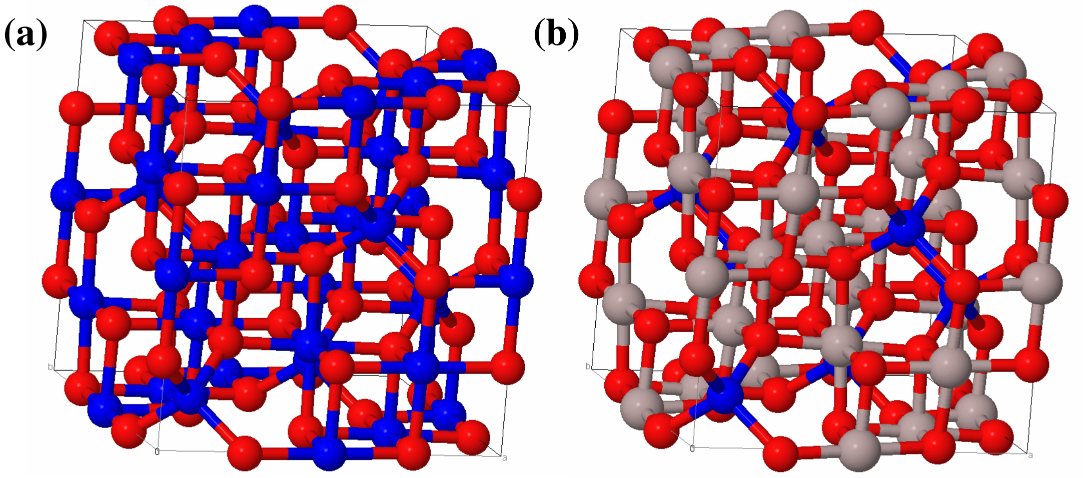

Figure 4.6: Illustration of the cubic Fd-3m structure of (a) Fe_3O_4 and (b) $FeO{\cdot}Al_2O_3$ (ICSD, 2010). Blue, grey and red spheres represent Fe, Al and O atoms, respectively.

N_2 over 10 cycles. The full peak widths at half of the maximum intensity (FWHM) were typically 0.3 – 0.5° and suggested peak broadening for $20° < 2\theta < 80°$. For comparison, the instrument broadening estimated from a pure sample of Fe_3O_4 of known crystallite size gave $\sim 0.17°$ (FWHM) at $2\theta = 34.8°$. Peak broadening is common in samples with either small crystallites below 1 μm or those where there is significant lattice stress. In the present case, lattice stress owing to chemical heterogeneity is likely, since the lattice dimensions vary from $a = b = c = 8.39$ Å to 8.16 Å for Fe_3O_4 and $FeO{\cdot}Al_2O_3$, respectively (ICSD, 2010). Figure 4.6 shows a schematic illustration of the structure of Fe_3O_4 and $FeO{\cdot}Al_2O_3$, where it is noted that both compounds are cubic. The diffraction pattern for the sample in Fig. 4.5 also suggested a mixture of crystallites of Fe_3O_4 and $FeO{\cdot}Al_2O_3$ (JCPDS, 2005c). The maximum peak for the sample consistently lies within the bounds of 2θ given by pairs of vertical lines corresponding to the peaks for identical Bragg reflection (hkl) planes of Fe_3O_4 (left, red) and $FeO{\cdot}Al_2O_3$ (right, black). Phase identification, using published information (JCPDS, 2005c), revealed the presence of Fe_3O_4 and $FeO{\cdot}Al_2O_3$; the peak at 41.90° was attributed to FeO which is also cubic and has a listed primary peak at 41.93°. The lack of intensity at 25.58° was used to rule out the presence of corundum, Al_2O_3. A multi-phase Rietveld refinement using standards from the ICSD database (ICSD, 2010) was performed to quantify each phase. Figure 4.5 shows the experimental diffraction pattern for the oxygen carrier given by points, the predicted diffraction pattern shown by the fitted line from the quantitative Rietveld analysis and the difference between the two. Good reproduction of peaks and peak shoulders was obtained. The quantitative estimate of each phase gave 76 mol % $FeO{\cdot}Al_2O_3$, 20 mol % Fe_3O_4 and 4 mol %

FeO. The actual mole fraction of $FeO{\cdot}Al_2O_3$ in the sample assuming it is composed entirely of Fe_3O_4 and $FeO{\cdot}Al_2O_3$ consistent with thermodynamics, was 75 mol %, in good agreement. The formation of $FeO{\cdot}Al_2O_3$ has therefore been quantitatively confirmed and is consistent with Topsøe *et al.* (1973) who suggested the formation of $FeO{\cdot}Al_2O_3$ during reduction of an iron based ammonia catalyst.

4.4 Discussion

The redox reactions of iron oxide enable synthesis gas derived from either coal or biomass to be upgraded to H_2 with the simultaneous capture of CO_2. Figure 4.2 showed that oxygen carriers prepared using a sol-gel method with 60, 80 and 90 wt. % Fe_2O_3 could successfully produce H_2 over 10 cycles at 1123 K. For increased numbers of cycles of operation, a noticeable drop in X_{H_2} with cycle number was observed for oxygen carriers with 80 and 90 wt. % Fe_2O_3, giving $X_{H_2} < 0.35$ after 35 cycles, as shown in Fig. 4.3. By contrast, carriers with 60 wt. % Fe_2O_3, 40 wt. % Al_2O_3 gave stable quantities of H_2 over 40 cycles with an average conversion of $X_{H_2} = 0.75$. In general, for experiments involving additional oxidation in air, Fig. 4.3 demonstrates that higher conversions, X_{H_2}, are obtained with sol-gel carriers with higher initial surface areas, *viz* (X_{H_2} for $x_w = 0.6 > X_{H_2}$ for $x_w = 0.8 > X_{H_2}$ for $x_w = 0.9$). Higher surface area composite particles might be obtainable by using iron alkoxide as the iron precursor rather than the iron nitrate used here. The measured BET surface area for the 90 wt. % Fe_2O_3 particles used for Fig. 4.3 after 42 cycles was 0.1 m^2/g; the surface area for the 60 wt. % Fe_2O_3 particles used for experiments in Fig. 4.3 after 40 cycles was 0.4 m^2/g.

It has already been shown in Figs.4.2(a) and (b) that without support, Fe will not produce H_2 over repeated cycles. One question remaining though is how much Al_2O_3 support is required *per* mole of Fe to achieve stable conversions over repeated cycles. Specifically, whether the amount of Al_2O_3 required is equal to that found in $FeO{\cdot}Al_2O_3$. If two moles of Al were able to stabilise one mole of Fe, the expected conversions for carriers with $x_w = 0.9, 0.8$ and 0.6 would be $X_{H_2} = 0.09, 0.20$ and 0.52, respectively. The observed conversions after 40 cycles are slightly higher than these values and are $X_{H_2} = 0.25, 0.35$ and 0.75. Thus it seems that only considering the Fe capable of forming $FeO{\cdot}Al_2O_3$ at some point during the reduction or oxidation cycle is nearly, but not totally, sufficient to account for all of the H_2 produced. The molar ratio of Al to Fe necessary to achieve stable conversions over repeated cycles therefore appears to be slightly less than 2. Agglomeration between the Al_2O_3 packing material and the oxygen carrier was not observed in any experiment on emptying the tube containing the packed bed. The stable conversions observed for the reduction of a 60 wt. % Fe_2O_3, 40 wt. % Al_2O_3 oxygen carrier prepared using the sol-gel process are consistent with Li *et al.* (2009).

Composite particles of iron oxide from other research groups often contain a variety of different additives. From Fig. 8 of Galvita and Sundmacher (2007), the quantity of hydrogen produced *per* unit mass of oxygen carrier with a composition of 5 wt. % Cr_2O_3, 38 wt. % Fe_2O_3 and 57 wt. % of equimolar CeO_2 and ZrO_2 was calculated to be, on average, 1.7 mmol/g carrier. The equivalent conversion, X_{H_2}, was then determined by multiplying the quantity of hydrogen produced *per* unit mass of oxygen carrier by $M_{Fe_2O_3} \times 3/8$ and dividing by the mass fraction of Fe_2O_3, $x_w = 0.38$, as in Eq. (4.5). The average conversion over the first 40 cycles was therefore $X_{H_2} = 0.27$, as shown in Fig. 4.3. Assuming that the iron oxide reduces sequentially according to $Fe_2O_3 \rightarrow Fe_3O_4 \rightarrow FeO \rightarrow Fe$, this conversion suggests that the reduced state of the oxygen carrier was a mixture of FeO and Fe, shown by the reported values lying between the ticks for these phases on the right hand ordinate of Fig. 4.3. An identical procedure was applied to Fig. 10(a)-(c) of Galvita *et al.* (2008a) for samples with (a) 2 wt. % Mo, 78 wt. % Fe_2O_3, 20 wt. % CeO_2 and ZrO_2, (b) 5 wt. % Mg, 76 wt. % Fe_2O_3, 19 wt. % CeO_2 and ZrO_2 and (c) 5 wt. % Cu, 78 wt. % Fe_2O_3, 19 wt. % CeO_2 and ZrO_2. Assuming sequential conversion, the most reduced state of the oxygen carrier in Galvita *et al.* (2008a) was a mixture of Fe_3O_4 and FeO. The current research has shown however that if FeO is the lowest oxide, no support is necessary since from Fig. 4.3 for reduction to FeO over 40 cycles, unmodified Fe_2O_3 gave a stable yield of H_2 of 3.0 mmol H_2/g carrier with low CO contamination, confirmed in Chapter 2, Fig. 2.10. Overall, Fig. 4.3 demonstrated that in terms of conversion, X_{H_2}, the oxygen carriers prepared by the sol-gel process compare favourably to those from the literature.

4.5 Conclusions

Oxygen carriers with different ratios of Fe_2O_3 and Al_2O_3 by mass (60:40, 80:20 and 90:10 wt./wt.) were prepared using a sol-gel technique and tested for use in the production of hydrogen. Samples were characterised using scanning electron microscopy and by measuring crushing stress, BET surface area and BJH pore volume. A packed bed reactor at 1123 K was used to reduce 0.3 g of the oxygen carrier in a mixture of CO and N_2; oxidation was performed in a mixture of steam and N_2, followed by oxidation in air in some cases. It was found that:

1. For reduction to the FeO phase, no Al_2O_3 support is required for stable conversions over 40 cycles.
2. For reduction to the Fe phase, 10 wt. % Al_2O_3 is required to give stable conversions of $X_{H_2} > 0.9$ over 10 cycles. This conversion dropped to < 0.35 after 30-40 cycles.
3. For reduction to the Fe phase over 40 cycles, 40 wt. % Al_2O_3 is required and gave stable conversions of $X_{H_2} = 0.75$. No loss in conversion with cycle number was observed, suggesting that the 40 wt. % Al_2O_3 could endure longer cycling. The stability of the 40 wt. % Al_2O_3 was definitively linked to the formation of $FeO{\cdot}Al_2O_3$, which was confirmed quantitatively with X-ray diffraction.
4. Steam followed by air is the recommended sequence for oxidising carrier particles.

The 60 wt. % Fe_2O_3, 40 wt. % Al_2O_3 oxygen carrier produced using the sol-gel process gave conversions competitive with those in other studies and seems the most promising of the sol-gel carriers for use in chemical looping applications for the production of H_2.

Chapter 5

Kinetics of the reduction of iron oxide by mixtures containing CO and CO_2

5.1 Introduction

For the production of hydrogen using the redox reactions of iron oxide, understanding the kinetics of reduction is necessary for a fundamental understanding of the process. The reduction of Fe_2O_3 by CO occurs by reactions (1.9)-(1.11) in Table 1.2, repeated here for convenience:

$$3\,Fe_2O_3 + CO \rightleftarrows 2\,Fe_3O_4 + CO_2 \qquad \Delta H^\circ_{1023\,K} = -44.3\ \mathrm{kJ/mol} \tag{5.1}$$

$$1.2\,Fe_3O_4 + CO \rightleftarrows 3.8\,Fe_{0.947}O + CO_2 \qquad \Delta H^\circ_{1023\,K} = +27.1\ \mathrm{kJ/mol} \tag{5.2}$$

$$Fe_{0.947}O + CO \rightleftarrows 0.947\,Fe + CO_2. \qquad \Delta H^\circ_{1023\,K} = -20.3\ \mathrm{kJ/mol} \tag{5.3}$$

While the equilibrium constants for reactions (5.1)-(5.3) are well-established and derivable from standard thermodynamic data (Barin and Knacke, 1973; McBride *et al.*, 2002), their intrinsic kinetics are less easily obtained. Historically, research on the kinetics of the reduction of iron oxide has stemmed from the steel industry and has been characterised by a progression towards increasingly-complicated rate models. Initial investigations used a single-step reduction mechanism, whereby Fe_2O_3 was reduced to Fe without the intermediates Fe_3O_4 and $Fe_{0.947}O$ (Omori, 1987) being explicitly considered. McKewan (1958, 1962) studied single-step reduction using H_2. Later, two-step models including wuestite, $Fe_{0.947}O$, were developed (Omori, 1987). A model involving all four species of iron and its oxides was then proposed by Spitzer *et al.* (1966) for porous pellets, the reduction of which in H_2 was controlled by internal transport and reaction resistances at three, sharply-defined shrinking cores corresponding to the boundaries, at successively decreasing radii, between Fe, $Fe_{0.947}O$, Fe_3O_4 and Fe_2O_3. Murayama *et al.* (1977) applied this shrinking core approach to the reduction of iron oxide with mixtures of CO and CO_2. Implicit in these models is the assumption that reactions occur at sharp interfaces.

To address reduction with diffuse interfaces, Szekely and Evans (1970) proposed a grain model where the overall pellet is comprised of dense spherical subparticles which themselves are chemically reduced at sharp interfaces. This model has been applied to the reduction of iron oxide, *e.g.* Valipour and Saboohi (2007). Alternatively, Trushenski *et al.* (1974) proposed a model for reaction occurring over a specific volume of the pellet, rather than over the surface area of an interface. Both the model from Szekely and Evans (1970) and that from Trushenski *et al.* (1974) have been successfully employed to describe experimental results over broad ranges of temperature and gas composition.

The motivation for further research into the kinetics of the reduction of iron oxide is twofold. First, the rate parameters in the previous models were obtained by fitting theoretical predictions to experimental results influenced by intra-particle gaseous diffusion, *e.g.* Trushenski *et al.* (1974); Szekely *et al.* (1976). As such, the rate constants did not have as significant an effect on the models' predictions as would be the case in a purely kinetically-controlled regime. Second, for gas-solid looping cycles, the kinetics of the reduction of iron oxide need to be studied over repeated cycles of reduction and oxidation, instead of just during an initial cycle. It has already been shown in Chapter 2 that repeated reduction to Fe by reaction (5.3) for particles made purely of Fe_2O_3 is not possible, since yields of H_2 far below those predicted from the stoichiometry of reactions (1.15)-(1.16) are obtained. Therefore here, only the reduction of Fe_2O_3 to Fe_3O_4, reaction (5.1), and the reduction of Fe_3O_4 to $Fe_{0.947}O$, reaction (5.2), are investigated for pure iron oxide. The objectives were therefore:

1. to determine pre-exponential factors and activation energies for the reduction of the iron oxides by mixtures of CO and CO_2 in the kinetically-controlled regime at industrially-relevant temperatures and pressures;

2. to investigate any changes in the kinetics with increasing numbers of cycles and;

3. to compare theoretical predictions with measurements obtained in experiments different from those used to derive the kinetic parameters, *e.g.* by using the rate parameters obtained in a fluidised bed to predict the reduction of a fixed bed of iron oxide.

5.2 Experimental

Mechanically-mixed particles of iron oxide were prepared, as described in Chapter 2, section 2.2, by spraying water from reverse osmosis on to Fe_2O_3 powder (Sigma-Aldrich; purity > 99.9 wt. %) while mechanically mixing. The resulting agglomerates were heated at 1173 K for 3 h and then sieved to the desired size ranges. The BET surface area of the sintered Fe_2O_3 particles with $d_\mathrm{p} = +300, -425\ \mu$m was 1.0 ± 0.5 m^2/g (Micromeritics, Tristar 3000); the porosity, measured by Hg porosimetry (Micromeritics, Autopore IV) was 0.60 ± 0.06. The surface area of particles of Fe_3O_4 with $d_\mathrm{p} = +300, -425\ \mu$m, prepared by reducing the particles of Fe_2O_3 at 1173 K in 3 vol. % CO, 15 vol. % CO_2, 82 vol. % N_2, was 1.0 ± 0.5 m^2/g with a porosity of 0.58 ± 0.06.

The fluidised bed reactor is shown in Fig. 5.1 and consisted of a tube of recrystallised Al_2O_3 (I.D. 20 mm) with a perforated plate distributor, also of Al_2O_3; both had purities > 99.9 wt. %. The plate had 5 holes, each 1 mm dia., four aligned in a square array of side 8 mm, with one central hole. The tube and disc were joined using ceramic cement (ALCS, Multilab). Approximately 10 g of Al_2O_3 ($d_\mathrm{p} = +1400, -1700\ \mu$m; $\rho_{Al_2O_3} = 3770$ kg/m^3; Boud Mineral) formed a packed bed beneath the distributor, held in place with quartz wool; this packing preheated the gas entering the reactor, as shown in Fig. 5.1. The depth of the unfluidised bed, H_0, was 30 mm, giving an aspect ratio, $H_0/d_\mathrm{bed} = 1.5$. At typical operating conditions of 1023 K, the pressure drop across the distributor was 0.02 bar, considerably in excess of the pressure drop across the material fluidised (typically 15 g of Al_2O_3 (purity > 99.9 wt. %) sieved to $d_\mathrm{p} = +300, -425\ \mu$m) given by the weight of the bed divided by the nominal cross-sectional area, *viz.* amounting to 0.003 bar, hence ensuring uniform fluidisation. The reactor was placed in a tubular furnace, and its temperature was measured by a type K thermocouple, positioned 5 mm above the distributor, inside the bed. In all experiments, the particles were added to the reactor as Fe_2O_3 and the mass of the batch was measured using a balance with a precision of 10^{-4} g (OHaus). A packed bed reactor made of 316 stainless steel (I.D. 10.2 mm), described in 2.2, replaced the fluidised bed in the experiments in section 5.4.3.

Gas was supplied to the reactor from cylinders (BOC plc.) and steam was supplied using a syringe pump, as described in Chapter 2, section 2.2. The total flowrate of gas was adjusted in all experiments to give $U/U_\mathrm{mf} \sim 7$ determined, for the mixture of reducing gas and Al_2O_3 bed particles, from the correlation of Wen and Yu (1966). The effluent gas was monitored by continuously withdrawing a sample at a flowrate of 1.67×10^{-5} m^3/s, as measured at 298 K and

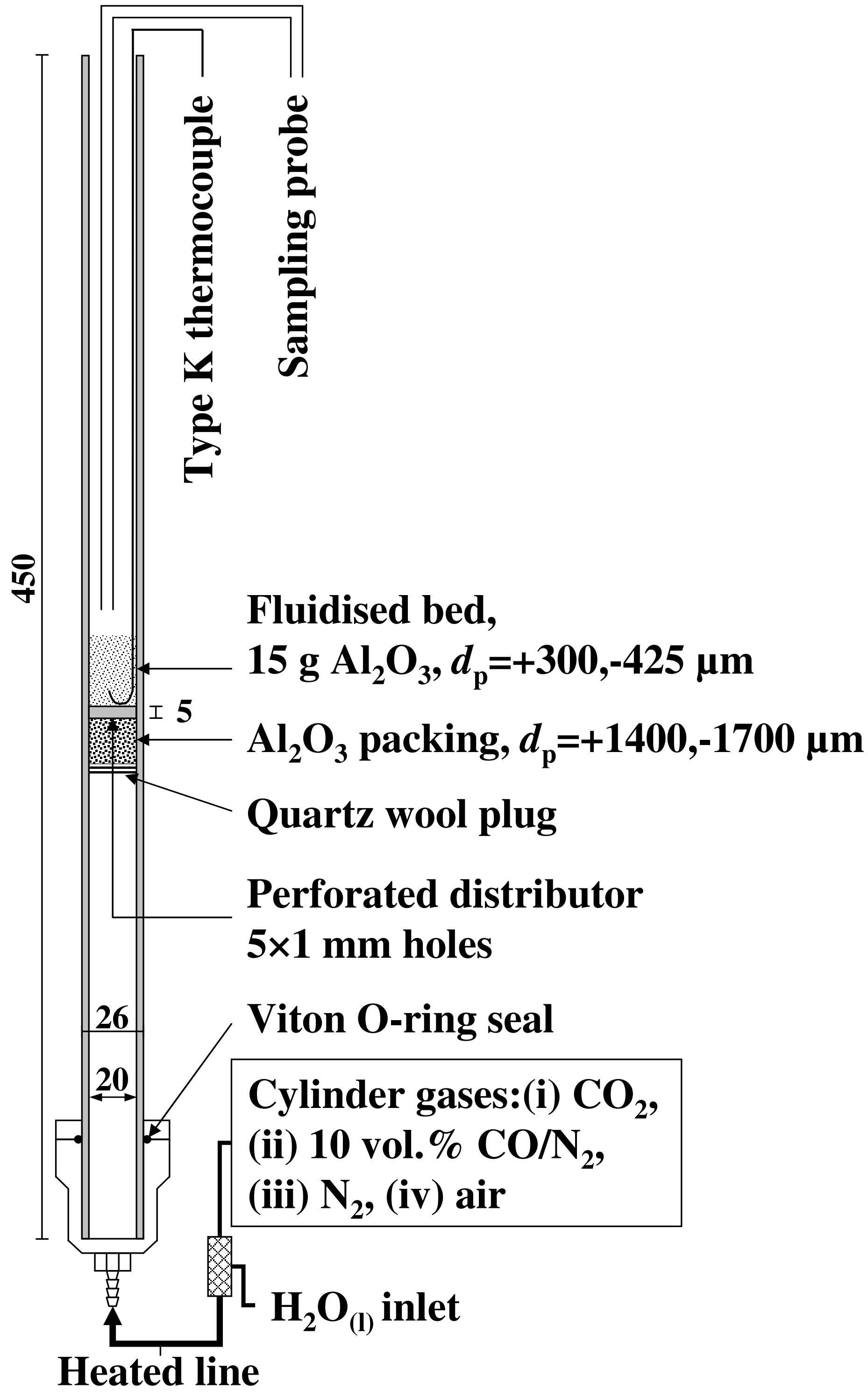

Figure 5.1: Schematic diagram of the fluidised bed reactor. The inert bed material was 15 g of Al_2O_3 with $d_p = +300, -425$ μm; active iron oxide, Fe_2O_3, in various size ranges was added to the top of the bed. All dimensions are in mm.

10^5 Pa, through a quartz probe (5 mm I.D.) and measuring its composition by nondispersive infrared and thermal conductivity analysers as described in Chapter 2.

Since steam was used to convert the $Fe_{0.947}O$ to Fe_3O_4, three impinger tubes immersed in an ice bath (273 K), followed by a tube filled with $CaCl_2$, were used to dry the sampled gas prior to analysis. Experiments involving cycling between Fe_2O_3 and Fe_3O_4 did not require the sampled gas to be dried. The response time of the sampling line in series with the analysers was determined by placing the quartz probe in a flow of calibration gas, either 10 vol. % CO, balance N_2 (BOC plc.) or 10 vol. % CO_2, balance N_2 (BOC plc.) for CO or CO_2, respectively, and rapidly removing the probe manually in order to approximate a step change. The response times with and without the drying tubes, respectively, were then determined for the infrared analysers to be $\tau_{\mathrm{CO}}^{\mathrm{mix}} = 2.0$ s, $\tau_{\mathrm{CO_2}}^{\mathrm{mix}} = 3.5$ s and $\tau_{\mathrm{CO}}^{\mathrm{mix}} = 1.0$ s, $\tau_{\mathrm{CO_2}}^{\mathrm{mix}} = 2.5$ s. Deconvolution of the CO and CO_2 signals was performed, but did not significantly alter the results, since in all cases the total time for reaction was at least one order of magnitude greater than the reported time constants and the rate was determined over a large range of conversion, $0.1 < X < 0.7$, as discussed later.

The transition from Fe_2O_3 to Fe_3O_4 was studied between 723 and 973 K, using mixtures of N_2+CO+CO_2 (respectively, 82, 3 and 15 vol. %) during the reduction of Fe_2O_3 and mixtures of N_2+air+CO_2 (respectively, 82, 3 and 15 vol. %) during the oxidation of Fe_3O_4. For the transition from Fe_3O_4 to $Fe_{0.947}O$, mixtures of N_2+CO+CO_2 (respectively, 82, 9 and 9 vol. %) were used to reduce Fe_3O_4 and mixtures of N_2+steam (respectively, 82 and 18 vol. %) were used to oxidise $Fe_{0.947}O$ over 923 - 1173 K. These values of CO and CO_2 were chosen from Fig. 1.1 in order to give the desired phase of iron oxide, assuming that thermodynamic equilibrium was established. A purge of N_2 for 60-120 s was employed between reduction and oxidation stages to prevent mixing, and therefore reaction, of the reducing and oxidising gases. Prior to any iron oxide being introduced into the reactor, one reduction and one oxidation, together constituting one cycle, were performed and satisfactorily verified the inertness of the reactor, its contents, and the thermocouple in each experiment. The iron oxide particles were then poured into the reactor during a period of N_2 flow, enabling equilibration to the bed's temperature and the displacement of any air inside the iron oxide particles prior to reduction. The requisite reduction and oxidation cycling was then performed.

5.3 Theory

In a single particle, the reduction reactions (5.1) and (5.2) could, in principle, be controlled by one or more of the following: (i) mass transport of gaseous reactant to the exterior of the particle, (ii) diffusion of the reactant through the particle matrix, (iii) chemical reaction, (iv) diffusion of the gaseous product through the particle matrix and (v) mass transport of gaseous product into the bulk gas. Assuming (a) pseudo-steady state and (b) first order kinetics of the form $r' \propto (c_{\mathrm{CO}} - c_{\mathrm{CO_2}}/K_p)$, a material balance over a differential volume of a single spherical particle gives:

$$D_{\mathrm{e,CO}} \left[\frac{2}{r} \frac{dc_{\mathrm{CO}}}{dr} + \frac{d^2 c_{\mathrm{CO}}}{dr^2} \right] = k_i \left(c_{\mathrm{CO}} - \frac{c_{\mathrm{CO_2}}}{K_p} \right), \tag{5.4}$$

where c_{CO} is the concentration of CO, $D_{\mathrm{e,CO}}$ is the effective diffusivity of CO, k_i is the intrinsic rate constant for the forward step of reaction (5.1) or (5.2) and r is the radial position within the particle. Substituting (Smith and Amundson, 1951) $u_{\mathrm{CO}} = c_{\mathrm{CO}} r$ and employing boundary conditions of c_{CO} = constant = $c_{\mathrm{CO,s}}$ at $r = R$ and finiteness of c_{CO} at $r = 0$ gives:

$$c_{\mathrm{CO}}(r) = b_1 + \frac{2c_1}{r} \sinh(r\sqrt{P}), \tag{5.5}$$

where b_1, c_1 and P are constants given in Appendix 4 and $c_{\mathrm{CO,s}}$ and $c_{\mathrm{CO_2,s}}$ are the concentrations at the external surface of the particle. A similar procedure can be used to solve for $c_{\mathrm{CO_2}}(r)$.

The effectiveness factor and Thiele modulus are then given, respectively, by:

$$\eta = \frac{3}{\phi^2}(\phi \coth \phi - 1), \qquad \phi = R\sqrt{\frac{k_i}{D_{\mathrm{e,CO}}} + \frac{k_i}{K_p D_{\mathrm{e,CO_2}}}}. \tag{5.6}$$

This definition is similar to that of Levenspiel (1999), except that ϕ includes the reverse reaction represented by the term containing K_p. Incorporating the resistance to external mass transfer through the film layer, the specific rate of reaction, r', in mol/(s g) for the particle can be written as:

$$\left.\begin{aligned} r' &= \frac{k}{\rho_{\mathrm{Fe_2O_3}}} \left(c_{\mathrm{CO,p}} - \frac{c_{\mathrm{CO_2,p}}}{K_p} \right) \\ \frac{1}{k} &= \frac{R}{3k_{\mathrm{g,CO}}} + \frac{1}{k_i \eta} + \frac{R}{3k_{\mathrm{g,CO_2}} K_p}. \end{aligned}\right\} \tag{5.7}$$

Here, $c_{\mathrm{CO,p}}$ and $c_{\mathrm{CO_2,p}}$ are the concentrations in the particulate or bulk phase of the reactor, $\rho_{\mathrm{Fe_2O_3}}$ is the density of the particle, $k_{\mathrm{g,CO}}$ and $k_{\mathrm{g,CO_2}}$ are the mass transfer coefficients, k_i is the intrinsic rate constant for reaction (5.1) or (5.2) and R is the external radius of the particle. Unless otherwise specified, the equilibrium constant, K_p, was determined from published thermodynamic data (Barin and Knacke, 1973).

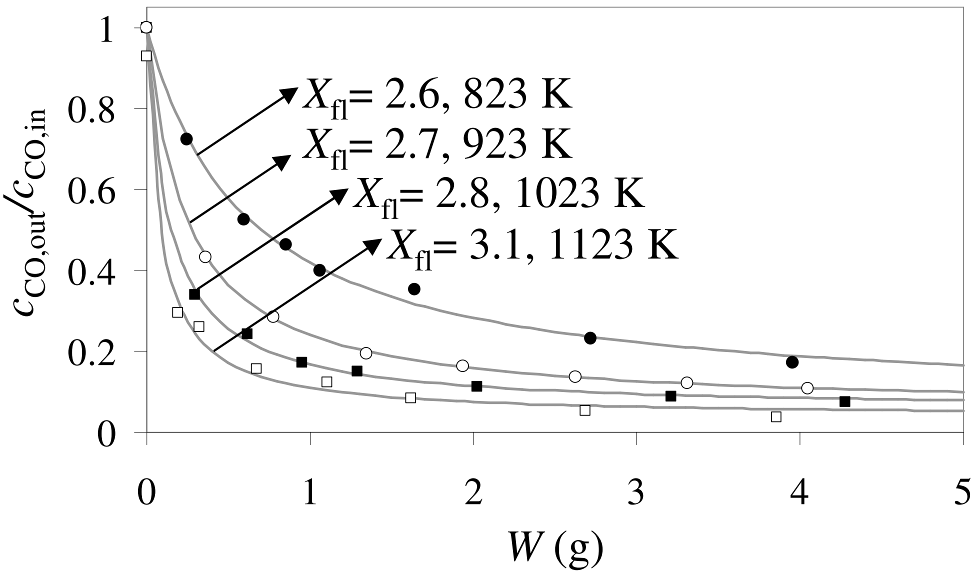

Figure 5.2: The measured ratio, $c_{\mathrm{CO,out}}/c_{\mathrm{CO,in}}$, as increasing masses of Fe_2O_3, W, were added to the fluidised bed at (●) 823 K, (○) 923 K, (■) 1023 K and (□) 1123 K. The grey lines indicate least squares fits using Eq. (5.8) and were used to determine X_{fl}.

The bubble to particulate phase resistance of the fluidised bed was considered using the two-phase model of Davidson and Harrison (1963) with crossflow factor, X_{fl}. In poorly-mixed fluidised beds, some of the entering reactant will bypass the particulate phase as bubbles and thus never react. Experimentally, the crossflow factor, which quantifies bypassing, was evaluated by measuring the ratio of $c_{\mathrm{CO,out}}/c_{\mathrm{CO,in}}$ when increasing masses of Fe_2O_3 were added to the bed and reduced to Fe_3O_4 in 3 vol. % CO, 15 vol. % CO_2, balance N_2 at the operating condition $U/U_{\mathrm{mf}} \sim 7$. Results were then fitted using Eq. (6.9) from (Davidson and Harrison, 1963):

$$c_{\mathrm{CO,out}}/c_{\mathrm{CO,in}} = \beta e^{-X_{\mathrm{fl}}} + \frac{(1-\beta e^{-X_{\mathrm{fl}}})^2}{\left(\frac{kW}{q\rho_{\mathrm{Fe_2O_3}}}\right) + 1 - \beta e^{-X_{\mathrm{fl}}}}, \tag{5.8}$$

where $\beta = (1 - U/U_{\mathrm{mf}}) = 6/7$, k is the rate constant including mass transfer effects, W is the mass of particles added to the bed, q is the superficial volumetric flowrate through the bed, $\rho_{\mathrm{Fe_2O_3}}$ is the initial particle density and any back reaction was ignored owing to the large equilibrium constant, $K_p = 1.47 \times 10^5$. In deriving the term in brackets in the denominator of Eq. (5.8), it was assumed the volume of particles *per* unit volume of the particulate phase was constant and equal to $W/(\rho_{\mathrm{Fe_2O_3}} H_0 A_s)$. Fig. 5.2 shows $c_{\mathrm{CO,out}}/c_{\mathrm{CO,in}}$ *versus* W at temperatures of 823, 923, 1023 and 1123 K. Here, $c_{\mathrm{CO,out}}$ corresponds to the maximum initial rate of consumption of CO. The terms $(kW/q\rho_{\mathrm{Fe_2O_3}})$ and X_{fl} were then determined by performing a least squares fit to the experimental values in Fig. 5.2 using Eq. (5.8). For all experiments, $X_{\mathrm{fl}} > 2.5$, suggesting complete mixing within the whole bed. The particles of Al_2O_3 and iron oxide were also of similar size and density such that no segregation was observed upon emptying the bed after it was rapidly defluidised and cooled to room temperature. The absence of segregation and the high crossflow factor imply that the bed behaves like a CSTR with respect to both the gas and solids. Values of k are presented later with the discussion of Fig. 5.7.

In this study, the final rate expression used to analyze the reduction of Fe_2O_3 particles with particle density, $\rho_{\mathrm{Fe_2O_3}}$, is expressed in units of mol/(s g) as:

$$r' = \frac{k}{\rho_{\mathrm{Fe_2O_3}}}\left(c_{\mathrm{CO,out}} - \frac{c_{\mathrm{CO_2,out}}}{K_p}\right). \tag{5.9}$$

Here, the mass transfer coefficients, $k_{\mathrm{g,CO}}$ and $k_{\mathrm{g,CO_2}}$, in the expression for k in Eq. (5.7) for one particle were estimated from $Sh = 2\varepsilon_{\mathrm{mf}} + 0.69Re_{\mathrm{p}}^{1/2}Sc^{1/3}$, similar to LaNauze (1985), where $Sh = k_{\mathrm{g}}d_{\mathrm{p}}/D_{\mathrm{mix}}$ with $\varepsilon_{\mathrm{m}f} = 0.45$; Re_{p} is based on the size of the bed material, *viz.* $d_{\mathrm{p}} = +300, -425$ μm. The effective diffusivity of CO or CO_2 in Eqs. 5.4-5.6 was calculated from $D_{\mathrm{e}} = \varepsilon_p(1/D_{\mathrm{k}} + 1/D_{\mathrm{mix}})^{-1}/\tau_{\mathrm{p}}$ using either values for CO or for CO_2. Values for the diffusion coefficients, D_{mix}, were taken from Hirschfelder *et al.* (1954). The Knudsen diffusivity was calculated (Satterfield, 1980) using $D_{\mathrm{k}} = 2r_{\mathrm{e}}(8\mathrm{R}T/\pi M_{\mathrm{w}})^{1/2}/3 = 2.13\varepsilon_p(\mathrm{R}T/M_{\mathrm{w}})^{1/2}/(S_{\mathrm{g}}\rho_{\mathrm{Fe_2O_3}})$, where r_{e} is the effective radius of a cylindrical pore, $\varepsilon_p = 0.6$ is the porosity for Fe_2O_3 and Fe_3O_4; τ_{p} was a fitted tortuosity, found to be 2.4 and 2.5 for Fe_2O_3 and Fe_3O_4, respectively; $\rho_{\mathrm{Fe_2O_3}} = 2060$ kg/m^3 and $\rho_{\mathrm{Fe_3O_4}} = 2180$ kg/m^3; T is the absolute temperature; $S_{\mathrm{g}} = 1.0$ m^2/g is the specific surface area for Fe_2O_3 and Fe_3O_4 and M_w is the molecular mass of the gaseous species. The influence of Knudsen diffusion on the overall effective diffusivity, D_{e}, was found to be minimal for both CO and CO_2. Table 5.1 lists typical values of parameters used. Values of k_i are reported in section 5.4.1 for the reduction of Fe_2O_3 to Fe_3O_4 and in section 5.4.2 for the reduction of Fe_3O_4 to $Fe_{0.947}O$.

Table 5.1: Parameters used in the determination of the intrinsic rate constant, k_i, for particles with $d_p = +300, -425\ \mu$m. The superficial flow of gas through the reactor in (m^3/s) is $q = 7U_{mf}A_s$, where the cross-sectional area is $A_s = \pi(0.02\ m)^2/4$. Here, $1/D_{e,CO} = \tau_p(1/D_{k,CO} + 1/D_{mix,CO})/\varepsilon_p$. A value of $Nu = hd_p/\lambda_{mix} = 2$ was used to estimate h; $Bi = hd_p/6\lambda_e$.

Reduction of Fe_2O_3 to Fe_3O_4

T (K)	W (g)	U_{mf} (m/s)	ε_p	τ_p	$\rho_{Fe_2O_3}$ (kg/m^3)	S_g (m^2/kg)	$k_{g,CO}$ (m/s)	k_{g,CO_2} (m/s)	$D_{mix,CO}$ (m^2/s)	D_{mix,CO_2} (m^2/s)	$D_{k,CO}$ (m^2/s)	D_{k,CO_2} (m^2/s)	$D_{e,CO}$ (m^2/s)	D_{e,CO_2} (m^2/s)	λ_e (W/(m K))	λ_{mix} (W/(m K))	h (W/(m^2 K))	Bi
723	1.99	0.090	0.6	2.4	2060	10^3	0.43	0.35	9.13×10^{-5}	7.17×10^{-5}	2.87×10^{-4}	2.29×10^{-4}	1.73×10^{-5}	1.36×10^{-5}	0.5	0.052	285	0.03
773	0.74	0.086	0.6	2.4	2060	10^3	0.47	0.38	1.02×10^{-4}	8.01×10^{-5}	2.97×10^{-4}	2.37×10^{-4}	1.90×10^{-5}	1.50×10^{-5}	0.5	0.054	300	0.04
823	0.50	0.084	0.6	2.4	2060	10^3	0.51	0.41	1.13×10^{-4}	8.90×10^{-5}	3.06×10^{-4}	2.44×10^{-4}	2.07×10^{-5}	1.63×10^{-5}	0.5	0.057	315	0.04
873	0.20	0.080	0.6	2.4	2060	10^3	0.55	0.44	1.25×10^{-4}	9.82×10^{-5}	3.15×10^{-4}	2.52×10^{-4}	2.24×10^{-5}	1.77×10^{-5}	0.5	0.060	329	0.04
923	0.13	0.077	0.6	2.4	2060	10^3	0.59	0.47	1.37×10^{-4}	1.08×10^{-4}	3.24×10^{-4}	2.59×10^{-4}	2.41×10^{-5}	1.90×10^{-5}	0.5	0.062	344	0.04
973	0.07	0.074	0.6	2.4	2060	10^3	0.63	0.51	1.50×10^{-4}	1.18×10^{-4}	3.33×10^{-4}	2.66×10^{-4}	2.59×10^{-5}	2.04×10^{-5}	0.5	0.065	358	0.04

Reduction of Fe_3O_4 to $Fe_{0.947}O$

T (K)	W (g)	U_{mf} (m/s)	ε_p	τ_p	$\rho_{Fe_3O_4}$ (kg/m^3)	S_g (m^2/kg)	$k_{g,CO}$ (m/s)	k_{g,CO_2} (m/s)	$D_{mix,CO}$ (m^2/s)	D_{mix,CO_2} (m^2/s)	$D_{k,CO}$ (m^2/s)	D_{k,CO_2} (m^2/s)	$D_{e,CO}$ (m^2/s)	D_{e,CO_2} (m^2/s)	λ_e (W/(m K))	λ_{mix} (W/(m K))	h (W/(m^2 K))	Bi
923	2.18	0.077	0.58	2.5	2180	10^3	0.53	0.43	1.37×10^{-4}	1.08×10^{-4}	2.96×10^{-4}	2.36×10^{-4}	2.18×10^{-5}	1.72×10^{-5}	0.5	0.063	345	0.04
973	1.52	0.073	0.58	2.5	2180	10^3	0.57	0.46	1.50×10^{-4}	1.18×10^{-4}	3.04×10^{-4}	2.42×10^{-4}	2.33×10^{-5}	1.84×10^{-5}	0.5	0.065	359	0.04
1023	0.80	0.072	0.58	2.5	2180	10^3	0.61	0.49	1.63×10^{-4}	1.28×10^{-4}	3.11×10^{-4}	2.48×10^{-4}	2.48×10^{-5}	1.96×10^{-5}	0.5	0.068	374	0.05
1073	0.77	0.070	0.58	2.5	2180	10^3	0.65	0.52	1.77×10^{-4}	1.39×10^{-4}	3.19×10^{-4}	2.54×10^{-4}	2.64×10^{-5}	2.08×10^{-5}	0.5	0.070	388	0.05
1123	0.52	0.067	0.58	2.5	2180	10^3	0.68	0.55	1.91×10^{-4}	1.49×10^{-4}	3.26×10^{-4}	2.60×10^{-4}	2.79×10^{-5}	2.20×10^{-5}	0.5	0.073	402	0.05
1173	0.39	0.066	0.58	2.5	2180	10^3	0.73	0.58	2.05×10^{-4}	1.61×10^{-4}	3.33×10^{-4}	2.66×10^{-4}	2.94×10^{-5}	2.32×10^{-5}	0.5	0.075	416	0.05

5.4 Results

5.4.1 Transition from Fe_2O_3 to Fe_3O_4

The reduction of Fe_2O_3 to Fe_3O_4 was studied between 723 and 973 K with inlet mole fractions of CO and CO_2 from 1.5 to 3.5 vol. % and 14 to 16 vol. %, respectively. Figure 5.3(a) shows the effluent mole fractions of CO and CO_2 for a typical experiment at 823 K. Here, 0.5 g of Fe_2O_3 particles with $R \sim 180$ μm were introduced into the hot bed when fluidised by N_2. After the first reduction and oxidation, the fluidising gas was suddenly switched from N_2 to the mixture of CO, CO_2 and N_2 at $t = 30$ s. A fraction of the entering CO reacted with the Fe_2O_3 to form Fe_3O_4 and was thereby converted to CO_2. From stoichiometry, the production of CO_2 must be commensurate with the consumption of CO, and Fig. 5.3(a) shows that the CO and CO_2 curves are indeed complementary.

Upon completion of the reaction at $t = 100$ s, the CO and CO_2 mole fractions returned to their inlet values of 2.2 vol.% and 14.8 vol.%, respectively. Following a period of purging with N_2, the particles were then reoxidised with a mixture of N_2+air before undergoing subsequent reduction cycles.

The conversion of the solid at a specific time can be calculated by integrating a plot (against time) of the decrease in CO, and, or, increase in CO_2. The grey area in Fig. 5.3(a), for example, corresponds to a conversion of 0.4 for the reduction of Fe_2O_3 to Fe_3O_4. The rate at this specific conversion was then obtained by taking the instantaneous difference between the inlet and outlet mole fractions of CO or CO_2, depicted by the grey circles in Fig. 5.3(a), multiplying by the molar flowrate, and dividing by the mass of particles added: this gave the rate of reaction, r', moles/(s g). Thus, from the graph in Fig. 5.3(a) a plot of rate *versus* conversion can be constructed and is shown in Fig. 5.3(b). The point corresponding to the rate at $X = 0.4$ is shown by the grey circle in Fig. 5.3(b). Good agreement between the rates calculated using the CO and CO_2 signals is observed, although the reduced noise in the CO signal makes it preferable for determining the rate.

The initial rate, or rate at $X = 0$, can be derived from either Fig. 5.3(a) or (b). In Fig. 5.3(a), the effluent mole fraction of CO can be approximated by a linear fit shown by the grey line and extrapolated back to the point of the gas switch. This method gives $r' = 5.3 \times 10^{-5}$ mol/(s g). In Fig. 5.3(b), the initial rate can be calculated by a linear fit of r' *versus* X in the interval $0.1 < X < 0.7$. The intercept of the best fit line then gives the rate at $X = 0$, shown by point

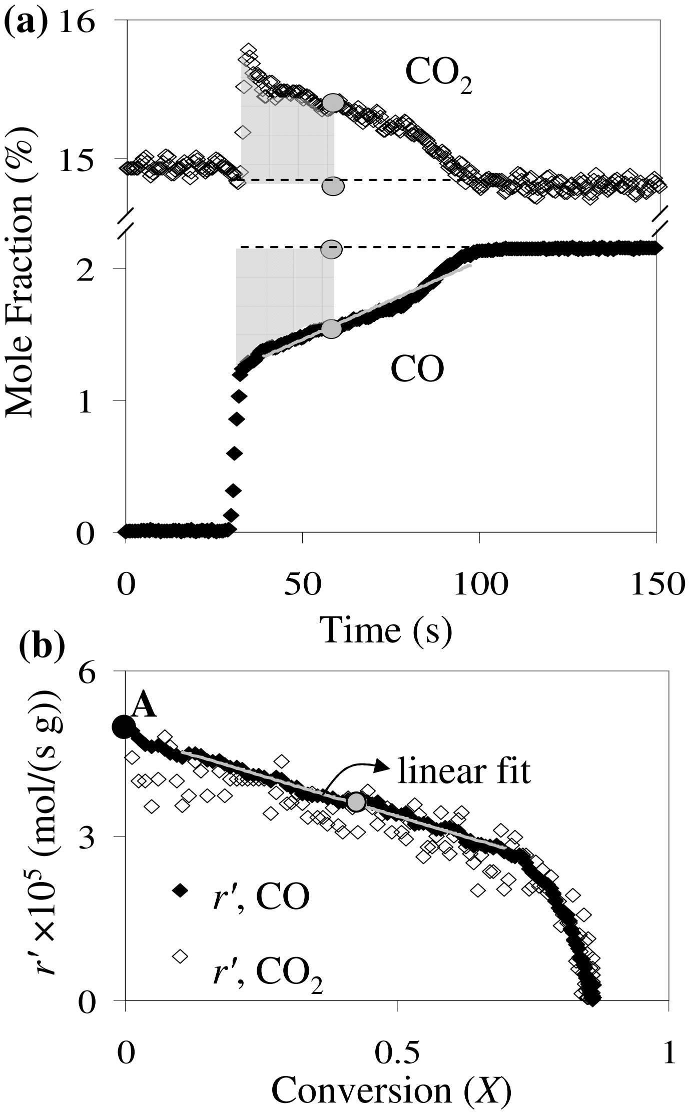

Figure 5.3: (a) Mole fraction of CO (♦) and CO_2 (◊) in the effluent gas *versus* time for the reduction of 0.5 g of Fe_2O_3 to Fe_3O_4 at 823 K. Grey circles show the difference between the inlet and outlet CO and CO_2 at $X = 0.4$. (b) Rate *versus* conversion calculated from the CO (♦) and CO_2 (◊) analyser signals in (a). The initial rate is given by the intersection of the fitted line with the ordinate at $X = 0$, shown by point A. The grey circle indicates the rate at $X = 0.4$.

A. This method gives, $r' = 4.8 \times 10^{-5}$ mol/(s g), which is in agreement to within 10 % of that found from Fig. 5.3(a). For consistency, the rates reported hereinafter were determined from the plots of r' *versus* X. Rates for the first reduction cycle are not reported, as it was found that the plots of [CO] and [CO_2] in the effluent were markedly different from those for cycles 2 to 10, perhaps owing to a morphological change or the presence of adsorbed gaseous species in cycle one. The anomalous behaviour during the first cycle remains puzzling and highlights the importance of investigating the rate over repeated cycles. To prevent all the inlet CO from being consumed at higher temperatures, the mass of Fe_2O_3 added to the bed was decreased progressively with temperature from 2.0 g at 623 K to 0.1 g at 973 K, so that the maximum deviation over the inlet [CO] was 30 %.

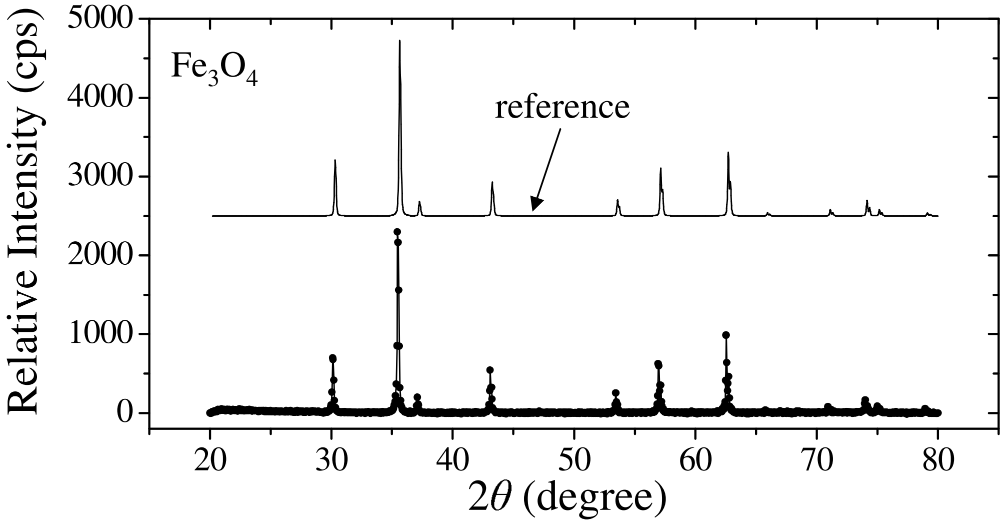

Figure 5.4: (a) Relative intensity (cps) against 2θ for the reduced iron oxide as Fe_3O_4; a simulated scan from a standard reference (JCPDS, 2005b) is shown with a vertical offset and demonstrates good agreement.

X-ray diffraction (Philips model PW1830/00, Cu Kα, 40 kV and 40 mA, scanning rate 0.01 degrees s^{-1}, in air at 298K) confirmed the presence of Fe_3O_4 after reduction of 5 g of Fe_2O_3 of sieve size $d_p = +300, -425$ μm only in CO, CO_2 and N_2 at 973 K, *i.e.* without any Al_2O_3 in the bed, and is shown in Fig. 5.4. The experimental diffraction pattern is shown below that of a simulated scan from a standard reference for Fe_3O_4 (JCPDS, 2005b) and definitively demonstrates the presence of Fe_3O_4 with no unexplained contaminants. In Chapter 3, no Al_2O_3 contamination had been detected from X-ray diffraction patterns of modified Fe_2O_3 reacted in a packed bed between layers of inert Al_2O_3, suggesting that the Al_2O_3 was indeed inert.

The previous analysis assumed that the rate was first order in the outlet concentrations of

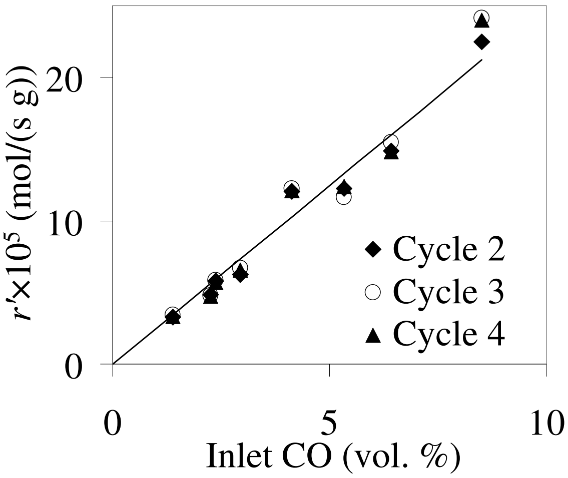

Figure 5.5: Initial measured rate, r', at $X = 0$ *versus* inlet fraction of CO for reduction of Fe_2O_3 to Fe_3O_4 at 823 K. The straight line through the origin is a best fit, exhibiting a first order dependence on [CO]. The inlet fraction of CO_2 was fixed at 15 vol.%.

CO and CO_2, *i.e.* $r' \propto (c_{\mathrm{CO,out}} - c_{\mathrm{CO_2,out}}/K_p)$ in Eq. (5.9). Envisaging the reactor as a well-mixed CSTR operating at constant temperature and pressure enables one to replace $c_{\mathrm{CO,out}}$ and $c_{\mathrm{CO_2,out}}$ with expressions of $c_{\mathrm{CO,in}}$, $c_{\mathrm{CO_2,in}}$ using the material balances:

$$r' = \left(\frac{q}{W}\right)(c_{\mathrm{CO,in}} - c_{\mathrm{CO,out}}) = \left(\frac{q}{W}\right)(c_{\mathrm{CO_2,out}} - c_{\mathrm{CO_2,in}}), \tag{5.10}$$

where q is the total volumetric flowrate of gas through the reactor and W is the total mass of Fe_2O_3 initially introduced. Using Eq. (5.10) and substituting for $c_{\mathrm{CO,out}}$ and $c_{\mathrm{CO_2,out}}$ in $r' \propto (c_{\mathrm{CO,out}} - c_{\mathrm{CO_2,out}}/K_p)$ gives $r' \propto [1/(1+W/q+W/qK_p)](c_{\mathrm{CO,in}} - c_{\mathrm{CO_2,in}}/K_p) \propto (c_{\mathrm{CO,in}} - c_{\mathrm{CO_2,in}}/K_p)$ for constant q, W and K_p, which is a useful expression since the inlet concentrations were easily measurable and controllable. By fixing the inlet mole fraction of CO_2 at 15 vol. % and varying the inlet mole fraction of CO between 0 and 10 vol. %, the dependence of the rate on the inlet CO was investigated. Figure 5.5 shows a plot of r' *versus* the mole fraction of CO in the inlet gas; the mass of Fe_2O_3 added ranged from 0.3 to 0.8 g, with smaller masses used for higher mole fractions of CO. From Fig. 5.5, the rate can be satisfactorily described by a first order fit. The dependence on CO_2 could not be measured, since the large equilibrium constant, $K_p = 1.47 \times 10^5$, overwhelms any effect of CO_2. The back reaction is therefore negligible.

The effect of external mass transfer was found to be negligible and is examined quantitatively in the discussion. Next, to determine whether the reduction of particles of Fe_2O_3 to Fe_3O_4 was limited by intrinsic kinetics or intraparticle diffusion, the rate was investigated for particles of varying radii at 823 K, fixed inlet mole fractions of CO and CO_2 of 2.5 vol.% and

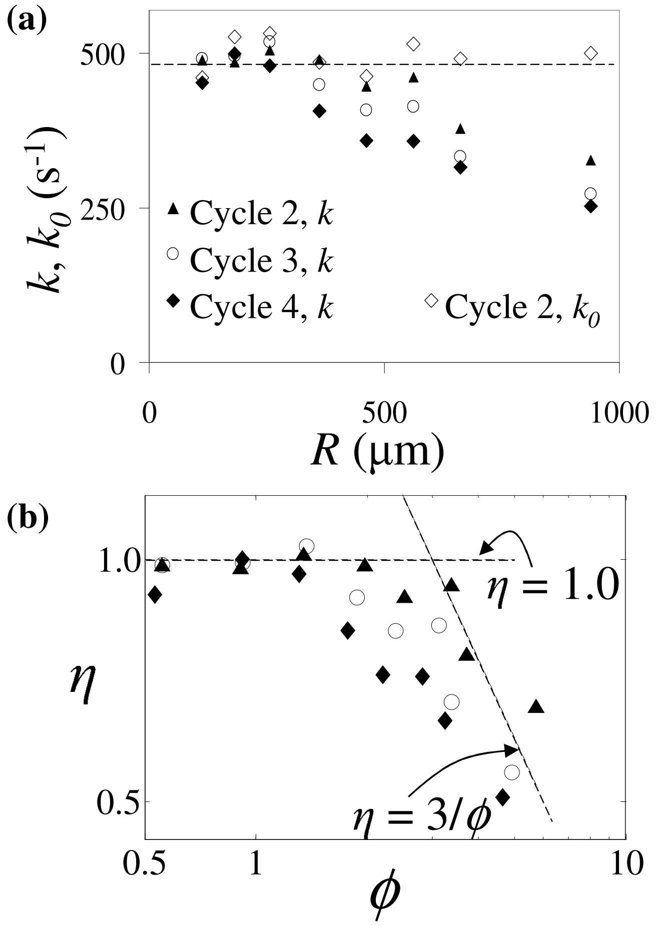

Figure 5.6: Reduction of 0.5 g of Fe_2O_3 to Fe_3O_4 at 823 K.
(a) Plot of initial rate constant k at $X = 0$ *versus* average radius, R, of the iron oxide particles for cycles 2 (▲), 3 (○) and 4 (◆). The corrected intrinsic rate constant at zero conversion, k_0, which accounts for $\eta < 1$ is also shown for cycle 2 (◇) and has an average value given by the dashed line of 490 s^{-1}.
(b) Effectiveness factor, $\eta = k/490\ s^{-1}$, *versus* calculated ϕ from Eq. (5.6) for cycles 2 (▲), 3 (○) and 4 (◆), corresponding to the points in (a). For smaller particles $\eta = 1.0$; as particle size increases η approaches $3/\phi$.

15 vol.%, respectively, and a fixed batch mass of 0.5 g of Fe_2O_3. The observed rate constant, k, was found by dividing the rate, r', by the concentration driving force of the outlet gas and multiplying by the bulk density, *i.e.* rearranging Eq. (5.9). The initial intrinsic rate constant, k_0, which is simply k_i at $X = 0$, was obtained by iteratively solving for η using Eqs. (5.6) and (5.9). For example, starting with Eq. (5.9) and assuming $\eta = 1$, an initial estimate of k_0 was determined. This k_0 was then used in Eq. (5.6) to obtain an estimate for ϕ, which was subsequently used in Eq. (5.6) to find a new value for η. This new value for η was then inserted into Eq. (5.9) to generate a new estimate of k_0. The procedure was repeated until η converged to a single value. Here, the value of the tortuosity used in the determination of the effective diffusivities was a fitting parameter and was determined based on the ability to recover a constant k_i from the values of k obtained from reacting particles of various sizes. Here, $\tau_\mathrm{p} = 2.4$ was chosen. This value is typical of commercial pellets of catalyst (Satterfield, 1980). Figure 5.6 (a) shows the observed initial rate constant, k, plotted *versus* particle radius, R. For $R < 300$ μm, k remains approximately constant at 490 s^{-1}. As R increases, k decreases; this pattern holds for the three reduction cycles investigated. Figure 5.6 (a) also shows the initial intrinsic rate constant, k_0, for cycle 2. Applying the effectiveness factor correction has little effect on the rate constant for particles with $R < 300$ μm, since here $k = k_0$, implying $\eta = 1$. For larger particles, however, the correct value of $k_0 = 490$ s^{-1} can be recovered from the values of k. Plotting $\eta = k/490$ s^{-1} *versus* the calculated ϕ from Eq. (5.6) for each point, Fig. 5.6(b) confirms that $\eta \sim 1$ for $R < 300$ μm. Also, it can be seen that for the largest particles η approaches $3/\phi$. This region corresponds to where intraparticle diffusion dominates the observed reaction rate. The size range of the particles which can be used for a kinetic study was therefore bounded by the transition to internal diffusion control at R greater than about 300 μm and the experimental observation of elutriation for R less than about 100 μm. Therefore, particles with 150 μm $< R <$ 210 μm were used to determine the rate constants in subsequent experiments.

To determine whether heat transfer to the particle was limiting, an order of magnitude estimate of the Biot number, $(hd_\mathrm{p}/6\lambda_\mathrm{e})$, for a single particle with $R \sim 180$ μm was performed and gave $Bi << 1$ and typically, $Bi \approx 0.04$ as shown in Table 5.1, indicating that the temperature across a single particle was uniform. Here, $\lambda_\mathrm{e} = 0.5$ W/(m K) was used (Takegoshi *et al.*, 1984), and h was estimated conservatively using the thermal conductivity of the gas with $Nu = hd_\mathrm{p}/\lambda_\mathrm{mix} = 2$ as listed in Table 5.1. Next, a simple heat balance was used to estimate the maximum temperature difference between a single particle and the bed during reduction, given by:

$$r'\Delta H^{\circ}_{T_\infty}\rho_{\mathrm{Fe_2O_3}}\left(\frac{4\pi R^3}{3}\right) = h\left(4\pi R^2\right)(T - T_\infty)\,, \tag{5.11}$$

in which it has been assumed that the radiative component of heat transfer is small. The temperature in the particle, T, was assumed uniform since $Bi << 1$; the rate was assumed equal to the initial rate at $X = 0$; h listed in Table 5.1 was used; $(T - T_\infty)$ was the temperature difference between the particle, T, and the bed, T_∞. The maximum temperature difference between the reacting particle and the surrounding bed was found to be < 10 K for all cases. Thus, it is reasonable to conclude that the temperature within a particle was the same as that of the bed.

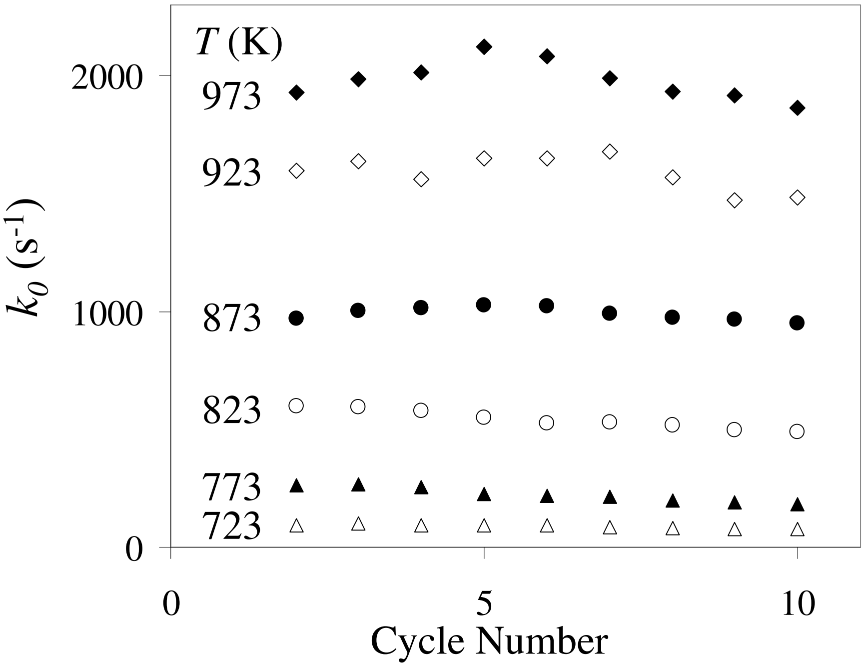

Figure 5.7: Initial rate constant, k_0, at zero conversion over multiple cycles of reduction and temperatures of 723 K (△), 773 K (▲), 823 K (○), 873 K (●), 923 K (◊) and 973 K (♦) for the reduction of Fe_2O_3 to Fe_3O_4. Here, k_0 increases with temperature and remains approximately constant over multiple cycles.

From Fig. 5.7, it can be observed that the rate constant at zero conversion increases monotonically with temperature and remains approximately constant from cycle 2 to cycle 10 for a fixed temperature. The rate constant initially increases with cycle number in experiments above 873 K.

The initial rate constant was assumed to be of Arrhenius form with $k_0 = A\exp(-E/\mathrm{R}T)$, where A is the pre-exponential factor, E the activation energy, R the gas constant and T the

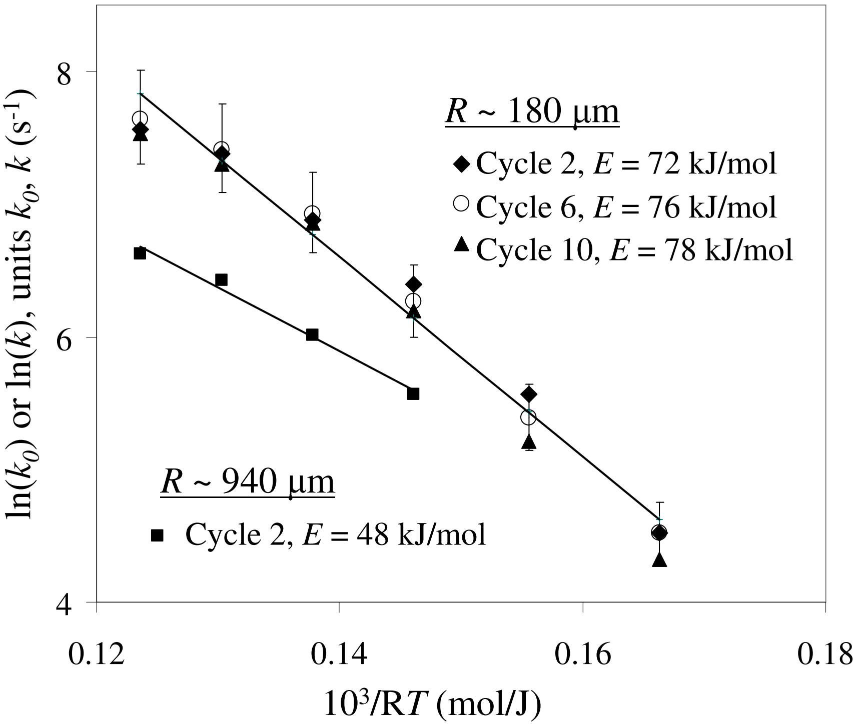

Figure 5.8: Arrhenius plot showing the activation energy, E, based on the initial rate constant, k_0, for the reduction of Fe_2O_3 to Fe_3O_4 for cycles 2, 6 and 10 for particles with $R \sim 180\ \mu$m. The average value was $E = 75$ kJ/mol. The E calculated from k for particles with $R \sim 940\ \mu$m, where intraparticle diffusion is rate-limiting, was slightly greater than 1/2 that of particles with $R \sim 180\ \mu$m, where intrinsic kinetics were rate-limiting.

absolute temperature. The plot of $\ln(k_0)$ *versus* $10^3/(\mathrm{R}T)$ is shown in Fig. 5.8 and was used to determine the activation energy for particles with $R \sim 180\ \mu$m. The activation energy was found to be $E = 72 \pm 12$ kJ/mol, 76 ± 9 kJ/mol and 78 ± 11 kJ/mol for cycles 2, 6 and 10, respectively. The activation energy was approximately constant over nine cycles with an average of $E = 75 \pm 11$ kJ/mol. The pre-exponential factor from the intercept of the best fit line with the ordinate at $10^3/\mathrm{R}T = 0$, was determined as $\ln(A) = 17.0 \pm 1.6$, giving $A = 2.4 \times 10^7\ \mathrm{s}^{-1}$. The experimental error is reported as an error in both the activation energy and pre-exponential factor using the standard error for the line's slope and intercept, respectively, multiplied by the t-statistic for a 90 % confidence interval with $(m-2)$ degrees of freedom, where m is the number of experimental points. The errors in the activation energy and pre-exponential factor should not be combined, since they were derived from a single error in k_0 and such a combination would lead to inflated error estimates for k_0. Also shown in Fig. 5.8 is the activation energy obtained from k for particles with $R \sim 940\ \mu$m. For all particles in Fig. 5.7, external mass transfer was negligible, so $k = \eta k_i$. It has already been shown in Fig. 5.6 that for the 940 μm particles, $\eta = 3/\phi$; combining this with $k = \eta k_i$ gives $k = 3k_i/\phi$ and using the relation $\phi \propto k_i^{1/2}$

from Eq. (5.6) gives $k \propto k_i^{1/2}$. This relation demonstrates that the activation energy of the larger particles should be approximately one half that for the particles controlled by intrinsic kinetics, assuming the effective diffusivity does not change appreciably with temperature. Figure 5.8 shows that the activation energy for the particles with $R \sim 940$ μm is 48 ± 12 kJ/mol, which overlaps with half the value of $E = 75 \pm 11$ kJ/mol for particles with $R \sim 180$ μm.

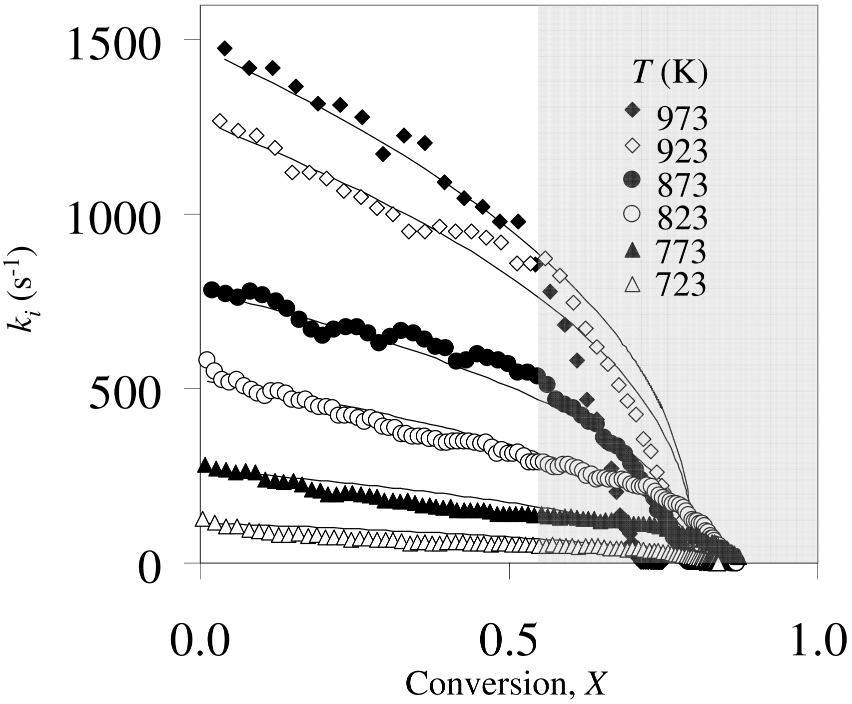

Figure 5.9: Plot of rate constant, k_i, against conversion, X, for cycle 2 at various temperatures. For $X > 0.54$, depicted by the shaded region, k_i begins to descend to zero and the monotonic increase of k_i with temperature is lost. The solid lines represent the fit, $k_0(1 - X/0.8)^{0.4}$. The maximum conversion of $X = 0.8$ indicates that some of the weighed Fe_2O_3 never reacts.

To model chemical reactions, predicting the variation of r' with the conversion of Fe_2O_3 is important. Figure 5.9 is a plot of k_i *versus* X for cycle 2 at six different temperatures. Higher values of k_i were found for higher temperatures when $X < 0.5$, as shown by the shaded region in Fig. 5.9. For all temperatures, k_i reaches zero at $X \approx 0.8$. Since conversion does not reach unity, some of the material never reacts. The variation of k_i can be quantified by fitting $k_0 f(X) = k_0(1 - X/0.8)^a$ to the experimental points in Fig. 5.9. This choice of $f(X)$ is the simplest function which satisfies the constraints $f(X)_{X=0} = 1$ and $f(X)_{X=0.8} = 0$. A least squares analysis gave $a = 0.4$ and the resulting fits are shown by the solid lines in Fig. 5.9. The rate of reduction of Fe_2O_3 to Fe_3O_4 as a function of temperature and conversion over repeated cycles of reduction can finally be summarised as

$$r' = \frac{2.4 \times 10^7 \exp(\frac{-75000}{\mathrm{R}T})}{\rho_{\mathrm{Fe_2O_3}}} \left(c_{\mathrm{CO}} - \frac{c_{\mathrm{CO_2}}}{K_p}\right)\left(1 - \frac{X}{0.8}\right)^{0.4}, \tag{5.12}$$

where the pre-exponential factor has units (1/s), R has units J/(mol K), T is the absolute temperature in kelvin, $\rho_{\mathrm{Fe_2O_3}}$ is the bulk density of the $\mathrm{Fe_2O_3}$ starting material in (g/m^3), c_{CO} and $c_{\mathrm{CO_2}}$ are concentrations in (mol/m^3), K_p is the dimensionless equilibrium constant, and X is the dimensionless conversion.

5.4.2 Transition from $\mathrm{Fe_3O_4}$ to $\mathrm{Fe_{0.947}O}$

The reduction of $\mathrm{Fe_3O_4}$ to $\mathrm{Fe_{0.947}O}$ was studied between 923 K and 1173 K with inlet mole fractions of CO and $\mathrm{CO_2}$ both set between 8.5 and 9.5 vol.%. The rate at various conversions was determined from the corresponding plots of r' *versus* X. X-ray diffraction confirmed the presence of $\mathrm{Fe_{0.947}O}$ after reduction of 5 g of $\mathrm{Fe_2O_3}$ of sieve size $d_\mathrm{p} = +300, -425\ \mu$m in 9 vol.% CO, 9 vol.% $\mathrm{CO_2}$, balance $\mathrm{N_2}$ at 1173 K without any $\mathrm{Al_2O_3}$ in the bed and is shown in Fig. 5.10. The experimental diffraction pattern is shown below that of a simulated scan from a standard reference (JCPDS, 2005b) and clearly demonstrates the presence of $\mathrm{Fe_{0.947}O}$.

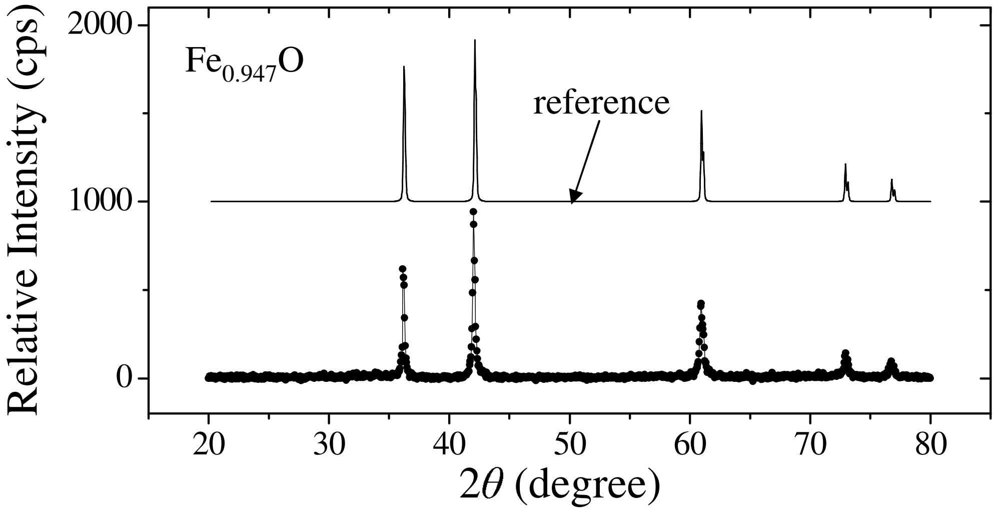

Figure 5.10: Relative intensity (cps) against 2θ for the reduced iron oxide as $\mathrm{Fe_{0.947}O}$; a simulated scan from a standard reference (JCPDS, 2005b) is shown with a vertical offset and demonstrates good agreement

Prior to attempting to determine the activation energy and pre-exponential factor, the assumption that the reaction is first order with respect to CO was investigated at a fixed temperature of 1023 K with a fixed batch mass of 0.8 g of Fe_2O_3. Using material balances and assuming the bed behaves as a CSTR, the rate given by Eq. (5.9) as $r' \propto (c_{\mathrm{CO,out}} - c_{\mathrm{CO_2,out}}/K_p)$ can be expressed in terms of the inlet concentrations so that $r' \propto (c_{\mathrm{CO,in}} - c_{\mathrm{CO_2,in}}/K_p)$, as was explained previously in the text following Eq. (5.10). Figure 5.11 (a) shows the observed initial rate at $X = 0$ obtained by holding the inlet CO_2 constant at 9 vol. % and varying the inlet CO. The rate can be described satisfactorily by a linear fit, indicating that the reaction is indeed first order with respect to [CO]. The circles on the abscissa in Fig. 5.11 (a) indicate the thermodynamic equilibrium points at the boundary between phases Fe_3O_4 and $Fe_{0.947}O$ (i) and $Fe_{0.947}O$ and Fe (ii), calculated from thermodynamic tables (Barin and Knacke, 1973). The intersection of the linear fit in Figure 5.11 (a) with the abscissa gives an experimental value of $K_p = 1.7$ for the transition from Fe_3O_4 to $Fe_{0.947}O$, found by dividing the inlet CO_2 value of 9 vol.% by the CO intercept value of 5.2 vol.%. Figure 5.11 (b) shows the observed initial rate at $X = 0$ obtained by holding the inlet CO constant at 9 vol. %, but varying the inlet CO_2. The rate varies linearly with the inlet concentration of CO_2. The circles in Fig. 5.11(b) represent the thermodynamic boundaries between phases Fe_3O_4 and $Fe_{0.947}O$ (i) and $Fe_{0.947}O$ and Fe (ii) calculated from thermodynamic tables (Barin and Knacke, 1973). Here, the intersection of the solid fit line with the abscissa gave $CO_2 = 18$ vol% and $K_p = 2.1$ for the equilibrium between phases Fe_3O_4 and $Fe_{0.947}O$. The theoretical calculated equilibrium value (Barin and Knacke, 1973) of 1.87, therefore lies between the two experimentally-determined values from Fig. 5.11(a) and (b) of 1.7 and 2.1, respectively, for the transition from Fe_3O_4 and $Fe_{0.947}O$ at 1023 K.

The effect of external mass transfer was also found to be negligible and is examined quantitatively in the discussion. Next, to determine the regime where intrinsic kinetics solely control the observed rate, the initial rate at $X = 0$ was measured at a fixed temperature of 1023 K and fixed batch mass of 0.8 g of Fe_2O_3, whilst varying the size of the particles. The observed initial rate constant, k, is related to the true initial rate constant, k_0, by $k = k_0\eta$ in the absence of external mass transfer. Figure 5.12(a) plots k as a function of particle radius, R, over three cycles. As the particle size increases, k falls roughly proportionally to $3/\phi$. For particles with $R < 300\ \mu$m, k is approximately constant at 640 s^{-1}. The true initial rate constant at zero conversion, $k_0 = 640\ s^{-1}$, was found by iteratively solving for k_0 and η using Eqs. 5.6 and 5.9 as previously outlined. The resulting values for k_0 are shown in Fig. 5.12 for cycle 2. Applying the iterative effectiveness factor correction has little effect on the rate constant for particles with $R < 300\ \mu$m, since $k = k_0$. Here, the tortuosity, τ_{p}, was a fitting parameter

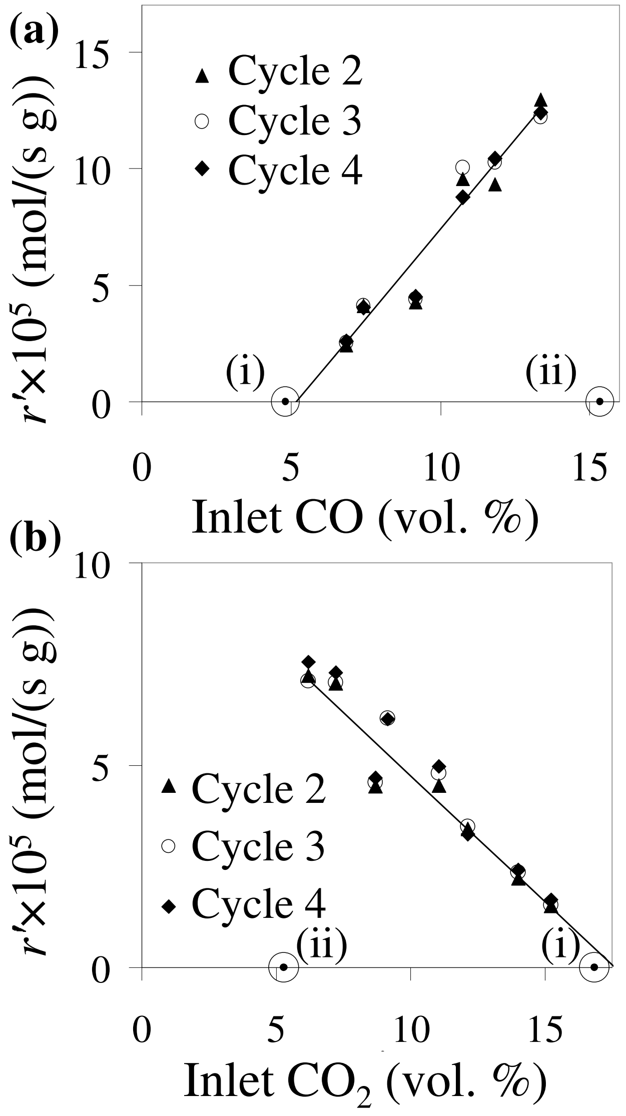

Figure 5.11: (a) The order of reaction for [CO] for the reduction of Fe_3O_4 to $Fe_{0.947}O$ at 1023 K. The inlet mole fraction of CO_2 was held constant at ~ 9 vol. %, and a first order fit is satisfactory. The circles on the abscissa show thermodynamic equilibrium (Barin and Knacke, 1973) of (i) 9 vol% CO_2 and 4.8 vol% CO with a mixture of Fe_3O_4 and $Fe_{0.947}O$ and (ii) 9 vol.% CO_2 and 15.4 vol% CO with $Fe_{0.947}O$ and Fe.
(b) Relation between reaction rate and $[CO_2]$ for the reduction of Fe_3O_4 to $Fe_{0.947}O$ at 1023 K. Here, the inlet mole fraction of CO was maintained at ~ 9 vol. %. The rate varies linearly with inlet $[CO_2]$. The circles on the abscissa show thermodynamic equilibrium of (i) 16.8 vol.% CO_2 and 9 vol% CO with a mixture of Fe_3O_4 and $Fe_{0.947}O$ and (ii) 5.3 vol% CO_2 and 9 vol% CO with a mixture of $Fe_{0.947}O$ and Fe.

as was determined based on the ability to recover a constant k_i from the values of k obtained from reacting particles of various sizes. The value of τ_p was set to 2.5, typical of porous pellets (Satterfield, 1980). Figure 5.12(b) shows an approximation for the effectiveness factor, $\eta = k/640\ \mathrm{s}^{-1}$, *versus* the calculated value of ϕ from Eq. (5.6) over three cycles. For particles with $R < 300\ \mu\mathrm{m}$, $\eta \sim 1$ indicating that the observed rate is limited by intrinsic kinetics. For larger particles, η approaches $3/\phi$, indicating that the rate is governed by intraparticle diffusion. Therefore, to avoid elutriation whilst still capturing the intrinsic kinetics, particles with $150\ \mu\mathrm{m} < R < 210\ \mu\mathrm{m}$ were used in all subsequent experiments.

To determine whether heat transfer was limiting, an order of magnitude estimate of the Biot number, $(hd_\mathrm{p}/6\lambda_\mathrm{e})$, for a single particle with $R \sim 180\ \mu\mathrm{m}$ was performed and gave $Bi << 1$ and typically, $Bi \approx 0.05$, as shown in Table 5.1, indicating that the temperature across a single particle was uniform. Next, a simple heat balance using Eq. (5.11) was used to estimate the maximum temperature difference between the particle and the bed during reduction. The temperature in the particle was assumed uniform since $Bi << 1$, and the rate was assumed equal to the initial rate at $X = 0$; a conservative estimate of the heat transfer coefficient was obtained using $Nu = 2$ and the thermal conductivity of the reactant gas. The maximum temperature difference between the reacting particle and the surrounding bed was found to be < 6 K for all cases. Thus, it is reasonable to conclude that the temperature within a particle was the same as that of the bed.

Previously, to determine the order of reaction and the regime where intrinsic kinetics dominate the reduction of $\mathrm{Fe_2O_3}$ to $\mathrm{Fe_3O_4}$, the initial rate at $X = 0$ was used. To determine the pre-exponential factor and activation energy for the reduction of $\mathrm{Fe_3O_4}$ to $\mathrm{Fe_{0.947}O}$, however, better precision in the value of the rate constant, k_i, was achieved by using rates evaluated at $X > 0$. The reason derives from Eq. (5.9) for k_i, which gives $k_i \propto r'/(c_{\mathrm{CO,out}} - c_{\mathrm{CO_2,out}}/K_p)$ for negligible mass transfer resistance and $\eta = 1$. For large rates, fast kinetics permit nearly complete conversion of CO to the equilibrium limit. The evaluation of the rate constant, k_i, therefore relies on division by a concentration term of small magnitude. Using smaller rates, *i.e.* at $X > 0$, reduces the uncertainty in k_i introduced by this term. Figure 5.13(a) shows the concentration of CO and $\mathrm{CO_2}$ in the effluent gas as a function of time for the reduction of $\mathrm{Fe_3O_4}$ to $\mathrm{Fe_{0.947}O}$ at 1023 K. Figure 5.13(b) then shows the corresponding concentration term, $(c_{\mathrm{CO,out}} - c_{\mathrm{CO_2,out}}/K_p)$, calculated from the results in Fig. 5.13(a), where only every fifth point is plotted. The tradeoff between (i) a large enough batch mass to give measurable changes in the outlet concentrations during reaction as well as reduction times significantly greater than the

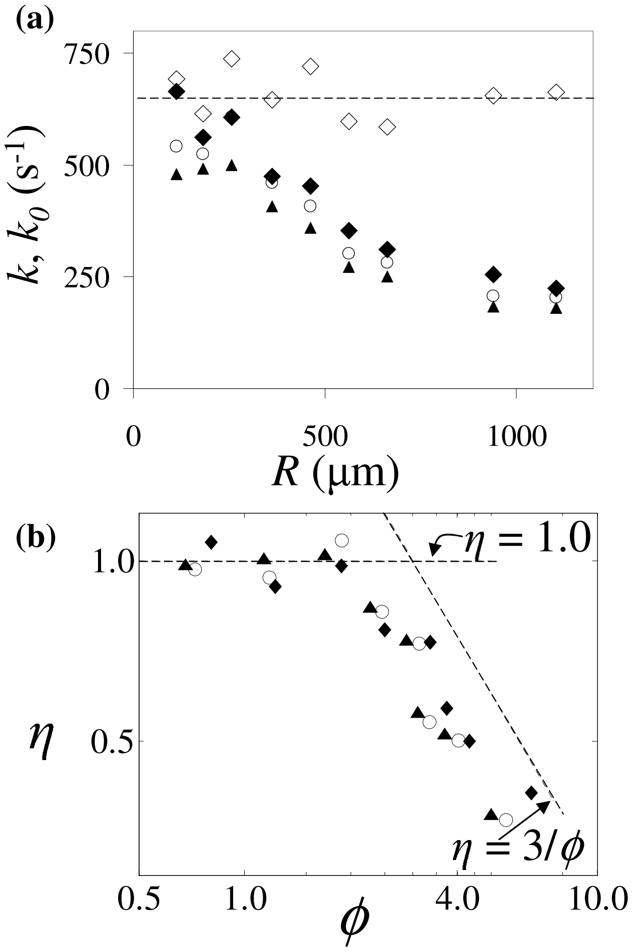

Figure 5.12: Reduction of Fe_3O_4 to $Fe_{0.947}O$ at 1023 K.
(a) Plot of initial rate constant k at $X = 0$ *versus* average radius, R, of the iron oxide particles for cycles 2 (♦), 3 (○) and 4 (▲). The corrected intrinsic rate constant at zero conversion, k_0, is also shown for cycle 2 (◊) and has an average value of 640 s^{-1}.
(b) Effectiveness factor, $\eta = k/640\ s^{-1}$, *versus* ϕ for particles of various radii for cycles 2 (♦), 3 (○) and 4 (▲), corresponding to the points in (a). For smaller particles, $\eta = 1.0$; as particle size increases η approaches $3/\phi$.

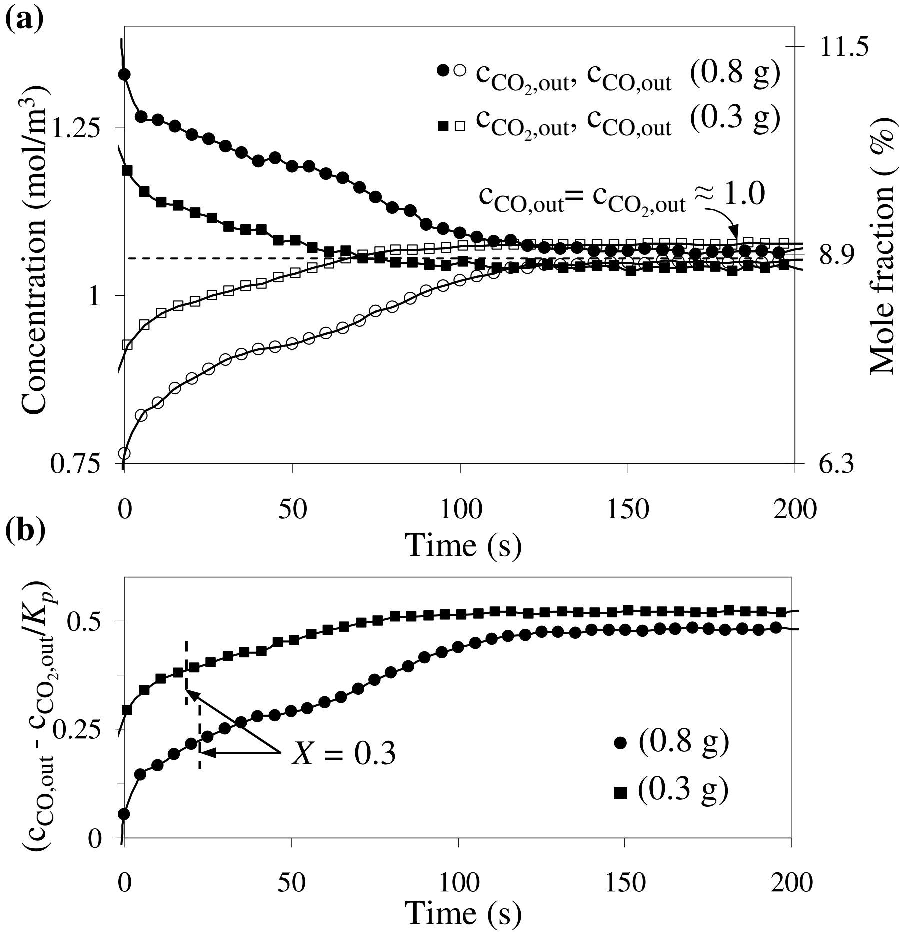

Figure 5.13: (a) Concentration of CO and CO_2 in the effluent gas as a function of time for the reduction of Fe_3O_4 to $Fe_{0.947}O$ in a fluidised bed for cycle 2 at 1023 K. The initial charge was either 0.3 g or 0.8 g as Fe_2O_3 and had been reduced to $Fe_{0.947}O$ in a mixture of CO, CO_2 and N_2 and then oxidised to Fe_3O_4 in a mixture of steam and N_2 prior to $t = 0$.
(b) Concentration term, $\left(c_{CO,out} - c_{CO_2,out}/K_p\right)$, against time corresponding to the experiments in (a).

mixing times of the analysers and (ii) a small enough batch mass to give non-zero values of $\left(c_{CO,out} - c_{CO_2,out}/K_p\right)$ must be made. Here, k_i was determined at $X = 0.3$ and at 1023 K; 0.7 g of Fe_2O_3 was used. The rate constant k_i is then no longer the initial intrinsic rate constant, k_0, but the intrinsic rate constant, k_i, at the specific conversion of $X = 0.3$.

Figure 5.14 shows k_i evaluated at $X = 0.3$ over nine cycles and temperatures from 923 K to 1173 K. The inlet CO and CO_2 were both fixed at 9 vol.% for all cases. Unlike the rate constant for the transition from Fe_2O_3 to Fe_3O_4, which remained approximately constant with cycle number, k_i decreases with cycle number. The drop in k_i is more pronounced at higher temperatures.

The rate constant was assumed to be of Arrhenius form with $k_i = A\exp(-E/\mathrm{R}T)$. A plot

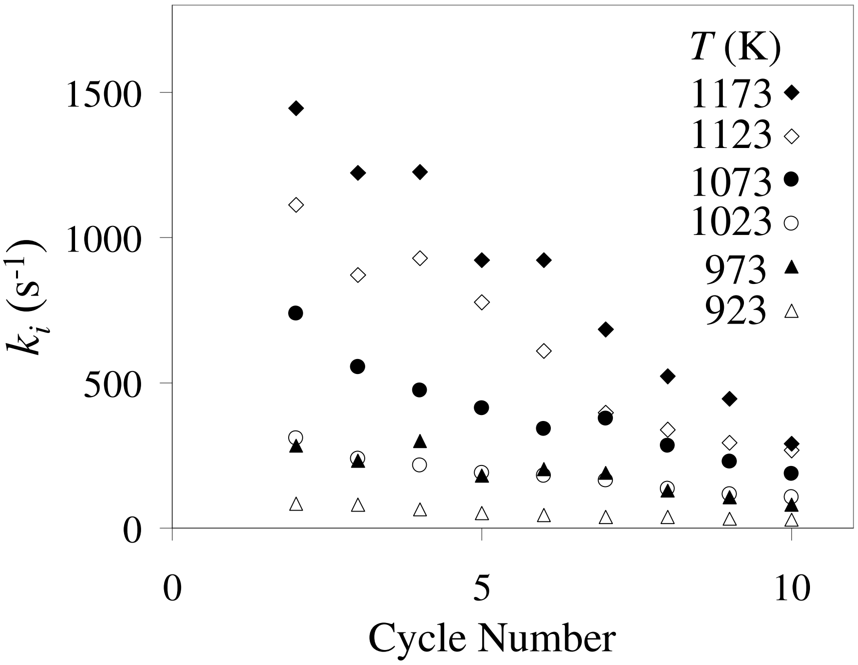

Figure 5.14: Intrinsic rate constant, k_i, at $X = 0.3$ for the reduction of Fe_3O_4 to $Fe_{0.947}O$. Here, k_i increases with temperature, but decreases with the number of cycles.

of $\ln(k_i)$ *vs.* $10^3/\mathrm{R}T$ is shown in Fig. 5.15. From Fig. 5.15, the activation energy decreased slightly with cycle number for particles with $R \sim 180\ \mu$m, ranging from $E = 106 \pm 28$ kJ/mol for cycle 2 to $E = 91 \pm 14$ kJ/mol for cycle 10. The average activation energy for the transition can be summarised by $E = 94 \pm 25$ kJ/mol. Since E decreases slightly with cycle number, the decrease in the observed rate highlighted previously in Fig. 5.14 must be a result of a decrease in the pre-exponential factor. The intercepts of the lines in Fig. 5.15 with the ordinate at $10^3/\mathrm{R}T = 0$, give the pre-exponential factors for a fixed conversion of $X = 0.3$. If the average value, $E = 94$ kJ/mol, is used for all cycles, the best fit lines yield $ln(A) = 17.0 \pm 2.1,\ 16.5 \pm 1.9$ and 15.8 ± 1.8, for cycles 2, 6 and 10, respectively, giving corresponding values of $A = 2.4 \times 10^7,\ 1.5 \times 10^7$ and $7.3 \times 10^6\ \mathrm{s}^{-1}$. Figure 5.15 also shows that for particles with $R \sim 940\ \mu$m the experimental activation energy calculated from k is $E = 44$ kJ/mol. The predicted activation energy from an effectiveness factor argument is one half of the E determined with particles of $R \sim 180\ \mu$m, giving $94/2 = 47$ kJ/mol. The agreement of these values is satisfactory and suggests that the rate of reduction for the smaller particles is controlled by intrinsic kinetics, whereas that for the larger particles is influenced by intraparticle diffusion.

To model the reduction of Fe_3O_4 to $Fe_{0.947}O$, the variation of the rate, r', with conversion, X must be determined. Figure 5.16 is a plot of k_i against X. As shown by the shaded regions, for values of $X > 0.6$ the monotonic increase in k_i with temperature is lost; for values of

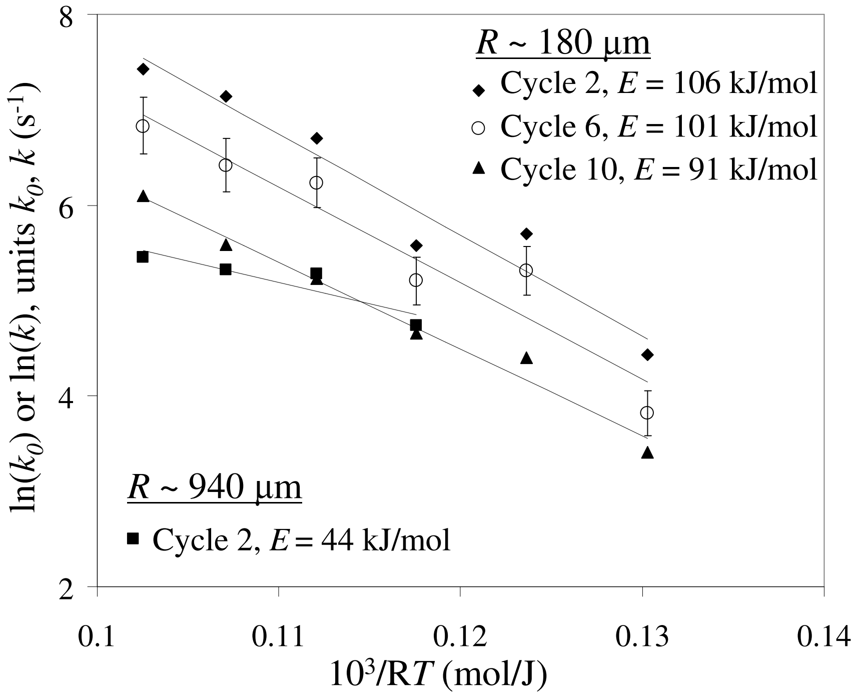

Figure 5.15: Activation energy diagram for the reduction of Fe_3O_4 to $Fe_{0.947}O$. A slight decrease in E with cycle number is observed. The E calculated from k for particles with $R \sim 940\ \mu$m is half that observed for particles with $R \sim 180\ \mu$m.

$X < 0.2$ above 1023 K, k_i increases rapidly: the rate of reaction was too fast to obtain results for $X < 0.2$. The range of conversions where values of k_i could reasonably be obtained was $0.2 < X < 0.6$. In this range, values for E agreed well with those determined earlier for $X = 0.3$. A least-squares fit with the functional form $k_i = k_0(1 - X/0.8)^a$ gave $a = 1.2$. The fit was performed such that the correct value of k_i at $X = 0.3$ was recovered. The pre-exponential factor, A, for the initial rate constant, k_0, could then be obtained from the previously reported values of A for k_i at $X = 0.3$ by adding $-1.2\ln(1 - 0.3/0.8) \sim 0.55$ to $\ln(A)$. Hence, the pre-exponential factors for k_0 are $\ln(A) = 17.6 \pm 2.1, 17.1 \pm 1.9$ and 16.3 ± 1.8 for cycles 2, 6 and 10 respectively, corresponding to $A = 4.3 \times 10^7$, 2.5×10^7 and 1.2×10^7 s^{-1}. Thus, the rate constants as a function of temperature and conversion for the reduction of Fe_3O_4 to $Fe_{0.947}O$ for cycles 2, 6 and 10 can be summarised by:

$$\left.\begin{aligned}
r' &= \frac{4.3 \times 10^7 \exp(\frac{-94000}{RT})}{\rho_{Fe_2O_3}}\left(c_{CO} - \frac{c_{CO_2}}{K_p}\right)\left(1 - \frac{X}{0.8}\right)^{1.2} \\
r' &= \frac{2.5 \times 10^7 \exp(\frac{-94000}{RT})}{\rho_{Fe_2O_3}}\left(c_{CO} - \frac{c_{CO_2}}{K_p}\right)\left(1 - \frac{X}{0.8}\right)^{1.2} \\
r' &= \frac{1.2 \times 10^7 \exp(\frac{-94000}{RT})}{\rho_{Fe_2O_3}}\left(c_{CO} - \frac{c_{CO_2}}{K_p}\right)\left(1 - \frac{X}{0.8}\right)^{1.2}.
\end{aligned}\right\} \tag{5.13}$$

where r' again has units of mol/(s g of original particle as Fe_2O_3).

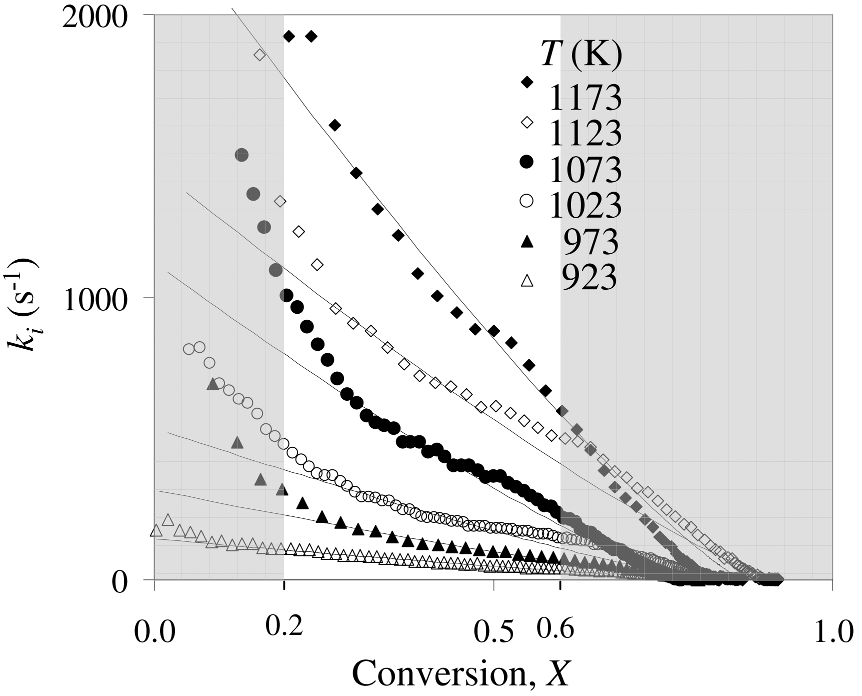

Figure 5.16: Plot of the rate term, k_i, *versus* conversion, X, for cycle 2 at various temperatures. The rapid rise of k_i for $X < 0.2$ and the decrease of k_i towards zero with $X > 0.6$ is evident, as shown by the shaded regions. Rates within the interval $0.2 < X < 0.6$ gave a best fit of $k_i = k_0(1 - X/0.8)^{1.2}$; this fit is indicated by the solid lines.

5.4.3 Packed Bed

To verify the kinetic parameters obtained from the fluidised bed experiments, the reduction of iron oxide was investigated in a packed bed at 1023 K. A simplified 1D model of a packed bed, which used the rate constants determined from the fluidised bed experiments given in Eqs. (5.12) and (5.13), was constructed to compare experimental results with theory. To formulate a mathematical description of the system, it was assumed that (i) the bed was isothermal, (ii) only axial concentration gradients were significant, *i.e.* the problem was treated as one-dimensional, (iii) the reaction rate was limited only by intrinsic kinetics and external mass transfer, not by intraparticle diffusion, (iv) the dispersion coefficient was constant for both CO and CO_2 along the bed, (v) gas flowed through the interstices only, not through the porous particles, and (vi) frictional losses were insignificant so that pressure did not vary along the bed. The assumption of isothermal operation was based on the experimental observation that the maximum measured change in temperature during reduction was small, < 30 K, compared to the operating temperature 1023 K. The evolution of the gaseous and metal oxide species in the pseudohomogeneous bed as a function of time, *t*, and position, *x*, are then given for CO and Fe_2O_3 by:

$$\left(\frac{\partial c_{CO}}{\partial t}\right)_x = -\,v\left(\frac{\partial c_{CO}}{\partial x}\right)_t + D\left(\frac{\partial^2 c_{CO}}{\partial x^2}\right)_t \tag{5.14}$$

$$-\,\frac{(1-\varepsilon_{bed})}{\varepsilon_{bed}}\left[\underbrace{k\left(c_{CO}-\frac{c_{CO_2}}{K_p}\right)\left(1-\frac{X}{0.8}\right)^{0.4}}_{\text{reaction 5.1}} + \underbrace{k\left(c_{CO}-\frac{c_{CO_2}}{K_p}\right)\left(1-\frac{X}{0.8}\right)^{1.2}}_{\text{reaction 5.2}}\right]$$

$$\left(\frac{\partial n_{Fe_2O_3}}{\partial t}\right)_x = -\,3\left[\underbrace{k\left(c_{CO}-\frac{c_{CO_2}}{K_p}\right)\left(1-\frac{X}{0.8}\right)^{0.4}}_{\text{reaction 5.1}}\right], \tag{5.15}$$

where the parameters, k, K_p and X, are defined as appropriate for whether reaction (5.1) or (5.2) is being considered, consistent with Eqs. (5.12) and (5.13) in the previous discussion. Here, $\varepsilon_{bed} = 0.36$ is the mean measured interstitial porosity of the bed, $v = 3.88$ m/s is the interstitial velocity, K_p are the equilibrium constants, $n_{Fe_2O_3}$ is the number of moles of Fe_2O_3 *per* unit volume particle, −3 is the stoichiometric coefficient from reaction (5.1), and $D = 8\times10^{-4}$ m^2/s is the dispersion coefficient, calculated using Eq. (12) from Gunn (1968) and verified with Levenspiel's Fig. 13.17 (Levenspiel, 1999). The mass transfer coefficients, $k_{g,CO}$ and k_{g,CO_2}, from the bulk gas to the surface of the particles, which appear in the rate constant, k, were calculated using the correlation of Wakao and Funazkri (1978), $Sh = 2.0 + 1.1Re^{0.6}Sc^{1/3}$ and gave $k_{g,CO} = 1.96$ m/s and $k_{g,CO_2} = 1.61$ m/s. Hence, the values of k for reactions (5.1) and (5.2) are

$$\left.\begin{array}{ll} Fe_2O_3 \rightarrow Fe_3O_4: & \dfrac{1}{k} = \dfrac{R}{3k_{g,CO}} + \dfrac{1}{2.4\times10^7\exp(\frac{-75000}{RT})} + \dfrac{R}{3k_{g,CO_2}K_p} = \dfrac{1}{3200}\mathrm{s} \\ Fe_3O_4 \rightarrow Fe_{0.947}O: & \dfrac{1}{k} = \dfrac{R}{3k_{g,CO}} + \dfrac{1}{4.3\times10^7\exp(\frac{-94000}{RT})} + \dfrac{R}{3k_{g,CO_2}K_p} = \dfrac{1}{660}\mathrm{s} \end{array}\right\}, \tag{5.16}$$

respectively, for the second cycle of reduction. It is noted that the effect of the mass transfer is minimal: eliminating terms with $k_{g,CO}$ and k_{g,CO_2} in Eq. (5.16) results in values of k of 3580 s^{-1} and 680 s^{-1} for reactions (5.1) and (5.2), respectively, less than 12 % change in k for reaction (5.1) and less than 3 % change in k for reaction (5.2). Thus, all the parameters were determined experimentally with the exception of the mass transfer and dispersion coefficients.

Furthermore, the effect of the dispersion coefficient was small due to the large Péclet number, $Pe = vL/D = 160$. The equations were discretised using an upwind finite difference scheme. The length of the bed was $L = 33$ mm and the number of grid points used was 100. Boundary conditions were chosen to be of the Danckwerts form and were expressed for the case of CO as: $v[c_{\text{CO}}(0) - c_{\text{CO,in}}] - D(\partial c_{\text{CO}}/\partial x)_{x=0} = 0$ and $(\partial c_{\text{CO}}/\partial x)_{x=L} = 0$ at the inlet and outlet, respectively (Beers, 2007). Here, $c_{\text{CO}}(0)$ is the concentration of CO at the grid point at the inlet to the bed, whereas $c_{\text{CO,in}}$ is the specified inlet concentration, which for an approximately 9 vol. % fraction at 1023 K and 10^5 Pa gives $c_{\text{CO,in}} = 1$ mol/m^3. The inlet [CO_2] was also 1 mol/m^3. To prevent the model from producing negative amounts of $Fe_{0.947}O$, an additional thermodynamic constraint was added: the reduction of Fe_3O_4 to $Fe_{0.947}O$, reaction (5.2), in a differential element was not permitted unless locally $p_{\text{CO}_2}/p_{\text{CO}} < 2.1$, which represents the experimental equilibrium constant. Finally, once a conversion $X = 0.8$ had been reached for a reaction in a differential cell, the corresponding k_i was set to 0.

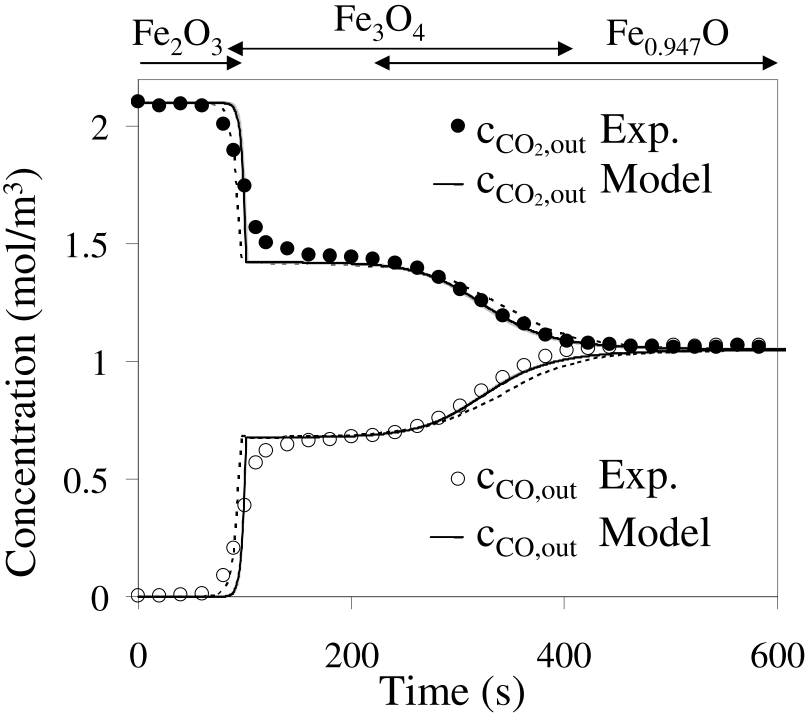

Figure 5.17: Comparison between the effluent concentration of CO and CO_2 as a function of time for experimental results (○, •) and model predictions (—), respectively, with $D = 8 \times 10^{-4}$ m^2/s for the reduction of 5 g of Fe_2O_3 to $Fe_{0.947}O$ at 1023 K. Results with an increased dispersion of $D = 8 \times 10^{-3}$ m^2/s are shown by the dashed lines (- - -); results for a decreased dispersion of $D = 8 \times 10^{-5}$ m^2/s are similar to the original result (—).

The packed bed, containing 5 g of Fe_2O_3 particles with $R \sim 180\,\mu$m, was heated to 1023 K in a stream of air. The reactor was subsequently purged with N_2 for 500 s. At $t = 0$, the gas was suddenly changed from N_2 to a mixture of N_2+CO+CO_2 (respectively, 82, 9 and 9 vol. %), which from thermodynamics will reduce the Fe_2O_3 to $Fe_{0.947}O$, forming Fe_3O_4 as an intermediate. Reoxidation was performed with N_2+steam (respectively, 82 and 18 vol. %) and N_2+air (respectively, 82 and 18 vol.%). Figure 5.17 shows the concentrations of CO and CO_2 at the reactor outlet, $x = L$, as a function of time for the second reduction cycle. Initially, for 0 s $< t <$ 90 s, Figure 5.17 shows that the entering CO is fully converted to CO_2. In this interval, a front corresponding to the reduction of Fe_2O_3 to Fe_3O_4 in reaction (5.1), propagates down the bed. The intrinsic kinetics are sufficiently fast to permit equilibrium to be reached, so that the ratio $c_{\mathrm{CO,out}}/c_{\mathrm{CO_2,out}} = 1/K_p \approx 0$. The relation between the residence time of the gas and the characteristic kinetic time constant also demonstrates that reactant gases have sufficient time to react fully, since $1/k < L/v$. The breakthrough of the front after $t \sim 95$ s is characterised by a rapid rise and fall in the concentrations of CO and CO_2, respectively. At this stage the Fe_2O_3 along the bed has been fully converted to Fe_3O_4; also $Fe_{0.947}O$ has appeared at the reactor inlet. The conversion of Fe_3O_4 to $Fe_{0.947}O$, which has already commenced at the beginning of the bed for $t < 95$ s, continues until $t \sim 410$ s. For $t > 200$ s, the curvature of the outlet concentrations is primarily governed by kinetics and the accuracy of the value of k for reaction (5.2) is demonstrated by the good agreement between the experimental and modelled concentration curves. For $t > 410$ s no more reaction occurs and the concentrations of CO and CO_2 in the outlet are equal to those at the inlet, *i.e.* 1 mol/m^3. The arrows in Fig. 5.17 indicate the times when various metal oxide species eligible of undergoing reaction were present above 5 mol % at the reactor outlet, *i.e.* in the final computational cell. The narrow overlap between the Fe_2O_3 and Fe_3O_4 lines indicates a sharp front, compared to the more gradual transition between Fe_3O_4 and $Fe_{0.947}O$.

The influence of the dispersion coefficient was also investigated by increasing and decreasing D in the range $D = 8 \times 10^{-3}$ m^2/s to $D = 8 \times 10^{-5}$ m^2/s. Figure 5.17 shows that altering D by two orders of magnitude does not influence the results, as expected given the large Pe number, $Pe = 160$.

Figure 5.18 shows how changes in k_i for the reduction of Fe_3O_4 to $Fe_{0.947}O$ affect $c_{\mathrm{CO,out}}$ and $c_{\mathrm{CO_2,out}}$ predicted by the model. Values of $1/2k_i$, k_i, $2k_i$ and $10k_i$, giving $k = 340, 660, 1280$ and 5060 s^{-1} were used. Figure 5.18 shows that the front corresponding to the transition from Fe_2O_3 to Fe_3O_4 does not change appreciably; this is expected since the rate parameter for this transition was not altered and since reduction of Fe_2O_3 to Fe_3O_4 was limited by the inflow of reactant CO. In contrast, the front corresponding to the transition from Fe_3O_4 to

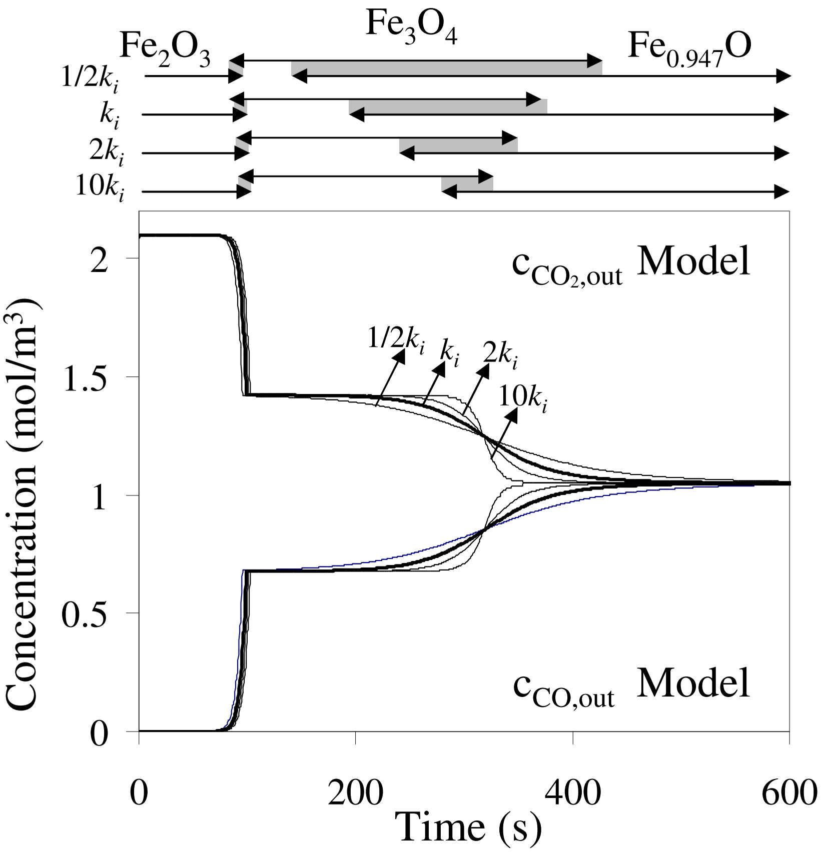

Figure 5.18: Effluent concentration of CO and CO_2 against time for the reduction of 5 g of Fe_2O_3 to $Fe_{0.947}O$ at 1023 K. The effect of changing k_i for the reduction of Fe_3O_4 to $Fe_{0.947}O$, reaction (5.2) on the effluent concentrations, front thickness and front speed is shown.

$Fe_{0.947}O$ grows sharper with increasing k_i, depicted by the decreasing overlap between species of Fe_3O_4 to $Fe_{0.947}O$, shown by grey regions above the graph in Fig. 5.18. Here, the CO and CO_2 effluent curves approximate step functions when k_i is raised 10×. Interestingly, the CO and CO_2 effluent curves for each simulation intersect at $t = 320$ s, suggesting that for the given inlet flowrate and inlet concentrations, an infinitely large k_i would cause an infinitely thin front to emerge at this time. Also interesting to note is how the total quantity of $Fe_{0.947}O$ in the bed changes at a fixed time, say $t = 90$ s or just before CO_2 breakthrough, in order to understand how the theoretical yield of H_2 could change with increased kinetics. Summing the quantity of $Fe_{0.947}O$ in each node along the reactor at $t = 90$ s, shows that for $1/2k_i$, $2k_i$ and $10k_i$, 0.91×, 1.05× and 1.10× as much $Fe_{0.947}O$ is present compared to the case with k_i. More $Fe_{0.947}O$ in the bed will result in more H_2 upon subsequent oxidation in steam. Therefore, an experimental investigation into increasing the rate of reaction of the reduction of Fe_3O_4 to $Fe_{0.947}O$ is presented in the next Chapter.

5.5 Discussion

For the design of equipment to reduce Fe_2O_3 using CO with subsequent reoxidation in steam to produce H_2, the long-term stability of the rate of reduction over many cycles is important. Figure 5.7 shows that the initial rate constant, k_0, for the reduction from Fe_2O_3 to Fe_3O_4 did not decrease, but remained constant over nine cycles.

For the rate constants in Fig. 5.8 for particles with $R \sim 180\ \mu$m, the ratios of the resistance of external mass transfer of CO to the resistance of intrinsic kinetics, *i.e.* the ratio of the sum of the first and third terms in Eq. (5.7) divided by the second term, was ~ 0.01 and ~ 0.15 at 723 K and 923 K, respectively, thus ensuring that the experimental rates were dominated by intrinsic kinetics. Figure 5.6(b) confirmed that the effectiveness factor was near unity at 823 K for particles with $R \approx 150 - 210\ \mu$m. It was observed that the deduced activation energy was approximately halved when the particle size was increased, as seen in Fig. 5.8, suggesting that the effectiveness factor was unity for small particles and that the rate of reduction for the larger particles was controlled by intraparticle diffusion. For the initial rate constant, k_0, a pre-exponential factor of 2.4×10^7 s^{-1} and an activation energy of 75 ± 11 kJ/mol was obtained; both values were constant and reproducible over repeated cycles. By comparison, Trushenski *et al.* (1974) give 69.0 kJ/mol $< E <$ 100.0 kJ/mol and Szekely *et al.* (1976) report $E = 114$ kJ/mol. These authors' values were extracted from experiments with significant mass-transfer resistance. Figure 5.9 showed that the effect of conversion, X, can be represented by the function $(1 - X/0.8)^{0.4}$. Interpreting the exponent, $a = 0.4$, we find that terms of $(1 - X)^{1/3}$ and $(1 - X)^{1/2}$ are typical for theoretical rate expressions involving shrinking cores in spherical and cylindrical geometries, respectively, where the reaction is limited by intrinsic kinetics. However, in the current study, shrinking cores could not exist on the length scale of an individual particle, since the highly porous matrix allowed gas to diffuse across the entire cross-section and effectiveness factors near unity were calculated. A shrinking core interpretation might, however, be applicable at the subparticle, *e.g.* grain, length scale.

For the transition from Fe_3O_4 to $Fe_{0.947}O$, K_p is of order unity and the influence of the back reaction, because it reduced the overall rate, permitted higher temperatures and reactant concentrations to be used in the determination of the rate constant, k_i. At a conversion of $X = 0.3$, the ratio of the resistance due to external mass transfer of CO and CO_2 to that of the chemical reaction, *i.e.* the central term in the second equation of Eq. (5.7) divided by the sum of the two mass transfer terms in the second equation of Eq. (5.7), was given as ~ 0.02 and

~ 0.17 at 923 K and 1173 K, respectively, for particles with $R \sim 180\,\mu$m. The primary control of intrinsic kinetics was thus ensured and confirmed by effectiveness factors near unity for particles with $R \sim 180\,\mu$m, see Fig. 5.12. Unlike the transition from Fe_2O_3 to Fe_3O_4, Fig. 5.14 showed that the rate constant decreased with cycle number. Efforts to produce particles for the repeated generation of H_2 should therefore focus on reaction (5.2) and investigate how promoters or stabilising agents could be used to prevent the decrease in rate over a number of cycles.

That the observed decrease in rate with cycle number (Fig. 5.14) was a result of a decrease in the pre-exponential factor is demonstrated by the fact that the activation energy in Fig. 5.15 showed only a slight decrease with cycle number: the average value of E was 94 ± 25 kJ/mol. Interpreting the activation energy and pre-exponential factor as a chemical barrier and a probability of a reactive collision occurring at a surface, respectively, these observations imply that the probability of reaction decreases with cycle number whilst the intrinsic chemical barrier remains constant. Physically, this interpretation suggests a decrease in active surface area with cycle number, which was observed for the reduction of Fe_3O_4 to $Fe_{0.947}O$ in a packed bed and shown in Table 3.2, line 2. Figure 5.15 showed that E, found using the observed rate constant for particles which were one order of magnitude larger than those in the kinetic study, resulted in an apparent E half as large as that found in the kinetic study. Comparing $E = 94 \pm 25$ kJ/mol obtained here, Trushenski *et al.* (1974) gives 64.4 kJ/mol $< E <$ 78.2 kJ/mol and Szekely *et al.* (1976) report $E = 73.6$ kJ/mol. These authors' values were obtained from experiments with significant mass-transfer resistance, but fidelity to within the error estimate is obtained. Figure 5.16 showed that the effect of conversion for the transition from Fe_3O_4 to $Fe_{0.947}O$ was best represented by $(1 - X/0.8)^{1.2}$. The term $(1 - X)^a$ with $a = 1$ is typical for a uniform reaction over a porous sphere.

One question regarding the reduction of iron oxide in mixtures of CO and CO_2 which requires attention is that of the mechanism of reduction and of the corresponding rate-limiting step. While there is no consensus in the literature on the mechanism, the most accepted theory is that proposed by Birks *et al.* (2006) who studied oxidation in the context of corrosion, *i.e.* the reverse reactions of those here. They suggested that the interaction of CO and CO_2 with the surface of the metal was rate limiting when the external $Fe_{0.947}O$ layer was $< 18\,\mu$m. In other words, the limiting reaction is

$$CO_{(g)} + O_{ad} \rightleftarrows CO_{2(g)}\,, \tag{5.17}$$

which immediately lends itself to interpretation by the rate expression:

$$\frac{\text{mol}}{\text{m}^2\ \text{s}} = \frac{k_i}{S_0}\left(c_{\text{CO}} - \frac{c_{\text{CO}_2}}{K_p}\right), \tag{5.18}$$

where S_0 is the surface area of the particle *per* unit volume in m^2/m^3. Rate Eqs. (5.12) and (5.13) multiplied by S_g, the specific surface area in m^2/g, are of the form of Eq. (5.18) when $X = 0$. Here it should be noted that individual grains had diameters of 0.5 μm as shown in Fig. 4.1, considerably less than the < 18 μm limit for the validity of Eq. (5.18). In the current study a decrease in the reaction with X was observed. The dependence on X could be explained by a decrease in the surface area of the particle with conversion or due to the diffusion of cations or cation vacancies within the lattice becoming rate limiting (Birks *et al.*, 2006).

The rate constants were verified by investigating the consecutive reduction of Fe_2O_3 to $Fe_{0.947}O$ in a packed bed. Figure 5.17 showed good agreement between observed and predicted values of [CO] and [CO_2] in the effluent for the reduction of Fe_3O_4 to $Fe_{0.947}O$, for $t > 94$ s. The model showed that the reduction of Fe_2O_3 to Fe_3O_4 occurred at a sharper front than the more gradual reduction of Fe_3O_4 to $Fe_{0.947}O$, see Fig. 5.17. This observation is a direct result of the value of the rates, since r' for reaction (5.1) is much greater than r' for reaction (5.2) at a given temperature.

5.6 Conclusions

Results were obtained for the repeated reduction of iron oxide particles, 300-425 μm dia., by mixtures of CO, CO_2 and N_2 in a fluidised bed. The transitions from Fe_2O_3 to Fe_3O_4 and from Fe_3O_4 to $Fe_{0.947}O$ were studied at 10^5 Pa and at temperatures of 723-973 K and 923-1173 K, respectively. The following conclusions were reached:

- The order of reaction for CO was found to be unity in both reduction reactions.

- With the particle sizes used the rates of the reduction reactions are controlled by intrinsic chemical kinetics. The variation of the rate with solids' conversion and temperature was expressed as:

$$\mathrm{Fe_2O_3} \rightarrow \mathrm{Fe_3O_4} \qquad : r' = \frac{2.4\times10^7\exp(\frac{-75000}{\mathrm{R}T})}{\rho_{\mathrm{Fe_2O_3}}}\left(c_{\mathrm{CO}} - \frac{c_{\mathrm{CO_2}}}{K_p}\right)\left(1-\frac{X}{0.8}\right)^{0.4} \quad (5.19)$$

$$\mathrm{Fe_3O_4} \rightarrow \mathrm{Fe_{0.947}O} \qquad : r' = \frac{4.3\times10^7\exp(\frac{-94000}{\mathrm{R}T})}{\rho_{\mathrm{Fe_2O_3}}}\left(c_{\mathrm{CO}} - \frac{c_{\mathrm{CO_2}}}{K_p}\right)\left(1-\frac{X}{0.8}\right)^{1.2}, \quad (5.20)$$

where the pre-exponential factor in Eq. (5.20) is reported for cycle 2. The activation energies were verified by showing that for larger particles where intraparticle diffusion limits the rate, the observed activation energy approximately halves.

- The first cycle gave anomalous results, but (a) the rate of reduction of Fe_2O_3 to Fe_3O_4 remained constant over cycles 2-10; (b) the rate of reduction of Fe_3O_4 to $Fe_{0.947}O$ declined by 60-85 % over cycles 2-10.

- The rate constants, determined in a fluidised bed, were used to predict successfully the reduction of iron oxide in a packed bed.

Chapter 6

Increasing the rate of reduction of Fe_3O_4 to $Fe_{0.947}O$

6.1 Introduction

The objective of the preliminary work presented in this Chapter is to survey a variety of chemical species to find a promoter, either physical or chemical, which increases the rate of reduction of Fe_3O_4 to $Fe_{0.947}O$ by increasing the rate constant, k_i. Since k_i is of Arrhenius form with $k_i = A\exp(-E/\mathrm{R}T)$, an increase in k_i can be obtained by either increasing the pre-exponential factor, A (physical promotion), or by decreasing the activation energy, E (chemical promotion).

6.2 Experimental

For the preparation of particles of iron oxide, three methods were used:

1. As a control, the technique given in Chapter 2, section 2.2 was followed. Water was sprayed on to Fe_2O_3 powder (< 5 μm, Sigma-Aldrich) with a purity $>$ 99+ wt. % to form agglomerates. The resulting mixture was mechanically stirred both during and after spraying, and then the granules were sieved to the desired size fraction of +300,-425μm. These particles were then sintered in an oven at 1173 K for 3 h, cooled in air and then re-sieved to +300,-425μm.
2. For the addition of promoter, 5 ml of a 0.05 M solution based on the promoter cation was added to 2 g of Fe_2O_3 powder in a beaker, stirred vigorously and placed in an oven

Table 6.1: Method of preparation, promoter, molar loading (x_m), Fe_2O_3 precursor, total calcining time and measured BET surface area for select samples with diameter +300,-425 μm prior to experiments. The figure number corresponding to the experiment in which each sample was used is listed.

Experimental Method	Particle Preparation			Calcining Time (h)	BET (m^2/g)	Figs.
	Cation	x_m	Fe_2O_3 Precursor			
(i)	unmodified	0.0	particle	3 h	1.2	6.1
(ii)	unmodified	0.0	powder	3 h	1.2	6.1
(ii)	with Ce	0.01	powder	3 h	2.8	6.2
(iii)	with Ce	0.01	particle	6 h	1.3	6.3

at 353 K until dry. The powder was then sintered at 1173 K for 3 h, cooled in air and sieved to +300,-425μm.

3. To simulate the addition of promoter to a naturally-occurring ore, appropriate volumes of a 0.05 M solution based on the promoter cation were added to a beaker containing 2 g of sintered Fe_2O_3 particles prepared following method (1) above. After drying in an oven at 353 K, the resulting particles were sintered at 1173K for 3 h, cooled in air and sieved to +300,-425μm.

The precursors for the promoter were $Ce(NO_3)_3 \cdot 6H_2O$ (Acros Organics; > 99.5 wt. %), $PtCl_2$ (Acros Organics; 73 wt. % Pt), $Ni(NO_3)_2{\cdot}6H_2O$ (Fisher; > 98 wt. %), $Cu(NO_3)_2{\cdot}2.5H_2O$ (Acros Organics; > 98 wt. %) and $ZrO(NO_3)_2 \cdot nH_2O$ (Fisher; 99.5 wt. % up to 4 wt. % Hf). While the use of Pt might be uneconomical in industrial applications, the focus of the study was to determine effective promoters and Pt has therefore been included. Dissolution of Pt was aided by the addition of 1 drop of 1 M of HCl. The loading of promoter using methods (2) and (3) is reported on a molar basis, and is defined identically to Chapter 3:

$$x_m = \frac{\text{mol}\, M}{\text{mol}\, M + \text{mol}\,\text{Fe}}, \tag{6.1}$$

where M is the promoter, *e.g.* Ce. No deposition of the precursor was observed on the beakers after drying indicating complete uptake by the iron oxide. As in Chapter 3 the molar loading was confirmed gravimetrically for particles prepared using method (3) with $x_m = 0.1$ and typically gave $x_m = 0.1 \pm 0.01$. Table 6.1 lists the method of preparation, promoter, molar loading, Fe_2O_3 precursor, total calcining time and BET surface area (Brunauer *et al.*, 1938) for selected particles, as well as the figure number corresponding to the experiment in which each was used.

Table 6.2: Redox cycling: gas mixtures (vol. %), flowrates (m^3/s) as measured at 298 K and 10^5 Pa, and corresponding flow durations (s) for experiments. The total cycle time was 600 s.

	purge	reduction	purge	steam oxidation	Figs.
time (s)	0-120	120-360	360-420	420-600	
flow (m^3/s)	3.33×10^{-5}	3.33×10^{-5}	3.33×10^{-5}	3.33×10^{-5} N_2, 8.33×10^{-9} $H_2O_{(l)}$	
Fe_3O_4 - $Fe_{0.947}O$	N_2	8.9% CO/8.9% CO_2/82.2% N_2	N_2	25% steam/75% N_2	6.1-6.3

The experimental apparatus used to measure rates of reaction was identical to that described in Chapter 5. The temperature of the fluidised bed was maintained at 1023 K in all experiments, as measured by a type K thermocouple inside the bed. The mass of unmodified Fe_2O_3 and promoted Fe_2O_3 added to the bed was fixed at 0.3 g in all cases. The compositions and flowrates of the inlet gas are listed in Table 6.2. The composition of the effluent gas was measured using identical analysers in the same arrangement as in Chapter 5, section 5.2.

6.3 Results

The measured rate at $X = 0.3$ was used with Eq. (5.9) from Chapter 5:

$$\left.\begin{aligned} r' &= \frac{k}{\rho_{\mathrm{Fe_2O_3}}}\left(c_{\mathrm{CO,out}} - \frac{c_{\mathrm{CO_2,out}}}{K_p}\right) \\ \frac{1}{k} &= \frac{R}{3k_{\mathrm{g,CO}}} + \frac{1}{k_i\eta} + \frac{R}{3k_{\mathrm{g,CO_2}}K_p}, \end{aligned}\right\} \tag{6.2}$$

to determine k_i as follows. For an effectiveness factor $\eta = 1$ an initial estimate for k_i was obtained. This value of k_i was then used in Eq. (5.6) to calculate a new value of η. Equations (6.2) and (5.6) were then used iteratively until k_i and η converged. Typically, $\eta = 0.95$, $k_i = O(10^2)\ \mathrm{s}^{-1}$ and since $R = 181\ \mu\mathrm{m}$, $k_{\mathrm{g,CO}} = 0.6$ m/s and $k_{\mathrm{g,CO_2}} = 0.5$ m/s, Eq. (6.2) could be simplified to

$$k_i \approx \frac{r'\rho_{\mathrm{Fe_2O_3}}}{\left(c_{\mathrm{CO,out}} - \frac{c_{\mathrm{CO_2,out}}}{K_p}\right)}. \tag{6.3}$$

For the results reported here, the iterative method involving the effectiveness factor was always applied to obtain values for k_i, which typically agreed with those from Eq. (6.3) to within 20 %. The final conversion for all of the experiments presented in this Chapter was $X \approx 0.8$.

Figure 6.1 shows k_i for the reduction of Fe_3O_4 to $Fe_{0.947}O$ in a mixture of 8.9 vol. % CO, 8.9 vol. % CO_2, balance N_2 using an initial charge of 0.3 g of unmodified Fe_2O_3 at 1023 K and served as a control. Particles were prepared using either experimental method (1) or method

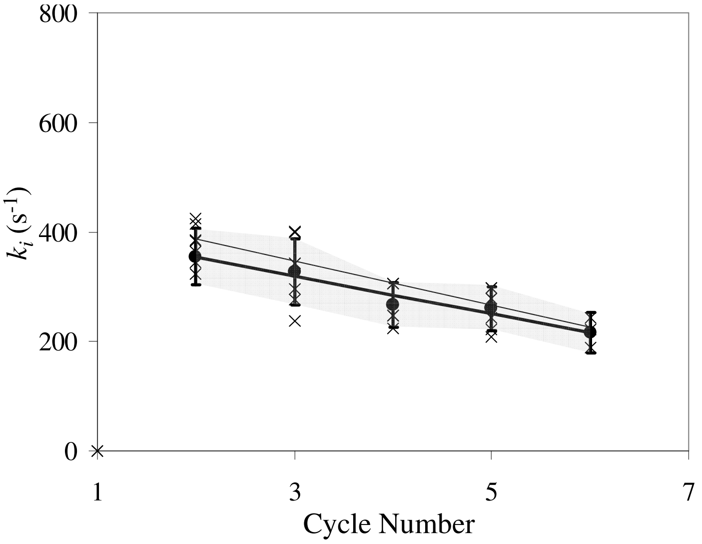

Figure 6.1: Intrinsic rate constant, k_i, against cycle number for the reduction of unmodified Fe_3O_4 to $Fe_{0.947}O$ in a mixture of 8.9 vol. % CO, 8.9 vol. % CO_2, balance N_2 at 1023 K. The initial charge was 0.3 g of unmodified Fe_2O_3 particles of diameter +300,-425 μm. Values of k_i for individual experiments (×) are shown. The lower line represents a least squares fit to the mean values (●), with error bars representing the error calculated from a two-sided t-test with a confidence interval of 95 %. The upper line represents values of k_i from Eq. (5.13) and shows good agreement.

(2), with water substituted for the aqueous solution of promoter, and gave reproducible results. Mean values from at least 5 experiments are shown by the black dots and the corresponding error is given by the error bars comprising the shaded region; the values of k_i are listed in Table 6.3. The error was determined by multiplying the t-statistic for a two-tailed t-test, with the number of degrees of freedom, equal to the sample size minus one, for a 95 % confidence interval by the standard deviation of the sample and dividing by the square root of the sample size. The lower black line in Fig. 6.1 indicates a least-squares fit to the mean values; the upper black line indicates the values of k_i reported for cycles 2 and 6 from Eq. (5.13) in Chapter 5 and is in good agreement.

Next, iron oxide powder which had been promoted with $x_\mathrm{m} = 0.01$ of Ce or Pt using method (2) was examined at identical conditions to those used for the experiments in Fig. 6.1. Figure 6.2 shows k_i as a function of cycle number. An improvement in k_i by a factor of at least 1.5× is evident for particles promoted with Pt. An even larger improvement of k_i by at least 2.1× is evident for promotion with Ce. To make a meaningful statistical comparison with unmodified iron oxide, two assumptions were made. First, it was assumed that the true mean of k_i for unmodified iron oxide could be approximated by the sample mean calculated from

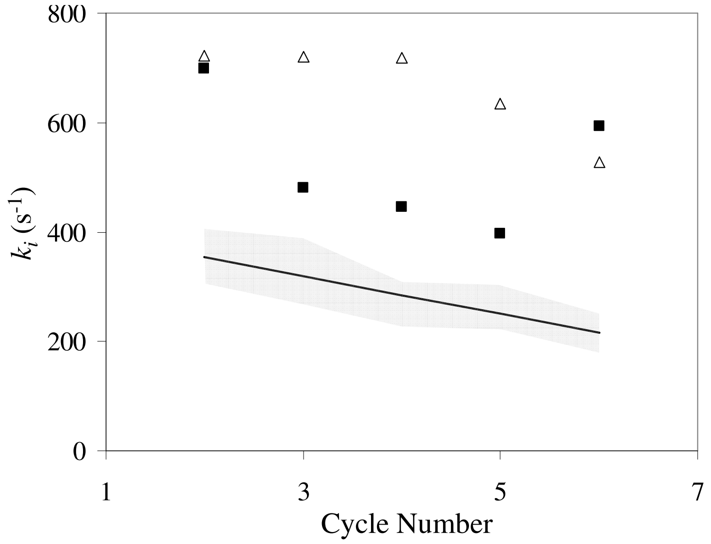

Figure 6.2: Intrinsic rate constant, k_i, against cycle number for the reduction of promoted Fe_3O_4 to $Fe_{0.947}O$ in a mixture of 8.9 vol. % CO, 8.9 vol. % CO_2, balance N_2 at 1023 K. The initial charge was 0.3 g of particles of diameter +300,-425 μm prepared by promoting Fe_2O_3 powder with x_m = 0.01 Ce (△) or x_m = 0.01 Pt (■). The black line represents the mean k_i for unmodified iron oxide and was taken from Fig. 6.1; promotion clearly increases k_i.

Fig. 6.1. Second, it was assumed that the k_i from a sample of iron oxide without an effective promoter has an equal probability, 1/2, of lying above and below the mean k_i for unmodified iron oxide. Statistical significance was then determined using a Bernoulli or binomial probability, calculated by

$$P_b = \binom{n_t}{n_s}\left(\frac{1}{2}\right)^{n_t}, \tag{6.4}$$

where n_t is the number of trials and n_s is the number of successes, *i.e.* the number of times k_i for the sample was greater than k_i for the unmodified iron oxide. Table 6.3 lists k_i for various samples over 5 cycles and the corresponding probability. Thus from Table 6.3 the addition of a small quantity, x_m = 0.01, of Ce or Pt promoter to the iron oxide powder prior to sintering can lead to a statistically significant increase in k_i.

For the proposed process involving the production of H_2 with simultaneous capture of CO_2 to be implemented on an industrial scale, naturally-occurring sponge iron would most likely be chosen as the starting iron oxide. It would therefore be invaluable to be able to increase the rate of reaction of a bulk particle of iron oxide by the addition of promoter. To simulate the addition of a promoter to porous sponge iron, sintered particles of Fe_2O_3 identical to those used for experiments in Fig. 6.1 were impregnated with aqueous solutions of various promoters, as outlined under method (3) in the experimental section. Figure 6.3 shows k_i as a function of

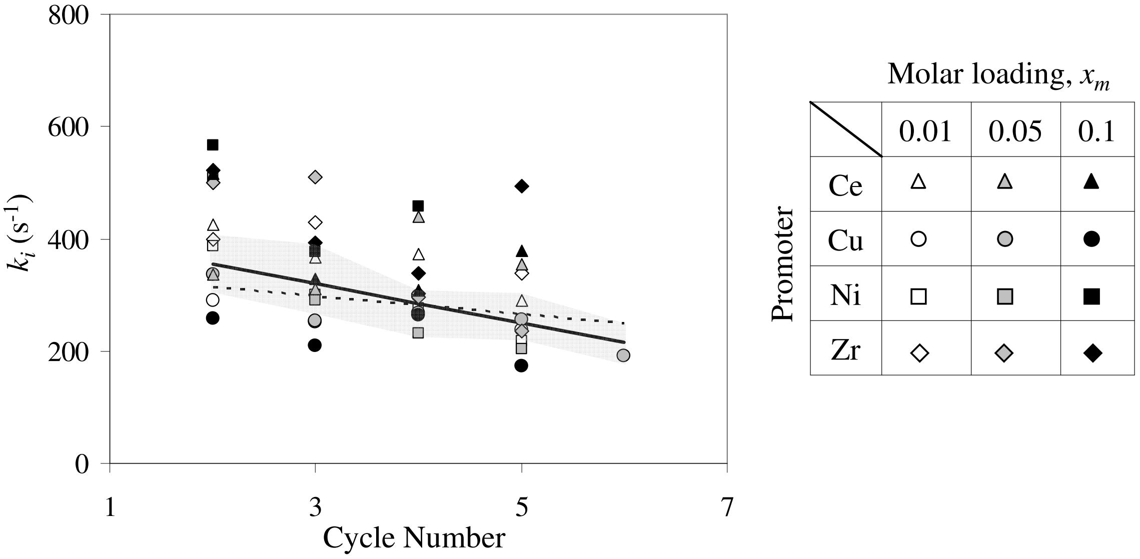

Figure 6.3: Intrinsic rate constant, k_i, against cycle number for the reduction of promoted Fe_3O_4 to $Fe_{0.947}O$ in a mixture of 8.9 vol. % CO, 8.9 vol. % CO_2, balance N_2 at 1023 K. The initial charge was 0.3 g of particles of diameter +300,-425 μm prepared by promoting calcined Fe_2O_3 particles with $x_\mathrm{m} = 0.01, 0.05$ and 0.1 Ce, Cu, Ni and Zr. The black line represents the mean k_i for unmodified iron oxide was taken from Fig. 6.1.

cycle number for particles prepared with $x_\mathrm{m} = 0.01, 0.05$ and 0.1 of Ce, Ni, Cu and Zr. The dashed line indicates k_i for particles of pure iron oxide mixed with water and was used as a control. The solid black line is identical to that in Fig. 6.1 for unmodified particles which had been sintered at 1173 K for 3 h and is in good agreement with the unmodified control particles which had been sintered for a total of 6 h. Most metal additives, with the exception of Cu, seem to increase k_i at some loading. However, from Fig. 6.1, no clear correlation between metal loading, x_m, and k_i exists. Interestingly, particles with $x_\mathrm{m} = 0.01$ Ce do not display values of k_i near those obtained for impregnated Fe_2O_3 powder, *c.f.* Figs. 6.2 and 6.3. It appears therefore that while Ce can promote reduction by increasing k_i, the method by which it is added is critical and merits further investigation.

6.4 Discussion

Overall, the results in Figs. 6.1 and 6.2 showed that the addition of a small quantity, $x_\mathrm{m} = 0.01$, of Ce could increase the intrinsic rate constant, k_i, by 2.1×. Comparing the surface area of the iron oxide particles with Ce added to that for unmodified iron from Table 6.1 gave 2.8 m^2/g compared to 1.2 m^2/g, respectively. Thus the increase in k_i is most likely a result of the increase in surface area, since (2.8 m^2/g)/(1.2 m^2/g) = 2.3. That the rate increases proportionally to

Table 6.3: Measured intrinsic rate constant, k_i, for various samples over cycles 2-6. The figure number for the corresponding k_i is listed.

Fe / promoter	cycle loading	2 k_i	3 k_i	4 k_i	5 k_i	6 k_i	Bernoulli probability, P_b	Fig.
Fe	mean	355	327	267	261	216		6.1
Fe	error	±51	±60	±41	±40	±37		6.1
Ce	0.01	723	720	719	635	528	**0.031**	6.2
Pt	0.01	699	481	445	397	593	**0.031**	6.2
Cu	0.01	289	252	299	238		0.250	6.3
Cu	0.05	337	255	268	255	192	0.156	6.3
Cu	0.1	257	210	264	173		**0.063**	6.3
Ni	0.01	386	300	277	218		0.375	6.3
Ni	0.05	509	290	233	204		0.250	6.3
Ni	0.1	566	377	458			0.125	6.3
Zr	0.01	398	429	303	339		**0.063**	6.3
Zr	0.05	500	510	295	235		0.125	6.3
Zr	0.1	522	392	338	493		**0.063**	6.3
Ce	0.01	425	366	373	290		**0.063**	6.3
Ce	0.05	337	311	439	354		0.375	6.3
Ce	0.1	516	329	308	379		**0.063**	6.3

the surface area lends further credence to the rate-limiting mechanism proposed in Chapter 5, *viz.*:

$$CO_{(g)} + O_{ad} \rightleftarrows CO_{2(g)}. \tag{6.5}$$

Thus, expressing $k_i = k_s S_0$, where k_i is the rate calculated in Chapters 5 and 6, k_s is the intrinsic rate for the surface reaction (6.5) in (m/s), and S_0 is the surface area *per* unit volume (m^2/m^3), would give a single intrinsic rate constant k_s independent of surface area. The ability of Ce to maintain surface area in mixed oxides of Fe and Ce, is well established in catalysis literature (Perez-Alonso *et al.*, 2006). Since k_i was only increased in particles where Ce was added prior to sintering, *c.f.* Figs. 6.2 and 6.3, the effect of Ce as a physical promoter seems certain.

The objective of the current preliminary experiments was to identify a promoter which could increase the rate of reduction of Fe_3O_4 to $Fe_{0.947}O$ by increasing the rate constant, k_i. This objective was achieved for the addition of Ce. It appears that Ce acts as a physical promoter by maintaining the surface area, rather than as a chemical promoter. Further experiments which study reduction at different temperatures, *e.g.* using temperature programmed reduction (TPR) or fluidised bed experiments at two different temperatures, could be used to determine activation energies and clarify whether Ce promotes chemically. For reduction of a packed bed of Fe_2O_3, an increase in the intrinsic rate constant for the reduction of Fe_3O_4 to $Fe_{0.947}O$

by ~ 2× would result in a front between $Fe_{0.947}O$ and Fe_3O_4 that is 1.7× as sharp, as shown in Chapter 5, Fig. 5.18.

6.5 Conclusions

The addition of a promoter to iron oxide was shown to increase the rate of reduction of Fe_3O_4 to $Fe_{0.947}O$ in a mixture of CO, CO_2 and N_2 over 6 cycles at 1023 K. The conclusions were as follows:

- Addition of a promoter, $x_\mathrm{m} = 0.01$ of Ce, to iron oxide powder which was subsequently sintered to form particles with $d_\mathrm{p} = +300, -425\ \mu\mathrm{m}$, led to an increase in the rate constant, k_i, for the reduction of Fe_3O_4 to $Fe_{0.947}O$ by 2.1×.
- This increase in k_i seems to be a result of the ability of Ce to maintain the active surface area of the particle, *i.e.* Ce acts as a physical promoter.

Chapter 7

Production of hydrogen from solid fuels

7.1 Introduction

The previous Chapters have demonstrated that the production of hydrogen from mixtures of gases from cylinders is feasible. However, for the production of hydrogen using the redox reactions of iron oxide to be implemented on an industrial scale, it must be demonstrated that separate streams of hydrogen and carbon dioxide of high purity can be produced from a solid fuel. A proof-of-concept for the steam-iron process is not new. The steam-iron process has long been known to produce high purity hydrogen from a carbon feedstock, with 99 vol. % H_2 achieved in 1920 (Taylor, 1921). Current circumstances - the increasing need to incorporate carbon capture technologies and the requirement of low temperature polymeric membrane fuel cells for H_2 uncontaminated with CO - provide a setting which merits a more fundamental analysis of the process. Particularly, the purity of the H_2 at a ppmv level and the capture of CO_2 provide new perspectives on the technology overlooked in past literature.

In Chapter 1 it was shown that large reserves of coal are well distributed amongst Western countries. The composition of coal is generally presented as a proximate analysis, which parallels carbonisation, and an ultimate analysis, which gives the elemental composition of the coal. Carbonisation is the extent to which the original plant mass has been converted by geological action to pure carbon, and is used to determine the rank of a coal according to the following categories on an air dried, mineral matter free basis (Laurendeau, 1978): lignite (65-72% C) < sub-bituminous (72-80% C) < bituminous (75-90% C) < anthracite (90-95% C).

The objectives of this study are (i) to demonstrate that hydrogen can be produced from three representative coals - a German lignite, a UK sub-bituminous coal, and a Russian sub-bituminous coal, (ii) to demonstrate that high conversions of the iron oxide over multiple cycles can be achieved, (iii) to determine whether other constituents, not present in cylinder gases, *e.g.* SO_2 and CH_4, affect the production of hydrogen, (iv) to demonstrate that the H_2 is of high purity and (v) to discuss the process in the light of industrial application.

7.2 Experimental

The experimental apparatus consisted of a gasifier in series with a packed bed of iron oxide and gas analysers, as shown in Fig. 7.1. The gasifier was an externally-heated fluidised bed reactor of 316 stainless steel with an internal diameter of 76 mm, provided with a perforated plate as the distributor containing 37 holes, each 0.4 mm in diameter. At maximum heating power, the furnace supplied a total power output of $\sim$ 13 kW; to heat the bed from 298 K to 1123 K took approximately 1.5 h. At typical fluidising conditions (1 m^3/h of N_2 and 0.07 m^3/h of CO_2 as measured at 293 K and 10^5 Pa) with the bed maintained at 1123 K, the pressure drop across the distributor was at least 0.3 bar, considerably in excess of the pressure drop across the material fluidised (typically $\sim$ 1.2 kg carrier solids) given by the mass multiplied by the acceleration due to gravity and divided by the nominal cross-sectional area, *viz.* amounting to 0.025 bar, hence ensuring uniform fluidisation. The temperature of the bed was measured by a K-type thermocouple inserted from the top of the bed so that the tip was about 100 mm above the distributor. All flowrates to the fluidised bed were measured using calibrated rotameters.

The stainless steel packed bed reactor was independent of the gasifier and identical to that in Chapter 2, shown in Fig. 2.1. The particles of iron oxide were prepared, as in Chapter 2, and had a sieve size of +425, −600 μm. The packed bed was loaded by placing 3 g of Fe_2O_3 particles between two layers of inert Al_2O_3 each $\sim$ 7 g with a sieve size of +1.4, −1.7 mm. The reactor was operated in a downflow arrangement; the temperature was monitored by a type K thermocouple (O.D. 1.5 mm) placed within the layer of iron oxide.

The proximate and ultimate analysis for the three representative coals - a lignite from Hambach, Germany (GER-lig), a sub-bituminous coal from Littleton Colliery, UK (UK-sub) and a Russian sub-bituminous coal from Talkdinskaya Fuel and Energy Company (RUS-sub) - are listed in Table 7.1. The German lignite and Russian sub-bituminous coal were supplied by RWE npower Swindon, UK; the UK sub-bituminous coal was supplied by the former Coal Research Establishment Stoke Orchard, UK. The fuels were crushed and sieved to +1.0, −2.4 mm and kept in sealed containers prior to experiments.

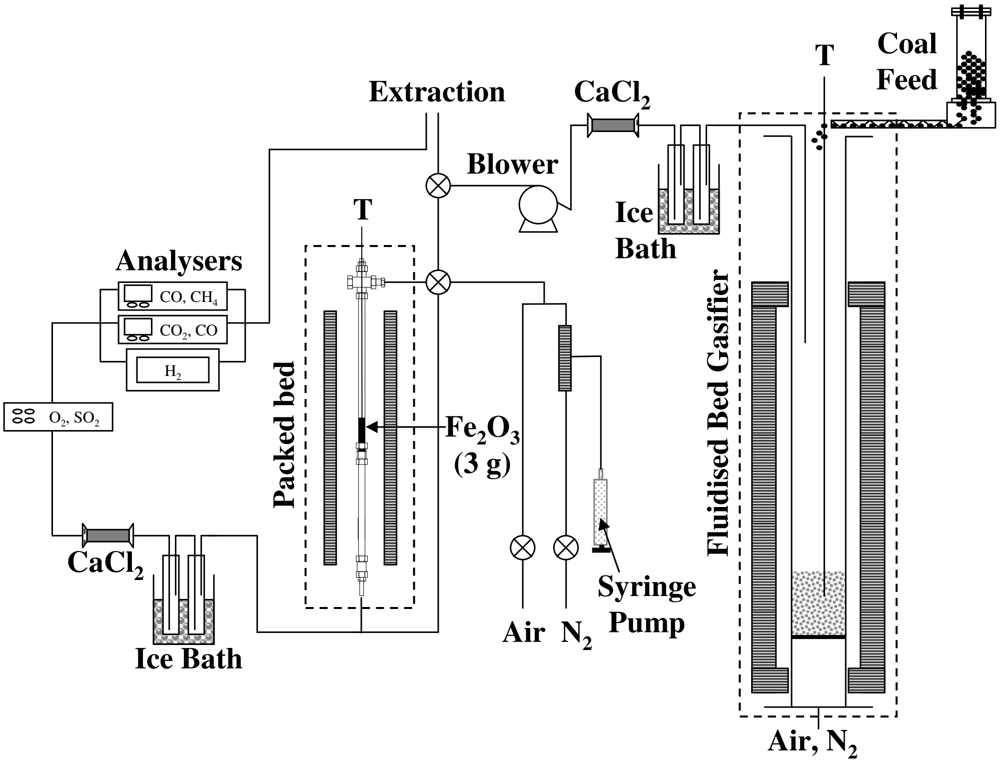

Figure 7.1: Schematic diagram of the experimental apparatus and sampling lines.

Table 7.1: Proximate (air dried basis) and ultimate (air dried, mineral matter free basis) analyses for the three coals.

Sample	Proximate analysis, wt. %				Ultimate analysis, wt. %				
	Moisture	Volatile Matter	Fixed Carbon	Ash	C	H	O	N	S
GER-lig	18.0	41.0	37.5	3.5	69.6	5.5	23.4	0.9	0.3
UK-sub	7.1	33.7	54.9	4.3	80.7	5.1	8.9	1.7	1.1
RUS-sub	9.2	32.7	44.7	13.4	82.4	6.1	8.2	2.5	0.9

Fuel was added to the top of the gasifier using a screwfeeder. The feeder consisted of an aluminium screw (O.D. 9 mm, pitch 35 mm, width of thread 2 mm, length 250 mm) protruding into the bottom of the hopper and was connected *via* a drive shaft and ball bearings to an aluminium block. A stepper motor (McLennan, 34HSX-208) controlled the speed of feeding by altering the rotation of the screw in the range 0-25 rot/s. Finding a satisfactory feeder design was not trivial: a motor with sufficient torque to prevent jamming of the screw was necessary; vibrations from the large motor also prevented bridging of the coal particles in the neck of the hopper.

The sampling line was arranged as in Fig. 7.1. Moisture and substances which were not gaseous at 273 K (*e.g.* tars) were removed from the effluent gas by two impinger tubes immersed in an ice bath, followed by a tube with granulated $CaCl_2$ prior to entering the packed bed. Using solenoid valves (Burkert), the effluent gas from the gasifier could either be (i) fed into the packed bed reactor (ii) bypassed to the extraction vent or (iii) fed into the sampling line following the packed bed for analysis in the gas analysers. Owing to the collection of ash, the blower required cleaning after most experiments.

The composition of the effluent gas from either the gasifier or the packed bed was determined using (i) nondispersive infrared analysers measuring [CO] and [CO_2] in the range 0-20 vol. % (ABB, EasyLine), (ii) a nondispersive infrared analyser measuring [CH_4] in the range 0-30 vol. % (ABB, EasyLine), (iii) a nondispersive infrared analyser measuring [SO_2] in the range 0-10000 ppmv (ABB, EL3020), (iv) a nondispersive infrared analyser measuring [CO] in the range 0-2000 ppmv (ABB, EasyLine), (v) a thermal conductivity analyser measuring [H_2] in the range 0-30 vol. % (ABB, Caldos27) and (vi) a paramagnetic analyser measuring O_2 in the range 0-100 vol. % (ABB, EL3020) giving a total of four analysers. Cylinders of pure gases (BOC) with compositions of (i) 10 vol. % CO, balance N_2 and 10 vol. % CO_2, balance N_2, (ii) 20 vol. % CH_4, balance N_2, (iii) 1000 ppmv SO_2, balance N_2, (iv) 1 vol. % CO, balance N_2, (v) 10 vol. % H_2, balance N_2 and (vi) laboratory air were used for calibration. The total flow through the packed bed was 0.06 – 0.12 m^3/h as measured at 298 K and 10^5 Pa.

Cycling of the iron oxide proceeded in three stages, summarised by the following reactions:

$$\mathrm{Fe_2O_3} + \mathrm{CO} \rightleftarrows 2\,\mathrm{FeO} + \mathrm{CO_2} \qquad \Delta H^\circ_{1123\,\mathrm{K}} = 0.3\ \mathrm{kJ/mol} \tag{7.1}$$

$$3\,\mathrm{FeO} + \mathrm{H_2O_{(g)}} \rightleftarrows \mathrm{Fe_3O_4} + \mathrm{H_2} \qquad \Delta H^\circ_{1123\,\mathrm{K}} = -61\ \mathrm{kJ/mol} \tag{7.2}$$

$$2\,\mathrm{Fe_3O_4} + \frac{1}{2}\mathrm{O_2} \rightleftarrows 3\,\mathrm{Fe_2O_3}. \qquad \Delta H^\circ_{1123\,\mathrm{K}} = -238\ \mathrm{kJ/mol} \tag{7.3}$$

In reaction (7.1), CO from the gasification of coal with steam was used to reduce Fe_2O_3. After the partial reduction of the iron oxide in the bed, passing steam through the reactor generated hydrogen and reoxidised the reduced iron oxide to Fe_3O_4 in reaction (7.2). Complete reoxidation to Fe_2O_3 in air produced a stream of N_2 with residual O_2 *via* reaction (7.3). Once the entire packed bed had been regenerated to Fe_2O_3, the cycle could begin anew at step 1.

In a typical experiment, the gasifier and packed bed containing the iron oxide were initially treated as independent units and heated to operating temperatures of 1123 K and 1073 K, respectively, under the flow of air. Next, feeding of the coal into the gasifier was commenced for ~ 40 min until a stable effluent composition - a mixture of CO, CO_2, H_2, CH_4 and N_2 after drying - was achieved. For sufficiently high partial pressures of CO, H_2 and CH_4, this mixture was capable of reducing the Fe_2O_3 to Fe; generally, reduction of the Fe_2O_3 only proceeded to FeO by limiting the reduction time. Oxidation occurred in a mixture of 30 vol. % steam, balance N_2, followed by air mixed with N_2 to give ~ 4 vol. % O_2, balance N_2. The reactor was purged with N_2 for 120 s between each reduction and oxidation step.

7.3 Results

Figure 7.2 shows the mole fractions of CO, CO_2, H_2, CH_4 and O_2 in the effluent gas from the packed bed as a function of time over three cycles for experiments involving (a) the German lignite, (b) the UK sub-bituminous coal and (c) the Russian sub-bituminous coal. All of the entering CO and H_2 is converted to CO_2 and H_2O, respectively, at the start of each reduction cycle. For carbon capture this period is paramount and could be extended by increasing the residence time in the bed, through *e.g.* decreasing the flowrate of the gas or increasing the amount of iron oxide in the bed, as was demonstrated in Fig. 2.2 of Chapter 2. The high flowrates used in the current study of 0.06-0.12 m^3/h as measured at 298 K and 10^5 Pa gave a residence time within the iron oxide of ~ 0.03 s and were chosen to increase the number of cycles achievable in a given time. As reduction of the iron oxide progresses, the mole fractions in the effluent gas approach those at the exit of the gasifier, which can be approximated for Fig. 7.2(a) to be [5.4, 5.5, 1.4, 0.2] mol. % for CO, CO_2, H_2 and CH_4, respectively. Since oxidation of 1 mole of CO in the presence of iron oxide produces 1 mole of CO_2, the CO and CO_2 mole fractions should be complementary and Fig. 7.2 confirms that this is indeed the case. Next, oxidation in steam generated hydrogen of high purity. Finally, air was used to oxidise the Fe_3O_4 to Fe_2O_3 before beginning a new cycle.

Figure 7.2(a) shows that gasification of the German lignite produced no CH_4 and a lower fraction of H_2 compared to that of either the Russian or the UK sub-bituminous coals. Thus, longer cycles of reduction were required. For reduction using the gasification of the UK sub-bituminous coal, steam was inadvertently added to the reduction gas, giving approximately 20 mol. % of the total mixture with flowrate of 0.08 m^3/h as measured at 298 K and 10^5 Pa, prior to its passing through the packed bed. The approximate mixture fractions from the gasifier on a dry basis were [5.2, 4.8, 2.6, 0.7] mol. % for CO, CO_2, H_2 and CH_4, respectively, as shown in Fig. 7.2(b). For reduction using the gasification of the Russian sub-bituminous coal, the average mixture fractions from the gasifier were [4.7, 5.3, 3.0, 1.2] mol. % for CO, CO_2, H_2 and CH_4, respectively. The higher values of H_2 in Fig. 7.2(c) compared to those in Figs. 7.2(a)

(a) GER-lig

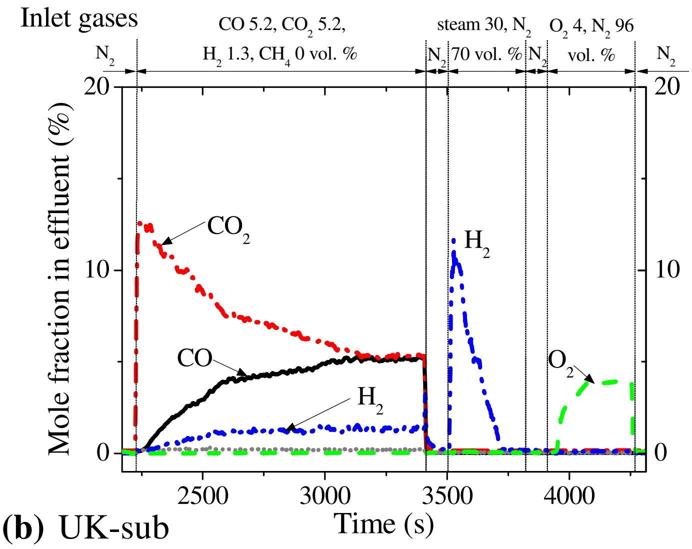

(b) UK-sub

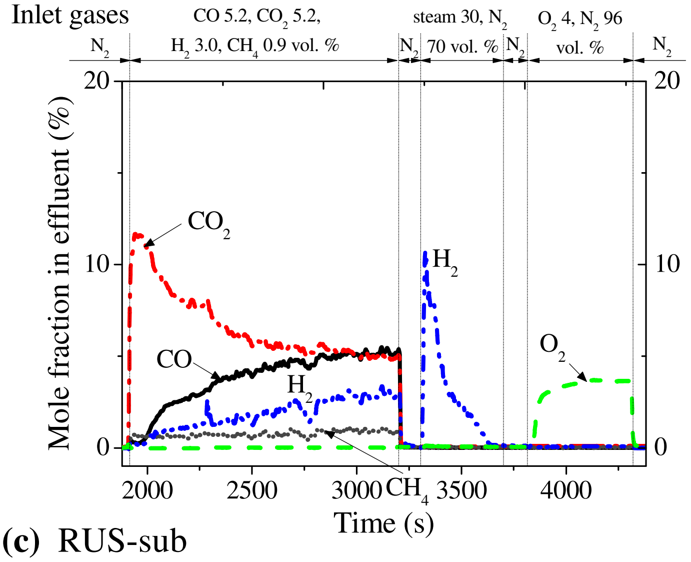

(c) RUS-sub

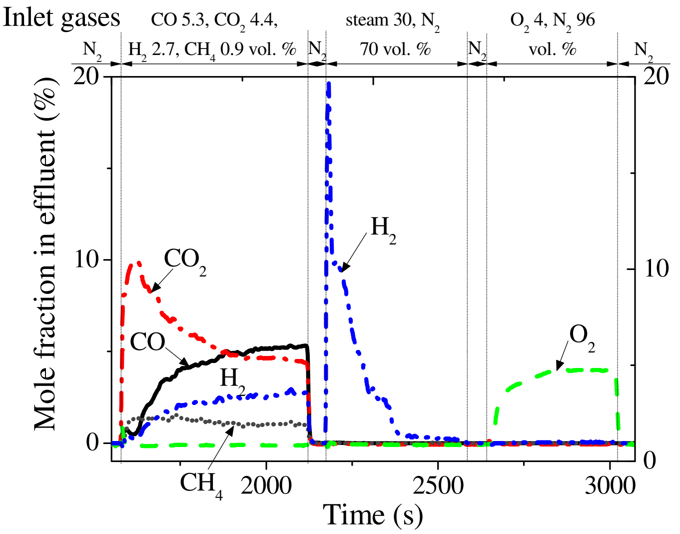

Figure 7.2: Mole fractions of CO, CO_2, H_2, CH_4 and O_2 in the effluent gas from the packed bed operated at 1123 K with an initial charge of 3 g of Fe_2O_3 for cycle 2. The reducing gas was produced from the gasification of (a) a German lignite, (b) a UK sub-bituminous coal, and (c) a Russian sub-bituminous coal. Oxidation occurred in a mixture of steam and N_2, followed by a mixture of air and N_2.

or (b) at the very start of oxidation are not indicative of higher quantities of total H_2 produced, but rather were caused by the sudden inflow of steam at the switch of the solenoid valve. In Fig. 7.2(c), the portion of the line above 10 mol. % consist of fewer than 10 points comprising only 10 s since sampling occurred at 1 Hz. A mass balance for the H_2 produced was calculated and is deferred until the discussion of Fig. 7.4. Reduction times varied from 500 s for cycle 1 in Fig. 7.2(c) to 1800 s for cycle 3 in Fig. 7.2(b); the time for oxidation with steam was constant at $\sim$ 500 s; the time for oxidation with air varied between 300 s in (a) and (c) to a maximum of 500 s for cycles 2 and 3 in (b). The objective in all cases was to reach steady state in each stage for each cycle prior to switching the inlet gas.

Figure 7.3 shows the mole fractions of H_2 and O_2 (mol %) and CO and SO_2 (ppmv) in the effluent against time for the oxidation period corresponding to Fig. 7.2. During oxidation with air, it is clear from Fig. 7.3(c) that CO and SO_2 are released. Comparing the rise in CO and O_2 in Fig. 7.3(c) at $t = 2650$ s shows that all of the incoming O_2 is consumed for a period at the start of oxidation giving a stream of pure N_2 with [CO] $<$ 10 ppmv. Also, the rise in SO_2 is concurrent with the rise in O_2, indicating that deposited sulphurous species are released as SO_2 in a strongly oxidising environment. Comparing SO_2 traces across experiments demonstrates that SO_2 is only found during oxidation with air for experiments with the Russian and UK sub-bituminous fuels. The maximum SO_2 value was 22 and 15 ppmv in each case, respectively. No SO_2 was observed for experiments with the German lignite coal. From Table 7.1, the UK and Russian sub-bituminous fuels have the highest sulphur contents of 1.1 and 0.9 wt. %, respectively. Noticeably, no SO_2 was detected during oxidation with steam indicating that the H_2 was without SO_2 contamination. Calculations based on the feed rate of coal and the flowrates of gas to the gasifier and packed bed indicated that the SO_2 released during oxidation with air is $<$ 0.5 mol. % of the total sulphur fed during reduction, *i.e.* the adsorption of sulphurous species or the formation of FeS during reduction is negligible. In Fig. 7.3, comparing the CO traces during oxidation with steam shows that [CO] $\lesssim$ 50 ppmv for all experiments except those with the Russian sub-bituminous fuel, where [CO] reached a maximum of 215 ppmv before dropping below 50 ppmv. The CO trace is most likely a result of residual carbon, deposited during reduction, being oxidised with steam.

Figure 7.4 shows the total quantity of H_2 produced in each of the 5 cycles performed. The dashed horizontal line at 12.5 mmol equals the quantity of H_2 expected from an initial charge of 3 g of Fe_2O_3, which had been reduced to FeO. For reduction to Fe, the expected quantity of H_2 is 4× the previous value, *i.e.* 50.0 mmol. It can be seen from Fig. 7.4 that in some cases

(a) GER-lig

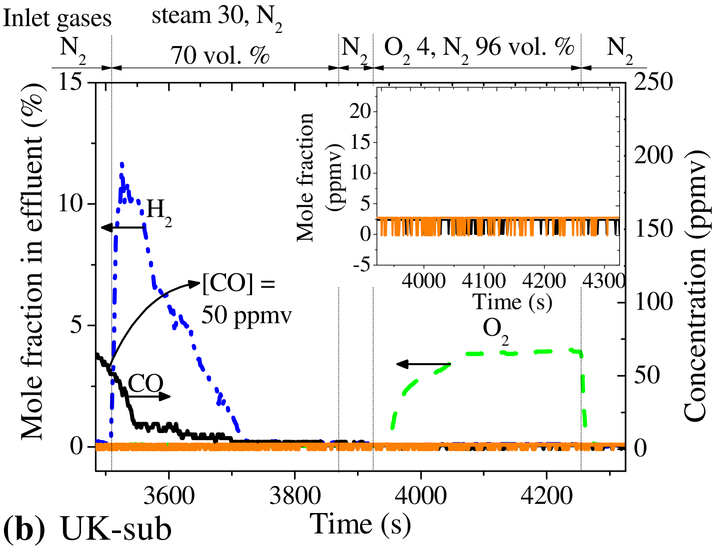

(b) UK-sub

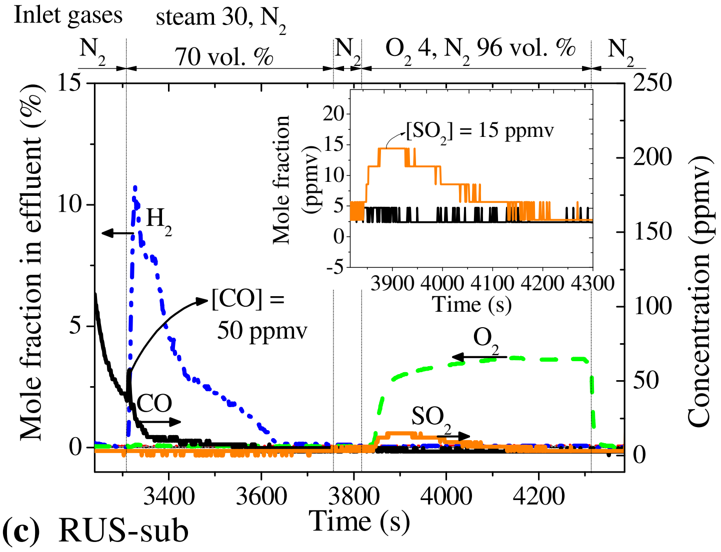

(c) RUS-sub

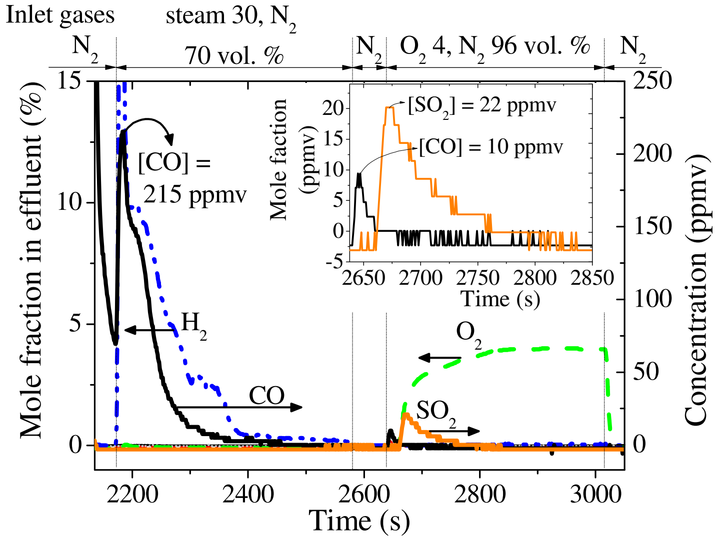

Figure 7.3: Mole fractions of H_2 and O_2 (mol. %) and of CO and SO_2 (ppmv) in the effluent gas from the packed bed operated at 1123 K with an initial charge of 3 g of Fe_2O_3 for cycle 2. The reducing gas was produced from the gasification of (a) a German lignite, (b) a UK sub-bituminous coal and (c) a Russian sub-bituminous coal. The H_2 is not contaminated by SO_2; except for (c) the H_2 has CO $\lesssim$ 50 ppmv.

reduction beyond FeO to a mixture of Fe and FeO occurred, as indicated by points lying above the dashed line. Nevertheless, stable quantities of H_2 were achieved over 5 cycles in all cases.

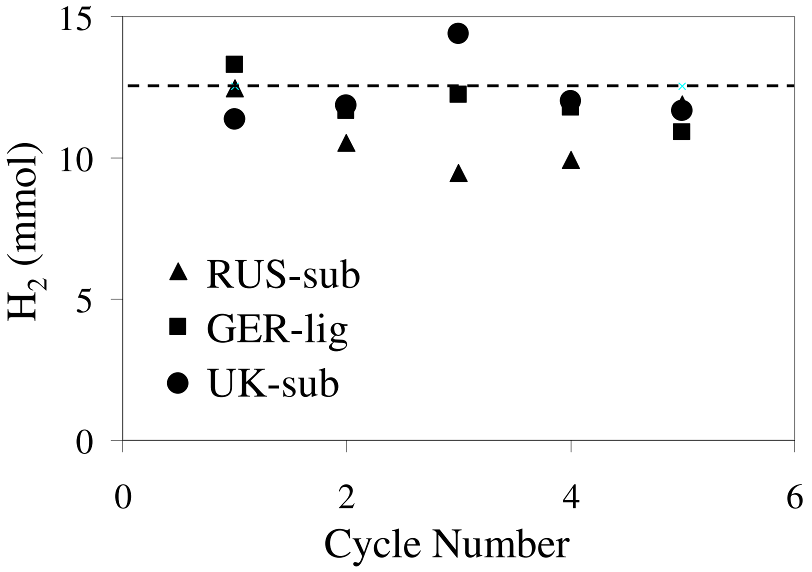

Figure 7.4: Total quantity of H_2 produced over 5 cycles using an initial charge of 3 g of Fe_2O_3 reduced with gas from the gasification of a German lignite, a UK sub-bituminous coal or a Russian sub-bituminous coal and oxidised in a mixture of steam and N_2, followed by a mixture of air and N_2 at 1123 K.

7.4 Discussion

The effluent profile per unit mass carrier for the reduction of a 3 g charge of Fe_2O_3 with synthesis gas is similar to that obtained for the reduction of a 1 g charge of Fe_2O_3 in a mixture of N_2, CO and CO_2 from cylinder gases, *c.f.* Figs. 7.2 and 2.3. The constancy of yields of H_2, *c.f.* Figs. 7.4 and 2.5(b), also suggest that simulated syngas, produced by mixing pure gases from cylinders, provides a good approximation for true syngas produced from the gasification of coal.

If the deposition of solid carbon during reduction of the iron oxide can be avoided, the purity of the H_2 upon subsequent oxidation will improve. One method of avoiding the deposition of carbon is to introduce steam with the reducing gas (Ishida *et al.*, 1998). Figure 7.3 showed that for experiments with a fuel of high moisture content (Fig. 7.3(a)) or when steam was co-fed with the reducing gas (Fig. 7.3(b)), the resulting H_2 had a contamination of [CO] $\lesssim$ 50 ppmv. However, even experiments with the Russian sub-bituminous fuel gave H_2 with [CO] $\lesssim$ 200 ppmv, a significant improvement in purity compared to conventional methods such as the steam reforming of methane. The high moisture content of the German lignite might also explain the lower levels of CH_4 and H_2 in the gasifier outlet compared to the effluent gas from the gasification of the Russian and UK sub-bituminous coals, as seen in Fig. 7.2. Steam could also prevent the deposition of sulphurous species during reduction and could explain why the experiment with the UK sub-bituminous coal (1.1 wt. % S), where steam was co-fed with the reducing gas, produced a lower total quantity of SO_2 compared to that with the Russian sub-bituminous coal (0.9 wt. % S). From thermodynamics (McBride *et al.*, 2002) at 1073 K and 10^5 Pa, the formation of FeS is inhibited by steam, which permits gaseous species H_2S and SO_2 to be formed instead. Importantly, since SO_2 was only observed during oxidation with air, and was not released during oxidation with steam; the H_2 was free from SO_2. Finally, based on the SO_2 released during oxidation with air, it appears that a small fraction, < 0.5 mol. %, of the sulphur entering the bed during reduction was fixed. Quantifying the contamination of the H_2 produced by H_2S was, however, outside the scope of the present study.

Previous experiments in Chapters 2, 3 and 4 demonstrated that reduction to Fe resulted in a decrease in the quantity of H_2 produced with cycle number, with almost no H_2 being produced after 10 cycles. In some cases here, however, reduction proceeds beyond FeO so that the metal is present as a mixture of Fe and FeO, as shown in Fig. 7.4 by points above the dashed horizontal line. The quantity of H_2 produced, however, shows no indication of a decrease after 5 cycles. Investigation of how much of the iron oxide can be reduced to Fe before the detrimental effects associated with complete reduction to Fe are observed would therefore be interesting for further research.

In the original steam-iron process, oxidation of the metal oxide to Fe_2O_3 in air during each cycle was not proposed by Messerschmitt (1910) and was only later incorporated by Lane (1913). Currently other groups, *e.g.* Galvita *et al.* (2008a) and Li *et al.* (2009), do not include oxidation with air in their research. From Fig. 7.3(a) at the start of oxidation with air, all of the incoming O_2 is consumed and a stream of pure N_2 with $[CO] \lesssim 10$ ppmv is produced. This gas could in theory be captured and used for the N_2 purge between reduction and oxidation steps. Figure 7.3 also showed that the introduction of air permits accumulated carbonaceous and sulphurous species to be eliminated from the surface of the metal oxide. Since oxidation in air also provides useful heat, *c.f.* the enthalpy for reaction (7.3), it is recommended to incorporate this step into the overall reaction scheme.

7.5 Conclusions

The production of separate streams of pure H_2 and CO_2 from a solid fuel was demonstrated using the redox reactions (7.1)-(7.3) of iron oxide in a packed bed at 1073 K. The conclusions were as follows:

- During the initial stage of reduction, CO_2 is produced with little H_2 or CO slip which would be suitable for sequestration.
- Pure H_2 with [CO] $\lesssim$ 50 ppmv can be obtained from low-rank coal.
- This H_2 is free from SO_2, since SO_2 was only released during oxidation with air.
- Contaminants found in syngas which are gaseous above 273 K apparently do not adversely affect the iron oxide material as stable quantities of pure H_2 were produced over 5 cycles.
- Since oxidation with air removes contaminants, *e.g.* sulphurous and carbonaceous species deposited during reduction, and generates useful heat and pure N_2 for purging, it should be included in the operating cycle.

Overall, it has been demonstrated that crude syngas produced by the gasification of low-rank coals can be upgraded to pure H_2, representing a substantial increase in calorific value, whilst capturing CO_2, a greenhouse gas.

Chapter 8

Development and validation of a lattice Boltzmann model

8.1 Introduction

A detailed model of the production of hydrogen in a packed bed requires the simultaneous solution of equations for the conservation of mass, momentum and energy. Historically, simple 1D advection-diffusion-reaction models have been applied to packed beds. Here, the bed is considered to be a pseudo-homogeneous medium and bulk parameters representing, *e.g.* average flow per unit cross-section or average rate of reaction per unit volume, are used. Integration of the descriptive partial differential equations is generally not feasible by analytical methods, so numerical integration using *e.g.* finite differences is employed. A 1D mass conservation model was presented for the reduction of iron oxide in Chapter 5. Two-dimensional models, accounting for axial and radial gradients, have also been developed (Froment, 1967).

To resolve fully the flow field, however, more detailed models are required. Table 8.1 lists a hierarchy of strategies for modelling fluid flows arranged by Knudsen number, Kn, a ratio of the mean free path of a molecule to the characteristic length scale. For $Kn < 0.01$, a fluid comprised of individual molecules can be treated as a continuum. Here, the frequency of contacts between molecules is significantly higher than that between molecules and physical boundaries and the Navier-Stokes equation can be applied. As the characteristic length decreases, the continuum assumption breaks down, and for $Kn > 1$, molecules must be treated as discrete entities.

The lattice Boltzmann method (LB) (Succi, 2001) is based on kinetic theory of gases and

Table 8.1: Hierarchy of modelling strategies for resolving fluid flow at different length scales.

Classification	**Fluid**	**Mathematics**	**Method (Abbreviation)**	**Length (m)**
macroscopic ($0 < Kn < 0.01$)	simplified	advection/dispersion Eq.	plug flow, packed bed reactors (PFR, PBR);	10-10^{-1}
	continuum	Euler Eqs.	computational fluid dynamics (CFD)	
	continuum	Navier-Stokes Eqs. (NS)	computational fluid dynamics (CFD)	$10^{-1} - 10^{-5}$
mesoscopic ($Kn < 0.1$)	continuum: atomic distribution functions	Boltzmann Eq.	lattice Boltzmann method (LB)	$10^{-3} - 10^{-6}$
transition ($0.1 < Kn < 10$)	atomic	Liouville Eq.	direct simulation Monte Carlo (DSMC)	$10^{-6} - 10^{-8}$
microscopic ($Kn > 1$)	atomic	streaming/collision rules Newton's law	lattice gas cellular automata (LGCA) molecular dynamics (MD)	$< 10^{-7}$

can be used to resolve fluid flow over a wide range of length scales as shown in Table 8.1. In packed beds at moderate fluid velocities, the LB method has proved to be effective in predicting fluid dynamic quantities such as velocity (Freund *et al.*, 2003; Sullivan *et al.*, 2007), pressure drop (Zeiser, 2007) and drag force (Yu *et al.*, 2003). The kinetic formulation of the LB method permits the incorporation of a wide range of physical phenomena such as multicomponent flows (Asinari, 2008; Flekkøy, 1993), particle laden flows (Ladd, 1994), bubbles (Inamuro *et al.*, 2004), surface wetting (Raiskinmäki *et al.*, 2000), flow at low Knudsen number (Toschi and Succi, 2005), turbulence (Teixeira, 1998), and compressible flows (Yu and Zhao, 2000; Asinari and Ohwada, 2009). Detailed comparison between experiment and LB results with reactive flows has received less attention and remains a promising area of research.

The lattice Boltzmann (LB) method has several advantages for modelling reactive fluid flow through porous media. Thus, (i) it is inherently discrete and all computations are local so that it can be implemented on several processors in parallel with little information exchange required at each time step. (ii) It uses linear advection and collision operators, but still recovers the incompressible Navier-Stokes equations in the low Mach number limit, thereby avoiding the computationally-difficult solution of either the Boltzmann or the Navier-Stokes equations. (iii) Advection is calculated in a discrete velocity space with arithmetic operations to avoid rounding errors. (iv) It accounts for irregularly-shaped boundaries in a straightforward way. The LB method is, in fact, suitable for direct numerical simulation (DNS) of incompressible, or slightly-compressible, flows with ($Ma < 0.1$) (Chen and Doolen, 1998). The disadvantages of the LB approach include the computational cost, the difficulty of including temperature gradients for non-isothermal flows and the mathematical imprecision of much of the lattice Boltzmann literature. Indeed, the lattice Boltzmann method can only be considered a competitive technique for incompressible, single-phase, isothermal flows or for problems approximated as such. In the present Chapter, a three-dimensional lattice Boltzmann model is presented to model the reduction of (i) a single particle and (ii) a packed bed of Fe_2O_3 to Fe_3O_4 with a dilute mixture of $CO+CO_2+N_2$. The bulk fluid is taken to be a single phase, gaseous N_2, at a fixed temperature and the reactive species, CO , is incorporated as a passive scalar. Model predictions are validated with experimental results.

8.2 The lattice Boltzmann method

8.2.1 Lattice gas cellular automata and lattice Boltzmann methods

The dynamics of a simple continuum fluid are governed by the conservation of mass and momentum, given by the continuity and Navier-Stokes equation:

$$\partial_t \rho + \nabla \cdot (\rho \mathbf{u}) = 0 \tag{8.1}$$

$$\rho[\partial_t \mathbf{u} + \mathbf{u} \cdot \nabla \mathbf{u}] = -\nabla P + \nabla \cdot \mathbf{T}, \tag{8.2}$$

where $\partial_t = \partial/\partial t$, ρ is the mass density, $\mathbf{u}$ is the velocity of the bulk fluid, P is the pressure, ν is the kinematic viscosity and $\mathbf{T}$ is the deviatoric stress tensor. Unlike traditional methods which rely on a top-down approach to discretise Eqs. (8.1) and (8.2), *e.g.* using finite difference, finite element or finite volume methods, the lattice Boltzmann method is a bottom-up approach (Chen and Doolen, 1998), as outlined in Fig. 8.1. Macroscopic parameters such as, density and momentum, are derived from a mass distribution function.

The lattice Boltzmann method has its origin in lattice gas cellular automata (LGCA) (Wolfram, 1986) and consists of three basic elements:

- a domain of interconnected sites, the *lattice*,
- *state variables* defined at each site, such as a real-valued mass distribution function, f_i,
- a set of *update rules*, defined locally, consisting of two steps: (*streaming*) permitting information exchange between neighbouring sites and (*collision*) defining the interaction of the state variables at each site.

In the present dissertation, the lattice Boltzmann equation will be presented as a particular discretisation of the continuous Boltzmann equation, though historically it evolved from LGCA.

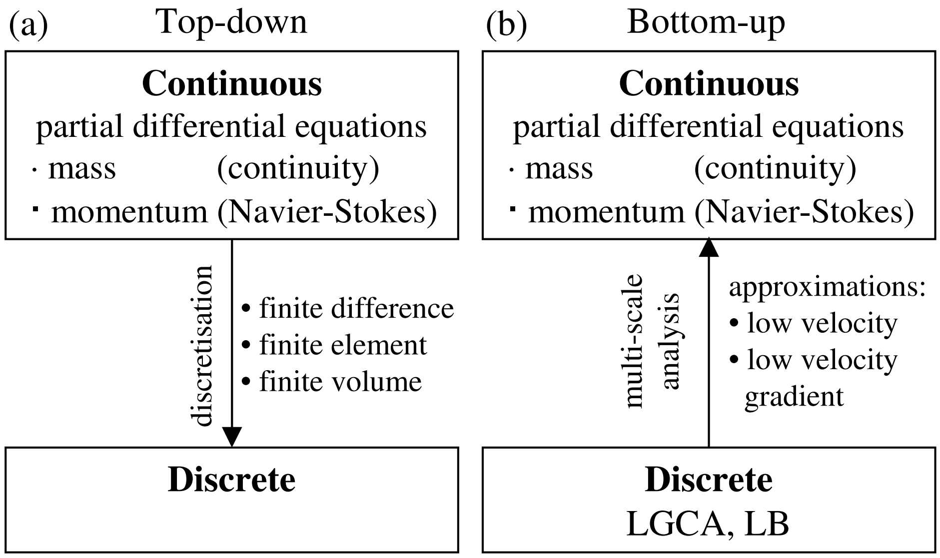

Figure 8.1: Overview of the modelling of fluid flow. (a) Traditionally, top-down methods were used to discretise the partial differential equations governing fluid motion. (b) Recently, bottom-up approaches based on kinetic theory which recover the same macroscopic partial differential equations have attracted growing interest (WebofKnowledge, 2009).

For the interested reader, an overview of the lattice Boltzmann method is given by Succi (2001) and Chen and Doolen (1998); a good introduction into the mathematics of the method is provided by Wolf-Gladrow (2000); a simple introduction into writing lattice Boltzmann code is presented in Sukop and Thorne (2006).

8.2.2 The continuous Boltzmann equation

Since it is known that the Navier-Stokes equation can be derived from the Boltzmann equation (Wolf-Gladrow, 2000), it is reasonable to use the Boltzmann equation as a starting point for modelling fluid flow. The Boltzmann equation describes the mass distribution of single particles $f \equiv f(\mathbf{x}, \mathbf{v}, t)$ in a fluid as a function of particle position, $\mathbf{x}$, particle velocity, $\mathbf{v}$, and time, t:

$$\frac{\partial f(\mathbf{x}, \mathbf{v}, t)}{\partial t} + \mathbf{v} \cdot \nabla f(\mathbf{x}, \mathbf{v}, t) = \Omega(\mathbf{x}, \mathbf{v}, t), \tag{8.3}$$

$$\mathbf{v} = \begin{bmatrix} v_x \\ v_y \\ v_z \end{bmatrix} \qquad \nabla f = \begin{bmatrix} \frac{\partial f}{\partial x} \\ \frac{\partial f}{\partial y} \\ \frac{\partial f}{\partial z} \end{bmatrix}$$

where Ω is a collision integral describing interactions with other particles. The simplest form of the collision operator involves the Bhatnagar-Gross-Krook (BGK) (Bhatnagar *et al.*, 1954) approximation, which expresses Ω as a linear relaxation towards an equilibrium:

$$\frac{\partial f}{\partial t} + \mathbf{v} \cdot \nabla f = -\frac{1}{\tau'}\left(f - f^{(\mathrm{eq})}\right), \tag{8.4}$$

the local Maxwell-Boltzmann distribution function:

$$f^{(\mathrm{eq})}(\mathbf{x}, \mathbf{v}, t) = \rho \left(\frac{m}{2\pi k_{\mathrm{B}} T}\right)^{\frac{\mathrm{D}}{2}} \exp\left[-\frac{m}{2k_{\mathrm{B}}T}(\mathbf{v} - \mathbf{u})^2\right]. \tag{8.5}$$

Here, $\mathbf{u}$ and T are the macroscopic velocity and absolute temperature of the bulk fluid, k_{B} is Boltzmann's constant, m is the mass of a single, monatomic particle and D is the dimension of space, *e.g.* 3 for 3D. The conserved macroscopic variables ρ and $\mathbf{u}$ are the microscopic velocity moments of f and $f^{(\mathrm{eq})}$:

$$\rho = \int f d\mathbf{v} = \int f^{(\mathrm{eq})} d\mathbf{v} \tag{8.6}$$

$$\rho\mathbf{u} = \int f \mathbf{v} d\mathbf{v} = \int f^{(\mathrm{eq})} \mathbf{v} d\mathbf{v}. \tag{8.7}$$

The microscopic velocity set $\mathbf{v}$ comprises the velocities of all single particles; the macroscopic velocity of the bulk fluid, $\mathbf{u}$, is thus related to $\mathbf{v}$ by summing over all particles, as shown in Eq. (8.7).

8.2.3 Derivation of the discrete lattice Boltzmann equation

Evaluating Eq. (8.4) over the continuous velocity space $\mathbf{x} = \mathbb{R}^{\mathrm{D}} = \mathbb{V}$ and $\mathbf{v} = \mathbb{R}^{\mathrm{D}} = \mathbb{V}$, where D is again the dimension of the velocity space, is computationally impracticable, and so a finite velocity set $\mathbf{v}_i$ over which evaluation will take place is chosen. For lattice Boltzmann models, the Cartesian cube is typically taken as the basis for the velocity set. Here, each point defined at (0,0,0) has six nearest neighbours $(\pm1, 0, 0), (0, \pm1, 0), (0, 0, \pm1)$, twelve second nearest neighbours $(\pm1, \pm1, 0), (\pm1, 0, \pm1), (0, \pm1, \pm1)$, and eight third nearest neighbours $(\pm1, \pm1, \pm1)$ (D'Humiéres *et al.*, 2002). The notation DDQQ is used to denote the dimension, D, and number of axisymmetric velocities, Q, of the chosen model. As shown in Fig. 8.2, which shows components of the mass distribution function, f_i, aligned according to lattice velocity, the D2Q9 model uses the velocities with squared moduli 0 and 1 lying in the 2D

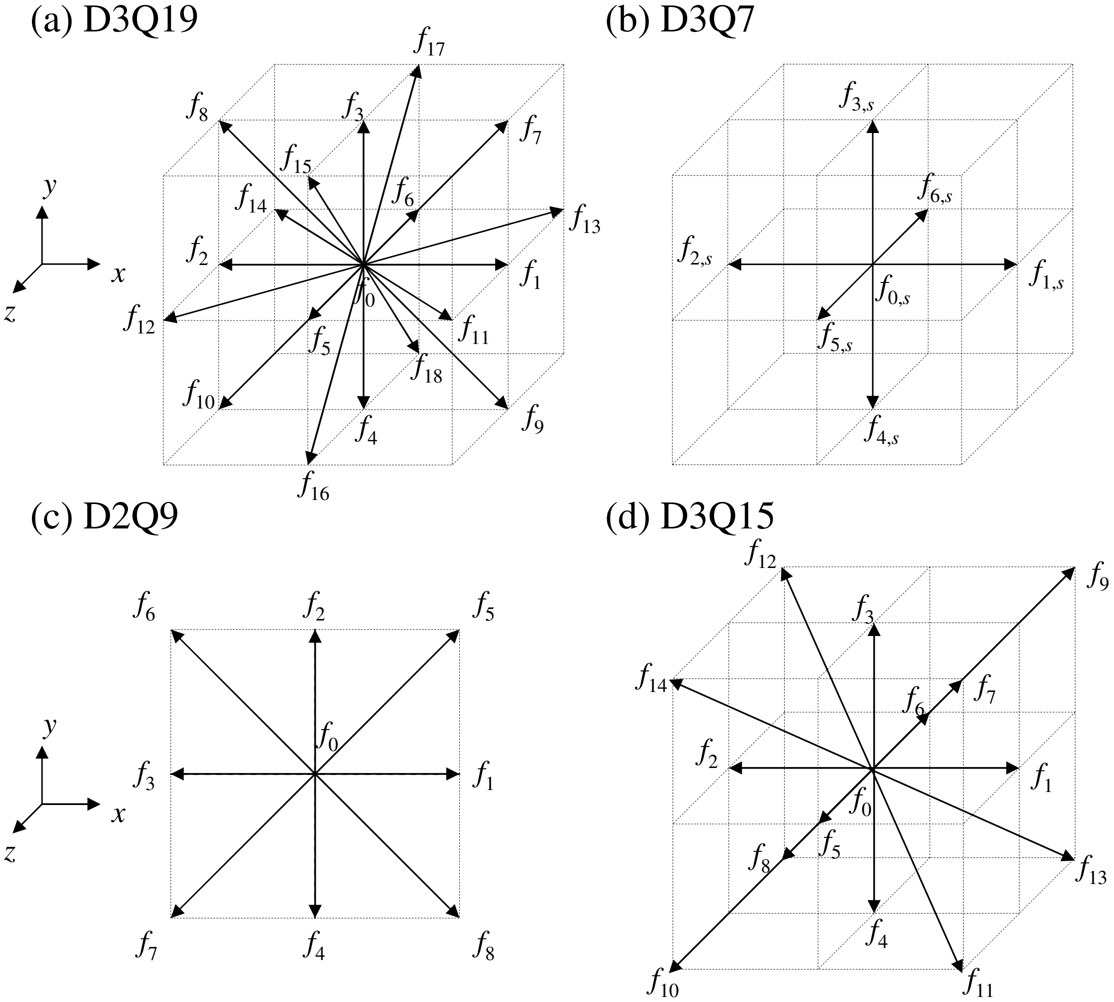

Figure 8.2: Lattice structure for the (a) D3Q19, (b) D3Q7, (c) D2Q9, (d) D3Q15 lattices.

plane (D'Humiéres *et al.*, 2002); the D3Q15 model uses velocities with squared moduli 0, 1 and 3; the D3Q19 model uses the velocities with squared moduli 0,1, and 2. In this work, the D3Q19 lattice is considered as shown in Fig. 8.2(a).

The choice of a discrete $\mathbf{v}_i$ permits the discretisation of physical space, $\mathbf{x}_i$, if only those $\mathbf{x}_i$ accessible by moving along the discrete $\mathbf{v}_i$ are considered. After fixing the velocity space, the continuous distribution function $f(\mathbf{x}_i, \mathbf{v}_i, t)$ need only be written as a function of $\mathbf{x}_i$ and t. Dropping the subscript i denoting the property of being discrete from all but the leading variable, the discrete distribution function becomes $f_i(\mathbf{x}, t)$. Thus, Eq. (8.4) can be written as:

$$\frac{\partial f_i}{\partial t} + \mathbf{v}_i \cdot \nabla f_i = -\frac{1}{\tau'}\left(f_i - f_i^{(\mathrm{eq})}\right). \tag{8.8}$$

Discretisation of Eq. (8.8) with respect to time is performed by defining the total derivative,

$$\frac{D}{Dt} \equiv \frac{\partial}{\partial t} + \mathbf{v}_i \cdot \nabla, \tag{8.9}$$

which permits Eq. (8.8) to be written explicitly as

$$\frac{Df_i}{Dt} = -\frac{1}{\tau'}\left(f_i - f_i^{(\mathrm{eq})}\right). \tag{8.10}$$

The left hand side of Eq. (8.10) can be evaluated using a truncated Taylor series expansion for small t, which yields the familiar result:

$$\frac{Df_i(t)}{Dt} = \frac{f_i(t+\Delta t) - f_i(t)}{\Delta t} + O(\Delta t). \tag{8.11}$$

Combining Eqs. (8.10) and (8.11) and multiplying through by Δt yields the discrete lattice Boltzmann equation:

$$f_i(\mathbf{x} + \mathbf{v}\Delta t, t + \Delta t) - f_i(\mathbf{x}, t) = -\frac{1}{\tau}\left[f_i(\mathbf{x}, t) - f_i^{(\mathrm{eq})}(\mathbf{x}, t)\right] + O(\Delta t^2), \tag{8.12}$$

where $\tau \equiv \tau'/\Delta t$ is the dimensionless relaxation time. Importantly, Eq. (8.12) is explicit in time and is accurate up to first order in Δt (Wolf-Gladrow, 2000). It can be shown (Appendix 5; Sterling and Chen, 1996) that the discretisation error of $O(\Delta t^2)$ can be incorporated into the viscosity during the derivation of the Navier-Stokes equations, effectively making Eq. (8.12) accurate to second, rather than first, order in time.

To ensure that the macroscopic variables, ρ and $\mathbf{u}$ are recovered by the discrete Boltzmann equation, the following definitions analogous to Eqs. (8.6)-(8.7) are used (He and Luo, 1997c):

$$\rho = \sum_i f_i = \sum_i f_i^{(\mathrm{eq})} \tag{8.13}$$

$$\rho\mathbf{u} = \sum_i f_i \mathbf{v}_i = \sum_i f_i^{(\mathrm{eq})} \mathbf{v}_i. \tag{8.14}$$

To summarise, the discrete lattice Boltzmann equation with linearised BGK collision operator (8.12) has been derived from the continuous Boltzmann equation by assuming a discrete microscopic velocity set and approximating the time derivative with a numerical Euler scheme. The rigorous derivation of the Navier-Stokes and continuity equation from the lattice Boltzmann equation is presented in Appendix 5.

8.2.4 Multiple relaxation time collision operators

Ignoring terms of $O(\Delta t^2)$, the lattice Boltzmann equation with the linear BGK collision operator was given in Eq. (8.12) as:

$$f_i(\mathbf{x} + \mathbf{v}\Delta t, t + \Delta t) - f_i(\mathbf{x}, t) = -\frac{1}{\tau}\left[f_i(\mathbf{x}, t) - f_i^{(\mathrm{eq})}(\mathbf{x}, t)\right], \tag{8.15}$$

or alternatively in vector notation,

$$\mathbf{f}(\mathbf{x} + \mathbf{v}\Delta t, t + \Delta t) - \mathbf{f}(\mathbf{x}, t) = -\mathbf{S}[\mathbf{f}(\mathbf{x}, t) - \mathbf{f}^{(\mathrm{eq})}(\mathbf{x}, t)], \tag{8.16}$$

where $\mathbf{f}(\mathbf{x}, t) = [f_0(\mathbf{x}, t), \ldots, f_{n-1}(\mathbf{x}, t)]^{\mathrm{T}}$, $\mathbf{S} = \mathrm{diag}(1/\tau, \ldots, 1/\tau)$ and n is the number of discrete velocities, *e.g.* 19 in the D3Q19 model. Here, the relaxation of $\mathbf{f}$ to $\mathbf{f}^{(\mathrm{eq})}$ is governed by a single time constant τ.

To increase the flexibility of the lattice Boltzmann approach, a more general collision operator with multiple relaxation times (MRT) has been introduced (D'Humiéres *et al.*, 2002; Lallemand and Luo, 2003). With MRT operators, collisions take place in moment space, $\mathbb{M}$, rather than in velocity space, $\mathbb{V}$. A transformation matrix, $\mathbf{M}$, provides the linear mapping such that

$$\mathbf{m} = \mathbf{M}\mathbf{f} \qquad \mathbf{m}^{(\mathrm{eq})} = \mathbf{M}\mathbf{f}^{(\mathrm{eq})}, \tag{8.17}$$

where it is noted that the square matrix, $\mathbf{M}$, must be consistent with the size of $\mathbf{f}$. A particular example of $\mathbf{M}$ is given for the D3Q19 model in Appendix 5, section A5.2. The concept of the lattice Boltzmann equation with a MRT collision operator is most straightforwardly explained through manipulation of Eq. (8.16):

$$\mathbf{f}(\mathbf{x} + \mathbf{v}\Delta t, t + \Delta t) - \mathbf{f}(\mathbf{x}, t) = -\mathbf{S}\mathbf{M}^{-1}\mathbf{M}[\mathbf{f}(\mathbf{x}, t) - \mathbf{f}^{(\mathrm{eq})}(\mathbf{x}, t)], \tag{8.18}$$

giving,

$$\mathbf{f}(\mathbf{x} + \mathbf{v}\Delta t, t + \Delta t) - \mathbf{f}(\mathbf{x}, t) == -\mathbf{M}^{-1}\hat{\mathbf{S}}\left[\mathbf{m}(\mathbf{x}, t) - \mathbf{m}^{(\mathrm{eq})}(\mathbf{x}, t)\right], \tag{8.19}$$

where,

$$\hat{\mathbf{S}} = \mathrm{diag}(s_1, s_2, \ldots, s_n), \tag{8.20}$$

is defined and Eq. (8.17) as well as the property, $\mathbf{I} = \mathbf{M}^{-1}\mathbf{M}$, have been used. Note that the MRT collision operator will reduce to the BGK collision operator for the special case, $\hat{\mathbf{S}} = \mathbf{MSM}^{-1} = \mathbf{S} = \mathrm{diag}(1/\tau, 1/\tau, \ldots, 1/\tau)$ for any choice of transformation matrix $\mathbf{M}$. Defining $\hat{\mathbf{S}} = \mathrm{diag}(s_1, s_2, \ldots, s_n)$, however, means that the MRT collision model has $s_1, s_2, \ldots, s_n$ adjustable relaxation rates rather than a single relaxation time τ. These additional tunable parameters provide several advantages over the single relaxation time (BGK) operator. For example, specific relaxation times can be optimised to improve the model stability and permit the simulation of higher *Re* number flow.

8.2.5 Transport of a passive scalar

The previous discussion, when considered with Appendix 5, has shown how the lattice Boltzmann equation (8.19) can be used to model single-phase flow of an incompressible or slightly-compressible fluid. For chemical engineering applications, however, transport of chemical species is of fundamental importance. The behaviour of a passive scalar in a fluid, *i.e.* a scalar which itself does not influence the underlying fluid momentum, is governed by the macroscopic advection and diffusion equation:

$$\frac{\partial \rho_s}{\partial t} + \nabla \cdot (\mathbf{u}\rho_s) - D_s \nabla^2 \rho_s = 0, \tag{8.21}$$

where ρ_s is a scalar quantity of arbitrary units, D_s is its diffusivity, and $\mathbf{u}$ is the macroscopic velocity of the bulk fluid, defined as before by Eq. (8.14). In the present dissertation, chemical species have been incorporated using a passive scalar approach with separate distribution functions $f_{i,s}$ for each scalar s considered. Here, the quantity of passive scalar is conserved, but not the momentum. Therefore, the passive scalar approach of the present LB model is only exact for situations with chemical species of identical molecular mass and no net consumption or production, but can be extended to situations where the reactive species are substantially diluted in an inert fluid.

To incorporate advection and diffusion of a scalar into a lattice Boltzmann type model, the approach of Flekkøy (1993) and Sullivan (2006) was used. Unlike the Navier-Stokes equation (8.2), the advection and diffusion equation (8.21) only has terms up to first order in $\mathbf{u}$. As a result, the number of discrete velocities required to recover the correct macroscopic behaviour can be significantly reduced compared to that required for the Navier-Stokes equations. For example, to recover the advection and diffusion equation up to $O(\mathbf{u}^2)$, a reduced velocity set, D2Q5 in 2D and D3Q7 in 3D, is sufficient and a reduced equilibrium distribution function which includes terms only up to first order in $\mathbf{u}$ is required (Sullivan, 2006). Reducing the number of velocity directions and truncating the equilibrium distribution function permits a significant increase in computational efficiency with almost no loss in computational accuracy. The evolution of the $f_{i,s}$ is governed by:

$$f_{i,s}(\mathbf{x} + \mathbf{v}\Delta t, t + \Delta t) - f_{i,s}(\mathbf{x}, t) = -\frac{1}{\tau_s}\left(f_{i,s}(\mathbf{x}, t) - f_{i,s}^{(\mathrm{eq})}(\mathbf{x}, t)\right), \tag{8.22}$$

which is the lattice Boltzmann equation (8.12) with BGK collision operator. In this work, the D3Q7 velocity set shown in Fig. 8.2(b) with

$$f_{i,s}^{(\mathrm{eq})} = w_i \rho_s \left[1 + 4\frac{(\mathbf{v}_i \cdot \mathbf{u})}{c^2}\right], \tag{8.23}$$

where

$$w_i = \frac{1}{4} \qquad i = 0 \quad \text{and} \quad w_i = \frac{1}{8} \qquad i = 1, ..., 6 \tag{8.24}$$

was used with Eq (8.22). As in Eqs. (8.13) and (8.14), the moments of $f_{i,s}$ are given by:

$$\rho_s = \sum_i f_{i,s} = \sum_i f_{i,s}^{(\mathrm{eq})} \tag{8.25}$$

$$\rho_s \mathbf{u}_s = \sum_i f_{i,s} \mathbf{v}_i = \sum_i f_{i,s}^{(\mathrm{eq})} \mathbf{v}_i. \tag{8.26}$$

Sullivan (2006) has shown that this choice of $f_{i,s}^{\mathrm{eq}}$ recovers the advection and diffusion equation (8.21) with an error of the order $O(\mathbf{u}^2)$ and diffusivity,

$$D_s = \frac{1}{4}(\tau_s - 1). \tag{8.27}$$

8.2.6 Reaction

To incorporate chemical reactions into the lattice Boltzmann model, the approach of Sullivan (2006) was used which permits product species to be both diffused and also advected at the correct macroscopic velocity, $\mathbf{u}$. Following Sullivan (2006), the change in density is calculated just prior to evaluation of the $f_{i,s}^{(\mathrm{eq})}$ as:

$$\Delta\rho_s = F(\rho_1, \ldots, \rho_s, \ldots, \mathbf{x}, t), \tag{8.28}$$

where $F(\rho_1, \ldots, \rho_s, \ldots, \mathbf{x}, t)$ is the function corresponding to the chosen rate expression. For example, $F = -k_i \rho_s \Delta t + O(\Delta t^2)$ would represent a first order reaction where k_i is the rate constant, ρ_s is the concentration of reactant species s and Δt is the time step. After calculating F, evaluation of $f_{i,s}^{(\mathrm{eq})}$ in Eq. (8.23) is then performed using $\rho_s + \tau_s \Delta\rho_s$ in place of ρ_s to give:

$$f_{i,s}^{(\mathrm{eq})} = w_i \left(\rho_s + \tau_s \Delta\rho_s\right)\left[1 + 4\frac{(\mathbf{v}_i \cdot \mathbf{u})}{c^2}\right]. \tag{8.29}$$

Inserting Eq. (8.29) into Eq. (8.22) and summing over all i, then gives:

$$\begin{aligned}\sum_i \left[f_{i,s}(\mathbf{x} + \mathbf{v}\Delta t, t + \Delta t) - f_{i,s}(\mathbf{x}, t)\right] &= \sum_i -\frac{1}{\tau_s}\left[f_{i,s}(\mathbf{x}, t) - \left(\rho_s + \tau_s\left(\rho_s\big|_{t+1} - \rho_s\right)\right) w_i \left(1 + 4\frac{\mathbf{v_i} \cdot \mathbf{u}}{c^2}\right)\right] \\ &= -\frac{\rho_s}{\tau_s} + \frac{\rho_s}{\tau_s} + \rho_s|_{t+1} - \rho_s = \Delta\rho_s,\end{aligned} \tag{8.30}$$

which recovers the correct $\Delta\rho_s$ at each time step as desired. Greater accuracy in the method can be achieved by evaluating F up to higher order in Δt. In the present dissertation evaluation up to first order in Δt, as in the previous example, was found to give satisfactory results.

8.2.7 Implementation

Implementation of the lattice Boltzmann equations, (8.19) and (8.22), involves two basic steps: *streaming* and *collision*. Where $'$ denotes the post-collision values:

- *collision*
  for BGK: $f'_{i,s}(\mathbf{x}, t) = f_{i,s}(\mathbf{x}, t) - \frac{1}{\tau_s}\left[f_{i,s}(\mathbf{x}, t) - f_{i,s}^{\mathrm{eq}}(\mathbf{x}, t)\right]$,
  for MRT: $\mathbf{f}'(\mathbf{x}, t) = \mathbf{f}(\mathbf{x}, t) - \mathbf{M}^{-1}\hat{\mathbf{S}}\left[\mathbf{m}(\mathbf{x}, t) - \mathbf{m}^{\mathrm{eq}}(\mathbf{x}, t)\right]$,

- *streaming*
  $f_{i,s}(\mathbf{x} + \mathbf{v}\Delta t, t + \Delta t) = f'_{i,s}(\mathbf{x}, t)$,
  $f_i(\mathbf{x} + \mathbf{v}\Delta t, t + \Delta t) = f'_i(\mathbf{x}, t)$.

A computational flow chart giving an overview of the lattice Boltzmann algorithm is given in Fig. 8.3.

Because the lattice Boltzmann equation is explicit in time and only involves local interactions among the distribution functions during streaming, it is inherently suited for parallel computing. Consequently, a parallel version of the program was developed in Fortran 90. The non-blocking message passing interface (MPI) commands MPI_Isend and MPI_Ireceive were

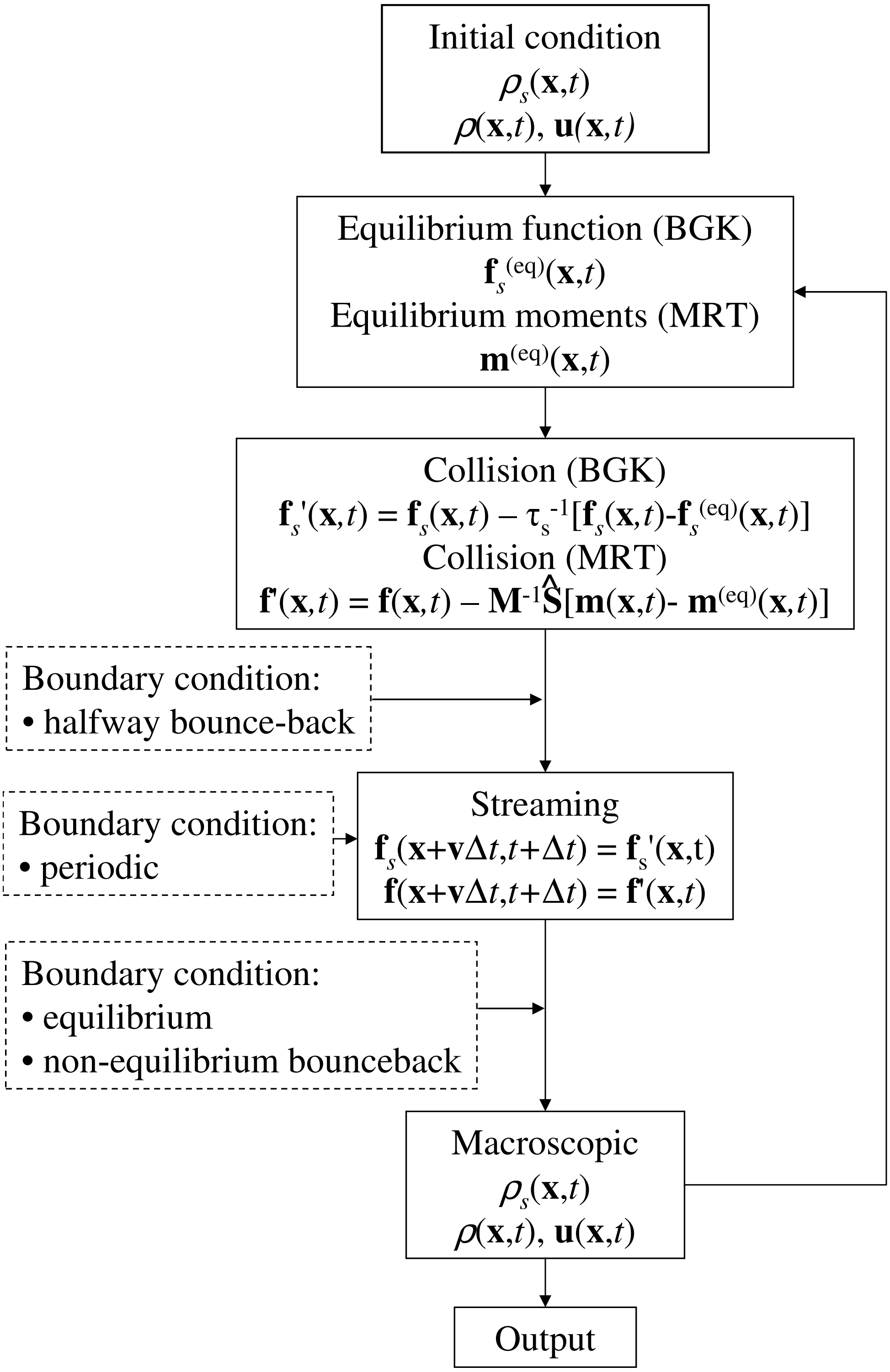

Figure 8.3: Computational flowsheet for the lattice Boltzmann method.

used. After each time step, the f_i or $f_{i,s}$ for the boundary nodes of each domain were exchanged and all domains synchronised prior to the start of the next time step. In the present dissertation, the fluid flow and passive scalar programs were decoupled. Thus, the flow profile through a geometry was first calculated before models for mass transport and reaction kinetics were overlayed.

8.2.8 Boundary conditions and initial conditions

Four types of boundary conditions, arranged in order of increasing complexity and increasing accuracy, were used in this work: periodic, equilibrium, zero flux outlet, halfway bounce-back and non-equilibrium bounce-back. In the following, the notation $f_i(\mathbf{x}, t) = f_i(x, y, z, t)$ and $f_{i,s}(\mathbf{x}, t) = f_{i,s}(x, y, z, t)$ is used to denote the x, y and z location of f_i and $f_{i,s}$, respectively, in the 3D domain. The domain is comprised of an integer number of nodes bounded by $1 \leq x \leq L_x$, $1 \leq y \leq L_y$ and $1 \leq z \leq L_z$.

Periodic. Periodic boundary conditions are implemented during streaming and treat the domain as continuous. For example, for flow in the positive x direction the outflowing $f_1(L_x, y, z, t)$ becomes the inflowing $f_1(1, y, z, t + 1)$ for a fluid, or, for a passive scalar, $f_{1,s}(1, y, z, t + 1) = f_{1,s}(L_x, y, z, t)$ (Sukop and Thorne, 2006).

Equilibrium. The equilibrium boundary condition is typically implemented after streaming and involves using the specified ρ or ρ_s and $\mathbf{u}$. For flow simulations, ρ and $\mathbf{u}$ are used with Eqs. (A5.26) and (A5.27) to calculate $\mathbf{m}^{(\mathrm{eq})}$; next, $\mathbf{f}^{(\mathrm{eq})} = \mathbf{M}^{-1}\mathbf{m}^{(\mathrm{eq})}$ is used; then, $\mathbf{f} = \mathbf{f}^{(\mathrm{eq})}$ is set. For a passive scalar, ρ_s and $\mathbf{u}$ are used with Eq. (8.23) to evaluate $f_{i,s}^{(\mathrm{eq})}$; next, $f_{i,s} = f_{i,s}^{(\mathrm{eq})}$ is set. This boundary method is for Dirichlet type boundaries and, while initially dismissed as too simplistic, has recently been shown to achieve good accuracy in low *Re* flows (Mohamad and Succi, 2009).

Zero flux outlet. To impose zero flux at the outlet of a domain, a simple Neumann type boundary condition is used. For example, for flow in the positive z direction, the zero flux is incorporated by specifying:

$$f_i(x, y, L_z, t) = f_i(x, y, L_z - 1, t) \tag{8.31}$$

$$f_{i,s}(x, y, L_z, t) = f_{i,s}(x, y, L_z - 1, t), \tag{8.32}$$

for fluid flow (8.31) or flow of a passive scalar (8.32), respectively. That is the outlet nodes are copied from the preceding nodes in the flow direction. This boundary condition is derived from Taylor expansion of df_i/dz or $df_{i,s}/dz$ up to first order in Δz and is therefore accurate to first order in lattice spacing.

Halfway bounce-back. The halfway bounce-back boundary condition is a no-slip boundary condition for a solid lattice node. It is carried out after the collision step. The f_i or $f_{i,s}$ are reversed according to their respective lattice velocities. The reversed f_i are then streamed to neighbouring nodes in the *following* time step. If the true location of the boundary is considered to be halfway between the solid and fluid node, this scheme can be shown to be second order accurate (Cornubert *et al.*, 1991; He *et al.*, 1997) with respect to grid spacing for regular boundaries, *i.e.* when the solid boundary is not stair-stepped. Because it can be easily implemented on any geometry, the halfway bounce-back condition is often applied even to curved boundaries (Gallivan *et al.*, 1997).

Non-equilibrium bounce-back. For fluid flow, the non-equilibrium bounce-back boundary condition of Zou and He (1997) was used to fix velocity boundaries. For flow in the positive z direction with the D3Q19 velocity set, after streaming, the values of $\rho, f_5, f_{11}, f_{12}, f_{15}$ and f_{16} are unknown. As shown from Fig. 8.2(a), these values are relevant to the z direction and must be determined. Specifying $\mathbf{u}$ to be equal to the desired inlet value, the unknown ρ can be solved by adding Eq. (8.13) to the negative of Eq. (8.14) evaluated in the z direction and rearranging to solve for ρ. Next, to close the system and solve for the unknown f_i's, it is assumed that the bounce-back rule is correct for the non-equilibrium part (Zou and He, 1997) of the particle distribution (for example, $f_5 - f_5^{(\mathrm{eq})} = f_6 - f_6^{(\mathrm{eq})}$), giving overall:

$$
\begin{aligned}
\rho = \frac{[f_0 + f_1 + f_2 + f_3 + f_4 + f_7 + f_8 + f_9 + f_{10} + 2(f_6 + f_{13} + f_{14} + f_{17} + f_{18})]}{(1 - u_z)}& \\
f_5 = f_6 + (f_5^{\mathrm{eq}} - f_6^{\mathrm{eq}}) = f_6 + \frac{1}{3}\rho u_z& \\
f_{11} = f_{14} + (f_{11}^{(\mathrm{eq})} - f_{14}^{(\mathrm{eq})}) = f_{14} + \frac{1}{6}\rho(u_z + u_x)& \\
f_{12} = f_{13} + (f_{12}^{(\mathrm{eq})} - f_{13}^{(\mathrm{eq})}) = f_{13} + \frac{1}{6}\rho(u_z - u_x)& \\
f_{15} = f_{18} + (f_{15}^{(\mathrm{eq})} - f_{18}^{(\mathrm{eq})}) = f_{18} + \frac{1}{6}\rho(u_z + u_y)& \\
f_{16} = f_{17} + (f_{16}^{(\mathrm{eq})} - f_{17}^{(\mathrm{eq})}) = f_{17} + \frac{1}{6}\rho(u_z - u_y).&
\end{aligned}
\tag{8.33}
$$

For a passive scalar, a non-equilibrium bounce-back boundary condition to fix the concentration was employed following Zou and He (1997). For flow in the positive z direction with the D3Q7 velocity set, ρ_s at the inlet can be fixed by rearranging Eq. (8.25) to give:

$$f_{5,s} = \rho_s - (f_{0,s} + f_{1,s} + f_{2,s} + f_{3,s} + f_{4,s} + f_{6,s}). \tag{8.34}$$

Setting the velocity using Eq. (8.33) and setting the inlet density with Eq. (8.34), effectively fixes the inlet flux, $\rho_s\mathbf{u}$, of species, s.

Thus, periodic and halfway bounce-back boundaries do not require any macroscopic variables as inputs. Equilibrium boundaries require the macroscopic variables ρ and $\mathbf{u}$ for fluid simulations, or ρ_s and $\mathbf{u}$ for simulations with a passive scalar. Non-equilibrium bounce-back boundaries required $\mathbf{u}$ for fluid simulations and ρ_s for simulations with a passive scalar.

Initial conditions. The initial conditions for the hydrodynamic lattice Boltzmann model in the present work were determined from the initial macroscopic variables, ρ and $\mathbf{u}$. Using Eq. (A5.26) with Eq. (A5.27) substituted for the specified moments, $\mathbf{m}^{\mathrm{eq}}(\rho, \mathbf{u})$ was calculated. Then,

$$\mathbf{f}(\mathbf{x}, t)\big|_{t=0} = \mathbf{f}^{\mathrm{eq}}(\rho, \mathbf{u}) = \mathbf{M}^{-1}\mathbf{m}^{\mathrm{eq}}(\rho, \mathbf{u}), \tag{8.35}$$

was used to generate the starting values for the distribution function. Similarly, for a simulation involving a passive scalar the initial condition was determined from ρ_s and $\mathbf{u}$ by using Eq. (8.23) and setting $\mathbf{f}_s(\mathbf{x}, t)\big|_{t=0} = \mathbf{f}_s^{\mathrm{eq}}(\rho_s, \mathbf{u})$.

8.2.9 Conversion of lattice units to real units

Parameters in lattice units are related to corresponding parameters in physical units through scaling factors in length, Δx, time, Δt and mass, Δm (Maier *et al.*, 1998). The lattice resolution Δx gives the physical length corresponding to the distance between nodes in m/(lattice unit); Δt gives the physical time corresponding to each time step in s/(time step); Δm gives the physical mass associated with each unit volume of the lattice in kg/(lattice unit)^3 since $\rho_0 = 1$ was chosen as the equilibrium density. Writing physical units on the left hand side and lattice units, denoted by the subscript LB, on the right hand side, examples of scalings are as follows:

$$L_x = L_{x,\mathrm{LB}}\Delta x \tag{8.36}$$

$$\mathbf{u} = \mathbf{u}_{\mathrm{LB}}\frac{\Delta x}{\Delta t} \quad D_s = D_{s,\mathrm{LB}}\frac{\Delta x^2}{\Delta t} \quad \nu = \nu_{\mathrm{LB}}\frac{\Delta x^2}{\Delta t} \tag{8.37}$$

$$\rho = \rho_{\mathrm{LB}}\frac{\Delta m}{\Delta x^3}. \tag{8.38}$$

For a simulation, the choice of parameters is performed as follows:

1. Given the parameters for the problem of interest in physical units,
2. Choose a scaling Δx and Δt.
3. Calculate $|\mathbf{u}_{\mathrm{LB}}|$ using Eq. (8.37) and the physical velocity $\mathbf{u}$. Check that $|\mathbf{u}_{\mathrm{LB}}| < 0.15$ in lattice units for the simulation. Proceed if this condition is satisfied; otherwise, return to step (1) and make a new choice for Δx and Δt.
4. Calculate the relaxation parameters for the variables of interest, *e.g.* s_{10} and τ_s, using Eq. (8.37), ν and D_s in physical units, and Eqs. (A5.84) and (8.27) to evaluate ν_{LB} and $D_{s,\mathrm{LB}}$, respectively. Check that the relaxation parameters obtained lie within the range of stability and within the range that permits satisfactory accuracy for the given lattice Boltzmann model. Proceed if these conditions are met; otherwise, return to step (1) and make a new choice for Δx and Δt.

Later, in sections 8.4.5 and 8.4.6, Tables 8.3 and 8.4 give explicit details of the scalings used for simulations in this dissertation.

8.3 Validation of the lattice Boltzmann model

8.3.1 Validation of hydrodynamics

To verify the accuracy of the hydrodynamic calculations in the D3Q19 lattice Boltzmann program, Poiseuille flow in a channel was simulated. The analytical solution to the Navier-Stokes equation (A5.89) for Poiseuille flow between two plates with $\mathbf{u} = 0$ at the boundaries is given by a parabolic velocity profile:

$$u_z = \frac{4u_{z,\max}}{(L_x - 2)^2}\left(x - \frac{3}{2}\right)\left(L_x - \frac{1}{2} - x\right) \tag{8.39}$$

$$u_{z,\max} = \frac{F_z(L_x - 2)^2}{8\rho\nu}, \tag{8.40}$$

where $u_{z,\max}$ denotes the maximum centerline velocity, F_z is the driving force, $(L_x - 2)$ is the effective channel width, $\nu = 1/3 \times (1/s_{10} - 1/2)$ is the kinematic viscosity, $\rho = 1$ is the mass density, and x is the lattice position consistent with the simulation set-up in Fig. 8.4(a). The odd form of Eq. (8.39) is owing to the halfway bounce-back boundary condition and the

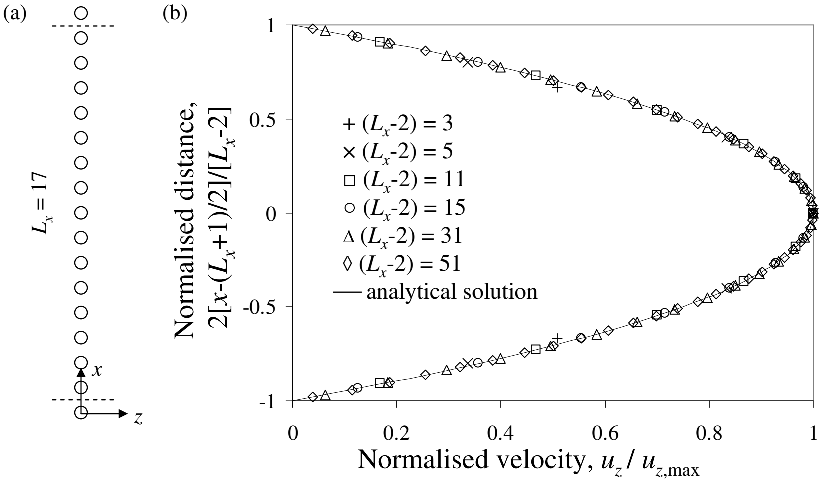

Figure 8.4: (a) Simulation geometry for Poiseuille flow in a channel with $L_x = 17$. The true channel width is $(L_x - 2)$. (b) Velocity profile for Poiseuille flow using halfway bounce-back boundary conditions with the D3Q19 MRT model and $1/s_{10} = 1.0$. The velocity was normalised by $u_{z,\max}$ from the simulation. The solid line represents the analytical solution.

definition of the computational domain: the first lattice node in a three dimensional domain is defined as $x = y = z = 1$ rather than $x = y = z = 0$. The lattice dimensions were $L_y = L_z = 1$, and L_x was varied over $5 \leq L_x \leq 53$. In addition for each value of L_x, the relaxation time was varied over $0.51 < 1/s_{10} < 2.5$. Thus, in the simulation the parameters which varied were channel width, $(L_x - 2)$, and relaxation time, $1/s_{10}$, *i.e.* viscosity; all other parameters were fixed. Halfway bounce-back boundary conditions were used in the x direction at the walls so that the boundary between the solid and fluid was one half of a lattice spacing from each respective node as shown in Fig. 8.4(a). Hence, for a domain with $L_x = 17$ nodes the true channel width is only $L_x - 2 = 15$. In the z direction (flow direction) and y direction, periodic boundary conditions were used. The domain was initialised with $\rho = 1$ and $\mathbf{u} = 0$ everywhere. The simulations were run for $10^5 - 1.5 \times 10^6$ time steps, where larger times were required for lower values of the relaxation time, $1/s_{10}$, until the convergence criterion of

$$\sum_{x=2}^{(L_x-1)} \frac{|u_z(\mathbf{x}, t) - u_z(\mathbf{x}, t-1)|}{u_z(\mathbf{x}, t)} < 10^{-10}, \tag{8.41}$$

was met in all cases.

The force to accelerate the fluid, $\mathbf{F} = (0, 0, F_z)^{\mathrm{T}}$, was incorporated in two steps to reduce numerical error (Lallemand and Luo, 2003; Ginzbourg and Adler, 1994):

Step 1,	Streaming of f_i;
Step 2,	Compute moments m_i from f_i;

Step 3, $\mathbf{j}' = \mathbf{j} + \frac{1}{2}\mathbf{F}\Delta t$;
Step 4, Compute $m_i^{(\mathrm{eq})}$ from $\rho, \mathbf{j}'$;
Step 5, Collision: relaxation of the moments to give $\mathbf{j}''$;
Step 6, $\mathbf{j}''' = \mathbf{j}'' + \frac{1}{2}\mathbf{F}\Delta t$;
Step 7, Compute f_i from the moments m_i.

The force, F_z, was varied to give $u_{z,\mathrm{max}} = 0.05$ from Eq. (8.40) in all cases. The momentum, $\mathbf{j}'$, with one-half of the force added, *i.e.* after step 3 and before step 4, was used as the output.

Fig. 8.4(b) shows that the simulated values of u_z for $1/s_{10} = 1$ were in good agreement with the parabolic analytical solution. Similar plots were obtained for $1/s_{10} = 0.51, 0.55$ and 2.5. In addition, $u_x < 10^{-15}$, $u_y < 10^{-16}$, and $\rho = 1.0 \pm 10^{-6}$ in all cases. The relative error in the centreline velocity, shown in Fig. 8.5, was determined by taking the absolute value of the difference between the analytical centreline velocity from Eq. (8.40) and the centreline velocity from the LB simulation, and dividing by the analytical centreline velocity. In theory, this error should be zero since F_z was chosen to give $u_{z,\mathrm{max}} = 0.05$. However, higher errors are observed for lower values of the relaxation time, $1/s_{10}$, *i.e.* higher *Re*, and for smaller channel widths. This dependence on *Re* is a result of the low *Ma* requirement in Appendix 5. For small channel widths, the centreline velocity was underpredicted by the lattice Boltzmann simulation. Figure 8.5 demonstrates that for $0.51 \leq 1/s_{10} \leq 2.5$ errors in the centreline

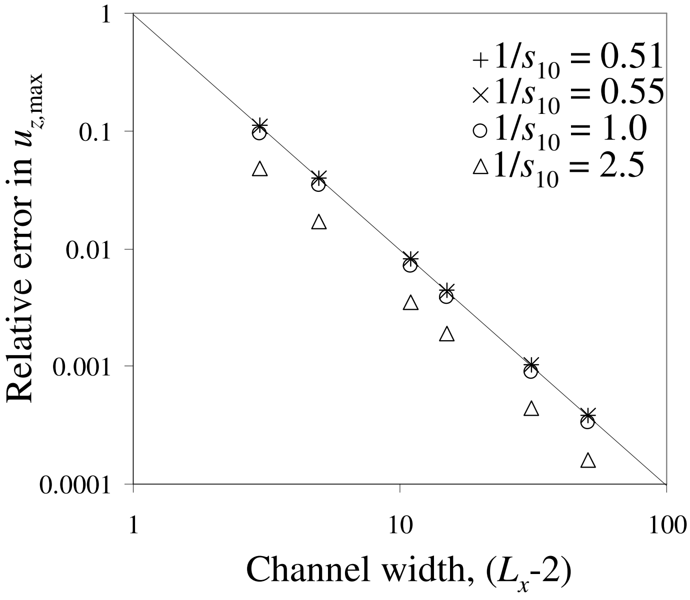

Figure 8.5: Relative error in the maximum centreline velocity, $u_{z,\mathrm{max}}$, from simulations *versus* the width of the channel, $(L_x - 2)$. From the slope, error is second order with respect to grid spacing.

velocity are < 11% for a channel of width 3, while errors are < 4% for a channel of width 5. Figure 8.5 also confirms that the halfway bounce-back boundary condition is accurate up to second order in grid spacing, as the errors conform to a line of slope -2 on the $\log_{10} - \log_{10}$ plot. However, second order accuracy is only achievable with halfway bounce-back boundary conditions when the boundary is regular and does not have a stair step pattern. For irregular boundaries, the order of the error lies between 1 and 2 (Yu *et al.*, 2003).

8.3.2 Validation of mass transport

To verify the accuracy of mass transport with the D3Q7 lattice Boltzmann program, the decay of a 1D convected sinusoidal concentration wave was modelled (Flekkøy, 1993; Sullivan *et al.*, 2007). The time-dependent solution of the advection diffusion equation (8.21) for this problem in a periodic domain is given by Flekkøy (1993):

$$\rho_s(x,t) = \frac{\rho_{s,\max}}{2}\left[1 + e^{-k_\mathrm{D}^2 D_s t}\sin k_\mathrm{D}(x - u_x t)\right], \tag{8.42}$$

where x is the direction in which the domain extends, $k_\mathrm{D} = 2\pi/L_x$, L_x is the number of lattice nodes, u_x is the macroscopic velocity of the bulk fluid in the x direction, and $\rho_{s,\max}$ is the maximum initial concentration. The diffusion coefficient, D_s, can be determined using:

$$D_s = \frac{1}{k_\mathrm{D}^2 t}\ln\frac{A(0)}{A(t)}, \quad A(t) = \int\left|\rho_s(x,t) - \frac{\rho_{s,\max}}{2}\right|. \tag{8.43}$$

For simulations, the integral on the right-hand side of Eq. (8.43) was calculated using the trapezium rule. The domain was $L_x = 128$, $L_y = L_z = 1$. The relaxation time was varied in the range $0.50001 < \tau_s < 10.5$, giving diffusion coefficients of $2.5 \times 10^{-6} < D_s < 2.5$ in lattice units. A value of $\rho_{s,\max} = 1$ was fixed. For each value of τ_s, three different steady uniform velocity fields of $u_x = 0.0, 0.1$ and 0.2 were employed. Thus, the parameters which varied were the relaxation time, τ_s, and the velocity, u_x; all other parameters were fixed. Simulations were run for a total of 10^4 time steps. Periodic boundary conditions were used in all directions. The initial condition for the mass density was determined from Eq. (8.42) with $t = 0$.

Figure 8.6(a) shows the concentration, $\rho_s(x,t)$ as a function of lattice position x, at various times for a simulation with $\tau_s = 1$ and $u_x = 0$. Good agreement between the analytical concentration profile and that predicted from the LB method is apparent. The relative error was calculated as the absolute value of the difference between the analytical solution, Eq. (8.27),

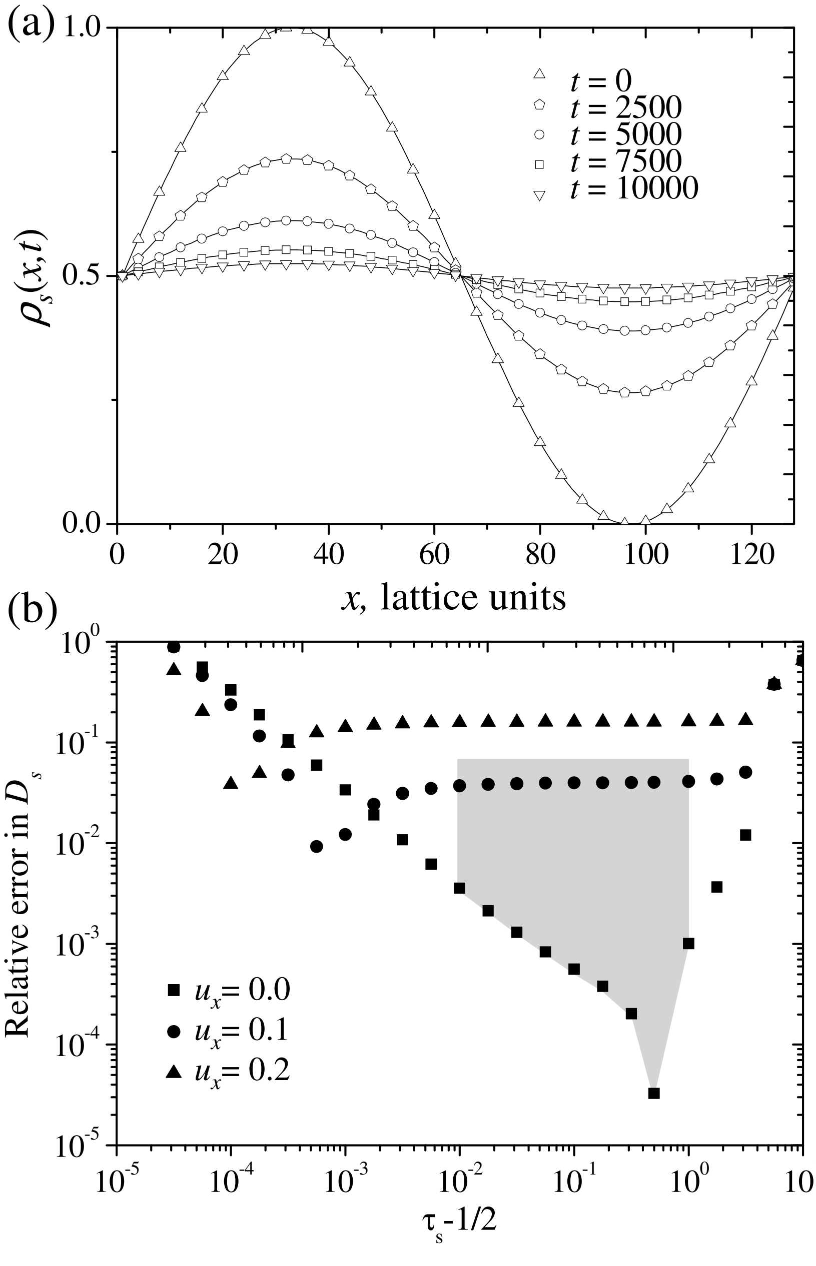

Figure 8.6: (a) Comparison between the analytical solution and LB results for the diffusive decay of a sinusoidal concentration profile, $\rho_s(x,t)$ against x after 0, 2500, 5000, 7500 and 10^5 time steps. Here, $\tau_s = 1$ and $u_x = 0$. (b) Relative error in the diffusion coefficient, D_s, as a function of $(\tau_s - 1/2)$ for $u_x = 0.0, 0.1$ and 0.2. The shaded region corresponds to values of τ_s used in sections 8.4.5 and 8.4.6.

and that calculated from Eq. (8.43), divided by the analytical solution. Figure 8.6(b) shows the relative error in D_s as a function of τ_s for the three different velocities, u_x. Here, for $0 < Pe < 10^6$ relative errors < 4 % in D_s were obtained. For simulations using double precision (8 byte, 64 bit), a value of $\tau_s = 1/2$ gave a finite diffusivity in lattice units of 4×10^{-6} and 6×10^{-6} for $u_x = 0$ and $u_x = 0.2$, respectively. For $\tau_s > 5$, ρ_s had equilibrated to a uniform density equal, within machine precision, to 1/2 after $t = 10^5$ time steps; therefore, errors were independent of u_x. The shaded region $0.51 \leq \tau_s \leq 1.0$ and $0.0 \leq u_x \leq 0.15$, corresponds to values used in the remainder of this dissertation.

8.3.3 Validation of reaction

Next, to verify the rate of reaction in the D3Q7 lattice Boltzmann program, a uniform concentration field undergoing a simple first order reaction was used:

$$\frac{d\rho_s(t)}{dt} = -k_i \rho_s(t). \tag{8.44}$$

The solution of the ODE given in Eq. (8.44) is:

$$\rho_s(t) = \rho_s(0)e^{-k_i t} \quad \text{or} \quad k_i = -\frac{1}{t}\ln\left[\frac{\rho_s(t)}{\rho_s(0)}\right], \tag{8.45}$$

where $\rho_s(0)$ is the initial concentration. A domain of $L_x = L_y = L_z = 3$ was used with periodic boundary conditions. Based on Eq. (8.30), the error in k_i is independent of velocity, $\mathbf{u}$, and relaxation time, τ_s. For the simulations, $\mathbf{u} = 0$ and $\tau_s = 1$ were used. The rate constant, the only parameter not fixed, was varied over the range $10^{-10} < k_i < 0.1$. Simulations were run over 10^5 time steps. The relative error in k_i was calculated as the absolute value of the difference between the theoretical value for k_i and that calculated from Eq. (8.45), divided by the theoretical value for k_i. Figure 8.7 shows the relative error in k_i against the theoretical value of k_i. For $k_i < 10^{-4}$, the relative error is $< 10^{-4}$; for $k_i > 10^{-4}$, the error increases as a result of the first-order forward Euler approximation to $\Delta\rho_s$. The shaded region corresponds to the values of k_i used in sections 8.4.5 and 8.4.6 with error < 0.035. Thus, the method for incorporating reaction in the lattice Boltzmann model for the current study gives satisfactory error estimates over a wide range of parameters.

Overall, sections 8.3.1-8.3.3 have used theoretical test problems with analytical solutions to demonstrate that hydrodynamics, mass transport and reaction can be accurately simulated with

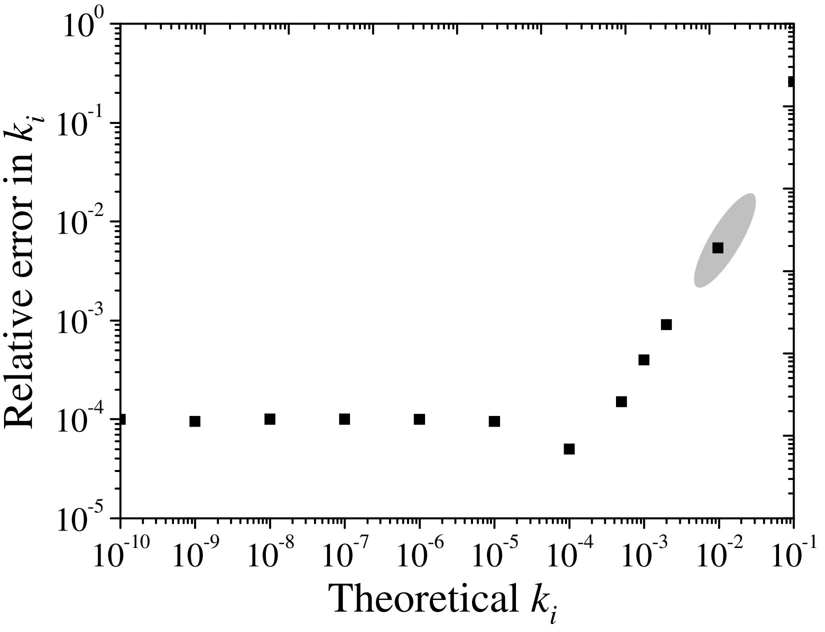

Figure 8.7: Relative error in the rate constant, k_i, from simulations *versus* theoretical k_i. The shaded region corresponds to the values of k_i used later in sections 8.4.5 and 8.4.6.

the lattice Boltzmann program implemented in this work. Next, verification of hydrodynamics, mass transport and reaction for systems containing a single sphere will be performed.

8.4 Comparison of the lattice Boltzmann model with experiments

8.4.1 Flow past a single sphere

To verify flow past a single sphere with the D3Q19 lattice Boltzmann model, the drag force as a function of *Re* was calculated. The domain size was $L_x = L_y = L_z = 50$. A single sphere was generated on the lattice Boltzmann grid by defining as solid all nodes (integer x, y, z) satisfying:

$$\left(x - \frac{L_x + 1}{2}\right)^2 + \left(y - \frac{L_y + 1}{2}\right)^2 + \left(z - \frac{L_z + 1}{2}\right)^2 \leq r^2, \qquad (8.46)$$

with $r = 4.8$. The non-integer value of r was found to give better results consistent with Mei *et al.* (2002). The centre of the sphere was off the lattice, *i.e.* not a lattice node. The sphere, shown in Fig. 8.8, was 10 lattice nodes across and contained a total of 480 nodes. Considering each node to have unit volume, the effective diameter of an equal-volume sphere was $d_\mathrm{p} = 9.714$, giving $L_x/d_\mathrm{p} \approx 5$.

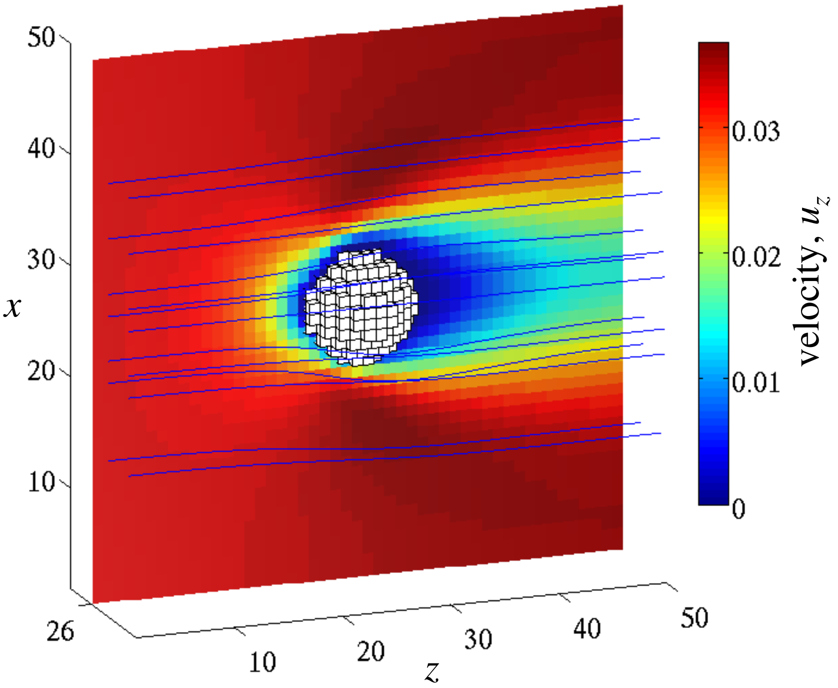

Figure 8.8: Velocity contours and streamlines for flow past a sphere at $Re = 20$. Here, the sphere is 10 lattice nodes across giving $d_\text{p} = 9.714$ and $1/s_{10} = 0.55$, $L_x = L_y = L_z = 50$ was used. The inlet conditions were $U = 0.0343$ and $\rho = 1$. Parameters given are in lattice units; flow was in the positive z direction.

Flow was in the positive z direction. At the inlet, the constant velocity boundary condition given by Eq. (8.33) was used to set U. At the outlet boundary, the no-flux condition of Eq. (8.31) was specified. In the x and y directions, periodic boundary conditions were applied. Halfway bounce-back boundary conditions were used at the interface between the solid sphere and fluid; no special treatment for the curved geometry was considered. The domain was initialised with $\rho = 1$ and $\mathbf{u} = 0$ everywhere, except at the inlet, where the inlet velocity condition was used. For the simulations, the parameter $1/s_{10} = 0.6$ was used to fix the kinematic viscosity from Eq. (A5.84) in all simulations except those with $Re = \{20, 50, 100, 150\}$ where $1/s_{10} = \{0.55, 0.56, 0.53, 0.52\}$ was used. The inlet velocity, U, was varied over $0.0001 \leq U \leq 0.1$. Thus, the parameters which were varied to alter the Re number were s_{10} and U; all other parameters were fixed. Simulations were run for 10^5 time steps until steady state was obtained. The Reynolds number was defined as:

$$Re = \frac{U d_\text{p}}{\nu}, \tag{8.47}$$

where U is the superficial inlet velocity.

Fig. 8.8 shows the velocity, u_z, for flow past a sphere with a diameter of 10 lattice nodes or, equivalently, with $d_{\mathrm{p}} = 9.714$ at $Re = 20$. The velocity near the surface of the sphere and in the wake of the sphere is nearly zero. A velocity increase from the inlet velocity is observed around the sphere and is necessary to accommodate for the constriction in the incompressible flow.

To determine the drag coefficient, C_{d}, the momentum-exchange method of Mei *et al.* (2002) was used. As *per* Mei *et al.* (2002), the scalar array $w_{\mathrm{s}}(\mathbf{x})$ is defined to take a value of 0 for a fluid node and 1 for a solid node. The scalar array $w_{\mathrm{b}}(\mathbf{x})$ is 0 everywhere except for those solid boundary nodes, $\mathbf{x}_{\mathrm{b}}$, which border the fluid. For a given non-zero velocity $\mathbf{v}_i$, $\mathbf{v}_i^-$ denotes the velocity in the opposite direction, so that $-\mathbf{v}_i = \mathbf{v}_i^-$. For a solid boundary node, $\mathbf{x}_{\mathrm{b}}$, with $w_{\mathrm{b}}(\mathbf{x}_{\mathrm{b}}) = 1$ and $w_{\mathrm{s}}(\mathbf{x}_{\mathrm{b}}) = 1$, the momentum exchanged with all neighbouring fluid nodes over a single time step $\Delta t = 1$ is then given by:

$$\sum_{i \neq 0} \mathbf{v}_i \left[f_i'(\mathbf{x}_{\mathrm{b}}, t) - f_i^{\prime -}(\mathbf{x}_{\mathrm{b}} + v_i^- \Delta t, t) \right] \left[1 - w_{\mathrm{s}}(\mathbf{x}_{\mathrm{b}} + v_i^- \Delta t) \right]. \tag{8.48}$$

The total force acting on a solid body can then be calculated by summing Eq. (8.48) over all boundary nodes belonging to it:

$$\mathbf{F} = \sum_{\mathbf{x}_{\mathrm{b}}} \sum_{i \neq 0} \mathbf{v}_i \left[f_i'(\mathbf{x}_{\mathrm{b}}, t) - f_i^{\prime -}(\mathbf{x}_{\mathrm{b}} + v_i^- \Delta t, t) \right] \left[1 - w_{\mathrm{s}}(\mathbf{x}_{\mathrm{b}} + v_i^- \Delta t) \right], \tag{8.49}$$

where the force is evaluated after the collision step. To summarise, the momentum exchanged between a solid body and the surrounding fluid can be calculated using those f_i which stream between solid and fluid phases in a given time step.

Next, for the simulated system,

$$C_{\mathrm{d}} = \frac{|F_z|}{\frac{\rho}{2} U^2 \pi \left(\frac{d_{\mathrm{p}}}{2} \right)^2}, \tag{8.50}$$

was calculated with $\rho = 1$ and $d_p = 9.714$. For $Re < 0.1$, *i.e.* Stokes' flow,

$$C_{\mathrm{d}} = \frac{24}{Re} \quad Re < 0.1, \tag{8.51}$$

whilst for larger Re, the empirical equation:

$$C_{\mathrm{d}} = \left(\sqrt{\frac{24}{Re}} + 0.5407 \right)^2 \quad Re < 6000, \tag{8.52}$$

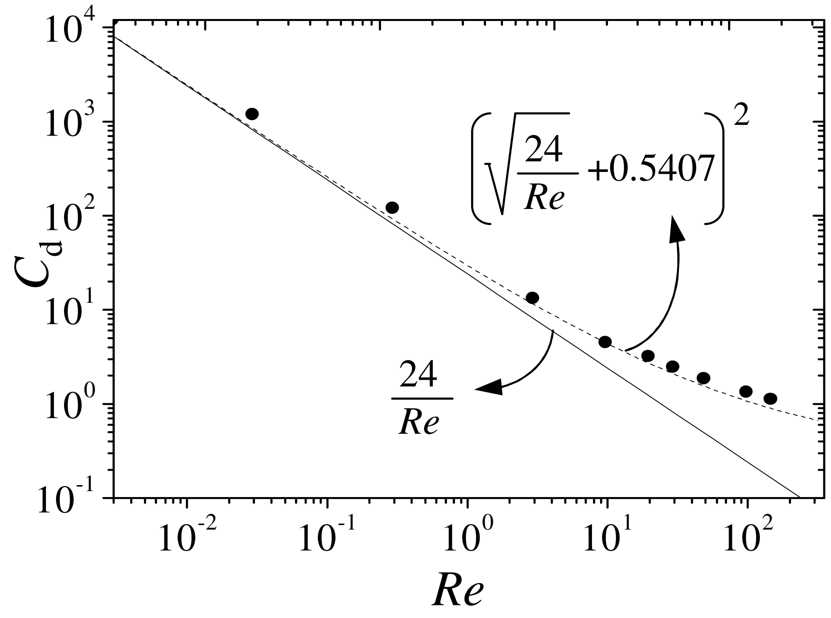

Figure 8.9: Drag coefficient, C_d, as a function of Reynolds number, *Re*, for laminar flow past a sphere. Correlations are lines; simulations results are shown by (●).

from Bird *et al.* (2007) can be used. Figure 8.9 shows that C_d derived from the lattice Boltzmann simulations agrees with the C_d predicted from Eqs. (8.51) and (8.52) for a sphere with as few as 10 lattice nodes in diameter and further validates the hydrodynamic results of the current lattice Boltzmann model.

8.4.2 Effectiveness factor for a single sphere

To validate the D3Q7 lattice Boltzmann program, the effectiveness factor for a first-order, irreversible reaction in a porous, spherical catalyst pellet was calculated. The analytical solution is given by (Thiele, 1939) as outlined in Appendix 4:

$$\eta = \frac{3}{\phi^2}(\phi\coth(\phi) - 1) \qquad \phi = \frac{d_\mathrm{p}}{2}\sqrt{\frac{k_i}{D_s}}. \tag{8.53}$$

It is assumed that the heat of reaction is negligible. Spheres of varying diameter were constructed using Eq. (8.46) with $r = \{2.8, 4.8, 9.8, 24.8, 49.8\}$, giving effective diameters in lattice units of $d_\mathrm{p} = \{5.519, 9.714, 19.549, 49.634, 99.594\}$. The domain size was varied so that the sphere was circumscribed by at least one fluid node in all directions. An equilibrium boundary condition was used to fix the concentration of the exterior fluid by specifying $\rho_s = 1$ and $\mathbf{u} = 0$ for all fluid nodes after each streaming step. The initial conditions were $\rho_s = 0,\ \mathbf{u} = 0$ for solid nodes and $\rho_s = 1,\ \mathbf{u} = 0$ for fluid nodes. The macroscopic fluid velocity used as input to the D3Q7 model was $\mathbf{u} = 0$ over the entire domain for all time. For the present simulations τ_s was fixed to 1 or 0.55 and k_i was varied to give $\phi = d_\mathrm{p}/2 \times \sqrt{k_i/D_s} = \{0.01, 0.1, 1, 10, 100\}$. Thus, the parameters which varied were k_i and d_p; only for $\phi = 10$ in Fig. 8.10(b) was τ_s also changed. All other parameters were fixed. Simulations were run for 10^5 time steps to permit a constant, steady state concentration profile to evolve within the catalyst pellet.

The observed rate at steady state was evaluated as:

$$k_i \sum_{\mathbf{x}} \rho_s(\mathbf{x}) w_\mathrm{s}(\mathbf{x}), \tag{8.54}$$

where $w_\mathrm{s}(\mathbf{x})$ is a scalar array which takes the value of 0 or 1 for fluid or solid nodes, respectively. The effectiveness factor from simulations was then calculated using:

$$\eta = \frac{k_i \sum_{\mathbf{x}} \rho_s(\mathbf{x}) w_\mathrm{s}(\mathbf{x})}{k_i \sum_{\mathbf{x}} w_\mathrm{s}(\mathbf{x})}, \tag{8.55}$$

where $\rho_s(\mathbf{x}) = 1$ in the surrounding fluid has been used in the denominator. Figure 8.10(a) shows the effectiveness factor calculated using Eq. (8.55) against Thiele modulus, ϕ. In all cases in Fig. 8.10(a), $\tau_s = 1$. Good agreement between simulations and the analytical solution for $\phi \leq 10$ is observed. The relative error in the effectiveness factor was found to be < 2.2 % for $\phi \leq 1$; the error increased with increasing ϕ, and decreased with increasing d_p.

The increasing error with increasing ϕ can be explained by two factors. First, to increase ϕ at a fixed d_p and τ_s, k_i must be increased as shown by Eq. (8.53) and using Eq. (8.27) to evaluate D_s. However, increasing k_i for this first-order reaction will eventually result in $O(k_i \rho_s) = O(\Delta\rho_s) \approx O(\rho_s)$. Once the change in ρ_s over a single time step is of the order of the existing ρ_s, the forward Euler method used in section 8.2.6 to incorporate $\Delta\rho_s$ will produce errors. Indeed, at $\phi = 100$, only the sphere with $d_\mathrm{p} = 99.594$ in Fig. 8.10(a) returned positive ρ_s over the entire domain; therefore, only this point has been plotted. Errors can be reduced by either reducing k_i or by using a more accurate scheme for numerical integration (Sullivan, 2006), *e.g.* Runge-Kutta. Figure 8.10(b) shows that better results were indeed obtained for simulations with $\tau_s = 0.55$ and k_i values one tenth those for simulations with $\tau_s = 1$. Second, as ϕ is increased the reaction only occurs near the boundary of the sphere. For large ϕ if the grid spacing Δx is not kept less than the width of the front $\sqrt{D_s/k_i}$ substantial errors as a result of the low accuracy of the equilibrium boundary conditions will be incurred. Overall, it has been shown that the present method for incorporating mass transfer and reaction can accurately

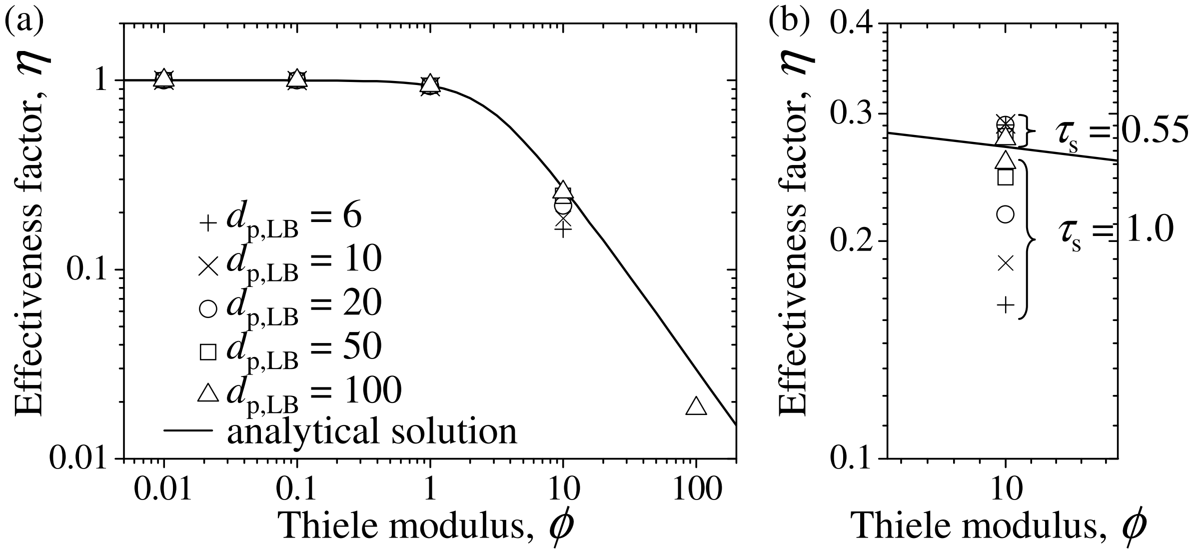

Figure 8.10: (a) Effectiveness factor, η, as a function of Thiele modulus, ϕ, for a first order reaction in a sphere of effective diameter, d_p. (b) Effectiveness factor, η, at $\phi = 10$ for spheres of varying diameter, d_p. For $\tau_s = 0.55$ the values of k_i used in simulations were smaller than those required for $\tau_s = 1$ for the same value of ϕ and better agreement with the analytical solution was observed.

predict the behaviour of catalyst pellets over a wide range of Thiele moduli, provided suitable values for k_i, τ_s, *i.e.* the diffusivity, and the grid spacing are chosen.

8.4.3 Mass transfer to the surface of a particle

To verify mass transfer to the surface of a sphere, the D3Q7 lattice Boltzmann model for mass transport of passive scalar was used together with the D3Q19 lattice Boltzmann model for hydrodynamics. The computational domain was of dimension $L_x = L_y = L_z = 50$, and the effective diameter of the sphere was $d_\mathrm{p} = 9.714$. The steady state macroscopic velocity field from the hydrodynamic simulations in section 8.4.1 was used as input for the mass transfer simulations with the velocity of solid nodes set to zero and was fixed for all time. Boundary and initial conditions will not be repeated.

For mass transport, the constant concentration boundary condition given by Eq. (8.34) such that $\rho_s = 1$ was used at the inlet ($z = 1$). At the outlet ($z = L_z$), a zero flux boundary given by Eq. (8.32) was used. In the x and y directions, periodic boundary conditions were applied. Any mass entering the sphere was destroyed by setting $f_{i,s} = 0$ for all i within the sphere prior to each streaming step. The initial conditions were $\rho_s = 0$ everywhere, except at the inlet where the inlet boundary condition, $\rho_s = 1$ was used. For simulations, the parameters which varied were U, the inlet velocity of the bulk fluid, $1/s_{10}$, the viscosity of the bulk fluid, and τ_s,

Table 8.2: Parameters used in simulations to produce Fig. 8.11.

U	0.01	0.03	0.033	0.1	0.1	0.1	0.1
$1/s_{10}$	0.6	0.6	0.55	0.6	0.56	0.53	0.52
τ_s	0.6	0.6	0.55	0.6	0.56	0.53	0.52
Re	3	9	20	29	49	98	148
Sc	1	1	1	1	1	1	1

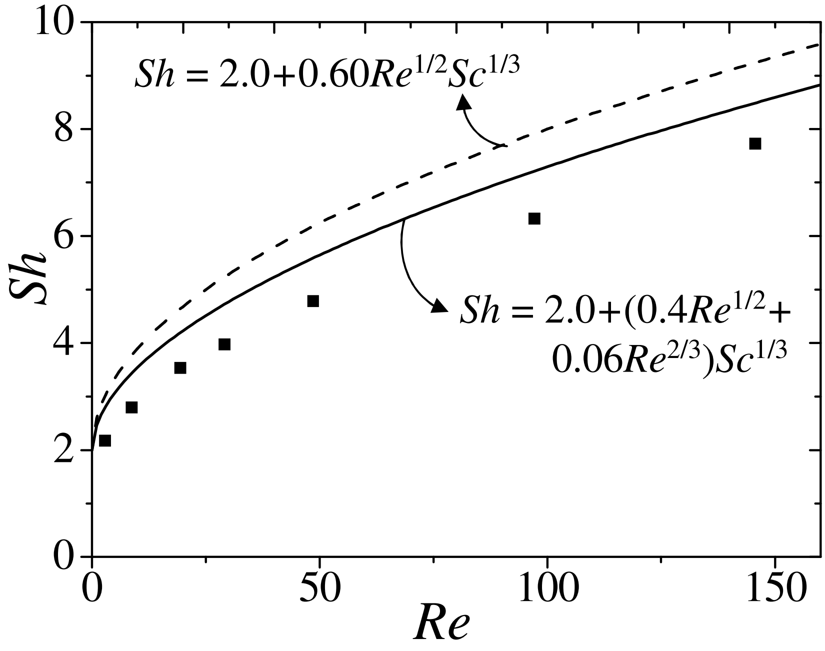

Figure 8.11: Sherwood number, Sh, as a function of Reynolds number, Re. Here, the Schmidt number, $Sc = 1$.

the diffusivity of the passive scalar; all other parameters were fixed. Table 8.2 lists the input parameters used to produce Fig. 8.11. Simulations were run for 10^5 time steps.

The rate was related to a mass transfer coefficient using the following expression at steady state:

$$\underbrace{k_g A_s (c_{out} - c_s)}_{\text{mass transfer rate}} = \underbrace{\sum_{x,y} \rho_s(x,y,1) u_z(x,y,1)}_{\text{mass in}} - \underbrace{\sum_{x,y} \rho_s(x,y,L_z) u_z(x,y,L_z)}_{\text{mass out}}, \tag{8.56}$$

where k_g is the mass transfer coefficient, $A_s = \pi d_p^2 = \pi(9.714)^2$ is the surface area of the sphere, $c_{out} = \rho_s \approx 1$ is the concentration in the bulk and $c_s = \rho_s \approx 0$ is the concentration at the surface of the sphere. The Sherwood number, Reynolds number, and Schmidt number were defined as follows:

$$Sh = \frac{k_g d_p}{D_{mix}}, \quad Re = \frac{U d_p}{\nu}, \quad Sc = \frac{\nu}{D_{mix}}, \tag{8.57}$$

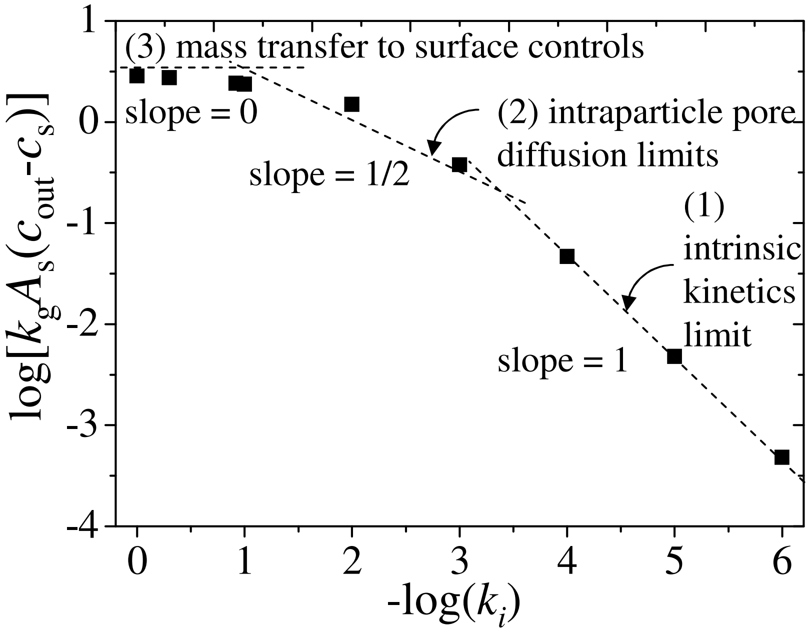

Figure 8.12: Calculated rate against the intrinsic rate constant, k_i. As k_i is increased or $-\log(k_i)$ is decreased, three regimes corresponding to (1) the rate being limited by intrinsic kinetics (2) the rate being limited by intraparticle diffusion and (3) the rate being limited by mass transfer to the particle surface are evident.

where $D_{\mathrm{mix}} = D_s$ is the diffusivity of the scalar in the bulk fluid mixture. To compare the simulated values of k_{g} with values from the literature, the most common correlation for $Sh(Re, Sc)$ given by Ranz and Marshall (1952) for $Re \geq 0$ was used:

$$Sh = 2.0 + 0.6Re^{1/2}Sc^{1/3}, \tag{8.58}$$

where it is noted that the original correlation was for the Nusselt number, the heat transfer analogue of the Sherwood number (Bird *et al.*, 2007). For $Re > 3.5$, Whitaker (1972) subsequently gave the correlation:

$$Sh = 2.0 + (0.4Re^{1/2} + 0.06Re^{2/3})Sc^{0.4}, \tag{8.59}$$

as an alternative to Eq. (8.58). Figure 8.11 shows the calculated Sherwood number based on k_g determined from simulations against Reynolds number compared to the correlations of Eqs. (8.58) and (8.59). The non-linear increase in Sh with Re is captured; however, the present LB simulations underpredict Sh. Better results for Sh might be obtained by either increasing the size of the sphere or by enforcing $\rho_s = 1$ for the bulk fluid on all six sides of the 3D cubic domain, not just at the inlet.

Next, rather than eliminating the passive scalar entering the sphere, reaction and diffusion within the sphere was incorporated for the flow with $Re = 20$. Thus, rather than setting $f_{i,s} = 0$ for all i within the sphere prior to each streaming step, the entering $f_{i,s}$ were streamed over the entire sphere. The effective diffusivity within the sphere was set to a value half that of the molecular diffusion in the fluid by setting $\tau_s = 0.55$ in the fluid and $\tau_s = 0.525$ within the sphere. The boundary and initial conditions were identical to those used previously to produce the point corresponding to $Re = 20$ in Fig. 8.11. The rate constant, k_i, was then varied between 10^{-6} and 1; all other parameters were fixed as specified by column 3 of Table 8.2 for flow at $Re = 20$. Figure 8.12 shows the rate, calculated using Eq. (8.56), against the rate constant, k_i. Three distinct kinetic regimes are apparent. In regime (1), intrinsic kinetics are rate limiting and any increase in k_i results in a commensurate increase in the rate. As such, the dashed line in regime (1) has a slope of unity. In regime (2), intraparticle diffusion begins to limit the rate and the slope decreases to approximately half that from the kinetically controlled regime (1). In regime (3), mass transfer to the particle surface is limiting. Here, increasing k_i does not result in an increase in the rate. The intercept of the horizontal dashed line in regime (3) with the ordinate corresponds to the value of the rate calculated using the left hand side of Eq. (8.56), with k_{g} determined from the correlation of Ranz and Marshall, Eq. (8.58). The numerical increase in k_i is tantamount to an increase in temperature in experimental work; and plots similar to Fig. 8.12 have been observed for experimental gas-solid reactions in porous catalyst, *e.g.* Fig. 11.2 in Satterfield (1980).

8.4.4 Flow in a packed bed

Next, flow through a packed bed was investigated with the D3Q19 lattice Boltzmann model. A computational domain of $L_x = L_y = 102$ and $L_z = 800$ lattice nodes was used. In total, 297 particles, each approximately 20 lattice nodes across were placed into the centre of the domain between lattice nodes $252 \leq z \leq 538$. The position of the particles was determined with a discrete element model (Third *et al.*, 2010) by dropping sheets of spheres into a cylinder and tapping. A schematic diagram of the packed bed is shown in Fig. 8.13(a).

Figure 8.13(b) shows the position of the centre of the 297 spheres in the $x - y$ plane. Two distinct rings and one central point can be seen. This is a typical packing arrangement for a system with $d_{\mathrm{bed}}/d_{\mathrm{p}} = 5$. The scatter of the location of the centre of the spheres increases towards the centre. Figure 8.13(c) shows the position of the centre of the spheres in the $x - z$ and $y - z$ planes. The centres corresponding to the initial row of spheres are located between

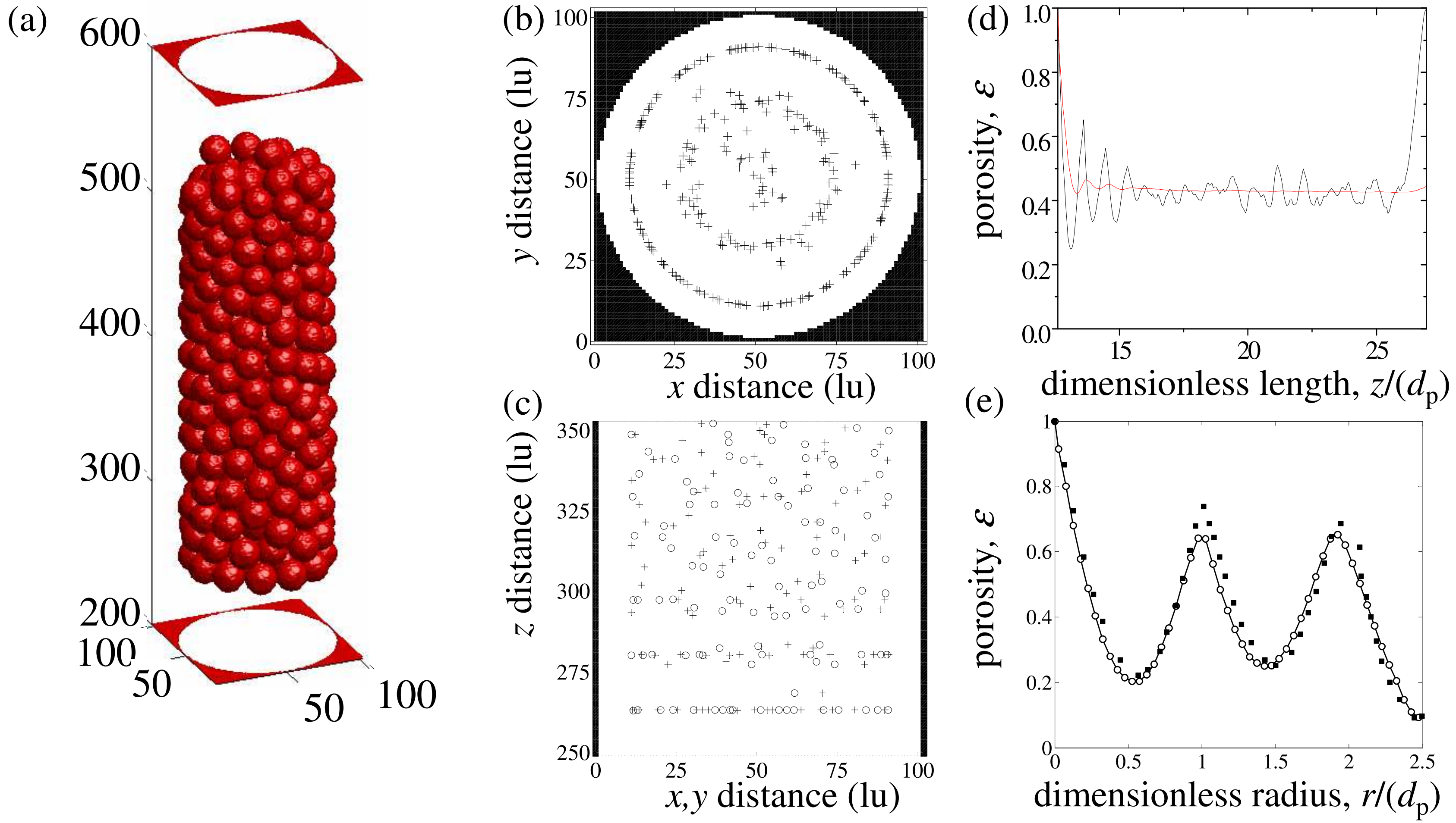

Figure 8.13: (a) Diagram of the packed bed comprising 297 particles each with $d_\mathrm{p} \approx 20$; the tube had a diameter of $d_\mathrm{p} \approx 100$. The computational domain consisted of $L_x = L_y = 102$ and $L_z = 800$ nodes. (b) Position, in the $x - y$ plane, of the centre points of the 297 spheres comprising the packed bed shown in (a). (c) Position, in the $x - z$ (+) and $y - z$ (○) planes, of the centres of the spheres forming an initial portion of the packing. (d) Porosity as a function of position, z, for a slice in the $x - y$ plane (black) and the average of all preceding slices (red). (e) Mean porosity as a function of radial position (○) and corresponding results from Zeiser (2008)(■). Here, $r = 0$ is defined to as the axis of the bed. All dimensions are in lattice units (lu); conversion to physical units for results in section 8.4.6 is performed using $\Delta x = 10^{-4}$ m/(lattice unit).

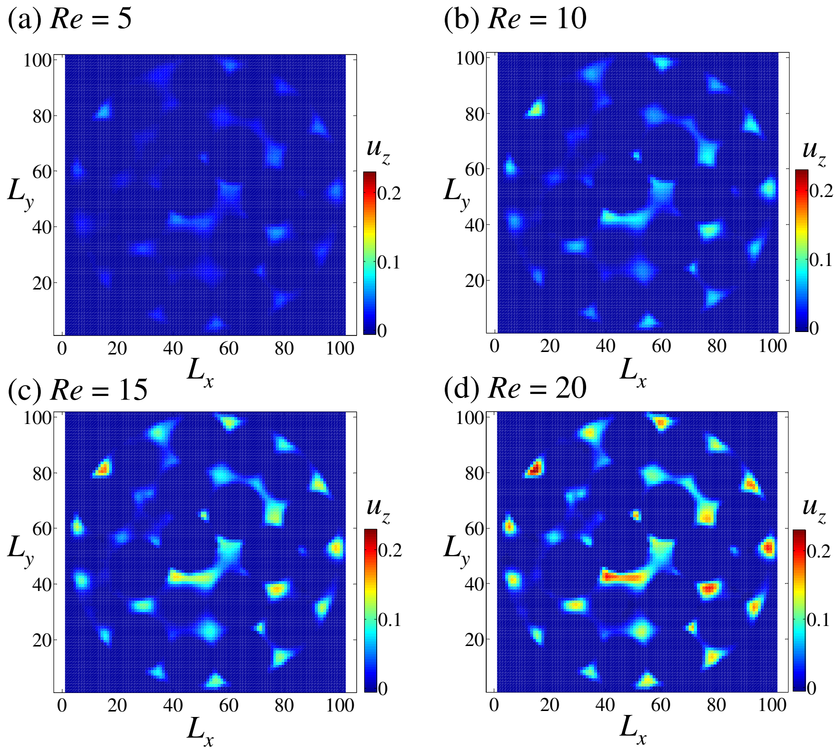
(a) $Re = 5$ (b) $Re = 10$ (c) $Re = 15$ (d) $Re = 20$

Figure 8.14: Cross-section of flow through the bed at $z = 400$ corresponding to the centre of the packing for (a) $Re = 5$ (b) $Re = 10$ (c) $Re = 15$ (d) $Re = 20$. The velocity, u_z, given in lattice units increases with Re.

$L_z = 262 - 263$; increasing scatter in the location of the centrepoints is evident with increasing z. Figure 8.13(d) shows the porosity of a single slice in the $x-y$ plane as a function of position z as well as the porosity averaged over all preceding slices in the $x - y$ plane as a function of position z. The porosity at $L_z = 251.5$, *i.e.* the start of the packing, was manually set to 0 owing to the halfway bounce-back boundary conditions. The mean porosity within the packing, calculated as the integer number of fluid nodes divided by the total number of nodes within the tube between $252 \leq z \leq 538$, was $\varepsilon = 0.429$, compared to a theoretical porosity from the DEM simulations of $\varepsilon = 0.413$. The difference is a result of discretisation of both the tube and the particles. Figure 8.13(e) shows the porosity as a function of radial position and was in good agreement with the results of Zeiser (2008).

For fluid flow, a non-equilibrium boundary condition (Zou and He, 1997) was used to fix the superficial inlet velocity, U, using Eq. (8.33). No special treatment of corner or edge nodes at the inlet was necessary. At the outlet, the zero flux boundary condition of Eq. (8.31) was applied after streaming. Halfway bounce-back boundaries were applied between fluid and solid nodes, *i.e.* between both the fluid and the tube and between the fluid and the solid particles. The superficial velocity at the inlet was ramped in a linear fashion over 5×10^4

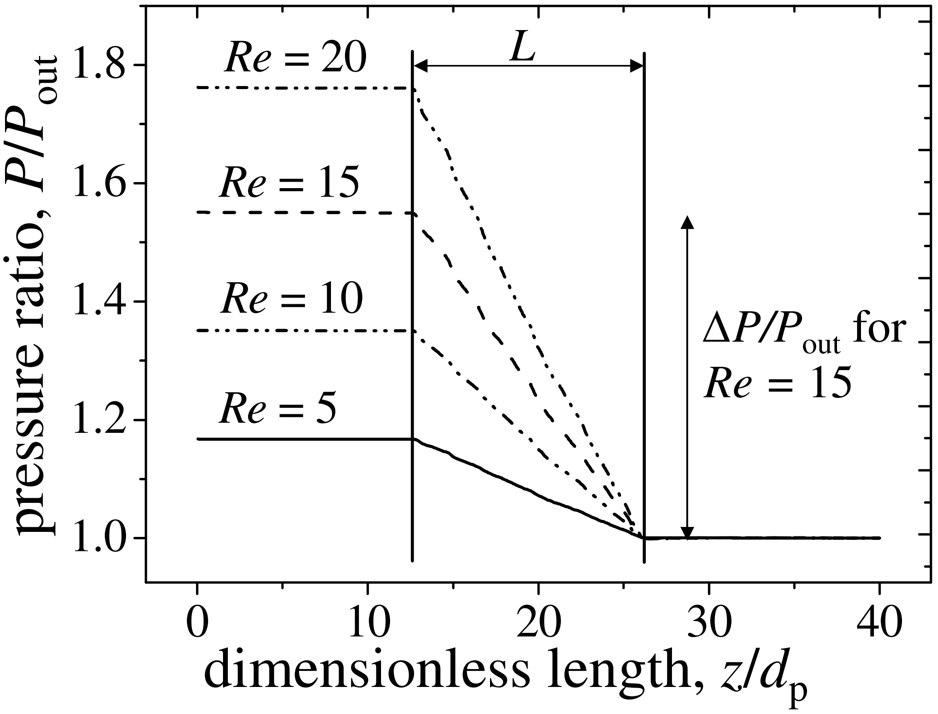

Figure 8.15: Pressure, P/P_{out} as a function of dimensionless length, z/d_{p}, showing a linear pressure drop through the packing.

time steps from a starting value of 0. The initial condition was $\rho = 1$ and $\mathbf{u} = 0$ over the entire domain. The Reynolds number was defined as $Re = Ud_{\mathrm{p}}/\nu$, where d_{p} is the effective particle diameter, U is the superficial velocity at the inlet, and ν is the kinematic viscosity. The flow through the packing was investigated at $Re = \{5, 10, 15, 20\}$ by setting $1/s_{10} = 0.55$ and varying $U = \{0.0042, 0.0083, 0.0125, 0.0167\}$. Thus, the only parameter which varied was U; all other parameters were fixed. Simulations were run until steady state for a total of 2×10^5 time steps.

The uniform velocity profile at the inlet changed to a parabolic velocity profile prior to the packing, then became distorted as the fluid passed through the interstices. High velocity flow through the interstices is evident from Fig. 8.14 which shows the velocity, u_z, through a central cross-section of the bed at $z = 400$ for $Re = \{5, 10, 15, 20\}$. As Re increases, the maximum magnitude of the velocity, u_z, increases.

The pressure drop through the packing was linear and is shown in Fig. 8.15. As a comparison, the pressure drop from the correlation of Zhavoronkov *et al.* (1949), which is similar to the correlation of Ergun and Orning (1949), but accounts for low ratios of tube to particle diameter was calculated as outlined in Freund *et al.* (2003). Agreement in the pressure drop, $\Delta P/L$ where L is the length of the packed bed and P is the pressure from Eq. (A5.90), with the simulated results was better than 0.6 % for all four values of *Re* using $\varepsilon = 0.413$, the true porosity predicted from the DEM simulation.

8.4.5 Reaction of a single particle

Next experimental results and simulations with the D3Q7 lattice Boltzmann model for the reduction of a single, spherical particle of Fe_2O_3 to Fe_3O_4 *via* reaction (1.9):

$$3\,\mathrm{Fe_2O_3} + \mathrm{CO} \rightleftarrows 2\,\mathrm{Fe_3O_4} + \mathrm{CO_2}, \qquad \Delta H^{\circ}_{1023\,\mathrm{K}} = -44.3\mathrm{kJ/mol} \tag{8.60}$$

were compared. The relevant physical parameters for the current problem were determined as follows. The diameter of the particle of Fe_2O_3 was 2 mm. From Table 5.1, the effective diffusivity of CO within a particle at 1023 K was $D_{\mathrm{e,CO}} = 2.5 \times 10^{-5}$ m^2/s. From Eq. (5.19), the intrinsic rate constant was $k_i = 2.4 \times 10^7 \exp(-75000/\mathrm{R}T) = 3550$ s^{-1}. The concentration of CO in the gas surrounding the particle was 0.6 mol/m^3. The molar density of reactive Fe_2O_3 initially present was determined using the mass density of Fe_2O_3 (5150 kg/m^3) and porosity of the particles ($\varepsilon_\mathrm{p} = 0.6$) as follows:

$$\begin{aligned} n_{\mathrm{Fe_2O_3}}\Big|_{t=0} &= \frac{5150\ \mathrm{kg}}{\mathrm{m}^3} \times \frac{1\ \mathrm{kmol\ Fe_2O_3}}{159.7\ \mathrm{kg}} \\ &\times \frac{(1-0.6)}{1} \times \frac{0.8}{1} = 10.3\ \frac{\mathrm{kmol}}{\mathrm{m}^3}, \end{aligned} \tag{8.61}$$

where the factor of 0.8 comes from the experimental observation that maximum conversions of ~ 80 % are achieved, as shown in Fig 5.9. Thus, for the current problem $\phi = d_\mathrm{p}/2 \times \sqrt{k_i/D_{\mathrm{e,CO}}} = 20$.

For the experiments, mechanically-mixed particles of Fe_2O_3 were prepared as described in Chapter 2, section 2.2. For reduction experiments, the fluidised bed, sampling line and analysers described in Chapter 5, section 5.2 were used. In all cases, the reduction of Fe_2O_3 to Fe_3O_4 was studied at 1023 K and 10^5 Pa, using mixtures of $CO+CO_2+N_2$ (respectively, 5, 15 and 80 vol. %) during reduction to give $c_{\mathrm{CO}} = 0.6$ mol/m^3; during oxidation, air (21 O_2, 79 vol. % N_2) was used. From thermodynamics (Barin and Knacke, 1973), these compositions will generate Fe_3O_4 and Fe_2O_3, respectively. The total flowrate of gas through the fluidised bed was fixed at 1.6×10^{-4} m^3/s, giving $U/U_{\mathrm{mf}} = 7$ as shown in Table 5.1. As in Chapter 5, the fluidised bed could be assumed to be well-mixed.

In a typical experiment, particles of Fe_2O_3 with $d_\mathrm{p} = 2$ mm were counted, weighed and then

Table 8.3: Table relating the parameters in physical units to lattice units. Here, $\Delta x = 4 \times 10^{-5}$ m/(lattice unit), $\Delta t = 1 \times 10^{-5}$ s/(time step), $\Delta n/\Delta x^3 = 0.6$ mol/m^3 .

	Physical			Lattice		
Symbol	**Value**	**Units**	**Symbol**	**Value**	**Relaxation**	**Scaling**
L_x	0.00208	m	$L_{x,\mathrm{LB}}$	52		$L_x = L_{x,\mathrm{LB}} \times \Delta x$
L_y	0.00208	m	$L_{y,\mathrm{LB}}$	52		$L_y = L_{y,\mathrm{LB}} \times \Delta x$
L_z	0.00208	m	$L_{z,\mathrm{LB}}$	52		$L_x = L_{z,\mathrm{LB}} \times \Delta x$
d_p	0.002	m	$d_{\mathrm{p,LB}}$	50		$d_\mathrm{p} = d_{\mathrm{p,LB}} \times \Delta x$
ρ_CO	0.6	mol/m^3	$\rho_{\mathrm{CO,LB}}$	1		$\rho_\mathrm{CO} = \rho_{\mathrm{CO,LB}} \times \Delta n/\Delta x^3$
$n_{\mathrm{Fe_2O_3}}$	10320	mol/m^3	$n_{\mathrm{Fe_2O_3,LB}}$	17200		$n_{\mathrm{Fe_2O_3}} = n_{\mathrm{Fe_2O_3,LB}} \times \Delta n/\Delta x^3$
k_i	$2.4 \times 10^7 \exp(-75000/\mathrm{R}T)$	s^{-1}	$k_{i,\mathrm{LB}}$	0.0355		$k_i = k_{i,\mathrm{LB}}/\Delta t$
$D_{\mathrm{e,CO}}$	2.5×10^{-5}	m^2/s	$D_{\mathrm{e,CO,LB}}$	$1/4(\tau_\mathrm{CO} - 1/2)$	$\tau_\mathrm{CO} = 1.0$	$D_{\mathrm{e,CO}} = D_{\mathrm{e,CO,LB}} \times \Delta x^2/\Delta t$

dropped into the fluidised bed operated at 1023 K. In each case, 20 particles corresponding to ~ 0.15 g of Fe_2O_3 were introduced to the bed and resulted in an initial change in the effluent CO by < 0.5 vol. % or < 10 % of the inlet value. After a specified time, the inlet gas to the bed was switched to inert N_2 to prevent further reaction using solenoid valves controlled by a timer. The bed was subsequently cooled to room temperature under the flow of N_2; the reacted particles were then sieved to separate them from the inert Al_2O_3 bed material which had a smaller diameter, $d_\mathrm{p} = +300, -425$ μm. Reacted particles were fixed in an acrylic resin (Kleer-Mount, MetPrep) and cross-sectioned by light sanding for analysis with an optical microscope (Leica DM/LM) at 5× magnification in dark field mode. Image analysis to measure the location of the phase boundary between Fe_2O_3 and Fe_3O_4 was performed with conventional software (analySIS Image Processing).

For the lattice Boltzmann simulations, the domain size was $L_x = L_y = L_z = 52$. A single particle was initialised using Eq. (8.46) with $r = 24.8$ in lattice units, giving a sphere 50 nodes across or 2 mm in physical units. Thus, the particle was enclosed by a minimum of one fluid node in every direction. No flow was modelled, *i.e.* the hydrodynamic D3Q19 model was not used; rather, only the D3Q7 model for a passive scalar for CO was employed as outlined in section 8.2.5 using a distribution, $f_{i,\mathrm{CO}}$. A separate variable, $n_{\mathrm{Fe_2O_3}}(\mathbf{x}, t)$, was used to follow the conversion of the Fe_2O_3. Because the Fe_2O_3 is not advected, however, a separate distribution function for Fe_2O_3 was not required.

As in section 8.4.2, equilibrium boundary conditions were used to set $\rho_\mathrm{CO}(\mathbf{x}, t) = 0.6$ mol/m^3 over all fluid nodes for all time. Additionally, $\mathbf{u}(\mathbf{x}, t) = 0$ was set over the entire domain for all time. Thus, only the D3Q7 model was required, not the D3Q19 model. The initial conditions were $\rho_\mathrm{CO}(\mathbf{x}, 0) = 0.6$ mol/m^3, $n_{\mathrm{Fe_2O_3}}(\mathbf{x}, 0) = 0$ for fluid nodes, whilst for the solid nodes of the sphere $\rho_{\mathrm{CO}}(\mathbf{x},0) = 0$, $n_{\mathrm{Fe_2O_3}}(\mathbf{x},0) = 10.3$ kmol/m^3 was used. Conversion between physical and lattice units was performed as outlined in section 8.2.9. The parameters used for the simulation are summarised in Table 8.3.

The rate of reduction of Fe_2O_3 to Fe_3O_4 was previously given in units of mol/(s g) by Eq. (5.19):

$$r' = \frac{2.4 \times 10^7 \exp(\frac{-75000}{RT})}{\rho_{\mathrm{Fe_2O_3}}} \left(c_{\mathrm{CO}} - \frac{c_{\mathrm{CO_2}}}{K_p} \right) \left(1 - \frac{X}{0.8} \right)^{0.4} . \qquad 0 \leq X \leq 0.8 \tag{8.62}$$

Based on the large equilibrium constant at 1023 K, $K_p = 1.47 \times 10^5$, the back reaction is however negligible. Additionally, the exponent, 0.4, was set to unity to simplify the rate expression. In the model, the conversion X at each lattice point was determined using:

$$X(\mathbf{x},t) = 0.8 \left(1 - \frac{n_{\mathrm{Fe_2O_3}}(\mathbf{x},t)}{n_{\mathrm{Fe_2O_3}}(\mathbf{x},0)} \right), \tag{8.63}$$

with $n_{\mathrm{Fe_2O_3}}(\mathbf{x},0) = 10.3$ kmol/m^3. Therefore, the overall expression for the rate of reaction as a function of conversion for the lattice Boltzmann model was in units of (mol/s m^3):

$$\frac{d\rho_{\mathrm{CO}}(\mathbf{x},t)}{dt} = -k_i \rho_{\mathrm{CO}}(\mathbf{x},t) \left(1 - \frac{X}{0.8} \right) = -k_i \rho_{\mathrm{CO}}(\mathbf{x},t) \left(\frac{n_{\mathrm{Fe_2O_3}}(\mathbf{x},t)}{n_{\mathrm{Fe_2O_3}}(\mathbf{x},0)} \right), \tag{8.64}$$

and was incorporated as outlined in section 8.2.6. It should be noted that the factor of 0.8 in Eqs. (8.61) and (8.63) permits a consistent definition of conversion, X, for both experiments and the LB simulation, *i.e.* the initial conversion is $X = 0$ and the final conversion is $X = 0.8$ in both cases. The simulation was run for a total of 6×10^6 time steps corresponding to 60 s. Finally it should be noted that the problem's symmetry was exploited and only one eighth of a particle was actually modelled.

Figure 8.16 shows the experimental cross-section and corresponding cross-section from the D3Q7 lattice Boltzmann simulation for the reduction of a single sphere of Fe_2O_3 to Fe_3O_4 as a function of time, t. Initially, at $t = 0$ the particle is entirely Fe_2O_3 and $X = 0$. As the reaction progresses, the front between Fe_2O_3 and Fe_3O_4 moves progressively towards the centre of the particle. Qualitatively good agreement between the model and simulation is observed by comparing the experimental and model predictions at $t = 10, 30$ and 40 s. Quantitatively, the thickness of the Fe_3O_4 shell at $t = 10, 30$ and 40 s determined from simulations using the arbitrary cut-off of $X = 0.4$ gave 280, 480 and 620 μm. For comparison, the experimental boundaries estimated from the intersection of black and red phases at identical times from the

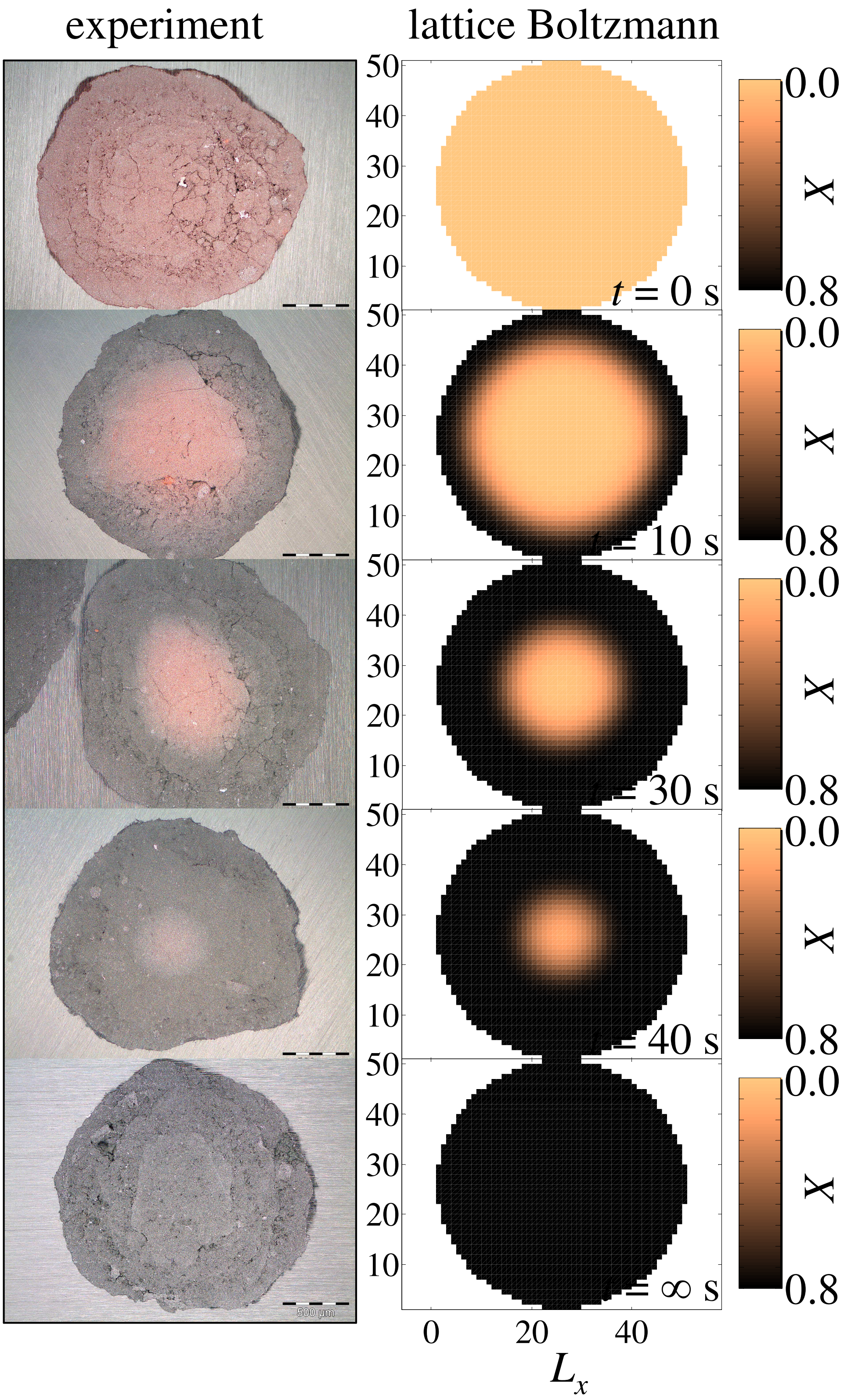

Figure 8.16: Experimental cross-section (left) and lattice Boltzmann simulation (right) for reduction of a particle of Fe_2O_3 ($X = 0$) to mostly Fe_3O_4 ($X = 0.8$) in $CO+CO_2+N_2$ (5, 15, 80 vol %, respectively) at 1023 K. The physical parameters were $D_{e,CO} = 2.5 \times 10^{-5}$ m^2/s, $k_i = 2.4 \times 10^7 \exp(-75000/RT) = 3550$ s^{-1} and $d_p = 2$ mm. Scalebar = 500 μm.

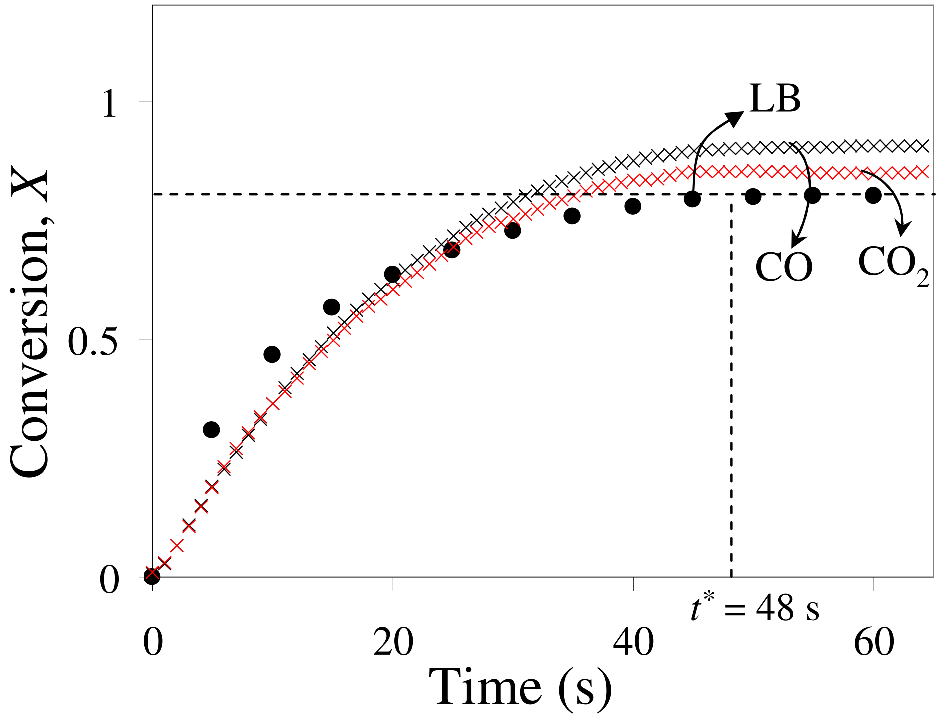

Figure 8.17: Conversion, X, *versus* time, t, for the reduction of a sphere, $d_p = 2$ mm, of Fe_2O_3 to mostly Fe_3O_4 ($X = 0.8$) at 1023 K and 10^5 Pa measured using experimental CO consumption (×), experimental CO_2 production (×) and the LB simulation (●). The time to reach the final conversion to Fe_3O_4, $X = 0.8$, is $t^* = 48$ s.

images on the left of Fig. 8.16 gave 260 ± 30, 490 ± 50 and 590 ± 50 μm, in good agreement. For the model, a cut-off of $X = 0.65$ gave the thicknesses of the Fe_3O_4 shells to be 200, 400 and 560 μm. For long times ($t = \infty$), the particle is reduced mostly to Fe_3O_4 and $X = 0.8$ in the simulations. From experiments, the time to reach the final conversion to Fe_3O_4 was independent of the mass of particles used for batches 0.05 – 0.2 g or 5 – 26 particles and was equal to $t^* \approx 48 \pm 4$ s, as shown in Fig. 8.17. Here, final conversions of $X = 0.85$ for CO_2 and $X = 0.90$ for CO were obtained. The simulation gave $X > 0.79$ for $t^* = 48$ s, in good agreement.

8.4.6 Reaction in a packed bed

Next, experimental and model results for the reduction of a packed bed of Fe_2O_3 to Fe_3O_4, similar to that described in Chapter 2, sections 2.2 and 2.3.1, were compared. The reactor was made from 316 stainless steel tubing (I.D. 10 mm; total length 450 mm). A stainless steel plate (1 mm thick) supported the bed: the plate contained 6 evenly spaced holes in a circular pitch, each with a diameter of 1 mm. The packed bed consisted of 12 g or ~ 1500 particles of Fe_2O_3 with $d_\mathrm{p} = 2$ mm; a layer of 2 g of Al_2O_3 with $d_\mathrm{p} = +1.4, -1.7$ mm was placed on either side of the reactive iron. Stainless steel thermocouples (O.D. 1.5 mm, type K) were positioned every 30 mm along the packed bed by welding fittings (Swagelok) to the steel tube, as shown in Fig. 8.18(a). The temperature of the thermocouples was recorded at a frequency of 1 Hz (Measurement Computing, USB-Temp). The reactor was placed in a tubular furnace to heat to the desired temperature of 1023 K. To obtain a uniform temperature along the length of the reactor, insulation was placed between the furnace wall and the reactor at both the top and bottom of the heated section. To avoid dampening of temperature fluctuations owing to the furnace control system: the bed was heated to 1023 K in air, the temperature was allowed to stabilise, and then the furnace was switched to a setting to provide constant power during the experiment. The gas sampling line and analyser set-up was identical to that in Chapter 5 for reduction of Fe_2O_3 to Fe_3O_4. The flowrate of the reducing gas with composition $CO+CO_2+N_2$ respectively, 5, 15 and 80 vol. % to give $c_\mathrm{CO} = 0.6$ mol/m^3 was 1.4×10^{-5} m^3/s. This corresponded to $Re = Ud_\mathrm{p}/\nu = 10$, where $U = 0.61$ m/s is the superficial velocity at the inlet at 1023 K and 10^5 Pa, $d_\mathrm{p} = 2$ mm is the particle diameter and $\nu = 1.28 \times 10^{-4}$ m^2/s is the kinematic viscosity of the inlet gas, which was assumed to be equal to that of pure N_2 and calculated from Hirschfelder *et al.* (1954). An identical flowrate of air (21 O_2, 79 N_2 vol. %) was used during oxidation to return the Fe_3O_4 to Fe_2O_3. Between oxidation and reduction stages, the reactor was purged with N_2 for 60 s. A total of 4 cycles of reduction and oxidation were performed.

Figure 8.18(b) shows the composition of the effluent as a function of time for cycles 2-4. At $t = 0$ s, the reducing gas is switched on. All of the entering CO was consumed in the reduction reaction for $t < 500$ s. For $t > 500$ s, the CO rapidly increased before reaching its inlet value of $c_\mathrm{CO} = 0.6$ mol/m^3 at $t = 700$ s. The effluent concentration profile thus suggests that reduction in the packed bed is characterised by a sharp reaction front which propagates down the reactor and ultimately breaks through over $500 < t < 700$ s. The experimental results demonstrate satisfactory reproducibility: the breakthrough profile of CO is nearly identical over the three cycles studied. Results for cycle 1 are not included owing to the anomalous behaviour observed during reduction of Fe_2O_3 to Fe_3O_4 in cycle 1, as described in Chapter 5.

Thermocouple measurements were used to track the progress of the reaction front. Figure 8.18(c) shows the temperature measured by three thermocouples spaced ~ 30 mm apart along the length of the bed as a function of time for cycles 2-4. The increase in the reactor temperature is sequentially observed for T_1, followed by T_2, then T_3, where T_1, T_2 and

Table 8.4: Table relating the parameters in physical units to lattice units. Here, $\Delta x = 10^{-4}$ m/(lattice unit), $\Delta t = 1.37 \times 10^{-6}$ s/(time step), $\Delta m/\Delta x^3 = 0.34$ kg/m^3 and $\Delta n/\Delta x^3 = 0.6$ moles/m^3.

	Physical			**Lattice**		
Symbol	**Value**	**Units**	**Symbol**	**Value**	**Relaxation Parameter**	**Scaling**
L_x	0.0102	m	$L_{x,\mathrm{LB}}$	102		$L_x = L_{x,\mathrm{LB}} \times \Delta x$
L_y	0.0102	m	$L_{y,\mathrm{LB}}$	102		$L_y = L_{y,\mathrm{LB}} \times \Delta x$
L_z	0.08	m	$L_{z,\mathrm{LB}}$	800		$L_x = L_{z,\mathrm{LB}} \times \Delta x$
d_p	0.002	m	$d_{\mathrm{p,LB}}$	20		$d_\mathrm{p} = d_{\mathrm{p,LB}} \times \Delta x$
ρ	0.34	kg/m^3	ρ_LB	1		$\rho = \rho_\mathrm{LB} \times \Delta m/\Delta x^3$
U	0.61	m/s	U_LB	0.00833		$U = U_\mathrm{LB} \times \Delta x/\Delta t$
ν	0.000122	m^2/s	ν_LB	$1/3(1/s_{10} - 1/2)$	$1/s_{10} = 0.55$	$\nu = \nu_\mathrm{LB} \times \Delta x^2/\Delta t$
ρ_CO	0.6	mol/m^3	$\rho_\mathrm{CO,LB}$	1		$\rho_\mathrm{CO} = \rho_\mathrm{CO,LB} \times \Delta n/\Delta x^3$
$n_{\mathrm{Fe_2O_3}}$	10320	mol/m^3	$n_{\mathrm{Fe_2O_3,LB}}$	17200		$n_{\mathrm{Fe_2O_3}} = n_{\mathrm{Fe_2O_3,LB}} \times \Delta n/\Delta x^3$
k_i	$2.4 \times 10^7 \exp(-75000/\mathrm{R}T)$	s^{-1}	$k_{i,\mathrm{LB}}$	0.00485		$k_i = k_{i,\mathrm{LB}}/\Delta t$
$D_\mathrm{mix,CO}$	1.5×10^{-4}	m^2/s	$D_\mathrm{mix,CO,LB}$	$1/4(\tau_\mathrm{CO} - 1/2)$	$\tau_\mathrm{CO} = 0.582$	$D_\mathrm{mix,CO} = D_\mathrm{mix,CO,LB} \times \Delta x^2/\Delta t$
$D_\mathrm{e,CO}$	2.5×10^{-5}	m^2/s	$D_\mathrm{e,CO,LB}$	$1/4(\tau_\mathrm{CO} - 1/2)$	$\tau_\mathrm{CO} = 0.511$	$D_\mathrm{e,CO} = D_\mathrm{e,CO,LB} \times \Delta x^2/\Delta t$

T_3 were thermocouples located progressively further along the length of the bed, as shown in Fig. 8.18(a). The mean rise in temperature for the three thermocouples over cycles 2-4, representing a total of 9 measurements, was 21.0 ± 1.5 K.

The lattice Boltzmann simulation was carried out in two stages. First, the D3Q19 lattice Boltzmann model was used to calculate a steady state velocity field through a representative packing of solid particles, 2 mm in diameter. Second, the D3Q7 lattice Boltzmann model with mass transport and reaction was used to model the consumption of the dilute reactant, CO, as a passive scalar. Thus, the final steady state velocity field from the D3Q19 model was used as input for the D3Q7 model. The two models were not coupled at each time step; rather the predetermined D3Q19 result fixed the macroscopic bulk velocity field in the D3Q7 model.

For the D3Q19 lattice Boltzmann model, details of the simulation set-up, boundary conditions and initial conditions were presented in section 8.4.4 for flow at $Re = 10$ and will not be repeated. Parameters used for the flow simulation are given in Table 8.4. It should be noted that the number of particles in the simulation (297) is considerably lower than the number of particles in the experiment (~ 1500). Once the sharpness of the experimental front between Fe_2O_3 and Fe_3O_4 had been observed, it was decided to simulate only a portion of the experimental packed bed.

For the D3Q7 lattice Boltzmann model, the domain size was $L_x = L_y = 102$, $L_z = 800$, identical to that for the D3Q19 flow simulation. The distribution of fluid and solid nodes was also identical. As in section 8.4.5, a variable, $n_{\mathrm{Fe_2O_3}}$, was used to track the conversion

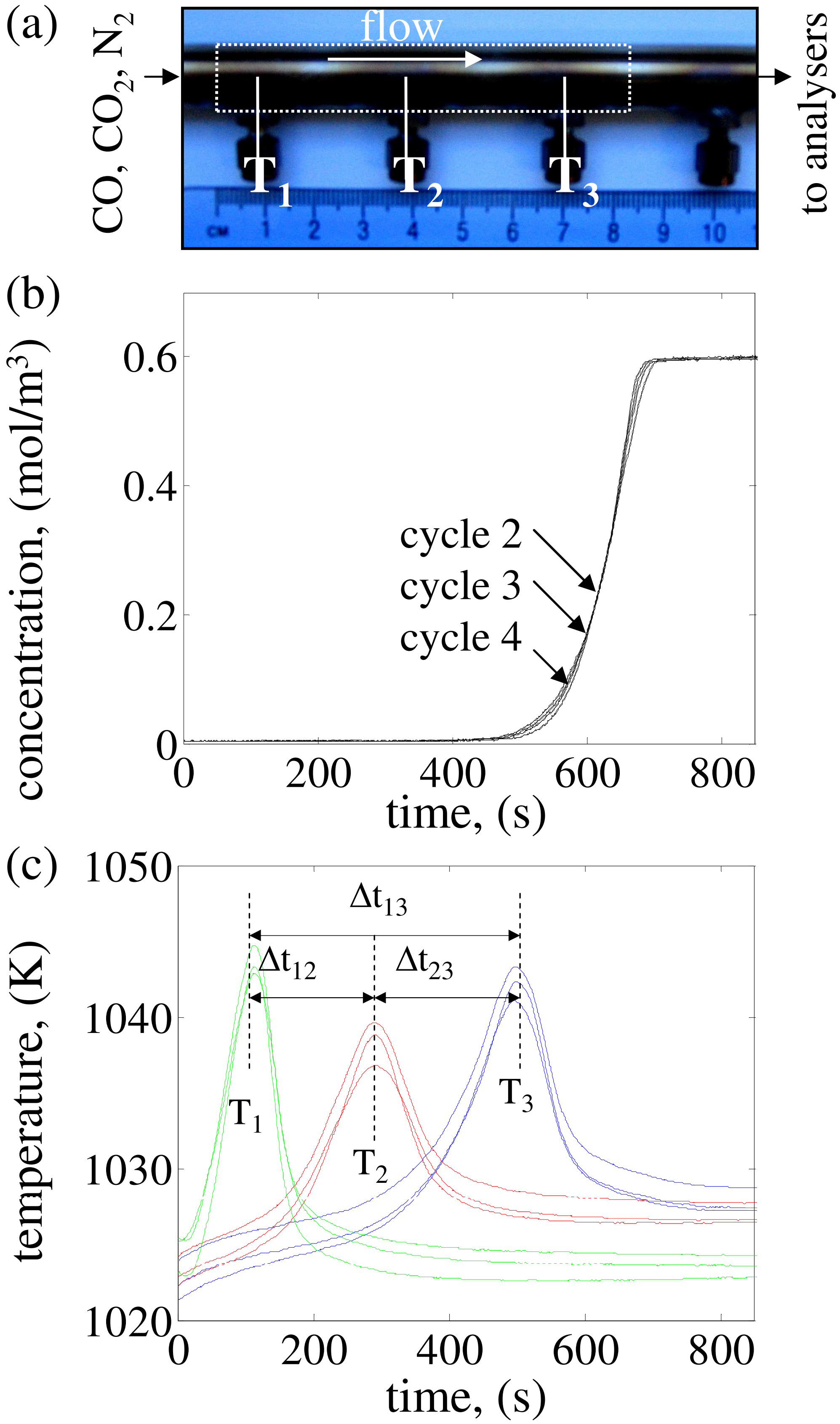

Figure 8.18: (a) Schematic diagram of the packed bed showing the thermocouples spaced 30 mm apart. (b) Concentration of CO in the effluent gas as a function of time for the reduction of a packed bed of 16 g of Fe_2O_3 to Fe_3O_4 using CO+CO_2+N_2 (5, 15, 80 vol %, respectively or c_{CO} = 0.6, c_{CO_2} = 1.8, c_{N_2} = 9.6 mol/m^3) at 1023 K. (c) Corresponding temperature excursion during reduction as a function of time measured by the thermocouples.

of solid nodes from Fe_2O_3 to Fe_3O_4. The reactant species, CO, was assigned a distribution function, $f_{i,\mathrm{CO}}$, capable of participating in streaming and collision steps. At the inlet, the non-equilibrium boundary condition of Eq. (8.34) (Zou and He, 1997) was used to fix the inlet density, $\rho_{\mathrm{CO}} = 0.6$ mol/m^3. No special treatment of corner or edge nodes at the inlet was necessary. At the outlet, the zero flux boundary condition of Eq. (8.32) was applied after streaming. Halfway bounce-back boundary conditions were applied between the fluid and those solid nodes forming the tube, so that mass was conserved within the tube. No boundary condition was applied between the fluid and those solid nodes comprising particles; rather, the $f_{i,\mathrm{CO}}$ were permitted to freely stream between fluid and particle nodes. The local relaxation time was however varied depending on whether a node comprised a solid particle or the fluid, so as to vary the internal and external molecular diffusivities, as shown in Table 8.4. For CO, the initial condition was $\rho_{\mathrm{CO}} = 0$ over the entire domain except at the inlet where the inlet boundary condition $\rho_{\mathrm{CO}} = 0.6$ mol/m^3 was applied. For solid particles, the initial condition was $n_{\mathrm{Fe_2O_3}} = 10.3$ kmol/m^3. Fluid nodes and those comprising the tube, were initiated with $n_{\mathrm{Fe_2O_3}} = 0$. The initial velocity condition was simply the predetermined flow field, $\mathbf{u}$, from the D3Q19 model with $\mathbf{u}$ set to 0 for all solid nodes. The flow field, $\mathbf{u}$, was held constant during the D3Q7 simulation. The parameters used in the D3Q7 lattice Boltzmann model are listed in Table 8.4 along with conversions between physical and lattice units. The first-order reduction reaction was incorporated using Eq. (8.64) as in section 8.4.5 just prior to the equilibrium step. Details on implementing the reaction were given in section 8.2.6. Simulations were run for a total of 4.5×10^6 time steps, corresponding to 6.15 s. The notable assumptions of the present lattice Boltzmann model were: (i) the reduction is considered isothermal, (ii) the change in momentum associated with the conversion of CO to CO_2 is negligible, and therefore only the momentum of the bulk gas, assumed to have identical properties to pure N_2, is conserved and (iii) solids do not change size upon reduction from Fe_2O_3 to Fe_3O_4.

Figure 8.19 shows a cross-sectional slice of (a) the location of the solid nodes, (b) the longitudinal velocity, u_z and (c) the concentration of CO after $t = 0.27$ s, all in lattice units. From Fig. 8.19(c) it is evident that the domain of interest is given by a narrow boundary corresponding to the consumption of CO at the start of the packing. Given the sharp reaction front, the particle does not see a uniform concentration of CO at the surface, a problem often overlooked in conventional models of packed beds. To reduce computational time, therefore, it was decided to shrink the domain to those nodes lying between $200 < z < 600$ in lattice units, *i.e.* to effectively cut the regions of inflow and outflow from the D3Q7 lattice Boltzmann model,

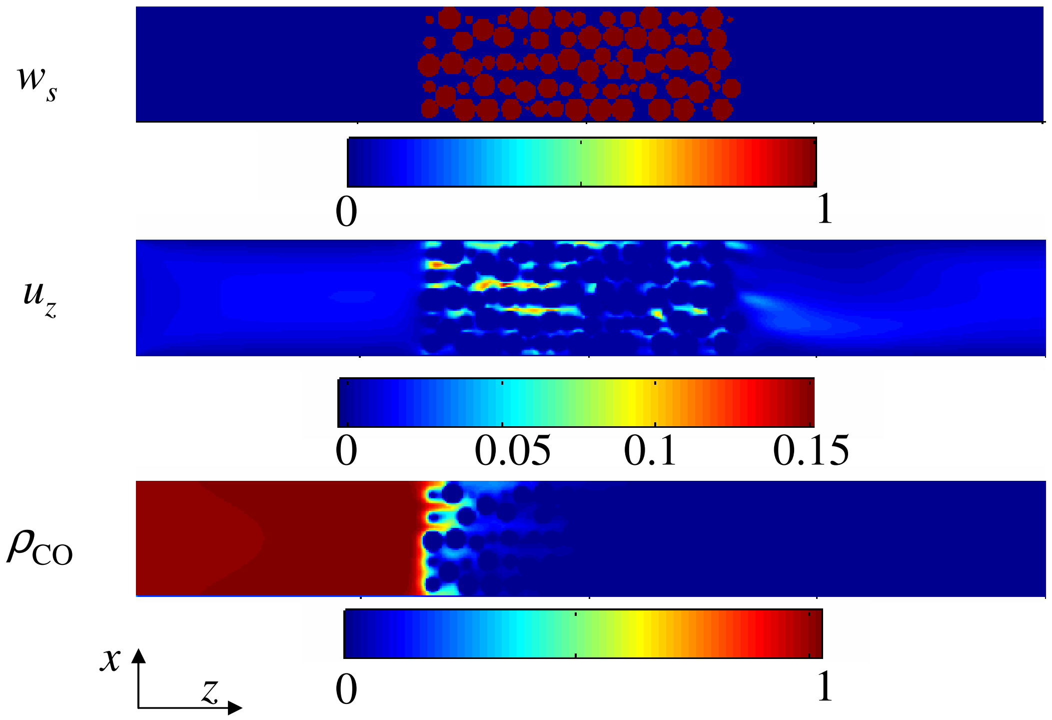

Figure 8.19: Instantaneous profiles showing (a) the location of solid nodes, (b) the longitudinal velocity, u_z, and (c) the concentration of reactant species, ρ_{CO} in the $x - z$ plane in lattice units after $t = 0.27$ s. Conversion to physical units as outlined in section 8.2.9 requires $\Delta x = 10^{-4}$ m/(lattice unit), $\Delta t = 1.37 \times 10^{-6}$ s/(time step) and $\Delta n/\Delta x^3 = 0.6$ moles/(lattice unit)^3.

since the velocity field had already been set over $1 \leq z \leq 800$ with the D3Q19 model. Finally, to avoid lengthy simulation times owing to the small time step, Δt and to compare the time-dependent experiments with the instantaneous concentration profile along the reactor length, a change in reference frame based on the speed of the reaction front was necessary. Using the distance between thermocouples (30 mm) and the times between temperature maxima, Δt_{12}, Δt_{23} and Δt_{13} in Fig. 8.18(c), the speed of the reaction front was measured to be:

$$\frac{dx}{dt} = 0.154 \pm 0.01 \text{ mm/s}. \tag{8.65}$$

To convert the time-dependent profile given in Fig. 8.18(b) to a profile with respect to reactor position, z, the absicissa in Fig. 8.18(b) was multiplied by $-dx/dt$ from Eq. (8.65) and offset so as to intersect the model predictions at half the maximum c_{CO} value.

Figure 8.20 shows the experimental effluent concentration as a function of position, z, as well as the prediction from the lattice Boltzmann model. The value of concentration, ρ_{CO}, from the LB simulation was determined by averaging over all fluid nodes on the inside of the cylinder. From Fig. 8.20 the modelled front is sharper than the experimentally-determined front at both $t = 0.27$ s and $t = 6.15$ s. However, from the lattice Boltzmann simulations, the front becomes more diffuse from $t = 0.27$ s to $t = 6.15$ s. Additionally, a slight increase in the concentration of CO between the inlet and the start of the packing is observed. This is a result of the compressibility error of the model and is more pronounced for simulations involving the entire domain ($1 \leq z \leq 800$) compared to the truncated domain ($200 \leq z \leq 600$). For a true comparison between model results and experiments, longer times must be simulated and are the focus of ongoing research.

When comparing the experimental concentration profile with that predicted from the simulation, the response time of the sampling line and infrared analyser for CO, and the response time of the thermcouples and acquisition system for T must be considered. The response time of the sampling line and analyser was estimated by flowing the reaction mixture, $\mathrm{CO}+\mathrm{CO}_2+\mathrm{N}_2$ with 5, 15 and 80 vol. %, respectively, through an inert bed of 16 g of $\mathrm{Al}_2\mathrm{O}_3$ particles of $d_{\mathrm{p}} = +1400, -1700\ \mu$m heated to 1023 K. A step change in the inlet concentration was approximated by automatically switching the solenoid valves to a flow of pure N_2. By measuring the decay in the CO signal at the specified flowrate, the response time was determined to be $\tau_{\mathrm{CO}}^{\mathrm{mix}} = 1$ s. Deconvolution of the signal did not therefore alter the shape of the front observed in Fig. 8.18(a) which takes $\sim$ 200 s to break through. Similarly, experiments to approximate

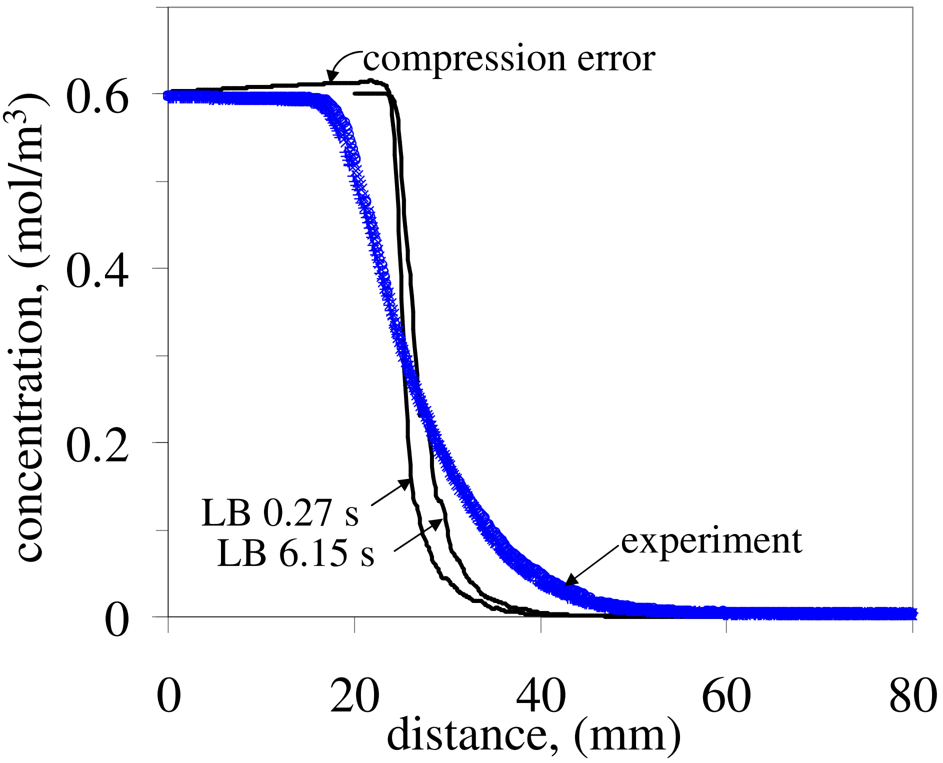

Figure 8.20: Concentration profile for the reduction of a packed bed of Fe_2O_3 to Fe_3O_4 in $CO+CO_2+N_2$ (5, 15, 80 vol %, respectively) at 1023 K obtained by rescaling the abscissa in Fig. 8.18 by the speed of the front, dx/dt = 0.15 mm/s.

the response time of the thermocouples and acquisition system were performed by rapidly moving the thermocouples between boiling water and an ice water bath, and *vice versa*, whilst vigorously stirring. The response time of the thermocouples was determined to be ~ 0.3 s and did not, therefore, alter the temperature results.

8.5 Conclusions

A lattice Boltzmann model which uses a multiple relaxation time approach to model fluid flow and a single relaxation time approach for a passive scalar to incorporate mass transfer was developed. The model was validated on a variety of test cases and the conclusions were as follows:

- The LB model accurately captures the physics of (i) Poiseuille flow between two parallel plates, (ii) the diffusive decay of a sinusoidal concentration wave, (iii) a first order reaction in a well-mixed reactor and (iv) the relationship between the effectiveness factor and Thiele modulus for a reacting spherical catalyst pellet. In all cases, excellent agreement between the model and analytical solutions was observed and it can be concluded that model correctly captures the fundamentals of advection, diffusion and reaction for dilute systems at low Ma number.
- The LB model accurately predicted (i) flow past a single sphere and the resulting drag force, (ii) the pressure drop through a packed bed, and (iii) a lower than first order increase in Sherwood number with increasing Reynolds number for mass transfer to the surface of a sphere. Since analytical solutions do not exist for these test cases, the LB model was validated with established empirical correlations.

In general, lattice Boltzmann implementations do not consider reactive solids and further development was required.

- The LB model was successfully extended to gas-solid reactions where the solid composition changes with time, while the solid boundaries remain fixed.

Direct comparison of the model with experimental measurements was then performed for the reduction of spherical particles of Fe_2O_3 to Fe_3O_4 in a mixture of $CO+CO_2+N_2$ at 1023 K and 10^5 Pa. The conclusions were as follows:

- The LB model correctly and quantitatively predicted the phase boundary between Fe_2O_3 and Fe_3O_4 for the reduction of a single particle.

- The LB model predicted a sharp front between Fe_2O_3 and Fe_3O_4 for the reduction of a packed bed of iron oxide; however, longer simulation times, which will be pursued in further research, are required for a substantive comparison between experiment and theory.

- The LB model permitted non-uniform mass transfer to a single particle in a packed bed with a sharp reaction front to be captured, a problem often overlooked by conventional modelling approaches.

Overall, the extension of the lattice Boltzmann method to gas-solid reactions has been demonstrated and appears a promising approach for capturing the fundamental physics involved in such processes.

Chapter 9

Conclusions

Given the current dependence on and large reserves of carbonaceous fuels, efficient conversion of these fuels to useful energy without the release of CO_2 is necessary. The production of pure H_2, a secondary and environmentally-benign energy vector, at a distributed scale is also pertinent. In the present dissertation, both of these issues have been investigated with respect to the redox reactions of iron and its oxides with CO and CO_2 and with H_2 and H_2O. These problems require multi-scale approaches, and experimental and numerical investigations from the particle scale to the reactor scale have been presented.

Particles of iron oxide were investigated for their ability to produce H_2 with the simultaneous capture of CO_2 using both packed and fluidised bed reactors over the temperature range, 873-1173 K. A variety of preparation techniques from physical chemistry were applied including: the mechanical mixing of oxide powder (pure Fe_2O_3) in Chapter 2, the wet-impregnation of Fe_2O_3 with a support (based on Al, Cr, Mg and Si) in Chapter 3 and the sol-gel preparation of Fe_2O_3 and Al_2O_3 composites in Chapter 4. The conclusions were as follows:

- Pure iron oxide, either Fe_2O_3 or Fe_3O_4, undergoing repeated redox cycling to FeO, *i.e.* the $Fe^{(2+)}$ cation, does not require chemical modification with a support. Stable conversions of H_2 were achieved over 40 cycles.

- For reduction of either Fe_2O_3 or Fe_3O_4 to metallic Fe, the yield of H_2 dramatically drops over ten cycles regardless of the reaction temperature - either 873, 1023 or 1173 K. Stable yields of hydrogen could only be obtained for reduction to Fe by the addition of Cr_2O_3 or Al_2O_3. Best results were achieved for the case of 40 wt. % Al_2O_3 and 60 wt. % Fe_2O_3, with stable conversions over 40 cycles.

- The ability of Al addition to improve the yield of H_2 over repeated cycles was shown to be definitively linked to the formation of the aluminate, $FeO{\cdot}Al_2O_3$. The presence of a significant amount of $FeO{\cdot}Al_2O_3$ was quantitatively confirmed using a Rietveld analysis on an X-ray diffraction (XRD) pattern.

- The element added as an oxide support, either Al, Cr, Mg or Si, cannot be considered inert. The prevailing assumption in chemical looping literature to treat additives as inert is therefore false.

- Providing some Fe_2O_3 was present near the gas outlet to the bed, all of the entering reactant CO was converted to CO_2 suitable for sequestration. Even for residence times as low as $t = 0.2$ s, the reduction Fe_2O_3 to Fe_3O_4 and simultaneous oxidation of CO to CO_2 *via* reaction (1.9) was sufficiently fast to entirely convert the entering CO.

- The hydrogen from experiments involving reduction to FeO was pure, with CO contaminations < 25 ppmv for temperatures 873-1173 K. By contrast reduction to Fe resulted in severe carbon deposition with CO contaminations up to 10000 ppmv. This observation is consistent with the thermodynamics for the the Boudouard reaction (1.18).

An investigation into the kinetic rates was undertaken in Chapters 5 and 6 for the reduction of Fe_2O_3 with mixtures of $CO+CO_2+N_2$ in a well-mixed fluidised bed:

$$3\,Fe_2O_3 + CO \rightleftarrows 2\,Fe_3O_4 + CO_2 \tag{9.1}$$

$$1.2\,Fe_3O_4 + CO \rightleftarrows 3.8\,Fe_{0.947}O + CO_2. \tag{9.2}$$

The present study provides a new contribution since it determined the rate in a regime predominantly controlled by intrinsic kinetics and presented the rate over multiple cycles. Additionally, the possibility of increasing the rate of reaction (9.2) by the addition of a small amount, 0.01 mol %, Ce was pursued. The conclusions were as follows:

- The order of reaction for CO was found to be unity for both reduction reactions (9.1) and (9.2).

- The activation energy for the reduction of Fe_2O_3 to Fe_3O_4 was found to be constant and equal to 75 kJ/mol over cycles 2-10. The pre-exponential factor for reduction of Fe_2O_3 to Fe_3O_4 was constant and equal to $A = 2.4 \times 10^7$ s^{-1} over cycles 2-10.

- The activation energy for reduction of Fe_3O_4 to $Fe_{0.947}O$ was approximately constant and equal to 94 kJ/mol over cycles 2-10. The pre-exponential factor decreased for the reduction of Fe_3O_4 to $Fe_{0.947}O$ from $A = 4.3 \times 10^7\ s^{-1}$ in cycle 2 to $A = 1.2 \times 10^7\ s^{-1}$ in cycle 10, a drop of 70%, suggesting a morphological change such as a decrease in active surface area.

- The presented rate parameters were validated using a 1D model which predicted, successfully, the reduction of a packed bed of unmodified iron oxide.

- The addition of 1 mol % Ce assisted in preventing the destruction of active surface area during sintering. Particles of Fe_2O_3 with 1 mol % Ce added, showed an increase in the surface area of 2× corresponding to a subsequent increase in the rate of reaction (9.2) by 2×. Hence, it seems that the reduction of Fe_3O_4 to $Fe_{0.947}O$ is limited by surface phenomena for grains < 500 nm.

The redox reactions involving iron and its oxides were investigated not only with simulated syngas from cylinders, but also with syngas from the gasification of coal which contains contaminants such as hydrocarbons, SO_x, H_2S and NO_x. The findings were as follows:

- During the initial stage of reduction, CO_2 and H_2O are produced with little slip of CO or H_2. Upon condensation of the H_2O, this CO_2 would be suitable for sequestration.

- Pure H_2 can be produced from syngas originating from the gasification of a low-rank coal, representing a significant increase in calorific value. Contamination levels were: $[CO] < 50$ ppmv and $[SO_2] \approx 0$ ppmv.

- Contaminants in syngas which are gaseous above 273 K apparently do not adversely affect the iron oxide material as stable quantities of pure H_2 were observed over 5 cycles.

- Since oxidation with air removes contaminants, *e.g.* sulphurous and carbonaceous species deposited during reduction, and generates useful heat and pure N_2 for purging, it should be included in the operating cycle.

The choice of which transitions and which temperatures to use for the proposed process in an industrial application is not straightforward. From the presented research, the overall recommended sequence for the production of pure H_2 with simultaneous capture of CO_2 is as follows:

1. *Production of CO_2 with oxide reduction.* Syngas from the gasification of coal or biomass with steam or CO_2 *via* reactions (1.7) and (1.8) in Table 1.2, is converted to a stream

of CO_2 and H_2O *via* reactions (1.9)-(1.10) or (1.12)-(1.13) in Table 1.2 by passing it through a packed bed of particles of Fe_2O_3. Condensing out the H_2O from the off-gas yields a pure stream of CO_2 suitable for sequestration. The concentration gradient along the reactor would enable $Fe_{0.947}O$ to exist at the gas inlet of the packed bed, while still maintaining Fe_2O_3 in the packed bed towards the gas outlet.

2. *Production of H_2 with partial reoxidation of metal oxide.* After the partial reduction of the iron oxide in the bed, passing steam through the reactor would generate hydrogen and reoxidise the reduced iron oxide to Fe_3O_4 *via* reaction (1.16) in Table 1.2.

3. *Complete reoxidation of metal oxide with air.* The reoxidation to Fe_2O_3 in air produces a stream of N_2 with residual O_2, reaction (1.17) in Table 1.2. Once the entire packed bed has been regenerated to Fe_2O_3, the cycle could begin anew at step 1.

If maximising the yield of H_2 is the primary objective and concerns about heat integration and the purity of the H_2 can be ignored, reduction to Fe in step (1) could be performed. However, the iron oxide would then need to be modified by the addition of Al to maintain high conversions over multiple cycles.

An LB model capable of resolving: (i) fluid flow through a packed bed (ii) mass transfer to the surface of a spherical particle of iron oxide and (iii) reaction and diffusion within a particle of iron oxide was developed in Chapter 7 and first comparisons with experimental results were performed. It was found that

- The LB model showed excellent agreement with analytical solutions for the test cases: (i) Poisieulle flow between two parallel plates, (ii) the decay of a sinusoidal concentration wave and (iii) a first order reaction in a well-mixed reactor.

- Further validation of the model with experimental measurements was performed for: (i) flow past a single sphere and the resulting drag force, (ii) the effectiveness factor in a reacting spherical catalyst pellet and (iii) mass transfer to the surface of a sphere. The LB model accurately predicted the drag force and effectiveness factor, and correctly predicted a non-linear increase in Sherwood number with increasing Reynolds number. However, the values of the Sherwood number predicted were generally lower than those given by established correlations (Bird *et al.*, 2007) and could be a result of the small diameter of the sphere, $d_p = 10$ in lattice units.

- Comparison between the the LB model and experimental results for the reduction of Fe_2O_3 to Fe_3O_4 in $CO+CO_2+N_2$ was achieved by considering the conversion profile of a single particle, $d_\mathrm{p} = 100$ in lattice units. The LB method quantitatively captured the boundary between Fe_2O_3 and Fe_3O_4 phases.
- A further comparison involving the reduction of a packed bed of Fe_2O_3 particles ($d_\mathrm{p} = 20$ in lattice units) to Fe_3O_4 in $CO+CO_2+N_2$ was conducted using a passive scalar approach. Agreement between the model and experiments was observed for the concentration profile in the packed bed.

Chapter 10

Future Work

The stabilisation of the production of hydrogen by Fe_2O_3 and Al_2O_3 composites has been shown both for impregnated particles and those prepared by the sol-gel process. However, the mechanism by which Al_2O_3 stabilises the iron oxide requires further investigation. The exact amount of Al_2O_3 required for stability and how rapidly, if at all, the Al_2O_3 is incorporated into the iron oxide lattice compared with the rapid sintering of pure Fe_2O_3 must be determined. If a single or even a few reduction and oxidation cycles are sufficient to form a homogeneous mixture of Fe and Al, then the more costly and labour-intensive sol-gel technique may be unnecessary. The use of redox cycling rather than the sol-gel technique to produce a material with specified homogeneity could have a significant impact on industrial processes.

In the future, catalyst supports not used in the present investigation, ZrO_2 and TiO_2, will also be investigated as candidates for stabilising the repeated reduction to Fe. In particular, ZrO_2 is an interesting candidate since it has a high melting temperature, $T_m \approx 2973$ K (Barin and Knacke, 1973) and is inert, *i.e.* should not form any intermediates with the iron species.

Longer LB simulations for the reduction of Fe_2O_3 to Fe_3O_4 in a packed bed will be pursued using the Hades cluster (Dept. of Engineering) with InfiniBand communication across 4 nodes each containing 8 CPU's. Despite the small time step on the order of $O(10^{-6}$ s) for the current simulations, the continuing rapid advance in computation will make the application of LB methods to transient gas-solid systems a reality in the future. The extension of the LB model to include further reduction steps, *e.g.* reactions (1.10)-(1.11), will therefore become feasible.

An inherent feature of the LB method is that it can be used to develop closure correlations for coarser modelling strategies. To be more specific, consider the mass transfer coefficient, $k_{g,CO}$. The present LB model does not require $k_{g,CO}$ as an input, but naturally incorporates the physical effect of $k_{\mathrm{g,CO}}$ through the molecular diffusivity and hydrodynamics of the flow. The LB method has already been successfully applied to provide a drag force correlation for fluidised bed models (Beetstra *et al.*, 2007) and to provide axial or radial dispersion coefficients (Khirevich *et al.*, 2007) for packed bed models. Determining correlations for mass and heat transfer coefficients in packed structures is therefore a natural extension, and only preliminary research in this area exists. Creating a correlation for the Sherwood number, Sh, for porous structures, where established empirical correlations such as those for a single sphere are lacking, is possible and would provide a fundamental contribution to scientific literature.

The development of a multiple-relaxation time (MRT) model for the advection and diffusion of a passive scalar in 2D and 3D will be pursued. The simplicity of the D2Q5 and D3Q7 lattices make such a development a good starting point for addressing the theory, rather than simply the application, of lattice Boltzmann models. A simple MRT model for a passive scalar would be a useful tool for engineers and physicists.

Appendix 1

Thermodynamics

A1.1 Calculation of thermodynamic properties

The Gibbs free energy of species i at a reference temperature, T, can be calculated using:

$$G_i^\circ(T) = H_i^\circ(T) - TS_i^\circ(T), \tag{A1.1}$$

where H_i° and S_i° are, respectively, the enthalpy and entropy of the pure substance at temperature, T, and pressure, P°. The standard state is defined by a reference temperature $T = 298.15$ K and pressure, $P^\circ = 10^5$ Pa; gases are considered ideal, and condensed species are considered to be purely crystalline or purely liquid. All thermodynamic properties are listed as molar quantities. Using standard thermodynamic tables (Barin and Knacke, 1973; McBride *et al.*, 2002) for the molar heat capacity at constant pressure, which is typically estimated by a polynomial of the form (Barin and Knacke, 1973):

$$C_{p,i}^\circ(T) = a_i + b_iT + c_iT^{-2} + d_iT^2, \tag{A1.2}$$

the enthalpy and entropy can be obtained by integration:

$$H_i^\circ(T) = \int C_{p,i}^\circ(T)dT = a_iT + \frac{b_iT^2}{2} - \frac{c_i}{T} + \frac{d_iT^3}{3} + e_i \tag{A1.3}$$

$$S_i^\circ(T) = \int \frac{C_{p,i}^\circ(T)}{T}dT = a_i \log T + b_iT - \frac{c_i}{2T^2} + \frac{d_iT^2}{2} + e_i, \tag{A1.4}$$

where a_i, b_i, c_i and d_i are fitted coefficients and e_i is a constant of integration which is different for Eqs. (A1.3) and (A1.4) and includes, *e.g.* in Eq. (A1.3) the enthalpy of formation and enthalpy of any phase transitions.

A1.2 Equilibrium

At a fixed temperature and pressure, a system is at equilibrium if the total Gibbs free energy of the system is at a global minimum (Denbigh, 1957). The total Gibbs free energy of a system, G, is defined as:

$$G = \sum_i^s \bar{G}_i n_i, \tag{A1.5}$$

where s is the total number of molecularly distinct species, n_i is the number of moles of species i and $\bar{G}_i$ is the partial molar Gibbs free energy, or chemical potential, of species i. Furthermore,

$$\bar{G}_i(T) = G_i^\circ(T) + \mathrm{R}T \log \frac{f_i}{f_i^\circ}, \tag{A1.6}$$

where G_i° is the Gibbs free energy of species i at temperature, T, and reference pressure, P°, f_i is the fugacity of i and f_i° is the fugacity of pure i in the reference state. For a gas at low to moderate pressures, the fugacity can be approximated by $f_i = y_i P \phi_i$, where y_i is the molar fraction of i in the gaseous mixture, ϕ_i is the fugacity coefficient used to capture deviations from ideal gas behaviour, and P is the total pressure of the system. For a gas in which molecular interactions are negligible, *e.g.* at high temperatures and low pressures as considered in this work, the ideal gas assumption holds and $\phi_i = 1$. Thus for gases,

$$\bar{G}_i(T) = G_i^\circ(T) + \mathrm{R}T \log \frac{y_i P}{P^\circ}, \tag{A1.7}$$

where P is the total pressure of the system, P° is the reference pressure and it is noted that $\bar{G}_i$ is a function of n_i since $y_i = n_i / \sum n_i$ where summation is only over the gaseous species. Unlike that of a gas, the fugacity for a pure solid or immiscible liquid is only weakly dependent on pressure and the following approximation is used:

$$\bar{G}_i(T) = G_i^\circ(T). \tag{A1.8}$$

To solve for the minimum Gibbs free energy, the first order necessary condition (FONC),

$$dG = \sum_i^s n_i d\bar{G}_i + \sum_i^s \bar{G}_i dn_i = 0, \tag{A1.9}$$

must be satisfied. From the Gibbs-Duhem equation ($-S\,dT + VdP - \sum_i^s n_i d\bar{G}_i = 0$) at a constant temperature and pressure, this simplifies to:

$$\boxed{dG = \sum_i^s \bar{G}_i dn_i = 0} \tag{A1.10}$$

The second order sufficient condition for a minimum is then $d^2G = \sum_i^s (d\bar{G}_i dn_i + \bar{G}_i d^2 n_i) > 0$.

In general, two mathematical approaches for determining the minimum Gibbs free energy exist: (i) the method of independent reactions and (ii) the constrained minimisation of the free energy. Both give equivalent results; however, as the number of species and potential reactions increases, the method of constrained minimisation is preferred.

A1.2.1 Method of independent reactions

In practice the method of independent reactions can be applied to any number of reactions; however, for simplicity only a single reaction will be considered. Take the general reaction given by:

$$\nu_1 M_1 + \cdots + \nu_{j-1} M_{j-1} \rightleftarrows \nu_j M_j + \cdots \nu_s M_s, \tag{A1.11}$$

where the ν_j represent the stoichiometric coefficients and M_j are the distinct molecular species of which there are s in total. For mathematical summation, the ν_j are defined to be negative for substances on the left of the equation and positive for those on the right. Reaction (A1.11) describes any chemical reaction, including those in Table 1.2. The state of M_j is not constrained and could be either liquid, gas, *etc.* For any substance which is inert, $\nu_j = 0$. Considering the reaction stoichiometry,

$$\frac{dn_1}{\nu_1} = \frac{dn_2}{\nu_2} = \cdots = \frac{dn_s}{\nu_s}. \tag{A1.12}$$

That is, the change in the number of moles of species i is not independent of the change in number of moles of other species. This dependency permits the elimination of all of the dn's from Eq. (A1.10) with the exception of one, say dn_1, to give:

$$\left(\bar{G}_1 + \frac{\nu_2}{\nu_1}\bar{G}_2 + \cdots + \frac{\nu_s}{\nu_1}\bar{G}_s\right) dn_1 = 0. \tag{A1.13}$$

Therefore, multiplying through by ν_1 gives the simple relation for the FONC

$$\sum_i^s \nu_i \bar{G}_i = 0, \tag{A1.14}$$

which is the starting point for determining the equilibrium for reaction (A1.11).

Defining the equilibrium constant,

$$K_p \equiv \prod_i \left(\frac{y_i P}{P^\circ}\right)^{\nu_i} = \prod_i (p_i)^{\nu_i}, \tag{A1.15}$$

where the product summation is only over the gaseous species, P° has been chosen to have the value of unity (*e.g.* 1 bar) consistent with convention and P is chosen to have identical units to P° such that the ratio P/P° is dimensionless, and using Eq. (A1.7), Eq. (A1.14) can be rewritten as

$$-\mathrm{R}T \log K_p = \sum_i^s \nu_i G_i^\circ. \tag{A1.16}$$

Thus, the equilibrium which satisfies the FONC of Eq. (A1.14) is defined by the equilibrium constant in Eq. (A1.16). In practice, this definition of K_p can be thought of as the product

$$K_p = \prod_i^s \left(\frac{f_i}{f_i^\circ}\right)^{\nu_i} = e^{-\sum_i^s \frac{\nu_i G_i^\circ}{\mathrm{R}T}}. \tag{A1.17}$$

Since for solids and immiscible liquids $f_i/f_i^\circ = 1$, the product summation need only be carried out for the gaseous species, whereas the algebraic summation is over all the substances in their standard state at temperature, T, and reference pressure, $P^\circ = 10^5$ Pa. Since G_i° refers to the reference pressure, P°, G_i° is only a function of T. Accordingly, K_p is only a function of T.

A1.2.2 Worked example

The equilibrium constant for reaction (1.10), reproduced here for the convenience of the reader,

$$1.2\,\mathrm{Fe_3O_4} + \mathrm{CO} \rightleftarrows 3.8\,\mathrm{Fe_{0.947}O} + \mathrm{CO_2}, \tag{A1.18}$$

will now be derived for a temperature of 1023 K and pressure of 10^5 Pa. Table A1.1 lists the Gibbs free energy for each of the four species in reaction (A1.18) relative to the standard state given by the reference temperature, $T = 298.15$ K, and pressure, $P^\circ = 10^5$ Pa. The values of $H^\circ_{1023\ \mathrm{K}}$, $S^\circ_{1023\ \mathrm{K}}$ and $G^\circ_{1023\ \mathrm{K}}$ were calculated as previously outlined in section A1.1. The change in Gibbs free energy for the overall reaction can then be calculated using the reported values for the individual species, listed in Table A1.1, and the stoichiometric coefficients from reaction (A1.18). Subtracting the Gibbs free energy of the reactants from that of the products

Table A1.1: Enthalpy, entropy and Gibbs free energy for reactant and product species from reaction (A1.18). The overall enthalpy, entropy and Gibbs free energy for the reaction is also listed.

Species	Fe_3O_4	$Fe_{0.947}O$	CO	CO_2	$\sum$
$H^\circ_{1023\ \mathrm{K}}$ (kJ/mol)	-968.8	-227.6	-88.1	-359.2	27.1
$S^\circ_{1023\ \mathrm{K}}$ (J/(mol K))	390.5	122.4	235.3	270.2	31.3
$G^\circ_{1023\ \mathrm{K}}$ (kJ/mol)	-1368.3	-352.7	-328.8	-635.7	-5.3

gives:

$$\Delta G^\circ_{1023\ \mathrm{K}} = \sum_i^s \nu_i G_i^\circ = (-635.7 - 3.8 \times 352.7) - (-1.2 \times 1368.3 - 328.8) = -5.3\ \frac{\mathrm{kJ}}{\mathrm{mol}}, \tag{A1.19}$$

shown by the final column in Table A1.1. Next, the equilibrium constant for the reaction is calculated using Eq. (A1.17):

$$K_p = \frac{p_{\mathrm{CO_2}}}{p_{\mathrm{CO}}} = e^{-\sum_i^s \frac{\nu_i G_i^\circ}{RT}} = e^{\frac{5324}{8.314 \times 1023}} = 1.87. \tag{A1.20}$$

Thus, for $\frac{p_{\mathrm{CO_2}}}{p_{\mathrm{CO}}} < 1.87$ CO and Fe_3O_4 will be consumed; for $\frac{p_{\mathrm{CO_2}}}{p_{\mathrm{CO}}} > 1.87$ CO_2 and $Fe_{0.947}O$ will be consumed.

A1.2.3 Method of constrained minimisation of the Gibbs free energy

For the method of constrained minimisation of the Gibbs free energy, two constraints must be considered along with the FONC of Eq. (A1.10), *viz.* (i) the non-negativity of each molecular species and (ii) atomic conservation:

$$\text{(i) } n_i \geq 0 \quad \text{(ii) } b_j - \sum_i^s a_{ij} n_i = 0, \tag{A1.21}$$

where b_j is the number of moles of element j entering the system and a_{ij} is the number of atoms of j in one molecule of species i.

The constrained minimisation problem can be solved using Lagrange's method of undetermined multipliers with an objective function given by a combination of Eqs. (A1.5) and (A1.21):

$$F = G + \sum_j^b \lambda_j \left(b_j - \sum_i^s a_{ij} n_i \right) + \sum_i^s \gamma_i n_i, \tag{A1.22}$$

where b is the total number of distinct atomic species and λ_j and γ_i are the Lagrange multipliers. The constrained minimum is found using the Karush-Kuhn-Tucker (KKT) equations, which provide the necessary conditions for an extremum in a constrained optimisation problem (Edgar *et al.*, 2001):

$$\frac{\partial F}{\partial n_i} = \frac{\partial G}{\partial n_i} - \sum_{j}^{m} \lambda_j a_{ij} + \gamma_i = 0 \tag{A1.23}$$

$$\lambda_j \left(b_j - \sum_{i}^{s} a_{ij} n_i \right) = 0 \quad j = 1 \ldots b \tag{A1.24}$$

$$\gamma_i \geq 0. \quad i = 1 \ldots s \tag{A1.25}$$

In this dissertation, the KKT equations were solved numerically using *fmincon* in the MATLAB® programming language which attempts to compute the Langrange multipliers directly by collecting second order information about the minimisation problem using a numerical approximation of the Hessian of the Langrangian given by:

$$\frac{\partial^2 F}{\partial n_i^2} = \frac{\partial^2 G}{\partial n_i^2}. \tag{A1.26}$$

The algorithm then updates values of the initially-guessed Lagrange multipliers using a quasi-Newton time-stepping scheme.

Appendix 2

Experimental measurements

This Appendix describes the physical principles underlying the measuring techniques used during experiments in this dissertation. It is separated into two categories: (i) techniques for the characterisation of a gas (*e.g.* infrared spectroscopy and thermal conductivity) and (ii) techniques for the characterisation of a porous solid (*e.g.* gas adsorption, mercury intrusion, X-ray diffraction and scanning electron microscopy).

A2.1 Infrared spectroscopy

Infrared (IR) spectroscopy operates on the principle that every molecule is made up of a unique configuration of chemical bonds. Each bond has a characteristic frequency at which it will absorb energy and translate it into vibrational motion. For a normal mode of vibration to be infrared active, *i.e.* to give rise to an observable infrared band, there must be a change in dipole moment of the molecule associated with vibration. Therefore, diatomic gases without dipole moments such as N_2, H_2 and O_2 are not detectable by IR spectroscopy (Colthup *et al.*, 1964). To identify organic gases (*e.g.* CO, CO_2, CH_4) and certain inorganic gases (*e.g.* SO_2), electromagnetic radiation within the mid-infrared spectrum with wave numbers of $450 - 4000$ cm^{-1} or equivalent wavelengths of $2.5 - 22.2$ μm can be used, so long as unique, non-overlapping frequencies exist by which each species in the mixture can be identified.

In a typical gas-phase IR analyser, a monochromatic light is directed into a cell containing the sample; the transmittance is measured by a detector of InGaAs or PbSe. At a specified wavelength, a transmittance of 1 indicates the absence of the species; a transmittance of 0 indicates the species is present in such quantity that all of the light is absorbed. The transmittance, Tr, and absorbance, Abs, are related by $\mathrm{Abs} = -\log_{10}(\mathrm{Tr})$. Figure A2.1 shows the IR

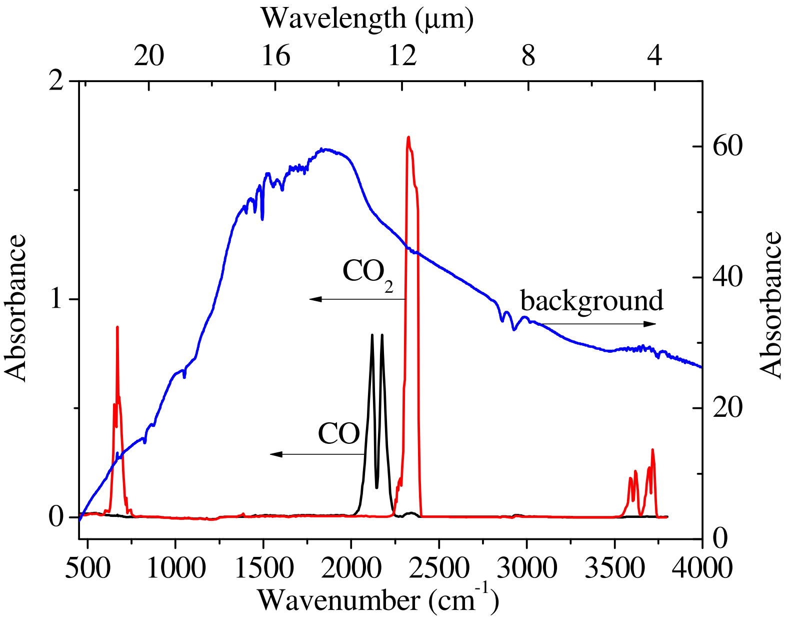

Figure A2.1: Absorbance *versus* wavelength for CO, CO_2 and a typical background scan.

spectra for CO and CO_2 as well as a typical background scan of the atmosphere (NIST, 2010). Identification of the C=O bond in CO_2 is apparent at 2380 cm^{-1}, the doublet for CO at 2120 and 2180 cm^{-1}. The background scan shows aberration from the smooth spectrum owing to H_2O and CO_2 in the atmosphere. Infrared analysers (Easyline, ABB) with response times of < 3 s were used in experiments.

A2.2 Thermal conductivity

For a monatomic gas obeying the Lennard-Jones 6-12 potential, the thermal conductivity can be calculated from (Fahien, 1983):

$$\lambda_0 = 8.322 \times 10^{-4} \frac{\sqrt{T/M_i}}{\sigma^2 \Omega} = (\mathrm{W/m\ K}), \tag{A2.1}$$

where the collision integral, Ω, can be evaluated as

$$\Omega = \frac{1.16145}{T^{\star 0.14874}} + 0.52487 e^{-0.7732 T^\star} + 2.16178 e^{-2.43787 T^\star}, \tag{A2.2}$$

for $0.4 < T^\star < 1.4$, where

$$T^\star = T \frac{k_b}{\xi}. \tag{A2.3}$$

Here,

T	Absolute temperature	(K)
M_i	Molecular mass of species i	(kg/kmol)
σ	Collision diameter from the Lennard-Jones function	(nm)
$\frac{k_B}{\xi}$	Lennard-Jones parameter	(K^{-1})

For polyatomic gases, a correction factor must be applied to determine the thermal conductivity (Fristrom and Westenberg, 1965),

$$\lambda_i = \lambda_0 \left(0.115 + \frac{0.178}{4.184} \times C^{\circ}_{p,i} \right), \tag{A2.4}$$

where $C^{\circ}_{p,i}$ can be calculated from Eq. (A1.2) and has units (J/mol K). The thermal conductivity of a mixture of n components can be determined from Bird *et al.* (2007):

$$\lambda_{\text{mix}} = \sum_{i}^{n} \frac{y_i \lambda_i}{\sum_j^n y_j \Phi_{ij}}, \tag{A2.5}$$

with

$$\Phi_{ij} = \frac{1}{\sqrt{8}} \left(1 + \frac{M_i}{M_j} \right)^{\frac{-1}{2}} \left[1 + \left(\frac{\lambda_i}{\lambda_j} \right)^{\frac{1}{2}} \left(\frac{M_j}{M_i} \right)^{\frac{1}{4}} \right]^2 . \tag{A2.6}$$

Thermal conductivities for selected gases at 300 K and 1000 K are listed in Table A2.2 and agree with experimental results reported in Fristrom and Westenberg (1965) to within 5 %, except for CO_2. Since the thermal conductivity of H_2 is approximately one order of magnitude larger than that for the other gases, measuring the thermal conductivity of a mixture provides a suitable method for determining its content of H_2. Using Eqs. (A2.5) and (A2.6) demonstrated that increasing the composition of CO or CO_2 in a mixture of N_2 and H_2 results in a change in thermal conductivity which is approximately linear with composition of the introduced species; corrections to the measured value of H_2 were therefore straightforward once the value of CO or CO_2 had been measured with IR spectroscopy. In experiments, the thermal

Table A2.2: Thermal conductivity (W/m K) of various gases at 300 K and 1100 K.

Species, i	H_2	CO	CO_2	N_2	O_2	CH_4
λ_i (300 K)	0.1757	0.0251	0.0162	0.0247	0.0256	0.0340
λ_i (1100 K)	0.4628	0.0721	0.0691	0.0720	0.0719	0.1777

conductivity of the gas was measured using a silicon micromechanic sensor (TCS208F) within a designated analyser (Caldos27, ABB). The total volume of the diffusion cavity was 0.2 mm^3 and response times, ignoring the sampling line, were < 0.5 s.

A2.3 Determination of morphology using gas adsorption

An isotherm is a measure of the equilibrium quantity of pure gas adsorbed on to a solid surface as a function of its relative pressure, P/P_{sat}, where P_{sat} is the saturation pressure of the gas at fixed temperature. The BET equation (Brunauer *et al.*, 1938) assumes that adsorption of the first layer of gas molecules is governed by the characteristic heat of adsorption, while adsorption of subsequent layers is governed by the heat of liquefaction, since molecules in higher layers only contact like neighbours. The linear BET equation provides a good approximation to the surface area for $P/P_{\text{sat}} < 0.3$, *i.e.* before pores have been completely filled with adsorbate. Since the surface area is given in units of m^2/g, accurate determination of the mass of particles used is necessary and was performed, after degassing the samples externally under a flow of He at 363 K for 1 h and then at 383 K for 1 h, using a balance with a precision of 10^{-4} g.

At $P/P_{\text{sat}} = 1$, physical adsorption and capillary condensation will ensure that all pores are filled. Measuring the volume of gas released at decreasing relative pressures and recognising that smaller pores will exhaust gas at lower values of P/P_{sat}, the BJH equation (Barrett *et al.*, 1951) can be employed to determine the distribution of pore sizes. The BJH equation is a composite of BET and capillary theory and assumes cylindrical pores. Because calculations near the limits of $P/P_{\text{sat}} = 0$ and $P/P_{\text{sat}} = 1$ are not practicable, an arbitrary cut-off of $0.01 < P/P_{\text{sat}} < 0.95$ is used, which for N_2 corresponds to pores with mean diameters within the range 2 – 200 nm. A gas adsorption analyser (Tristar 3000, Micromeritics), operated at 77 K with N_2 gas, was used in all adsorption experiments.

A2.4 Mercury intrusion porosimetry

Porosity and pore size distributions for pores with mean radii between 4 nm and 100 μm were determined using mercury porosimetry (Micromeritics, Autopore IV). Since Hg is a non-wetting liquid at 298 K, *i.e.* it forms a contact angle $> 90°$ with most solids, it will only enter a capillary under an applied pressure. Following Washburn (1921) and assuming the porous solid is comprised of cylindrical capillaries, a force balance on a single pore relates the pressure of Hg to capillary pressure:

$$P = \frac{-2\gamma\cos\theta}{r_\mathrm{e}}, \tag{A2.7}$$

where P is the pressure of the mercury at the inlet to the pore, γ is the surface tension of mercury, θ is the contact angle, and r_e is the radius of the cylindrical pore. The pore size distribution is determined from the volume intruded at each incremental pressure: the total porosity is determined using the volume of the particles and the total volume intruded. The particles were degassed prior to analysis; parameters for the triply-distilled mercury of θ = 130° and γ = 0.49 N/m were assumed.

A2.5 X-ray diffraction

Diffraction provides a method for measuring the interatomic distance, d, of a unit cell of a crystal, since X-rays (typical wavelength 2-25 nm) will interfere constructively when Bragg's law,

$$n\lambda = 2d\sin\theta, \tag{A2.8}$$

is satisfied, as shown in Fig. A2.2. Here, λ is the wavelength of the X-ray and n is an integer describing the order of diffraction. Since θ is the angle of both incidence and reflection, interference patterns are reported as a function of 2θ. To perform quantitative XRD on a powder, the powder must be randomly oriented in space. Scanning through a range of 2θ values will then permit interference from all of the Bragg reflection planes to be measured. The interference pattern provides a unique fingerprint for the identification of a crystalline phase; the intensity of the interference pattern provides an indication of the quantity of each crystalline phase. Using the method of relative intensity ratios (RIR), quantitative measurements to within ±10 wt. % are possible if all of the existing phases have been identified; the method of Rietveld refinement, which matches not only intensities, but also peak positions, can achieve quantitative measurements to within ±5 wt. %. Amorphous phases cannot be distinguished using XRD.

For the X-ray diffractometer used (Philips model PW1830/00, in air at 298 K), the sample and X-ray source (Cu-K$_\alpha$) were fixed, while the detector arm was rotated through an angle of $20° \leq 2\theta \leq 80°$ at a rate of $0.01°\mathrm{s}^{-1}$.

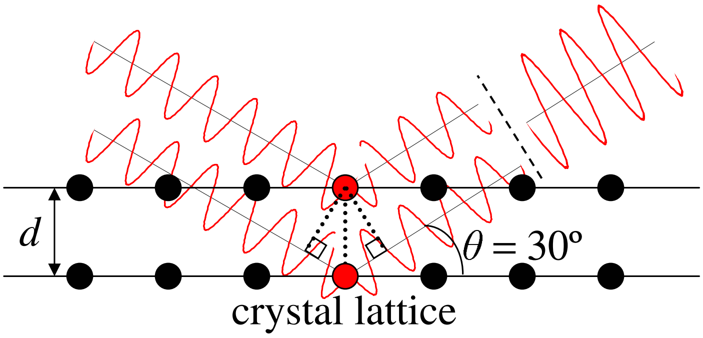

Figure A2.2: Schematic illustration of Bragg's law showing two constructively-interfering X-rays.

A2.6 Scanning electron microscopy

Scanning electron microscopy (SEM) permits the imaging of bulk specimens with nanometre resolution and improved depth of focus compared to optical microscopes. In SEM, electrons are thermally emitted from a metal filament with a high melting point, such as tungsten, in a vacuum (10^{-4} Pa) and focused to a spot size of ~ 5 nm using electromagnetic lenses (Reimer, 1998). Deflector plates are then used to direct the beam on to the sample to permit raster scanning of a rectangular portion of the surface of a specimen. The incident electrons of high energy will interact with the specimen and *e.g.* (i) cause secondary, lower-energy electrons to be emitted from the specimen, (ii) be reflected as high-energy back-scattered electrons or (iii) produce characteristic X-rays from electron interactions within the sample. In this dissertation, (i) secondary electron imaging (SEI) was used and (iii) the atomic composition was determined using energy dispersive X-ray spectroscopy (EDS, Oxford INCAPentaFET-×3). On a JSM-5800LV microscope, a beam energy of 15 kV was used to produce a spot size of ~ 7 nm with a typical resolution of 100 nm, as shown in Fig. 3.8. A field emission gun scanning electron microsocpe (FEG-SEM, JSM-6340F), which produced a more coherent electron beam with a smaller spot size (< 2 nm) and operated at 5 kV, offered an improved resolution of ~ 10 nm, as shown in Fig 4.1. For imaging, the specimen must be electrically conductive as well as grounded so as to avoid the accumulation of charge (Goldstein *et al.*, 2003). Here, a conductive phenolic resin (Conducto-Mount, Metprep) was used to mount samples.

Appendix 3

Temperature change during oxidation

To determine the temperature rise during the oxidation of Fe_3O_4 to Fe_2O_3 in air, reaction (1.17) in Table 1.2, reproduced below for convenience, is used:

$$2\,\mathrm{Fe_3O_4} + 1/2\,\mathrm{O_2} \rightleftarrows 3\,\mathrm{Fe_2O_3}, \qquad \Delta H^\circ_{1023\ \mathrm{K}} = -238\ \mathrm{kJ/mol} \tag{A3.1}$$

where the enthalpy is for the reaction as written. Conservation of energy within the packed bed dictates:

$$\Delta H^\circ_{1023\ \mathrm{K}} = \mathrm{Mass} \times C_p \times \Delta T, \tag{A3.2}$$

where the fact that the specific heat capacity at constant pressure is nearly constant for most substances on a mass basis and can be approximated by that for air, $C_p = 1000$ J/(kg K), has been used. In Eq. (A3.2), Mass denotes the mass of the bed affected by the change in temperature, and it has been assumed that C_p and $\Delta H^\circ_{1023\ \mathrm{K}}$ are approximately constant with temperature, which holds for small temperature excursions. Rearranging Eq. (A3.2) gives the familiar result:

$$\Delta T = \frac{\Delta H^\circ_{1023\ \mathrm{K}}}{\mathrm{Mass} \times C_p}. \tag{A3.3}$$

Choosing 2 mol Fe_3O_4 as a basis as *per* reaction (A3.1), the total mass of solid and gaseous species involved is 4.4 kg, as shown in Fig. A3.1. Thus, the total temperature rise for the oxidation reaction is:

$$\Delta T = \frac{238}{4.4 \times 1} = 54\ \mathrm{K}, \tag{A3.4}$$

sufficiently small to justify the assumption of constant C_p and $\Delta H^\circ_{1023\ \mathrm{K}}$. The above analysis assumes that 1 g of iron oxide and 8 g of sand are all at the same temperature.

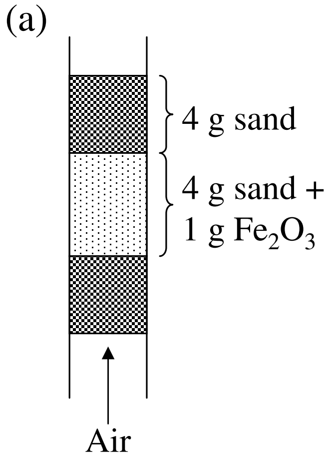

(b)

$$\text{Mass} = \frac{\overbrace{2\times(3\times56+4\times16)}^{Fe_3O_4}+\overbrace{16}^{\frac{1}{2}O_2}+\overbrace{\frac{79}{21}\times\frac{1}{2}\times28}^{N_2}}{1000}+\frac{\overbrace{\overbrace{3\times(2\times56+3\times16)}^{Fe_2O_3}\times8}^{\text{sand}}}{1000}=0.53+3.84=4.4\text{kg}$$

Figure A3.1: (a) Schematic diagram of the initial packed bed. (b) Calculation of the total mass in the system, including sand, for oxidation of 2 mol of Fe_3O_4 to 3 mol of Fe_2O_3.

Appendix 4

Determining the reaction rate

Reaction (1.9) and the corresponding rate expression can be written as:

$$3\,\mathrm{Fe_2O_3} + \mathrm{CO} \rightleftarrows 2\,\mathrm{Fe_3O_4} + \mathrm{CO_2} \tag{A4.1}$$

$$-\frac{dc_{\mathrm{CO}}}{dt} = \frac{dc_{\mathrm{CO_2}}}{dt} = k_i c_{\mathrm{CO}} - k_{-i} c_{\mathrm{CO_2}}, \tag{A4.2}$$

where k_i and k_{-i} are the intrinsic rate constants for the forward and reverse reaction, respectively. The derivation of the effectiveness factor and Thiele modulus will now be demonstrated for this specific case. However, an analogous analysis can be performed for any of the iron oxide reduction and oxidation steps in Table 1.2 and, more generally, for any gas solid reaction of the form of Eq. (A4.1) with first order kinetics.

Reaction of a single particle of $\mathrm{Fe_2O_3}$ will occur *via* the following five steps: (i) mass transfer of reactant CO from the bulk phase to the particle surface, (ii) diffusion of CO through the porous particle, (iii) reaction of CO to form $\mathrm{CO_2}$ and simultaneous, conversion of $\mathrm{Fe_2O_3}$ to $\mathrm{Fe_3O_4}$, (iv) diffusion of product $\mathrm{CO_2}$ through the porous particle, and (v) mass transfer of $\mathrm{CO_2}$ from the particle surface into the bulk phase. The following assumptions are made:

- no changes in the volume of the solid occur during the course of the reaction,
- temperature variations are minimal so that the isothermal approximation holds,
- the effective diffusivities, mass transfer coefficients and intrinsic rate constants are constant throughout the course of the reaction,
- the particles are uniform spheres,
- the change in concentration with respect to time within a sphere is negligible compared

to the change in concentration with respect to radial position, therefore, the pseudo-steady-state hypothesis holds.

A4.1 Relationship between intraparticle diffusion and chemical reaction

In a single reacting sphere, a mole balance on the spherical shell from r to $r + \Delta r$ for reactant CO yields:

$$\underbrace{4\pi r^2 D_{\mathrm{e,CO}} \frac{dc_{\mathrm{CO}}}{dr}\bigg|_{r+\Delta r}}_{\text{in}} \underbrace{- 4\pi r^2 D_{\mathrm{e,CO}} \frac{dc_{\mathrm{CO}}}{dr}\bigg|_{r}}_{\text{out}} \underbrace{- 4\pi r^2\bigg|_{r+\frac{\Delta r}{2}} \Delta r (k_i c_{\mathrm{CO}} - k_{-i} c_{\mathrm{CO_2}})}_{\text{reaction}} = 0 \tag{A4.3}$$

$$\frac{D_{\mathrm{e,CO}}}{r^2} \frac{d}{dr}\left(r^2 \frac{dc_{\mathrm{CO}}}{dr}\right) - (k_i c_{\mathrm{CO}} - k_{-i} c_{\mathrm{CO_2}}) = 0. \tag{A4.4}$$

Similarly, for product CO_2:

$$\frac{D_{\mathrm{e,CO_2}}}{r^2} \frac{d}{dr}\left(r^2 \frac{dc_{\mathrm{CO_2}}}{dr}\right) + (k_i c_{\mathrm{CO}} - k_{-i} c_{\mathrm{CO_2}}) = 0. \tag{A4.5}$$

Finiteness of $c_{\mathrm{CO}}(r)$ and $c_{\mathrm{CO_2}}(r)$ at $r = 0$ is required. Additionally, the following boundary condition holds:

$$\left.\begin{aligned} c_{\mathrm{CO}}(r) &= c_{\mathrm{CO,s}} \\ c_{\mathrm{CO_2}}(r) &= c_{\mathrm{CO,s}} \end{aligned}\right\} \quad r = R, \tag{A4.6}$$

where $c_{\mathrm{CO,s}}$ and $c_{\mathrm{CO_2,s}}$ are the concentration of CO and CO_2 at the surface of the sphere, $r = R$, respectively, and are assumed to be constant.

A4.2 Solving for $c_{\mathrm{CO}}(r)$ and $c_{\mathrm{CO_2}}(r)$

To solve Eqs. (A4.4) and (A4.5) for the intraparticle concentrations, $c_{\mathrm{CO}}(r)$ and $c_{\mathrm{CO_2}}(r)$, let $u_{\mathrm{CO}} = r c_{\mathrm{CO}}$ and $u_{\mathrm{CO_2}} = r c_{\mathrm{CO_2}}$. Rewriting Eqs. (A4.4) and (A4.5) gives for CO and CO_2:

$$D_{\mathrm{e,CO}} \frac{d^2 u_{\mathrm{CO}}}{dr^2} - (k_i u_{\mathrm{CO}} - k_{-i} u_{\mathrm{CO_2}}) = 0 \tag{A4.7}$$

$$D_{\mathrm{e,CO_2}} \frac{d^2 u_{\mathrm{CO_2}}}{dr^2} + (k_i u_{\mathrm{CO}} - k_{-i} u_{\mathrm{CO_2}}) = 0. \tag{A4.8}$$

Further differentiation and elimination gives:

$$\frac{d^4 u_{\mathrm{CO}}}{dr^4} - P\frac{d^2 u_{\mathrm{CO}}}{dr^2} = 0 \tag{A4.9}$$

$$\frac{d^4 u_{\mathrm{CO_2}}}{dr^4} - P\frac{d^2 u_{\mathrm{CO_2}}}{dr^2} = 0, \tag{A4.10}$$

where

$$P = \left(\frac{k_i}{D_{\mathrm{e,CO}}} + \frac{k_{-i}}{D_{\mathrm{e,CO_2}}}\right). \tag{A4.11}$$

Integration of these fourth order differential equations will give four constants of integration. For the case of u_{CO}:

$$u_{\mathrm{CO}} = a_1 + b_1 r + c_1 e^{r\sqrt{P}} + e_1 e^{-r\sqrt{P}} \tag{A4.12}$$

$$c_{\mathrm{CO}} = \frac{a_1}{r} + b_1 + \frac{c_1}{r}e^{r\sqrt{P}} + \frac{e_1}{r}e^{-r\sqrt{P}}. \tag{A4.13}$$

Mathematically, the restriction that the concentrations at $r = 0$ are finite implies $a_1 = 0$; also, $c_1 = -e_1$ otherwise the exponential terms are non-finite. Using

$$\sinh(r\sqrt{P}) = \frac{e^{r\sqrt{P}} - e^{-r\sqrt{P}}}{2}, \tag{A4.14}$$

gives for CO and CO_2, respectively:

$$c_{\mathrm{CO}} = b_1 + \frac{2c_1}{r}\sinh r\sqrt{P} \tag{A4.15}$$

$$c_{\mathrm{CO_2}} = b_2 + \frac{2c_2}{r}\sinh r\sqrt{P}. \tag{A4.16}$$

Here, it is noted that b_1 and b_2, and c_1 and c_2 are not independent, rather substituting into Eq. (A4.4) or (A4.5) and comparing terms:

$$b_2 = b_1\frac{k_i}{k_{-i}} \tag{A4.17}$$

$$c_2 = -\frac{D_{\mathrm{e,CO}}}{D_{\mathrm{e,CO_2}}}c_1. \tag{A4.18}$$

Therefore,

$$c_{\mathrm{CO}} = b_1 + \frac{2c_1}{r} \sinh r\sqrt{P} \tag{A4.19}$$

$$c_{\mathrm{CO_2}} = \frac{k_i}{k_{-i}} b_1 - \frac{2c_1}{r} \frac{D_{\mathrm{e,CO}}}{D_{\mathrm{e,CO_2}}} \sinh r\sqrt{P}. \tag{A4.20}$$

Next, the constants b_1 and c_1 are solved for by evaluating Eqs. (A4.19) and (A4.20) at the boundary, $r = R$, using Eq. (A4.6). This gives

$$b_1 = \frac{c_{\mathrm{CO_2,s}} + \frac{D_{\mathrm{e,CO}}}{D_{\mathrm{e,CO_2}}} c_{\mathrm{CO,s}}}{\left(\frac{k_i}{k_{-i}} + \frac{D_{\mathrm{e,CO}}}{D_{\mathrm{e,CO_2}}}\right)} \tag{A4.21}$$

$$c_1 = \frac{R}{2\sinh R\sqrt{P}} \cdot \frac{\frac{k_i}{k_{-i}} c_{\mathrm{CO,s}} - c_{\mathrm{CO_2,s}}}{\left(\frac{k_i}{k_{-i}} + \frac{D_{\mathrm{e,CO}}}{D_{\mathrm{e,CO_2}}}\right)}. \tag{A4.22}$$

With these constants and Eqs. (A4.19) and (A4.20), the values of c_{CO} and $c_{\mathrm{CO_2}}$ within the particle are now defined.

A4.3 Effectiveness factor and Thiele modulus

Next, following Levenspiel (1972), the effectiveness factor, η, is defined as the ratio of the observed rate of reaction over the intrinsic rate of reaction in the absence of mass transfer limitations due to intraparticle diffusion:

$$\eta = \frac{4\pi \int_0^R r^2 \left[k_i c_{\mathrm{CO}}(r) - k_{-i} c_{\mathrm{CO_2}}(r)\right] dr}{4\pi \int_0^R r^2 \left[k_i c_{\mathrm{CO,s}} - k_{-i} c_{\mathrm{CO_2,s}}\right] dr}. \tag{A4.23}$$

The denominator in Eq. (A4.23) is easily evaluated and gives:

$$4\pi \int_0^R r^2 \left(k_i c_{\mathrm{CO,s}} - k_{-i} c_{\mathrm{CO_2,s}}\right) dr = \frac{4\pi R^3}{3} \left(k_i c_{\mathrm{CO,s}} - k_{-i} c_{\mathrm{CO_2,s}}\right). \tag{A4.24}$$

The numerator in Eq. (A4.23) is evaluated using Eqs. (A4.19) and (A4.20) as follows:

$$\begin{aligned} 4\pi \int_0^R r^2 \left[k_i c_{\mathrm{CO}}(r) - k_{-i} c_{\mathrm{CO_2}}(r)\right] dr = {} & 4\pi \int_0^R r^2 \left[k_i \left(b_1 + \frac{2c_1}{r} \sinh r\sqrt{P}\right)\right] \\ & - 4\pi \int_0^R r^2 \left[k_{-i} \left(\frac{k_i}{k_{-i}} b_1 - \frac{2c_1}{r} \frac{D_{\mathrm{e,CO}}}{D_{\mathrm{e,CO_2}}} \sinh r\sqrt{P}\right)\right]. \end{aligned} \tag{A4.25}$$

Terms with b_1 cancel and substituting for c_1 after integration by parts then gives:

$$4\pi \int_0^R r^2 \left[k_i c_{\mathrm{CO}}(r) - k_{-i} c_{\mathrm{CO_2}}(r)\right] dr = \frac{4\pi R \left(k_i c_{\mathrm{CO,s}} - k_{-i} c_{\mathrm{CO_2,s}}\right)}{P} \left[R\sqrt{P}\coth(R\sqrt{P}) - 1\right]. \tag{A4.26}$$

Using the two integral results, *i.e.* Eqs. (A4.24) and (A4.26), in Eq. (A4.23), defining $\phi \equiv R\sqrt{P}$, and canceling terms then gives:

$$\eta = \frac{3}{\phi^2}\left[\phi \coth(\phi) - 1\right] \tag{A4.27}$$

$$\phi = R\sqrt{\frac{k_i}{D_{\mathrm{e,CO}}} + \frac{k_{-i}}{\mathrm{CO_2}}}. \tag{A4.28}$$

Note that for a negligible back reaction, *i.e.* $k_{-i} = 0$, Eq. (A4.27) is obtained with $\phi = R\sqrt{k_i / D_{\mathrm{e,CO}}}$.

A4.4 Relationship between the intraparticle and outlet concentrations

From the pseudo-steady-state assumption, the rate at which CO enters the sphere must be equal to the rate of reaction within the sphere and the rate of CO_2 leaving the sphere. Writing these rates in units of mol/(s g of particle as Fe_2O_3) gives:

$$r' = \frac{k_{\mathrm{g,CO}}\left(c_{\mathrm{CO,p}} - c_{\mathrm{CO,s}}\right) 4\pi R^2}{\frac{4\pi R^3}{3}\rho_{\mathrm{Fe_2O_3}}} \tag{A4.29}$$

$$r' = \frac{\left(k_i c_{\mathrm{CO,s}} - k_{-i} c_{\mathrm{CO_2,s}}\right)\eta}{\rho_{\mathrm{Fe_2O_3}}} \tag{A4.30}$$

$$r' = \frac{k_{\mathrm{g,CO_2}}\left(c_{\mathrm{CO_2,s}} - c_{\mathrm{CO_2,p}}\right) 4\pi R^2}{\frac{4\pi R^3}{3}\rho_{\mathrm{Fe_2O_3}}}, \tag{A4.31}$$

where $c_{\mathrm{CO,p}}$ and $c_{\mathrm{CO_2,p}}$ are the concentration of CO and CO_2 in the particulate phase, respectively. Rearranging Eqs. (A4.29)-(A4.31) gives:

$$\frac{r' R \rho_{\mathrm{Fe_2O_3}}}{3k_{\mathrm{g,CO}}} = c_{\mathrm{CO,p}} - c_{\mathrm{CO,s}} \tag{A4.32}$$

$$\frac{r' \rho_{\mathrm{Fe_2O_3}}}{\eta} = k_i c_{\mathrm{CO,s}} - k_{-i} c_{\mathrm{CO_2,s}} \tag{A4.33}$$

$$\frac{r' R \rho_{\mathrm{Fe_2O_3}}}{3k_{\mathrm{g,CO_2}}} = c_{\mathrm{CO_2,s}} - c_{\mathrm{CO_2,p}}. \tag{A4.34}$$

Summing Eqs. (A4.32)-(A4.34) after multiplying Eq. (A4.32) by k_i and Eq. (A4.34) by k_{-i} enables one to write the rate, r', in terms of the concentrations of the particulate phase only:

$$r' \rho_{\mathrm{Fe_2O_3}} \left(\frac{k_i R}{3k_{\mathrm{g,CO}}} + \frac{1}{\eta} + \frac{k_{-i} R}{3k_{\mathrm{g,CO_2}}} \right) = k_i c_{\mathrm{CO,p}} - k_{-i} c_{\mathrm{CO_2,p}}. \tag{A4.35}$$

After dividing by k_i and rearranging, Eq. (A4.35) becomes:

$$r' = \frac{k}{\rho_{\mathrm{Fe_2O_3}}} \left(c_{\mathrm{CO,p}} - \frac{c_{\mathrm{CO_2,p}}}{K_p} \right) \tag{A4.36}$$

$$\frac{1}{k} = \left(\frac{R}{3k_{\mathrm{g,CO}}} + \frac{1}{k_i \eta} + \frac{R}{3k_{\mathrm{g,CO_2}} K_p} \right), \tag{A4.37}$$

where $K_p = k_i / k_{-i}$. Assuming a well-mixed fluidised bed reactor, such that the concentration in the particulate phase is equal to the concentration at the outlet, *i.e.* $c_{\mathrm{CO,p}} = c_{\mathrm{CO,out}}$ and $c_{\mathrm{CO_2,p}} = c_{\mathrm{CO_2,out}}$, Eq. (A4.36) can be rewritten:

$$r' = \frac{k}{\rho_{\mathrm{Fe_2O_3}}} \left(c_{\mathrm{CO,out}} - \frac{c_{\mathrm{CO_2,out}}}{K_p} \right). \tag{A4.38}$$

Note that Eq. (A4.38) with k given by Eq. (A4.37) is the relation used in Chapter 5, section 5.3, to evaluate the rate of reduction of iron oxide. While derived for the case of a single sphere, Eq. (A4.38) gives the rate in units of mol/(s g of particle as Fe_2O_3) and is therefore a general rate expression for any number of particles.

Appendix 5

Lattice Boltzmann method

In the following, the derivation of the discrete equilibrium function, transformation matrix, and continuity and Navier-Stokes equations will be outlined. While the derivations are specific to the D3Q19 model, derivations for other LB models, *e.g.* D2Q9 or D3Q15, follow in an analogous and straightforward manner.

A5.1 Derivation of the discrete equilibrium distribution

The equilibrium distribution function in continuous space and time was the Maxwell-Boltzmann distribution, given by Eq. (8.5) for the BGK approximation. However, a discrete equilibrium distribution, $f_i^{(\mathrm{eq})}$, for the LB equation is required as shown by Eq. (8.12). Taylor expansion (He and Luo, 1997c) of the Maxwell-Boltzmann distribution, Eq. (8.5), with respect to the macroscopic velocity, $\mathbf{u}$, gives:

$$\begin{aligned} f^{(\mathrm{eq})} &= f^{(\mathrm{eq})}\Big|_{\mathbf{u}=0} + \frac{\partial f^{(\mathrm{eq})}}{\partial \mathbf{u}}\Big|_{\mathbf{u}=0}\mathbf{u} + \frac{\partial^2 f^{(\mathrm{eq})}}{\partial^2 \mathbf{u}}\Big|_{\mathbf{u}=0}\frac{\mathbf{u}^2}{2!} + O(\mathbf{u}^3) \\ &= \rho\left(\frac{m}{2\pi k_{\mathrm{B}}T}\right)^{\mathrm{D}/2}\exp\left(\frac{-m\mathbf{v}^2}{2k_{\mathrm{B}}T}\right)\left[1+\frac{m\mathbf{v}\cdot\mathbf{u}}{k_{\mathrm{B}}T}+\frac{m^2(\mathbf{v}\cdot\mathbf{u})^2}{2(k_{\mathrm{B}}T)^2}-\frac{m\mathbf{u}^2}{2k_{\mathrm{B}}T}\right]+O(\mathbf{u}^3). \end{aligned} \tag{A5.1}$$

Greater accuracy in $f^{(\mathrm{eq})}$ with respect to $\mathbf{u}$ can be obtained by expansion to higher orders in $\mathbf{u}$ if required. An analogous equation to Eq. (A5.1) in discrete space is then:

$$f_i^{(\mathrm{eq})} = \rho w_i\left(1+\frac{m\mathbf{v}_i\cdot\mathbf{u}}{k_{\mathrm{B}}T}+\frac{m^2(\mathbf{v}_i\cdot\mathbf{u})^2}{2(k_{\mathrm{B}}T)^2}-\frac{m\mathbf{u}^2}{2k_{\mathrm{B}}T}\right)+O(\mathbf{u}^3), \tag{A5.2}$$

where the w_i can be considered weighting factors which will be constant once the dimension, D, and velocity set, Q are chosen, that is, once the D-dimensions and Q-velocities in the DDQQ model have been specified.

To determine the w_i, the assumption of a closed system at equilibrium such that the macroscopic velocity, $\mathbf{u} = 0$, is sufficient and gives:

$$\rho_0 \left(\frac{m}{2\pi k_\mathrm{B} T} \right)^{\frac{\mathrm{D}}{2}} \exp\left(\frac{-m\mathbf{v}_i^2}{2k_\mathrm{B} T} \right) = f^{(\mathrm{eq})} \Big|_{\mathbf{u}=0} \tag{A5.3}$$

$$\rho_0 w_i = f_i^{(\mathrm{eq})} \Big|_{\mathbf{u}=0}, \tag{A5.4}$$

for the continuous (A5.3) and discrete (A5.4) cases, respectively, where ρ_0 is the mean mass density of the system, *i.e.* the density of the system at equilibrium. The w_i can then be determined by requiring the moments of the discrete lattice Boltzmann equilibrium distribution to be equal to the moments of the continuous Maxwell-Boltzmann distribution, both evaluated at $\mathbf{u} = 0$, up to fourth order. Thus, substituting $a = m/(2k_\mathrm{B}T)$ into the Maxwell-Boltzmann distribution, Eq. (8.5), and taking the moments up to fourth order gives for the three-dimensional, D = 3, case:

$$\int f^{(\mathrm{eq})} \Big|_{\mathbf{u}=0} d\mathbf{v} = \rho_0 \left(\frac{a}{\pi} \right)^{\frac{3}{2}} \int e^{(-av_x^2)} dv_x \int e^{(-av_y^2)} dv_y \int e^{(-av_z^2)} dv_z = \rho_0 = \rho_0 \sum_i w_i \tag{A5.5}$$

$$\begin{aligned} \int v_x f^{(\mathrm{eq})} \Big|_{\mathbf{u}=0} d\mathbf{v} &= \rho_0 \left(\frac{a}{\pi} \right)^{\frac{3}{2}} \int v_x e^{(-av_x^2)} dv_x \int e^{(-av_y^2)} dv_y \int e^{(-av_z^2)} dv_z = \\ &= 0 = \rho_0 \sum_i w_i v_{ix} \end{aligned} \tag{A5.6}$$

$$\begin{aligned} \int v_x^2 f^{(\mathrm{eq})} \Big|_{\mathbf{u}=0} d\mathbf{v} &= \rho_0 \left(\frac{a}{\pi} \right)^{\frac{3}{2}} \int v_x^2 e^{(-av_x^2)} dv_x \int e^{(-av_y^2)} dv_y \int e^{(-av_z^2)} dv_z = \\ &= \frac{\rho_0}{2a} = \rho_0 \frac{k_\mathrm{B} T}{m} = \rho_0 \sum_i w_i v_{ix}^2 \end{aligned} \tag{A5.7}$$

$$\begin{aligned} \int v_x^3 f^{(\mathrm{eq})} \Big|_{\mathbf{u}=0} d\mathbf{v} &= \rho_0 \left(\frac{a}{\pi} \right)^{\frac{3}{2}} \int v_x^3 e^{(-av_x^2)} dv_x \int e^{(-av_y^2)} dv_y \int e^{(-av_z^2)} dv_z = \\ &= 0 = \rho_0 \sum_i w_i v_{ix}^3 \end{aligned} \tag{A5.8}$$

$$\begin{aligned} \int v_x^4 f^{(\mathrm{eq})} \Big|_{\mathbf{u}=0} d\mathbf{v} &= \rho_0 \left(\frac{a}{\pi} \right)^{\frac{3}{2}} \int v_x^4 e^{(-av_x^2)} dv_x \int e^{(-av_y^2)} dv_y \int e^{(-av_z^2)} dv_z = \\ &= \frac{3\rho_0}{4a^2} = 3\rho_0 \left(\frac{k_\mathrm{B} T}{m} \right)^2 = \rho_0 \sum_i w_i v_{ix}^4 \end{aligned} \tag{A5.9}$$

$$\begin{aligned} \int v_x^2 v_y^2 f^{(\mathrm{eq})} \Big|_{\mathbf{u}=0} d\mathbf{v} &= \rho_0 \left(\frac{a}{\pi} \right)^{\frac{3}{2}} \int v_x^2 e^{(-av_x^2)} dv_x \int v_y^2 e^{(-av_y^2)} dv_y \int e^{(-av_z^2)} dv_z = \\ &= \frac{\rho_0}{4a^2} = \rho_0 \left(\frac{k_\mathrm{B} T}{m} \right)^2 = \rho_0 \sum_i w_i v_{ix}^2 v_{iy}^2, \end{aligned} \tag{A5.10}$$

where the integrals have been evaluated using the standard integrals listed in Table A5.3. It

Table A5.3: Table of standard integrals (Young, 2006).

$I(n) = \int_{-\infty}^{+\infty} x^n \exp(-ax^2)dx$			
n	$I(n)$	n	$I(n)$
0	$\sqrt{\frac{\pi}{a}}$	odd	0
2	$\frac{1}{2}\sqrt{\frac{\pi}{a^3}}$	4	$\frac{3}{4}\sqrt{\frac{\pi}{a^5}}$

is noted that in Eqs. (A5.5)-(A5.10), odd moments vanish; this holds for all odd moments not just those listed. Additionally, it is noted that Eqs. (A5.5)-(A5.10) hold for the 2D case as well, where the term $\int e^{(-av_z^2)}dv_z$ in the evaluation of $\int f^{(\mathrm{eq})}\big|_{\mathbf{u}=0}d\mathbf{v}$ would be dropped and D = 2 would be used. The derivation of the equilibrium distribution up to this point has been general. To solve for the w_i, however, a specific lattice and hence a specific set of $\mathbf{v}_i$ must be chosen.

Considering the D3Q19 lattice in Fig. 8.2(a), the lattice velocities are:

$$\begin{aligned} v_{ix} &= [0,\ 1,\ -1,\ 0,\ 0,\ 0,\ 0,\ 1,\ -1,\ 1,\ -1,\ 1,\ -1,\ 1,\ -1,\ 0,\ 0,\ 0,\ 0]^{\mathsf{T}}c \\ v_{iy} &= [0,\ 0,\ 0,\ 1,\ -1,\ 0,\ 0,\ 1,\ 1,\ -1,\ -1,\ 0,\ 0,\ 0,\ 0,\ 1,\ -1,\ 1,\ -1]^{\mathsf{T}}c \\ v_{iz} &= [0,\ 0,\ 0,\ 0,\ 0,\ 1,\ -1,\ 0,\ 0,\ 0,\ 0,\ 1,\ 1,\ -1,\ -1,\ 1,\ 1,\ -1,\ -1]^{\mathsf{T}}c, \end{aligned} \tag{A5.11}$$

where multiplication by $c = \Delta x/\Delta t$, with Δx = (m/lattice unit) and Δt = (s/time step), permits conversion from lattice units to physical units. From the symmetry of the lattice, it can further be seen that the w_i will be identical for directions with identical lattice speeds, $|\mathbf{v}_i|$. Thus, $w_0 = W_0$, $w_1 = w_2 = w_3 = w_4 = w_5 = w_6 = W_1$ and $w_7 = \ldots = w_{18} = W_2$ is assumed. Evaluating the right hand sides of Eqs. (A5.5)-(A5.10) with substitution of Eq. (A5.11) gives:

$$\text{0 moment :} \qquad \sum_i w_i = W_0 + 6W_1 + 12W_2 = 1 \tag{A5.12}$$

$$\text{2 moment :} \qquad \sum_i w_i v_{ix}^2 = 2W_1c^2 + 8W_2c^2 = \left(\frac{k_{\mathrm{B}}T}{m}\right) \tag{A5.13}$$

$$\text{4 moment :} \qquad \sum_i w_i v_{ix}^4 = 2W_1c^4 + 8W_2c^4 = 3\left(\frac{k_{\mathrm{B}}T}{m}\right)^2 \tag{A5.14}$$

$$\sum_i w_i v_{ix}^2 v_{iy}^2 = 4W_2c^4 = \left(\frac{k_{\mathrm{B}}T}{m}\right)^2 \tag{A5.15}$$

The four independent equations (A5.12-A5.15) can be used to solve for the four unknowns:

$$W_0 = \frac{1}{3}, \quad W_1 = \frac{1}{18}, \quad W_2 = \frac{1}{36}, \quad \frac{c^2}{3} = \frac{k_{\mathrm{B}}T}{m}, \tag{A5.16}$$

where generally $c^2 = \Delta x/\Delta t = 1$ is used.

Thus, the overall discrete equilibrium distribution for the D3Q19 model with error of order $O(\mathbf{u}^3)$ is given by evaluating Eq. (A5.2) with Eq. (A5.16),

$$f_i^{(\mathrm{eq})} = w_i \rho \left[1 + 3 \frac{\mathbf{v}_i \cdot \mathbf{u}}{c^2} + \frac{9}{2} \frac{(\mathbf{v}_i \cdot \mathbf{u})^2}{c^4} - \frac{3}{2} \frac{\mathbf{u}^2}{c^2} \right], \tag{A5.17}$$

where

$$w_i = \frac{1}{3} \quad i = 0 \tag{A5.18}$$

$$w_i = \frac{1}{18} \quad i = 1, 2, 3, 4 \tag{A5.19}$$

$$w_i = \frac{1}{36}. \quad i = 5, 6, ..., 18 \tag{A5.20}$$

For fluids with little variation in ρ, *e.g.* slightly-compressible flows, the equilibrium distribution function Eq. (A5.17) is sometimes written as:

$$f_i^{(\mathrm{eq})} = w_i \rho + w_i \rho_0 \left[3 \frac{\mathbf{v}_i \cdot \mathbf{u}}{c^2} + \frac{9}{2} \frac{(\mathbf{v}_i \cdot \mathbf{u})^2}{c^4} - \frac{3}{2} \frac{\mathbf{u}^2}{c^2}, \right] \tag{A5.21}$$

with the same w_i as before. This expression has been shown to reduce numerical errors due to the compressibility of the fluid (He and Luo, 1997b).

Finally, it is noted that Eq. (A5.16) has implications for the speed of sound, c_s, in the lattice model. If the definition of the isothermal speed of sound, $c_\mathrm{s}^2 = \left(\frac{\partial P}{\partial \rho}\right)_T$, is used with the equation of state for an ideal gas, $PV = n\mathrm{R}T$, then

$$c_\mathrm{s}^2 = \left(\frac{\partial P}{\partial \rho}\right)_T = \frac{\mathrm{R}T}{mN_\mathrm{A}} = \frac{k_\mathrm{B}T}{m} = \frac{c^2}{3}, \tag{A5.22}$$

where P is the pressure, ρ is the mass density, T is the temperature which is assumed constant, V is the volume of the system containing n moles of monatomic gas, R is the universal gas constant, m is the mass of a single monatomic particle and N_A is Avogadro's number. Hence, for the current lattice Boltzmann model with $c^2 = 1$ the speed of sound is $c_\mathrm{s} = \sqrt{1/3}$.

To summarise, the discrete analogue to the Maxwell-Boltzmann equilibrium distribution has been fully derived for a discrete lattice and is given by either Eq. (A5.17) for weakly-compressible flows or Eq. (A5.21) for incompressible flows.

A5.2 Transformation matrix for collisions with multiple relaxation times

Depending on the discrete velocity set chosen, the transformation matrix **M** for the collision operator with multiple relaxation times can be constructed from linear combinations of the discrete velocities, $\mathbf{v}_i$. The rows of **M** must be linearly independent and are typically chosen to be mutually orthogonal such that $\sum_k M_{ik}M_{jk} = 0$, where M_{ik} corresponds to the element on row i and column k of **M**. An example of the construction of **M** is given in Bouzidi *et al.* (2001). For the D3Q19 model, D'Humiéres *et al.* (2002) give,

$$\begin{gathered}
M_{1i} = |\mathbf{v}_i|^0\,; \quad M_{2i} = 19\,|\mathbf{v}_i|^2 - 30c^2; \quad M_{3i} = \frac{1}{2}\left(21\,|\mathbf{v}_i|^4 - 53c^2\,|\mathbf{v}_i|^2 + 24c^4\right); \; M_{4i} = \mathbf{v}_{ix}; \\
M_{5i} = \left(5\,|\mathbf{v}_i|^2 - 9c^2\right)\mathbf{v}_{ix}; \quad M_{6i} = \mathbf{v}_{iy}; \quad M_{7i} = \left(5\,|\mathbf{v}_i|^2 - 9c^2\right)\mathbf{v}_{iy}; \quad M_{8i} = \mathbf{v}_{iz}; \\
M_{9i} = \left(5\,|\mathbf{v}_i|^2 - 9c^2\right)\mathbf{v}_{iz}; \quad M_{10i} = 3\mathbf{v}_{ix}^2 - |\mathbf{v}_i|^2\,; \quad M_{11i} = \left(3\,|\mathbf{v}_i|^2 - 5c^2\right)\left(3\mathbf{v}_{ix}^2 - |\mathbf{v}_i|^2\right); \\
M_{12i} = \mathbf{v}_{iy}^2 - \mathbf{v}_{iz}^2; \quad M_{13i} = \left(3\,|\mathbf{v}_i|^2 - 5c^2\right)\left(\mathbf{v}_{iy}^2 - \mathbf{v}_{iz}^2\right); \quad M_{14i} = \mathbf{v}_{ix}\mathbf{v}_{iy}; \quad M_{15i} = \mathbf{v}_{iy}\mathbf{v}_{iz}; \\
M_{16i} = \mathbf{v}_{ix}\mathbf{v}_{iz}; \quad M_{17i} = \left(\mathbf{v}_{iy}^2 - \mathbf{v}_{iz}^2\right)\mathbf{v}_{ix}; \quad M_{18i} = \left(\mathbf{v}_{iz}^2 - \mathbf{v}_{ix}^2\right)\mathbf{v}_{iy}; \quad M_{19i} = \left(\mathbf{v}_{ix}^2 - \mathbf{v}_{iy}^2\right)\mathbf{v}_{iz}.
\end{gathered} \tag{A5.23}$$

For $c = 1$, an assumption that will apply from this point through Eq. (A5.79), the transformation matrix, **M**, is given by:

$$\mathbf{M} = \left[\begin{array}{rrrrrrrrrrrrrrrrrrr}
1 & 1 & 1 & 1 & 1 & 1 & 1 & 1 & 1 & 1 & 1 & 1 & 1 & 1 & 1 & 1 & 1 & 1 & 1 \\
-30 & -11 & -11 & -11 & -11 & -11 & -11 & 8 & 8 & 8 & 8 & 8 & 8 & 8 & 8 & 8 & 8 & 8 & 8 \\
12 & -4 & -4 & -4 & -4 & -4 & -4 & 1 & 1 & 1 & 1 & 1 & 1 & 1 & 1 & 1 & 1 & 1 & 1 \\
0 & 1 & -1 & 0 & 0 & 0 & 0 & 1 & -1 & 1 & -1 & 1 & -1 & 1 & -1 & 0 & 0 & 0 & 0 \\
0 & -4 & 4 & 0 & 0 & 0 & 0 & 1 & -1 & 1 & -1 & 1 & -1 & 1 & -1 & 0 & 0 & 0 & 0 \\
0 & 0 & 0 & 1 & -1 & 0 & 0 & 1 & 1 & -1 & -1 & 0 & 0 & 0 & 0 & 1 & -1 & 1 & -1 \\
0 & 0 & 0 & -4 & 4 & 0 & 0 & 1 & 1 & -1 & -1 & 0 & 0 & 0 & 0 & 1 & -1 & 1 & -1 \\
0 & 0 & 0 & 0 & 0 & 1 & -1 & 0 & 0 & 0 & 0 & 1 & 1 & -1 & -1 & 1 & 1 & -1 & -1 \\
0 & 0 & 0 & 0 & 0 & -4 & 4 & 0 & 0 & 0 & 0 & 1 & 1 & -1 & -1 & 1 & 1 & -1 & -1 \\
0 & 2 & 2 & -1 & -1 & -1 & -1 & 1 & 1 & 1 & 1 & 1 & 1 & 1 & 1 & -2 & -2 & -2 & -2 \\
0 & -4 & -4 & 2 & 2 & 2 & 2 & 1 & 1 & 1 & 1 & 1 & 1 & 1 & 1 & -2 & -2 & -2 & -2 \\
0 & 0 & 0 & 1 & 1 & -1 & -1 & 1 & 1 & 1 & 1 & -1 & -1 & -1 & -1 & 0 & 0 & 0 & 0 \\
0 & 0 & 0 & -2 & -2 & 2 & 2 & 1 & 1 & 1 & 1 & -1 & -1 & -1 & -1 & 0 & 0 & 0 & 0 \\
0 & 0 & 0 & 0 & 0 & 0 & 0 & 1 & -1 & -1 & 1 & 0 & 0 & 0 & 0 & 0 & 0 & 0 & 0 \\
0 & 0 & 0 & 0 & 0 & 0 & 0 & 0 & 0 & 0 & 0 & 0 & 0 & 0 & 0 & 1 & -1 & -1 & 1 \\
0 & 0 & 0 & 0 & 0 & 0 & 0 & 0 & 0 & 0 & 0 & 1 & -1 & -1 & 1 & 0 & 0 & 0 & 0 \\
0 & 0 & 0 & 0 & 0 & 0 & 0 & 1 & -1 & 1 & -1 & -1 & 1 & -1 & 1 & 0 & 0 & 0 & 0 \\
0 & 0 & 0 & 0 & 0 & 0 & 0 & -1 & -1 & 1 & 1 & 0 & 0 & 0 & 0 & 1 & -1 & 1 & -1 \\
0 & 0 & 0 & 0 & 0 & 0 & 0 & 0 & 0 & 0 & 0 & 1 & 1 & -1 & -1 & -1 & -1 & 1 & 1
\end{array}\right].$$

It is noted that while the individual rows of $\mathbf{M}$ are orthogonal, they are not normalised.

The moments, $\mathbf{m}$, are related to the distribution functions, $\mathbf{f}$, through the transformation matrix, $\mathbf{M}$, as given by Eq. (8.17). For consistency with the literature, each element of $\mathbf{m}$ is labeled according to standard convention (D'Humiéres *et al.*, 2002):

$$\mathbf{m} = \mathbf{M}\mathbf{f} = [\rho, e, e_2, j_x, q_x, j_y, q_y, j_z, q_z, 3p_{xx}, 3\pi_{xx}, p_{ww}, \pi_{ww}, p_{xy}, p_{yz}, p_{xz}, m_x, m_y, m_z]^{\mathsf{T}}, \quad \text{(A5.24)}$$

so that $m_1 = \rho$ is the density, $m_4 = j_x$ is the momentum in the $x-$direction, *etc.* This labeling makes the derivation of the Navier-Stokes equation in section A5.3 easier to understand.

Similarly, the equilibrium functions in moment space, $\mathbf{m}^{(\mathrm{eq})}$, are then related to those in velocity space, $\mathbf{f}^{(\mathrm{eq})}$, through Eq. (8.17) as follows:

$$\begin{aligned}\mathbf{m}^{(\mathrm{eq})} = \mathbf{M}\mathbf{f}^{(\mathrm{eq})} = [&\rho, e^{(\mathrm{eq})}, e_2^{(\mathrm{eq})}, j_x, q_x^{(\mathrm{eq})}, j_y, q_y^{(\mathrm{eq})}, j_z, q_z^{(\mathrm{eq})}, 3p_{xx}^{(\mathrm{eq})}, 3\pi_{xx}^{(\mathrm{eq})},\\ &p_{ww}^{(\mathrm{eq})}, \pi_{ww}^{(\mathrm{eq})}, p_{xy}^{(\mathrm{eq})}, p_{yz}^{(\mathrm{eq})}, p_{zx}^{(\mathrm{eq})}, m_x^{(\mathrm{eq})}, m_y^{(\mathrm{eq})}, m_z^{(\mathrm{eq})}]^{\mathsf{T}}. \qquad \text{(A5.25)}\end{aligned}$$

Thus, it is evident that for the conserved moments, ρ, j_x, j_y and j_z, *i.e.* the mass density and the momentum in the x, y and z directions, respectively, the following relation holds: $[m_i - m_i^{(\mathrm{eq})}] = 0$ for $i = \{1, 4, 6, 8\}$.

Expressions for the non-conserved or kinetic moments can be constructed through matrix multiplication of the transformation matrix, $\mathbf{M}$, and the local discrete Maxwellian, $\mathbf{f}^{(\mathrm{eq})}$, in Eq. (A5.21) and results in:

$$\begin{aligned}
&e^{(\mathrm{eq})} = -11\rho + 19\frac{(j_x^2 + j_y^2 + j_z^2)}{\rho_0}; \quad e_2^{(\mathrm{eq})} = 3\rho - \frac{11}{2}\frac{(j_x^2 + j_y^2 + j_z^2)}{\rho_0}; \quad q_x^{(\mathrm{eq})} = -\frac{2}{3}j_x;\\
&q_y^{(\mathrm{eq})} = -\frac{2}{3}j_y; \quad q_z^{(\mathrm{eq})} = -\frac{2}{3}j_z; \quad p_{xx}^{(\mathrm{eq})} = \frac{1}{3}\frac{\left[2j_x^2 - (j_y^2 + j_z^2)\right]}{\rho_0}; \quad \pi_{xx}^{(\mathrm{eq})} = -\frac{1}{2}p_{xx}^{(\mathrm{eq})};\\
&p_{ww}^{(\mathrm{eq})} = \frac{(j_y^2 - j_z^2)}{\rho_0}; \quad \pi_{ww}^{(\mathrm{eq})} = -\frac{1}{2}p_{ww}^{(\mathrm{eq})}; \quad p_{xy}^{(\mathrm{eq})} = \frac{j_x j_y}{\rho_0}; \quad p_{yz}^{(\mathrm{eq})} = \frac{j_y j_z}{\rho_0}; \quad p_{xz}^{(\mathrm{eq})} = \frac{j_x j_z}{\rho_0};\\
&m_x^{(\mathrm{eq})} = 0; \quad m_y^{(\mathrm{eq})} = 0; \quad m_z^{(\mathrm{eq})} = 0, \qquad \text{(A5.26)}
\end{aligned}$$

where $j_x = \rho_0 u_x$, $j_y = \rho_0 u_y$ and $j_z = \rho_0 u_z$. Here it is clear that the choice, $\rho_0 = 1$, simplifies the denominators in Eq. (A5.26). Optimisation with respect to the linear stability of the model (D'Humiéres *et al.*, 2002; Lallemand and Luo, 2000) gives the equilibrium values in

Eq. (A5.26), except:

$$e_2^{(\mathrm{eq})} = -\frac{475}{63}\frac{(j_x^2 + j_y^2 + j_z^2)}{\rho_0}; \quad \pi_{xx}^{(\mathrm{eq})} = 0; \quad \pi_{ww}^{(\mathrm{eq})} = 0. \tag{A5.27}$$

Either choice of equilibrium moments, Eq. (A5.26) or alternatively Eq. (A5.26) with Eq. (A5.27) substituted for the specified moments, can be used to derive the Navier-Stokes equations in the following section. For the current dissertation, the optimised equilibrium moments, Eq. (A5.26) with Eq. (A5.27) substituted for the specified moments, were used in simulations; however, the equilibrium moments given by Eq. (A5.26) will be used to derive the Navier-Stokes equation.

The collision matrix $\hat{\mathbf{S}}$ containing the inverse of the relaxation times, *i.e.* the relaxation rates, is (D'Humiéres *et al.*, 2002):

$$\begin{aligned}\hat{\mathbf{S}} &\equiv \mathrm{diag}\,(s_1, s_2, s_3, s_4, s_5, s_6, s_7, s_8, s_9, s_{10}, s_{11}, s_{12}, s_{13}, s_{14}, s_{15}, s_{16}, s_{17}, s_{18}, s_{19})^{\mathsf{T}} \\ &\equiv \mathrm{diag}\,(1.0, 1.19, 1.4, 1.0, 1.2, 1.0, 1.2, 1.0, 1.2, s_{10}, 1.4, s_{12}, 1.4, s_{14}, s_{15}, s_{16}, 1.98, 1.98, 1.98)^{\mathsf{T}}.\end{aligned} \tag{A5.28}$$

The relaxation rates for the conserved moments ρ, j_x, j_y and j_z are in principle inconsequential since the collision term $[m_i - m_i^{\mathrm{eq}}] = 0$ for $i = \{1, 4, 6, 8\}$ as previously highlighted. Only for the incorporation of a body force (Lallemand and Luo, 2003; Premnath and Abraham, 2007) or for multiple component simulations are the s_i corresponding to the conserved momentum important. In the present simulations, these relaxation rates were set to 1.

A5.3 Derivation of the continuity and Navier-Stokes equations

In this section, the continuity and Navier-Stokes equations for the lattice Boltzmann model will be derived using a Chapman-Enskog multiscale analysis for the D3Q19 model with multiple relaxation times as in Premnath and Abraham (2007). Although a straightforward extension to include body forces is possible, the following derivation, for simplicity, will not consider body forces. As in He and Luo (1997b), three expansions are introduced. First, a Taylor expansion is given by:

$$\mathbf{f}(\mathbf{x} + \mathbf{v}\Delta t, t + \Delta t) = \sum_{m=0}^{\infty} \frac{\Delta t^m}{m!} \mathbf{D}_t^m \mathbf{f}(\mathbf{x}, t). \tag{A5.29}$$

Second, two Chapman-Enskog expansions are introduced:

$$\mathbf{f}(\mathbf{x}, t) = \sum_{n=0}^{\infty} \varepsilon^n \mathbf{f}^{(n)}(\mathbf{x}, t) \tag{A5.30}$$

$$\partial_t = \sum_{n=0}^{\infty} \varepsilon^n \partial_{t_n}. \tag{A5.31}$$

Additionally, the definitions

$$\mathbf{D}_t \equiv \mathrm{diag}(\partial_t, \partial_t + \mathbf{v}_1 \cdot \nabla, \partial_t + \mathbf{v}_2 \cdot \nabla, , \ldots) \tag{A5.32}$$

$$\mathbf{D}_{t_n} \equiv \mathrm{diag}(\partial_{t_n}, \partial_{t_n} + \mathbf{v}_1 \cdot \nabla, \partial_{t_n} + \mathbf{v}_2 \cdot \nabla, \ldots) \tag{A5.33}$$

$$\partial_t \equiv \frac{\partial}{\partial t}, \tag{A5.34}$$

are used. Thus,

$$\mathbf{D}_t^2 \equiv \mathrm{diag}\left[\partial_t\partial_t, \partial_t\partial_t + 2\partial_t(\mathbf{v}_1 \cdot \nabla) + (\mathbf{v}_1 \cdot \nabla)^2, \partial_t\partial_t + 2\partial_t(\mathbf{v}_2 \cdot \nabla) + (\mathbf{v}_2 \cdot \nabla)^2, \ldots\right], \tag{A5.35}$$

which will be important later for evaluation of Eq. (A5.29). The lattice Boltzmann equation in vector notation:

$$\mathbf{f}(\mathbf{x} + \mathbf{v}\Delta t, t + \Delta t) - \mathbf{f}(\mathbf{x}, t) = -\mathbf{S}\left[\mathbf{f}(\mathbf{x}, t) - \mathbf{f}^{(\mathrm{eq})}(\mathbf{x}, t)\right], \tag{A5.36}$$

can then be rewritten using Eq. (A5.29) and subsequently Eqs. (A5.30) and (A5.31) as:

$$\Delta t \mathbf{D}_t \mathbf{f}(\mathbf{x}, t) + \frac{\Delta t^2}{2} \mathbf{D}_t^2 \mathbf{f}(\mathbf{x}, t) + O(\Delta t^3) = -\mathbf{S}\left[\mathbf{f}(\mathbf{x}, t) - \mathbf{f}^{(\mathrm{eq})}(\mathbf{x}, t)\right] \tag{A5.37}$$

$$\begin{aligned}
&\underbrace{\Delta t \mathbf{D}_{t_0} \mathbf{f}^{(0)}(\mathbf{x}, t)}_{O(\Delta t^1)} + \underbrace{\Delta t \varepsilon \partial_{t_1} \mathbf{f}^{(0)}(\mathbf{x}, t) + \Delta t \varepsilon \mathbf{D}_{t_0} \mathbf{f}^{(1)}(\mathbf{x}, t) + \frac{\Delta t^2}{2} \mathbf{D}_{t_0}^2 \mathbf{f}^{(0)}(\mathbf{x}, t)}_{O(\Delta t^2) \text{ or } O(\Delta t \varepsilon)} + O(\Delta t^3) = \\
&\qquad - \mathbf{S}\Big[\underbrace{\mathbf{f}^{(0)}(\mathbf{x}, t) - \mathbf{f}^{(\mathrm{eq})}(\mathbf{x}, t)}_{O(\varepsilon^0)} + \underbrace{\varepsilon \mathbf{f}^{(1)}(\mathbf{x}, t)}_{O(\varepsilon^1)} + \underbrace{\varepsilon^2 \mathbf{f}^{(2)}(\mathbf{x}, t)}_{O(\varepsilon^2)}\Big].
\end{aligned} \tag{A5.38}$$

Assuming a small time step (He and Luo, 1997b), so that $O(\Delta t) = O(\varepsilon)$, and separating terms based on orders of Δt and ε, then gives:

$$O(0): \qquad \mathbf{f}^{(0)}(\mathbf{x}, t) = \mathbf{f}^{(\mathrm{eq})}(\mathbf{x}, t) \tag{A5.39}$$

$$O(1): \qquad \Delta t \mathbf{D}_{t_0}\mathbf{f}^{(0)}(\mathbf{x}, t) = -\varepsilon \mathbf{S}\mathbf{f}^{(1)}(\mathbf{x}, t) \tag{A5.40}$$

$$O(2): \qquad \Delta t\varepsilon\partial_{t_1}\mathbf{f}^{(0)}(\mathbf{x}, t) + \Delta t\varepsilon\mathbf{D}_{t_0}\left(\mathbf{I} - \frac{1}{2}\mathbf{S}\right)\mathbf{f}^{(1)}(\mathbf{x}, t) = -\varepsilon^2\mathbf{S}\mathbf{f}^{(2)}(\mathbf{x}, t), \tag{A5.41}$$

where Eq (A5.40) has been substituted in to Eq. (A5.41) and **I** is the identity matrix. Premultiplying Eqs. (A5.39)-(A5.41) by the transformation matrix **M** gives:

$$O(0): \qquad \mathbf{m}^{(0)}(\mathbf{x}, t) = \mathbf{m}^{(\mathrm{eq})}(\mathbf{x}, t) \tag{A5.42}$$

$$O(1): \qquad \Delta t\mathbf{M}\mathbf{D}_{t_0}\mathbf{M}^{-1}\mathbf{M}\mathbf{f}^{(0)}(\mathbf{x}, t) = -\varepsilon\mathbf{M}\mathbf{S}\mathbf{M}^{-1}\mathbf{M}\mathbf{f}^{(1)}(\mathbf{x}, t)$$

$$\Delta t\mathbf{M}\mathbf{D}_{t_0}\mathbf{M}^{-1}\mathbf{m}^{(\mathrm{eq})}(\mathbf{x}, t) = -\varepsilon\hat{\mathbf{S}}\mathbf{m}^{(1)}(\mathbf{x}, t) \tag{A5.43}$$

$$O(2): \qquad \Delta t\varepsilon\partial_{t_1}\mathbf{M}\mathbf{f}^{(0)}(\mathbf{x}, t) + \Delta t\varepsilon\mathbf{M}\mathbf{D}_{t_0}\mathbf{M}^{-1}\mathbf{M}\left(\mathbf{I} - \frac{1}{2}\mathbf{S}\right)\mathbf{M}^{-1}\mathbf{M}\mathbf{f}^{(1)}(\mathbf{x}, t) = -\varepsilon^2\mathbf{M}\mathbf{S}\mathbf{M}^{-1}\mathbf{M}\mathbf{f}^{(2)}(\mathbf{x}, t)$$

$$\Delta t\varepsilon\partial_{t_1}\mathbf{m}^{(0)}(\mathbf{x}, t) + \Delta t\varepsilon\mathbf{M}\mathbf{D}_{t_0}\mathbf{M}^{-1}\left(\mathbf{I} - \frac{1}{2}\hat{\mathbf{S}}\right)\mathbf{m}^{(1)}(\mathbf{x}, t) = -\varepsilon^2\hat{\mathbf{S}}\mathbf{m}^{(2)}(\mathbf{x}, t), \tag{A5.44}$$

where $\mathbf{m} = \mathbf{M}\mathbf{f}$ from Eq. (8.17), $\hat{\mathbf{S}} = \mathbf{M}\mathbf{S}\mathbf{M}^{-1}$, $\mathbf{I} = \mathbf{M}^{-1}\mathbf{M}$ and the distributive property of matrix multiplication have been used. Next, the multiple relaxation time definition $\hat{\mathbf{S}} = \mathrm{diag}(s_1, s_2, \ldots, s_{19})$ is set.

The present derivation has been general up to this point, *i.e.* it was independent of the choice of the discrete velocity set. To evaluate Eqs. (A5.42)-(A5.44), however, the velocity set of the particular lattice Boltzmann model, in this case the D3Q19 model, is required. From Eq. (A5.43), the components of the first-order equations in moment space yield 19 equations, which were straightforwardly determined using, *e.g.* the symbolic toolbox of Matlab®:

$$\Delta t\left[\partial_{t_0}\rho + \left(\partial_x j_x + \partial_y j_y + \partial_z j_z\right)\right] = 0 \tag{A5.45}$$

$$\Delta t\left\{\partial_{t_0}\left[-11\rho + 19\frac{(j_x^2 + j_y^2 + j_z^2)}{\rho_0}\right] + \frac{5}{3}\left(\partial_x j_x + \partial_y j_y + \partial_z j_z\right)\right\} = -\varepsilon s_2 e^{(1)} \tag{A5.46}$$

$$\Delta t\left\{\partial_{t_0}\left[3\rho - \frac{11}{2}\frac{(j_x^2 + j_y^2 + j_z^2)}{\rho_0}\right] - \frac{2}{3}\left(\partial_x j_x + \partial_y j_y + \partial_z j_z\right)\right\} = -\varepsilon s_3 e_2^{(1)} \tag{A5.47}$$

$$\Delta t\left[\partial_{t_0} j_x + \partial_x\left(\frac{1}{3}\rho + \frac{j_x^2}{\rho_0}\right) + \partial_y\left(\frac{j_x j_y}{\rho_0}\right) + \partial_z\left(\frac{j_x j_z}{\rho_0}\right)\right] = 0 \tag{A5.48}$$

$$\Delta t\left\{\partial_{t_0}\left(-\frac{2}{3}j_x\right) + \partial_x\left[-\frac{2}{9}\rho + \frac{\left(-4j_x^2 + 5j_y^2 + 5j_z^2\right)}{6\rho_0}\right] + \partial_y\left(\frac{j_x j_y}{\rho_0}\right) + \partial_z\left(\frac{j_x j_z}{\rho_0}\right)\right\} = -\varepsilon s_5 q_x^{(1)} \tag{A5.49}$$

$$\Delta t\left[\partial_{t_0} j_y + \partial_x\left(\frac{j_x j_y}{\rho_0}\right) + \partial_y\left(\frac{1}{3}\rho + \frac{j_y^2}{\rho_0}\right) + \partial_z\left(\frac{j_y j_z}{\rho_0}\right)\right] = 0 \tag{A5.50}$$

$$\Delta t\left\{\partial_{t_0}\left(-\frac{2}{3}j_y\right) + \partial_x\left(\frac{j_x j_y}{\rho_0}\right) + \partial_y\left[-\frac{2}{9}\rho + \frac{\left(5j_x^2 - 4j_y^2 + 5j_z^2\right)}{6\rho_0}\right] + \partial_z\left(\frac{j_y j_z}{\rho_0}\right)\right\} = -\varepsilon s_7 q_y^{(1)} \tag{A5.51}$$

$$\Delta t\left[\partial_{t_0} j_z + \partial_x\left(\frac{j_x j_z}{\rho_0}\right) + \partial_y\left(\frac{j_y j_z}{\rho_0}\right) + \partial_z\left(\frac{1}{3}\rho + \frac{j_z^2}{\rho_0}\right)\right] = 0 \tag{A5.52}$$

$$\Delta t\left\{\partial_{t_0}\left(-\frac{2}{3}j_z\right) + \partial_x\left(\frac{j_x j_z}{\rho_0}\right) + \partial_y\left(\frac{j_y j_z}{\rho_0}\right) + \partial_z\left[-\frac{2}{9}\rho + \frac{\left(5j_x^2 + 5j_y^2 - 4j_z^2\right)}{6\rho_0}\right]\right\} = -\varepsilon s_9 q_z^{(1)} \tag{A5.53}$$

$$\Delta t\left\{\partial_{t_0}\left[\frac{\left(2j_x^2 - j_y^2 - j_z^2\right)}{3\rho_0}\right] + \frac{2}{3}\left(\partial_x(2j_x) - \partial_y j_y - \partial_z j_z\right)\right\} = -\varepsilon s_{10} 3 p_{xx}^{(1)} \tag{A5.54}$$

$$\Delta t\left\{\partial_{t_0}\left[-\frac{\left(2j_x^2 - j_y^2 - j_z^2\right)}{6\rho_0}\right] + \frac{1}{3}\left(\partial_x(-2j_x) + \partial_y j_y + \partial_z j_z\right)\right\} = -\varepsilon s_{11} 3\pi_{xx}^{(1)} \tag{A5.55}$$

$$\Delta t\left[\partial_{t_0}\left(\frac{j_y^2 - j_z^2}{\rho_0}\right) + \frac{2}{3}\left(\partial_y j_y - \partial_z j_z\right)\right] = -\varepsilon s_{12} p_{ww}^{(1)} \tag{A5.56}$$

$$\Delta t\left[\partial_{t_0}\left(-\frac{j_y^2 - j_z^2}{2\rho_0}\right) + \frac{1}{3}\left(-\partial_y j_y + \partial_z j_z\right)\right] = -\varepsilon s_{13}\pi_{ww}^{(1)} \tag{A5.57}$$

$$\Delta t\left[\partial_{t_0}\left(\frac{j_x j_y}{\rho_0}\right) + \frac{1}{3}\left(\partial_x j_y + \partial_y j_x\right)\right] = -\varepsilon s_{14} p_{xy}^{(1)} \tag{A5.58}$$

$$\Delta t\left[\partial_{t_0}\left(\frac{j_y j_z}{\rho_0}\right) + \frac{1}{3}\left(\partial_y j_z + \partial_z j_y\right)\right] = -\varepsilon s_{15} p_{yz}^{(1)} \tag{A5.59}$$

$$\Delta t\left[\partial_{t_0}\left(\frac{j_x j_z}{\rho_0}\right) + \frac{1}{3}\left(\partial_x j_z + \partial_z j_x\right)\right] = -\varepsilon s_{16} p_{xz}^{(1)} \tag{A5.60}$$

$$\Delta t\left[\partial_x\left(\frac{j_y^2 - j_z^2}{2\rho_0}\right) + \partial_y\left(\frac{j_x j_y}{\rho_0}\right) - \partial_z\left(\frac{j_x j_z}{\rho_0}\right)\right] = -\varepsilon s_{17} m_x^{(1)} \tag{A5.61}$$

$$\Delta t\left[-\partial_x\left(\frac{j_x j_y}{\rho_0}\right) + \partial_y\left(\frac{-j_x^2 + j_z^2}{2\rho_0}\right) + \partial_z\left(\frac{j_y j_z}{\rho_0}\right)\right] = -\varepsilon s_{18} m_y^{(1)} \tag{A5.62}$$

$$\Delta t\left[\partial_x\left(\frac{j_x j_z}{\rho_0}\right) - \partial_y\left(\frac{j_y j_z}{\rho_0}\right) + \partial_z\left(\frac{j_x^2 - j_y^2}{2\rho_0}\right)\right] = -\varepsilon s_{19} m_z^{(1)}. \tag{A5.63}$$

Here, after division by Δt, Eq. (A5.45) and Eqs. (A5.48), (A5.50) and (A5.52) are the Euler equations governing conservation of mass and momentum, respectively, for an inviscid fluid up to first order in the Chapman-Enskog expansion. Note that since $m_i = m_i^{(\mathrm{eq})}$ for the conserved moments, as shown by comparing Eqs. (A5.24) and (A5.25), the right hand sides of the above equations for conserved moments, *i.e.* Eqs. (A5.45), (A5.48), (A5.50) and (A5.52), have been set to zero.

The components for the second order equations in moment space can then be obtained from Eq. (A5.44) in a similar fashion. For the derivation of the macroscopic flow equations, only the second order equations for the conserved moments are necessary; therefore, only these equations have been listed:

$$\Delta t\varepsilon\partial_{t_1}\rho = 0 \tag{A5.64}$$

$$\begin{aligned}\Delta t\varepsilon\Big\{&\partial_{t_1} j_x + \partial_x\left(\frac{1}{57}\left[1-\frac{1}{2}s_2\right]e^{(1)} + \left[1-\frac{1}{2}s_{10}\right]p_{xx}^{(1)}\right) + \partial_y\left(\left[1-\frac{1}{2}s_{14}\right]p_{xy}^{(1)}\right)\\ &+ \partial_z\left(\left[1-\frac{1}{2}s_{16}\right]p_{xz}^{(1)}\right)\Big\} = 0\end{aligned} \tag{A5.65}$$

$$\begin{aligned}\Delta t\varepsilon\Big\{&\partial_{t_1} j_y + \partial_x\left(\left[1-\frac{1}{2}s_{14}\right]p_{xy}^{(1)}\right)\\ &+ \partial_y\left(\frac{1}{57}\left[1-\frac{1}{2}s_2\right]e^{(1)} - \frac{1}{2}\left[1-\frac{1}{2}s_{10}\right]p_{xx}^{(1)} + \frac{1}{2}\left[1-\frac{1}{2}s_{12}\right]p_{ww}^{(1)}\right)\\ &+ \partial_z\left(\left[1-\frac{1}{2}s_{15}\right]p_{yz}^{(1)}\right)\Big\} = 0\end{aligned} \tag{A5.66}$$

$$\begin{aligned}\Delta t\varepsilon\Big\{&\partial_{t_1} j_z + \partial_x\left(\left[1-\frac{1}{2}s_{16}\right]p_{xz}^{(1)}\right) + \partial_y\left(\left[1-\frac{1}{2}s_{15}\right]p_{yz}^{(1)}\right)\\ &+ \partial_z\left(\frac{1}{57}\left[1-\frac{1}{2}s_2\right]e^{(1)} - \frac{1}{2}\left[1-\frac{1}{2}s_{10}\right]p_{xx}^{(1)} - \frac{1}{2}\left[1-\frac{1}{2}s_{12}\right]p_{ww}^{(1)}\right)\Big\} = 0.\end{aligned} \tag{A5.67}$$

Adding the first and second order equations for the conserved moments, *i.e.* Eqs. (A5.45) and (A5.64), Eqs. (A5.48) and (A5.65), Eqs. (A5.50) and (A5.66), and Eqs. (A5.52) and (A5.67), and using $\partial_t \approx \partial_{t_0} + \varepsilon\partial_{t_1}$ from Eq. (A5.31) gives after division by Δt:

$$\partial_t\rho + \nabla\cdot(\mathbf{u}\rho_0) = 0 \tag{A5.68}$$

$$\begin{aligned}&\partial_t j_x + \partial_x\left(\frac{1}{3}\rho + \frac{j_x^2}{\rho_0} + \varepsilon\frac{1}{57}\left[1-\frac{1}{2}s_2\right]e^{(1)} + \varepsilon\left[1-\frac{1}{2}s_{10}\right]p_{xx}^{(1)}\right)\\ &\quad + \partial_y\left(\frac{j_x j_y}{\rho_0} + \varepsilon\left[1-\frac{1}{2}s_{14}\right]p_{xy}^{(1)}\right) + \partial_z\left(\frac{j_x j_z}{\rho_0} + \varepsilon\left[1-\frac{1}{2}s_{16}\right]p_{xz}^{(1)}\right) = 0\end{aligned} \tag{A5.69}$$

$$
\begin{aligned}
&\partial_t j_y + \partial_x\left(\frac{j_x j_y}{\rho_0} + \varepsilon\left[1 - \frac{1}{2}s_{14}\right]p_{xy}^{(1)}\right)\\
&\quad + \partial_y\left(\frac{1}{3}\rho + \frac{j_y^2}{\rho_0} + \varepsilon\frac{1}{57}\left[1 - \frac{1}{2}s_2\right]e^{(1)} - \varepsilon\frac{1}{2}\left[1 - \frac{1}{2}s_{10}\right]p_{xx}^{(1)} + \varepsilon\frac{1}{2}\left[1 - \frac{1}{2}s_{12}\right]p_{ww}^{(1)}\right)\\
&\quad + \partial_z\left(\frac{j_y j_z}{\rho_0} + \varepsilon\left[1 - \frac{1}{2}s_{15}\right]p_{yz}^{(1)}\right) = 0
\end{aligned}
\tag{A5.70}
$$

$$
\begin{aligned}
&\partial_t j_z + \partial_x\left(\frac{j_x j_z}{\rho_0} + \varepsilon\left[1 - \frac{1}{2}s_{16}\right]p_{xz}^{(1)}\right) + \partial_y\left(\frac{j_y j_z}{\rho_0} + \varepsilon\left[1 - \frac{1}{2}s_{15}\right]p_{yz}^{(1)}\right)\\
&\quad + \partial_z\left(\frac{1}{3}\rho + \frac{j_z^2}{\rho_0} + \varepsilon\frac{1}{57}\left[1 - \frac{1}{2}s_2\right]e^{(1)} - \varepsilon\frac{1}{2}\left[1 - \frac{1}{2}s_{10}\right]p_{xx}^{(1)} - \varepsilon\frac{1}{2}\left[1 - \frac{1}{2}s_{12}\right]p_{ww}^{(1)}\right) = 0.
\end{aligned}
\tag{A5.71}
$$

If the compressible form of the equilibrium distribution, *i.e.* Eq. (A5.17) for $\mathbf{f}^{(\mathrm{eq})}$, had been used instead of the incompressible form, Eq. (A5.21) for $\mathbf{f}^{(\mathrm{eq})}$, the recovered continuity equation would have been $\partial_t\rho + \nabla\cdot(\mathbf{u}\rho) = 0$. To recover incompressible flow, *i.e.* $\nabla\cdot\mathbf{u}$, thus requires small temporal variation in ρ, so that $\partial_t\rho \approx 0$. The assumption of small temporal variation in ρ will always hold for flows in steady state. Additionally, it can be shown (Martinez *et al.*, 1994) that $\partial_t\rho = O(\mathbf{u}^2)$. In Eqs. (A5.69)-(A5.71), the variables $e^{(1)}, p_{xx}^{(1)}, p_{ww}^{(1)}, p_{xy}^{(1)}, p_{yz}^{(1)}, p_{xz}^{(1)}$ are unknowns. Expressions for these variables can be obtained by rearranging Eqs. (A5.46), (A5.54), (A5.56), (A5.58) , (A5.59) and (A5.60), respectively, and employing the continuity and momentum equations, *i.e.* Eq. (A5.45) and Eqs.(A5.48), (A5.50) and (A5.52), to give (Premnath and Abraham, 2007; McCracken and Abraham, 2005):

$$e^{(1)} = -\frac{\Delta t}{\varepsilon}\frac{38}{3s_2}\left(\partial_x j_x + \partial_y j_y + \partial_z j_z\right) = -\frac{38}{3s_2}\nabla\cdot\mathbf{j} \approx e - e^{(\mathrm{eq})} \tag{A5.72}$$

$$p_{xx}^{(1)} = -\frac{\Delta t}{\varepsilon}\frac{2}{9s_{10}}\left(\partial_x(2j_x) - \partial_y j_y - \partial_z j_z\right) \approx p_{xx} - p_{xx}^{(\mathrm{eq})} \tag{A5.73}$$

$$p_{ww}^{(1)} = -\frac{\Delta t}{\varepsilon}\frac{2}{3s_{12}}\left(\partial_y j_y - \partial_z j_z\right) \approx p_{ww} - p_{ww}^{(\mathrm{eq})} \tag{A5.74}$$

$$p_{xy}^{(1)} = -\frac{\Delta t}{\varepsilon}\frac{1}{3s_{14}}\left(\partial_x j_y + \partial_y j_x\right) \approx p_{xy} - p_{xy}^{(\mathrm{eq})} \tag{A5.75}$$

$$p_{yz}^{(1)} = -\frac{\Delta t}{\varepsilon}\frac{1}{3s_{15}}\left(\partial_y j_z + \partial_z j_y\right) \approx p_{yz} - p_{yz}^{(\mathrm{eq})} \tag{A5.76}$$

$$p_{xz}^{(1)} = -\frac{\Delta t}{\varepsilon}\frac{1}{3s_{16}}\left(\partial_x j_z + \partial_z j_x\right) \approx p_{xz} - p_{xz}^{(\mathrm{eq})}, \tag{A5.77}$$

where terms of order $O(\mathbf{u}^3)$ and higher have been neglected to be consistent with the small velocity expansion of $\mathbf{f}^{(\mathrm{eq})}$ in Eq. (A5.2) up to the order of $O(\mathbf{u}^2)$.

Substituting Eqs. (A5.72)-(A5.77) into Eqs. (A5.69)-(A5.71), with $\Delta t = 1$ and

$$\zeta = \frac{2}{9}\left(\frac{1}{s_2} - \frac{1}{2}\right) \tag{A5.78}$$

$$\nu = \frac{1}{3}\left(\frac{1}{s_i} - \frac{1}{2}\right), \quad i = 10, 12, 14, 15, 16 \tag{A5.79}$$

the momentum equations simplify to:

$$\begin{aligned}
\partial_t j_x + \partial_x\left(\frac{j_x^2}{\rho_0}\right) + \partial_y\left(\frac{j_x j_y}{\rho_0}\right) + \partial_z\left(\frac{j_x j_z}{\rho_0}\right) = &-\partial_x\left(\frac{1}{3}\rho\right) + \partial_x\left(2\nu\left[\partial_x j_x - \frac{1}{3}\nabla\cdot\mathbf{j}\right] + \zeta\nabla\cdot\mathbf{j}\right) \\
&+ \partial_y\left(\nu[\partial_x j_y + \partial_y j_x]\right) + \partial_z\left(\nu[\partial_x j_z + \partial_z j_x]\right) \qquad \text{(A5.80)} \\
\partial_t j_y + \partial_x\left(\frac{j_x j_y}{\rho_0}\right) + \partial_y\left(\frac{j_y^2}{\rho_0}\right) + \partial_z\left(\frac{j_y j_z}{\rho_0}\right) = &-\partial_y\left(\frac{1}{3}\rho\right) + \partial_x\left(\nu[\partial_x j_y + \partial_y j_x]\right) \\
&+ \partial_y\left(2\nu\left[\partial_y j_y - \frac{1}{3}\nabla\cdot\mathbf{j}\right] + \zeta\nabla\cdot\mathbf{j}\right) \\
&+ \partial_z\left(\nu[\partial_y j_z + \partial_z j_y]\right) \qquad \text{(A5.81)} \\
\partial_t j_z + \partial_x\left(\frac{j_x j_z}{\rho_0}\right) + \partial_y\left(\frac{j_y j_z}{\rho_0}\right) + \partial_z\left(\frac{j_z^2}{\rho_0}\right) = &-\partial_z\left(\frac{1}{3}\rho\right) + \partial_x\left(\nu[\partial_x j_z + \partial_z j_x]\right) + \partial_y\left(\nu[\partial_y j_z + \partial_z j_y]\right) \\
&+ \partial_z\left(2\nu\left[\partial_z j_z - \frac{1}{3}\nabla\cdot\mathbf{j}\right] + \zeta\nabla\cdot\mathbf{j}\right). \qquad \text{(A5.82)}
\end{aligned}$$

Here, ζ and ν are the kinematic bulk and shear viscosities, respectively. Writing Eqs.(A5.80)-(A5.82) explicitly in terms of Δt and c, identical equations to Eqs.(A5.80)-(A5.82) would have been obtained, but with the transport coefficients defined as:

$$\zeta = \frac{2}{9}\left(\frac{1}{s_2} - \frac{1}{2}\right)c^2\Delta t \tag{A5.83}$$

$$\nu = \frac{1}{3}\left(\frac{1}{s_i} - \frac{1}{2}\right)c^2\Delta t, \quad i = 10, 12, 14, 15, 16 \tag{A5.84}$$

where $c = 1$ and $\Delta t = 1$ are typically used. For the correct viscous stress tensor, $s_{10} = s_{12} = s_{14} = s_{15} = s_{16}$ must be maintained. The left hand sides of Eqs. (A5.80)-(A5.82) can be expanded as

$$\rho_0\partial_t u_x + \rho_0\left(u_x\partial_x u_x + \cancel{u_x\partial_x u_x} + u_y\partial_y u_x + \cancel{u_x\partial_y u_y} + u_z\partial_z u_x + \cancel{u_x\partial_z u_z}\right) \tag{A5.85}$$

$$\rho_0\partial_t u_y + \rho_0\left(u_x\partial_x u_y + \cancel{u_y\partial_x u_x} + u_y\partial_y u_y + \cancel{u_y\partial_y u_y} + u_z\partial_z u_y + \cancel{u_y\partial_z u_z}\right) \tag{A5.86}$$

$$\rho_0\partial_t u_z + \rho_0\left(u_x\partial_x u_z + \cancel{u_z\partial_x u_x} + u_y\partial_y u_z + \cancel{u_z\partial_y u_y} + u_z\partial_z u_z + \cancel{u_z\partial_z u_z}\right), \tag{A5.87}$$

where the cancelation results from using continuity, $\nabla \cdot \mathbf{u} = \partial_x u_x + \partial_y u_y + \partial_z u_z = 0$. Thus the overall macroscopic flow equations for the D3Q19 lattice Boltzmann model, representing the conservation of mass and momentum, respectively, are given by:

$$\nabla \cdot \mathbf{u} = 0 + O(\varepsilon^2) + O(Ma^2) \tag{A5.88}$$

$$\rho_0[\partial_t \mathbf{u} + \mathbf{u} \cdot \nabla \mathbf{u}] = -\nabla P + \nabla \cdot \mathbf{T} + O(\varepsilon^2) + O(Ma^3), \tag{A5.89}$$

where ρ_0 is the constant density of the incompressible flow, P is the pressure given by

$$P = c_s^2 \rho = \frac{c^2}{3} \rho, \tag{A5.90}$$

and $\mathbf{T}$ is the deviatoric part of the viscous stress tensor:

$$\mathrm{T}_{ij} = \rho_0 \nu \left[\left(\partial_j u_i + \partial_i u_j \right) - \frac{2}{3} \nabla \cdot \mathbf{u} \delta_{ij} \right] + \rho_0 \zeta \nabla \cdot \mathbf{u} \delta_{ij}, \tag{A5.91}$$

where δ_{ij} is the Kronecker delta. In Eqs. (A5.88) and (A5.89) the error term, $O(\varepsilon^2)$, originates from the higher order terms in the original expansions, Eqs. (A5.29)-(A5.31), where $O(\varepsilon^2) = O(\Delta t^2)$ has been assumed. The term $O(Ma^2)$ in Eq. (A5.88) comes from $\partial_t = O(Ma^2)$ (Martinez *et al.*, 1994). By contrast the error term, $O(Ma^3)$, in Eq. (A5.89) originates from higher order terms in Eqs. (A5.85)-(A5.87) as well as from the expansion of the equilibrium distribution function. In the present dissertation, the Mach number is defined as

$$Ma = \frac{|\mathbf{u}|}{c_s} = \frac{|\mathbf{j}|}{\rho_0 c_s}, \tag{A5.92}$$

so that $O(\mathbf{u}) = O(\mathbf{j}) = O(Ma)$. Thus, the overall scheme is second order accurate in both time and space, since $O(\varepsilon^2) = O(\Delta t^2)$ and the time step was chosen equal to the lattice spacing, $c = \Delta x / \Delta t = 1$, so that $O(\Delta x^2) = O(\Delta t^2)$. Since terms of $\mathrm{O}(\Delta t^3)$ in the original lattice Boltzmann equation (8.12) are $O(\Delta t^2)$ in Eqs. (A5.88)-(A5.89), the low order discretisation error of $O(\Delta t^2)$ in Eq. (8.12) has effectively been absorbed into the transport coefficients, ν and ζ (Sterling and Chen, 1996). By having ν and ζ take the form $(1/s_i - 1/2)$ rather than simply $1/s_i$, Eq. (8.12) can be considered to have errors of order $O(\Delta t^3)$.

In general, the condition $Ma = |\mathbf{u}|/c_s < 0.15$ is maintained in numerical simulations of the LB method (He and Luo, 1997b) to satisfy incompressibility and was observed in all simulations in this dissertation except those in Figs. 8.14(c) and (d). Finally, it is noted that if the compressible form of the equilibrium distribution, *i.e.* Eq. (A5.17) for $\mathbf{f}^{(eq)}$, were used instead of the incompressible form, Eq. (A5.21) for $\mathbf{f}^{(eq)}$, the result would have been the compressible form of the continuity and Navier-Stokes equations (Dellar, 2003).

Nomenclature

a	Index for curve fitting in Chapter 5	
a	Constant, = $m/(2k_\mathrm{B}T)$ in Appendix 5	($\mathrm{s^2/m^2}$)
a_1	Constant in Eq. A4.13	($\mathrm{mol/m^2}$)
a_i	Constant in Eq. A1.2	(J/(mol K))
a_{ij}	Atoms of j in one molecule of i in Eq. A1.22	
A	Pre-exponential factor	(1/s)
A_s	Reactor cross-sectional area	($\mathrm{m^2}$)
Abs	Absorbance of an X-ray beam	
b	Number of distinct atomic species in Eq. A1.22	
b_1	Constant in Eqs. 5.5 and A4.13	($\mathrm{mol/m^3}$)
b_2	Constant in Eq. A4.16	($\mathrm{mol/m^3}$)
b_i	Constant in Eq. A1.2	($\mathrm{J/(mol\ K^2)}$)
b_j	Number of moles of element j in Eq. A1.22	
Bi	Biot number, = $hd_\mathrm{p}/6\lambda_\mathrm{p}$	
c	Lattice speed, = $\Delta x/\Delta t$	(m/s)
c_1, c_2	Constant in Eqs. 5.5, A4.13 and A4.16	($\mathrm{mol/m^2}$)
$c_\mathrm{CO}, c_\mathrm{CO_2}, c_\mathrm{N_2}$	Concentration of CO, CO_2, N_2	($\mathrm{mol/m^3}$)
$c_\mathrm{CO,in}, c_\mathrm{CO_2,in}$	Concentration at reactor inlet	($\mathrm{mol/m^3}$)
$c_\mathrm{CO,out}, c_\mathrm{CO_2,out}$	Concentration at reactor outlet	($\mathrm{mol/m^3}$)
$c_\mathrm{CO,p}, c_\mathrm{CO_2,p}$	Concentration in particulate phase	($\mathrm{mol/m^3}$)
$c_\mathrm{CO,s}, c_\mathrm{CO_2,s}$	Concentration at particle surface	($\mathrm{mol/m^3}$)
C_d	Drag coefficient	
c_i	Constant in Eq. A1.2	((J K)/mol)
c_s	Lattice speed of sound, = $\sqrt{k_\mathbf{B}T/m} = 1/\sqrt{3}$	(m/s)
C_p	Mass specific heat capacity at constant pressure	(J/(kg K))
$C^\circ_{p,i}$	Molar specific heat capacity at constant pressure for species i	(J/(mol K))
d	Distance	(m)
d_bed	Bed diameter	(m)
d_i	Constant in Eq. A1.2	($\mathrm{J/(mol\ K^3)}$)
d_p	Particle diameter	(m)
$\bar{d}_\mathrm{pore}$	Mean pore diameter	(nm)
D	Packed bed dispersion coefficient	($\mathrm{m^2/s}$)
D	Dimension, = 2 for 2D, = 3 for 3D	
$D_\mathrm{e,CO}, D_\mathrm{e,CO_2}$	Effective diffusivity within porous particle	($\mathrm{m^2/s}$)
$D_\mathrm{k,CO}, D_\mathrm{k,CO_2}$	Knudsen diffusivity within porous particle	($\mathrm{m^2/s}$)
$D_\mathrm{mix,CO}, D_\mathrm{mix,CO_2}$	Diffusivity of CO and CO_2 in a gas mixture	($\mathrm{m^2/s}$)

D_s	Diffusivity of scalar species s	(m^2/s)
$\mathbf{D}_t, \mathbf{D}_{t_n}$	Total derivative in Eq. (A5.32), Eq. (A5.33)	(1/s)
∂_t	Partial derivative with respect to t, $= \partial/\partial t$	(1/s)
$\partial_x, \partial_y, \partial_z$	Partial derivative with respect to x, y, z; $= \partial/\partial x$, $= \partial/\partial y, = \partial/\partial z$	(1/m)
e_1	Constant in Eq. A4.13	(mol/m^2)
e	Moment defined by Eq. (A5.24)	(kg/(m s^2))
e_2	Moment defined by Eq. (A5.24)	((kg m)/s^4)
$e^{(\mathrm{eq})}$	Equilibrium moment from Eq. (A5.26)	(kg/(m s^2))
$e_2^{(\mathrm{eq})}$	Equilibrium moment from Eq. (A5.27)	((kg m)/s^4)
e_i	Constant of integration in Eq. A1.3	(J/mol)
e_i	Constant of integration in Eq. A1.4	(J/(mol K))
E	Activation energy	(J/mol)
E_{an}	Electric potential difference between anode and normal hydrogen electrode	(V)
E_{cat}	Electric potential difference between cathode and normal hydrogen electrode	(V)
$f(X)$	Function of conversion, X, in Chapter 5	
f	Continuous mass distribution function	((kg s$^{\mathrm{D}}$)/(m^3 m$^{\mathrm{D}}$))
$f^{(\mathrm{eq})}$	Continuous equilibrium mass distribution function	((kg s$^{\mathrm{D}}$)/(m^3 m$^{\mathrm{D}}$))
f_i	Discrete mass distribution function	(kg/m^3)
$f_i^{(\mathrm{eq})}$	Discrete equilibrium mass distribution function	(kg/m^3)
$f_{i,s}$	Discrete distribution function for scalar s	(mol/m^3)
$f_{i,s}^{(\mathrm{eq})}$	Discrete equilibrium distribution function for scalar s	(mol/m^3)
f_i'	Discrete post-collision distribution function	(kg/m^3)
$f_{i,s}'$	Discrete post-collision distribution function for scalar s	(mol/m^3)
f_i	Fugacity of species i in Appendix 1, $= y_i P \phi_i$	(Pa)
f_i°	Fugacity of i in the reference state in Appendix 1	(Pa)
$\mathbf{f}$	Vectorised discrete mass distribution function	((kg s$^{\mathrm{D}}$)/(m^3 m$^{\mathrm{D}}$))
$\mathbf{f}^{(0)}, \ldots, \mathbf{f}^{(n)}$	Expansion parameters for $\mathbf{f}$ in Eq. (A5.30)	((kg s$^{\mathrm{D}}$)/(m^3 m$^{\mathrm{D}}$))
F	Faraday constant, = 96 485.34 C mol^{-1} in Chapter 1	(C mol^{-1})
F	Lagrangian for minimisation of free energy in Appendix 1	(J)
$\mathbf{F} = (F_x, F_y, F_z)^{\mathsf{T}}$	Force vector	(N)
G	Total Gibbs free energy of a system	(J)
$\bar{G}_i$	Chemical potential of species i	(J/mol)
G_i°	Standard Gibbs free energy for species i at T, 10^5 Pa	(J/mol)
ΔG_T°	Standard Gibbs free energy for reaction as written at T, 10^5 Pa	(J/mol)
h	External heat transfer coefficient for reacting particle	(W/(m^2 K))
H_0	Unfluidised bed height	(m)
H_i°	Standard enthalpy for species i at T, 10^5 Pa	(J/mol)
$\Delta \mathrm{H}_T^\circ$	Standard enthalpy for reaction as written at T, 10^5 Pa	(J/mol)
$I(n)$	Standard integral in Table A5.3	(m/s)$^{(}n + 1)$
$\mathbf{I}$	Identity matrix, = diag(1, 1, . . . , 1)	
$\mathbf{j} = (j_x, j_y, j_z)^{\mathsf{T}}$	Mass flux in x, y, z direction	(kg/ (m^2 s))
k	Rate constant, including mass transfer effects	(1/s)

k_0	Initial value of k_i at $X = 0$, $t = 0$	(1/s)
k_B	Boltzmann constant, $= 1.381 \times 10^{-23}$	(m^2 kg /(s^2 K))
k_B/ξ	Lennard-Jones parameter in Eq. (A2.3)	(1/K)
k_D	Constant in Eq. (8.42), $= 2\pi/L_x$	(1/m)
k_F	Dimensionless force constant in Eq. (4.4), = 0.22	
$k_g, k_{g,CO}, k_{g,CO_2}$	External mass transfer coefficient for a particle	(m/s)
k_i, k_{-i}	Forward and reverse intrinsic rate constant, chemical rate-controlled, $k_{-i} = k_i/K_p$	(1/s)
k_s	Forward intrinsic rate constant for surface reaction, chemical rate-controlled	(m/s)
Kn	Knudsen number	
K_p	Equilibrium constant, $= p_{CO_2}/p_{CO}$	
K_W	Equilibrium constant for water-gas shift, $= p_{H_2}/p_{H_2O} \times p_{CO_2}/p_{CO}$	
L	Length	(m)
L_x, L_y, L_z	Length in x, y, and z direction	(m)
m	Mass of single, monoatomic particle	(kg)
m_{CO}, m_{H_2}	Mass of CO, H_2	(kg)
m_{ox}	Mass of fully oxidised carrier	(kg)
m_x, m_y, m_z	Moments defined by Eq. (A5.24)	(kg/s^3)
$m_x^{(eq)}, m_y^{(eq)}, m_z^{(eq)}$	Equilibrium moments from Eq. (A5.26), = 0	(kg/s^3)
$\mathbf{m}$	Discrete moment vector, $= \mathbf{Mf}$	(varied)
$\mathbf{m}_i$	Element i of discrete moment vector	(varied)
$\mathbf{m}^{(eq)}$	Discrete equilibrium moment vector, $= \mathbf{Mf}^{(eq)}$	(varied)
$\mathbf{m}_i^{(eq)}$	Element i of discrete equilibrium moment vector	(varied)
M	Atomic specie	
$M_1, \ldots, M_s$	Molecular species in Eq. (A1.11)	
Ma	Mach number defined in Eq. (A5.92)	
$M_{CO}, M_{Fe_2O_3}, M_{H_2}$,	Molecular mass of CO, Fe_2O_3, H_2	(kg/kmol)
M_i, M_j, M_w	Molecular mass of species i, j or general gas	(kg/kmol)
M_V	Molar density	(kmol/m^3)
$\mathbf{M}$	Transformation matrix	(varied)
∇	Nabla vector differential operator	(1/m)
$n_{Fe_2O_3}, n_{Fe_3O_4}$	Moles of reactive iron oxide per unit volume particle	(mol/m^3)
n_{H_2}	Moles of H_2	(mol)
n_i	Moles of species i	(mol)
n_s, n_t	Number of successes, number of trials	
N_A	Avogadro constant, $= 6.02214 \times 10^{23}$	(1/mol)
Nu	Nusselt number, $= hd_p/\lambda_{mix}$	
$p_{CO}, p_{CO_2}, p_{H_2}$, p_{H_2O}, p_{O_2}, p_i	Partial pressure of CO, CO_2, H_2, H_2O, O_2, species i	
p_{ww}, p_{xx}, p_{xy}, p_{xz}, p_{yz}	Moments defined by Eq. (A5.24)	(kg/(m s^2))
$p_{ww}^{(eq)}, p_{xx}^{(eq)}, p_{xy}^{(eq)}$, $p_{xz}^{(eq)}, p_{yz}^{(eq)}$	Equilibrium moments from Eq. (A5.26)	(kg/(m s^2))
P	Constant in Appendix 4, Eq. (A4.11)	(1/m^2)
P	Total pressure of a system	(Pa)
P°	Reference pressure, 10^5 Pa	(Pa)

P_{b}	Binomial probability, [0,1]	
Pe	Péclet number, = vL/D	
P_{sat}	Saturation pressure at fixed T	(Pa)
q	Superficial volumetric flowrate of gas through reactor	(m^3/s)
q_x, q_y, q_z	Moments defined by Eq. (A5.24)	(kg/s^3)
$q_x^{(\mathrm{eq})}, q_y^{(\mathrm{eq})}, q_z^{(\mathrm{eq})}$	Equilibrium moments from Eq. (A5.26)	(kg/s^3)
Q	Number of discrete lattice velocities	
r	Radial position within particle	(m)
r'	Rate of reaction per unit mass of particle as $\mathrm{Fe_2O_3}$	(mol/(s g))
r_{e}	Effective radius of a cylindrical pore	(m)
R	External particle radius	(m)
R	Ideal gas constant	(J/(mol K))
Re	Reynolds number, = $\rho U d_{\mathrm{p}}/\mu = U d_{\mathrm{p}}/\nu$	
Re_{p}	Particle Reynolds number, = $\rho U_{\mathrm{mf}} d_{\mathrm{p}}/\mu\varepsilon_{\mathrm{mf}}$	
$s_1, s_2, \ldots, s_{19}$	Dimensionless relaxation rates	
S	Total entropy of a system	(J/K)
S_0	Particle surface area divided by volume	(m^2/m^3)
Sc	Schmidt number, = $\mu_g/\rho D_{\mathrm{mix}} = \nu/D_{\mathrm{mix}}$	
S_{g}	Specific surface area	(m^2/g)
Sh	Sherwood number, = $k_g d_{\mathrm{p}}/D_{\mathrm{mix}}$	
S_i°	Standard entropy for species i at T, 10^5 Pa	(J/(mol K))
$\mathbf{S}$	Dimensionless collision matrix, = $\mathrm{diag}(1/\tau, \ldots, 1/\tau)$	
$\hat{\mathbf{S}}$	Dimensionless collision matrix, = $\mathrm{diag}(s_1, \ldots, s_n)$	
t	Time	(s)
$\Delta t_{12}, \Delta t_{13}, \Delta t_{23}$	Time between temperature maxima	(s)
T	Absolute temperature	(K)
T_1, T_2, T_3	Temperature of thermocouple $1, 2$ and 3	(K)
T_{m}	Melting temperature	(K)
Tr	Transmittance of an X-ray beam, = $10^{-\mathrm{Abs}}$	
T_∞	Fluidised bed bulk temperature	(K)
$T^\star$	Dimensionless temperature, = $T k_{\mathrm{B}}/\xi$	
$\mathbf{T}$	Deviatoric viscous stress tensor in Eq. (A5.91)	(kg/(m s^2))
u_{CO}	Variable, = $c_{\mathrm{CO}} r$	(mol/m^2)
$\mathbf{u} = (u_x, u_y, u_z)^{\mathsf{T}}$	Velocity of bulk fluid	(m/s)
$\mathbf{u}_s$	Velocity of bulk fluid of species s	(m/s)
U	Superficial velocity of fluidising gas at inlet	(m/s)
U_{mf}	Value of U at incipient fluidisation	(m/s)
v	Packed bed interstitial velocity in flow direction	(m/s)
$\mathbf{v} = (v_x, v_y, v_z)^{\mathsf{T}}$	Microscopic velocity	(m/s)
$\mathbf{v}_i$	Discrete microscopic velocity, = $(v_{ix}, v_{iy}, v_{iz})^{\mathsf{T}}$	(m/s)
$\mathbf{v}_i^-$	Velocity in opposite direction of $\mathbf{v}_i$	(m/s)
V	Total volume of a system	(m^3)
$w_0, w_1, \ldots, w_{18}, w_i$	Weighting constants in discrete equilibrium distribution function	
$w_{\mathrm{b}}, w_{\mathrm{s}}$	Scalar boundary arrays defined in section 8.4.1	
W	Total mass of particles of $\mathrm{Fe_2O_3}$ added to reactor	(kg)
W_0, W_1, W_2	Weighting constants in Eq. (A5.16)	
x	Distance	(m)
x_{m}	Mole fraction of metal, = (mol M/(mol Fe + mol M))	

x_w	Mass fraction of Al_2O_3, = (g Al_2O_3/(g Fe_2O_3 + g Al_2O_3))	
$\mathbf{x} = (x, y, z)^\mathsf{T}$	Spatial position vector	(m)
$\mathbf{x}_\mathrm{b}$	Position of boundary node	(m)
X	Conversion of solid reactant $(n_{Fe_2O_3,t=0} - n_{Fe_2O_3})/n_{Fe_2O_3,t=0}$ or $(2n_{Fe_2O_3,t=0}/3 - n_{Fe_3O_4})/(2n_{Fe_2O_3,t=0}/3)$	
X_{CO}, X_{CO_2}	Conversion of solid based on moles of CO consumed, CO_2 produced during reduction in N_2+CO+CO+2	
X_fl	Crossflow factor in Eq. (5.8)	
X_{H_2}	Conversion of solid based on moles of H_2 produced during oxidation in N_2+steam	
y	Moles of H_2 produced per mole of $C_{(s)}$ in Eq. (1.20)	
$y_i, y_j, y_{CO}, y_{CO_2}$	Mole fraction of *i*, *j*, CO, CO_2 in gaseous mixture	

Greek Symbols

β	Constant in Eq. (5.8), = $(1 - U/U_\mathrm{mf})$	
γ	Surface tension in Eq. (A2.7)	(N/m)
γ_i	Lagrange multiplier in Eq. (A1.22)	(J/mol)
δ	Constant in Chapter 1, $0.05 < \delta < 0.17$	
δ_{ij}	Kronecker delta	
ε	Small expansion parameter	(s)
ε_bed	Packed bed porosity due to interstices	
ε_mf	Fluidised bed porosity at U_mf	
ε_p	Particle porosity	
ζ	Kinematic bulk viscosity	(m^2/s)
η	Effectiveness factor for sphere, = $3(\phi \coth \phi - 1)/\phi^2$	
θ	Angle	(degrees)
λ	Wavelength	(m)
λ_0	Thermal conductivity of monoatomic gas	(W/(m K))
λ_e	Effective thermal conductivity of the porous particle	(W/(m K))
λ_i, λ_j	Thermal conductivity of the gaseous species *i*, *j*	(W/(m K))
λ_j	Lagrange multiplier in Appendix 1, Eq. (A1.22)	(J)
λ_mix	Thermal conductivity of gaseous mixture	(W/(m K))
μ	Viscosity of the gas	(kg/(m s))
ν	Kinematic shear viscosity, = μ/ρ	(m^2/s)
$\nu_1, \ldots, \nu_s$	Stoichiometric integer coefficients in Eq. (A1.11)	
π_{xx}, π_{ww}	Moments defined by Eq. (A5.24)	((kg m)/s^4)
$\pi_{xx}^{(\mathrm{eq})}, \pi_{ww}^{(\mathrm{eq})}$	Equilibrium moments from Eq. (A5.27)	((kg m)/s^4)
ρ	Mass density of gas	(kg/m^3)
ρ_0	Mass density of gas in equilibrium	(kg/m^3)
ρ_{CO}	Molar density of CO	(mol/m^3)
$\rho_{Al_2O_3}$	Density of inert Al_2O_3 bed material	(kg/m^3)
$\rho_{Fe_2O_3}, \rho_{Fe_3O_4}$	Initial particle density (particle mass/particle volume)	(g/m^3)
ρ_s	Density of scalar *s*	(mol/m^3)
σ	Collision diameter in Lennard-Jones potential	(nm)
σ_T	Crushing stress	(Pa)
τ, τ_s	Dimensionless relaxation time	

τ'	Relaxation time	(s)
$\tau_{\mathrm{CO}}^{\mathrm{mix}}, \tau_{\mathrm{CO_2}}^{\mathrm{mix}}$	Mixing time constants of CO and CO_2 analysers	(s)
τ_{p}	Tortuosity for particle in Chapter 5	
ϕ	Thiele modulus, $= R[k_i/D_{\mathrm{e,CO}} + k_i/(K_p D_{\mathrm{e,CO_2}})]^{1/2}$	
ϕ_i	Fugacity coefficient	
Φ_{ij}	Mixture coefficient in Eq. A2.6	
Ω	Collision integral	$((\mathrm{kg\ s^D})/(\mathrm{m^3\ m^D\ s}))$

Acronyms

BET	Theory of Brunauer, Emmett and Teller (1938)
BGK	Theory of Bhatnagar, Gross and Krook (1954)
BJH	Theory of Barrett, Joyner and Halenda (1951)
CPU	Central processing unit
DNS	Direct numerical simulation
DSMC	Direct simulation Monte Carlo
EDS	Energy dispersive X-ray spectroscopy
FIB-SEM	Focused ion beam scanning electron microscopy
I.D.	Interior diameter
IR	Infrared radiation
LB	Lattice Boltzmann
LGCA	Lattice gas cellular automata
MD	Molecular dynamics
MPI	Message passing interface
MRT	Multiple relaxation time
NDIR	Non-dispersive infrared radiation
NS	Navier-Stokes
O.D.	Outer diameter
PEM	Polymeric electrolyte membrane
PBR	Packed bed reactor
PFR	Plug flow reactor
PROX	Preferential oxidation
RIR	Relative intensity ratio
SEM	Scanning electron microscopy
STEM	Scanning transmission electron microscopy
WGS	Water-gas shift
XRD	X-ray diffraction

References

Abad, A., Mattisson, T., Lyngfelt, A., Johansson, M., 2007. The use of iron oxide as oxygen carrier in a chemical-looping reactor. Fuel 86, 1021–1035.

Adachi, T., Meier, G., 1986. Oxidation of iron-silicon alloys. Oxid. Met. 27, 347–366.

Adánez, J., de Diego, L., García-Labiano, F., Gayán, P., Abad, A., Palacios, J., 2004. Selection of oxygen carriers for chemical-looping combustion. Energy Fuels 18, 371–377.

Asinari, P., 2008. Asymptotic analysis of multiple-relaxation-time lattice Boltzmann schemes for mixture modeling. Comput. Math. Appl. 55, 1392–1407.

Asinari, P., Ohwada, T., 2009. Connection between kinetic methods for fluid-dynamic equations and macroscopic finite-difference schemes. Comput. Math. Appl. 58, 841–861.

Awasthi, K., Srivastava, A., Srivastava, O., 2005. Synthesis of carbon nanotubes. J. Nanosci. Nanotechno. 5, 1616–1636.

Barin, I., Knacke, O., 1973. Thermodynamical properties of inorganic substances. Berlin: Springer-Verlag.

Barrett, E., Joyner, L., Halenda, P., 1951. The determination of pore volume and area distributions in porous substances. I. Computations from nitrogen isotherms. J. Am. Chem. Soc. 73, 373–380.

Beers, K., 2007. Numerical Methods for Chemical Engineering. Cambridge: Cambridge University Press.

Beetstra, R., van der Hoef, M., Kuipers, J., 2007. Drag force of intermediate Reynolds number flow past mono- and bidisperse arrays of spheres. AIChE J. 53, 489–501.

Bhatnagar, P., Gross, E., Krook, M., 1954. A model for collision processes in gases. I. Small amplitude processes in charged and neutral one-component systems. Phys. Rev. 94, 511–525.

Bird, R., Stewart, W., Lightfoot, E., 2007. Transport Phenomena, 2$^{\text{nd}}$ ed. London: John Wiley and Sons.

Birks, N., Meier, G., Pettit, F., 2006. High-Temperature Oxidation of Metals. Cambridge: Cambridge University Press.

Bouzidi, M., d'Humières, D., Lallemand, P., Luo, L., 2001. Lattice Boltzmann equation on a two-dimensional rectangular grid. J. Comput. Phys. 172, 704–717.

Brinker, C., Scherer, G., 1989. Sol-Gel Science: The Physics and Chemistry of Sol-Gel Processing. London: Academic Press.

Brunauer, S., Emmett, P., Teller, E., 1938. Adsorption of gases in multimolecular layers. J. Am. Chem. Soc. 60, 309–319.

Chen, S., Doolen, G., 1998. Lattice Boltzmann method for fluid flows. Annu. Rev. Fluid Mech. 30, 329–364.

Choudhary, T., Goodman, D., 2002. CO-free fuel processing for fuel cell applications. Catal. Today 77, 65–78.

CIA, 2009. CIA World Factbook. Online: www.cia.gov/library/publications/the-world-factbook.

Cleeton, J., Bohn, C., Müller, C., Dennis, J., Scott, S., 2009. Clean hydrogen production and electricity from coal *via* chemical looping: Identifying a suitable operating regime. Int. J. Hydrogen Energy 34, 1–12.

Colthup, N., Daly, L., Wiberley, S., 1964. Introduction to Infrared and Raman Spectroscopy. London: Academic Press.

Cornubert, R., D'Humières, D., Levermore, D., 1991. A Knudsen layer theory for lattice gases. Physica D 47, 241–259.

Davidson, J., Harrison, D., 1963. Fluidised Particles. Cambridge: Cambridge University Press, Ch. 6, pp. 97–106.

Dellar, P., 2003. Incompressible limits of lattice Boltzmann equations using multiple relaxation times. J. Comp. Phys. 190.

Denbigh, K., 1957. The Principles of Chemical Equilibrium. Cambridge: Cambridge University Press.

D'Humiéres, D., Ginzburg, I., Krafczyk, M., Lallemand, P., Luo, L., 2002. Multiple-relaxation-time lattice Boltzmann models in three dimensions. Phil. Trans. R. Soc. Lond. A 360, 437–451.

DOE, 2007. US Department of Energy. Multi-year research, development and demonstration plan: Planned program activities for 2005-2015, p. 3.3-1. Online: www1.eere.energy.gov/hydrogenandfuelcells/mypp/pdfs/storage.pdf.

DOE, 2009a. US Department of Energy. Hydgrogen data book: Hydrogen production capacities at individual refineries. Online: http://hydrogen.pnl.gov/cocoon/morf/hydrogen/article/706.

DOE, 2009b. US Department of Energy. 2008 Renewable energy data book. Online: http://www.nrel.gov/docs/fy09osti/45654.pdf.

Edgar, T., Himmelblau, D., Lasdon, L., 2001. Optimization of chemical processes, 2nd ed. New York: McGraw Hill, Ch. 8, pp. 273–284.

Ergun, S., Orning, A., 1949. Fluid flow through randmonly packed columns and fluidized beds. Ing. Eng. Chem. Res. 41, 1179–1184.

Ertl, G., Knözinger, H., Weitkamp, J., 1999. Preparation of Solid Catalysts. Weinheim: Wiley-VCH, Ch. 4.8, pp. 501–526.

Ewan, B., Allan, R., 2006. Limiting thermodynamic efficiencies of thermochemical cycles used for hydrogen generation. Green Chem. 8, 988–994.

Fahien, R., 1983. Fundamentals of Transport Phenomena. London: McGraw-Hill, Ch. 2, pp. 79–94.

Farrauto, R., Hwang, S., Shore, L., Ruettinger, W., Lampert, J., Giroux, T., Liu, Y., Ilinich, O., 2003. New material needs for hydrocarbon fuel processing: Generating hydrogen for the PEM fuel cell. Annu. Rev. Mater. Res. 33, 1–27.

Flekkøy, E., 1993. Lattice Bhatnagar-Gross-Krook models for miscible fluids. Phys. Rev. E 47, 4247–4257.

Freund, H., Zeiser, T., Huber, F., Klemm, E., Brenner, G., Durst, F., Emig, G., 2003. Numerical simulations of single phase reacting flows in randomly packed fixed-bed reactors and experimental validation. Chem. Eng. Sci. 58, 903–910.

Fristrom, R., Westenberg, A., 1965. Flame Structure. London: McGraw-Hill, Ch. 12, pp. 282–291.

Froment, G., 1967. Fixed bed catalytic reactors: Current design status. Ind. Eng. Chem. Res. 59, 18–27.

Gallivan, M., Noble, D., Georgiadis, J., Buckius, R., 1997. An evaluation of the bounce-back boundary condition for lattice Boltzmann simulations. Int. J. Numer. Meth. Fl. 25, 249–263.

Galvita, V., Hempel, T., Lorenz, H., Rihko-Struckmann, L., Sundmacher, K., 2008a. Deactivation of modified iron oxide materials in the cyclic water gas shift process for CO-free hydrogen production. Ind. Eng. Chem. Res. 47, 303–310.

Galvita, V., Schröder, T., Munder, B., Sundmacher, K., 2008b. Production of hydrogen with low CO_x-content for PEM fuel cells by cyclic water gas shift reactor. Int. J. Hydrogen Energy 33, 1354–1360.

Galvita, V., Sundmacher, K., 2007. Cyclic water gas shift reactor (CWGS) for carbon monoxide removal from hydrogen feed gas for PEM fuel cells. Chem. Eng. J. 134, 168–174.

Ginzbourg, I., Adler, P., 1994. Boundary flow condition analysis for the 3-dimensional lattice Boltzmann model. J. Phys. II France 4, 191–214.

Goldstein, J., Newbury, D., Joy, D., Lyman, C., Echlin, P., Lifshin, E., Sawyer, L., Michael, J., 2003. Scanning Electron Microscopy and X-ray Microanalysis. New York: Springer Science.

Grace, J., Elnashaie, S., Lim, C., 2005. Hydrogen production in fluidized beds with *in-situ* membranes. Int. J. Chem. React. Eng. 3, 1–17.

Grätzel, M., 2001. Phootoelectrochemical cells. Nature 414, 338–344.

Gunn, D., 1968. Mixing in packed and fluidised beds. Trans. Inst. Chem. Eng. 214, CE153–CE172.

Gupta, P., Velazquez-Vargas, L., Fan, L., 2007. Syngas redox (SGR) process to produce hydrogen from coal derived syngas. Energy Fuels 21, 2900–2908.

Hayward, T., 2009. BP statistical review of world energy. Online: www.bp.com.

He, X., Luo, L., 1997b. Lattice Boltzmann model for the incompressible Navier-Stokes equation. J. Stat. Phys. 88, 927–944.

He, X., Luo, L., 1997c. Theory of the lattice Boltzmann method: From the Boltzmann equation to the lattice Boltzmann equation. Phys. Rev. E 56, 6811–6817.

He, X., Zou, Q., Luo, L., Dembo, M., 1997. Analytic solutions of simple flows and analysis of nonslip boundary conditions for the lattice Boltzmann BGK model. J. Stat. Phys. 87, 115–136.

Hirschfelder, J., Curtiss, C., Bird, R., 1954. Molecular theory of gases and liquids. New York: John Wiley and Sons.

ICSD, 2010. Crystal Structure Database. Daresbury Laboratory. Fe_3O_4 (26410-ICSD), FeO (633038-ICSD), $FeO{\cdot}Al_2O_3$ (40093-ICSD).

IEA, 2004. IEA HIA 5-year plan: 2004-2009, p. 5. Online: www.ieahia.org/pdfs/ieahia.

IEA, 2009. International Energy Agency key world energy statistics 2009. Online: www.iea.org/textbase/nppdf/free/2009.

Inamuro, T., Ogata, T., Tajima, S., Konishi, N., 2004. A lattice Boltzmann method for incompressible two-phase flows with large density differences. J. Comp. Phys. 198, 628–644.

IPCC, 2007. Intergovermental Panel on Climate Change, Climate Change 2007: Synthesis Report. Cambridge: Cambridge University Press.

Isalski, W., 1989. Separation of Gases. Oxford: Clarendon, Ch. 2, pp. 29–32.

Ishida, M., Jin, H., 1996. A novel chemical-looping combustor without NO_x formation. Ind. Eng. Chem. Res. 35, 2469–2472.

Ishida, M., Jin, H., Okamoto, T., 1998. Kinetic behaviour of solid particle in chemical-looping combustion: Suppressing carbon deposition in reduction. Energy Fuels 12, 223–229.

Ishida, M., Takeshita, K., Suzuki, K., Ohba, T., 2005. Application of Fe_2O_3 - Al_2O_3 composite particles as solid looping material of the chemical-loop combustor. Energy Fuels 19, 2514–2518.

Jaeger, J., 1967. Failure of rocks under tensile conditions. Int. J. Rock Mech. Min. Sci. 4, 219–227.

JCPDS, 2005a. Powder diffraction files (PDF). JCPDS-international centre for diffraction data, Pennsylvania. Fe_2O_3 (PDF 033-0664), Fe_3O_4 (PDF 019-0629), Fe (PDF 006-0696), $FeO{\cdot}Cr_2O_3$ (PDF 034-0140), $Mgo{\cdot}Fe_2O_3$ (PDF 036-0398), MgO (PDF 043-1022).

JCPDS, 2005b. Powder diffraction files (PDF). JCPDS-international centre for diffraction data, Pennsylvania. Fe_3O_4 (PDF 019-0629), FeO (PDF 006-0615).

JCPDS, 2005c. Powder diffraction files (PDF). JCPDS-international centre for diffraction data, Pennsylvania. Fe_3O_4 (PDF 019-0629), FeO (PDF 006-0615), $FeO{\cdot}Al_2O_3$ (PDF 034-0192), Al_2O_3 (PDF 010-0173).

Jin, H., Okamoto, T., Ishida, M., 1999. Development of a novel chemical-looping combustion: Synthesis of a solid looping material of $NiO/NiAl_2O_4$. Ind. Eng. Chem. Res. 38, 126–132.

Kanan, M., Nocera, D., 2008. *In situ* formation of an oxygen-evolving catalyst in neutral water containing phosphate and Co^{2+}. Science 321, 1072–1075.

Khirevich, S., Höltzel, A., Hlushkou, D., Tallarek, U., 2007. Impact of conduit geometry and bed porosity on flow and dispersion in noncylindrical sphere packings. Anal. Chem. 79, 9340–9349.

Ladd, A., 1994. Numerical simulations of particulate suspensions via a discretized Boltzmann equation. Part 1. Theoretical foundation. J. Fluid Mech. 271, 285–309.

Lallemand, L., Luo, L., 2003. Theory of the lattice Boltzmann method: Acoustic and thermal properties in two and three dimensions. Phys. Rev. E 68, 1–25.

Lallemand, P., Luo, L., 2000. Theory of the lattice Boltzmann equation: Dispersion, dissipation, isotropy, Galilean invariance and stability. Phys. Rev. E 61, 6546–6562.

LaNauze, R., 1985. Fundamentals of coal combustion in fluidised beds. Chem. Eng. Res. Des. 63, 3–33.

Lane, H., 1913. Process for the production of hydrogen, U.S. Patent 1,078,686.

Laurendeau, N., 1978. Heterogeneous kinetics of coal char gasification and combustion. Prog. Energ. Combust. 4, 221–270.

Levenspiel, O., 1972. Chemical Reaction Engineering, 2nd ed. London: John Wiley and Sons.

Levenspiel, O., 1999. Chemical Reactor Engineering, 3rd ed. New York: John Wiley and Sons, Ch. 18, pp. 385–391.

Li, F., Kim, H., Sridhar, D., Wang, F., Zeng, L., Chen, J., Fan, L., 2009. Syngas chemical looping gasification process: Oxygen carrier particle selection and performance. Energy Fuels 23, 4182–4189.

Lund, C., Dumesic, J., 1981. Strong oxide-oxide interactions in silica-supported magnetite catalysts. 1. X-ray diffraction and Mössbauer spectroscopy evidence for interaction. J. Phys. Chem. 85, 3175–3180.

Maier, R., Kroll, D., Kutsovsky, Y., Davis, H., Bernard, R., 1998. Simultation of flow through bead packs using the lattice Boltzmann method. Phys. Fluids 10, 60–74.

Martinez, D., Matthaeus, W., Chen, S., Montgomery, D., 1994. Comparison of spectral method and lattice Boltzmann simulations of two-dimensional hydrodynamics. Phys. Fluids 6, 1285–1298.

Mattisson, T., Johansson, M., Lyngfelt, A., 2004. Multicycle reduction and oxidation of different types of iron oxide particles - Application to chemical-looping combustion. Energy Fuels 18, 628–637.

McBride, B., Zehe, M., Gordon, S., 2002. NASA Glenn coefficients for calculating thermodynamic properties of individual species. NASA Report: TP-2002-211556.

McCracken, M., Abraham, J., 2005. Multiple-relaxation-time lattice Boltzmann model for multiphse flow. Phys. Rev. E. 71, 1–9.

McKewan, W., 1958. Kinetics of iron ore reduction. Trans. Metall. Soc. AIME 212, 791–793.

McKewan, W., 1962. Reduction kinetics of hematite in hydrogen-water vapor-nitrogen mixtures. Trans. Metall. Soc. AIME 224, 2–5.

Mei, R., Yu, D., Shyy, W., Luo, L., 2002. Force evaluation in the lattice Boltzmann method involving curved geometry. Phys. Rev. E 65, 1–14.

Messerschmitt, A., 1910. Process of producing hydrogen, U.S. Patent 971,206.

Mohamad, A., Succi, S., 2009. A note on equilibrium boundary conditions in lattice Boltzmann fluid dynamic simulations. Eur. Phys. J. 171, 213–221.

Mohapatra, S., John, S., Banerjee, S., Misra, M., 2009. Water photooxidation by smooth and ultrathin α-Fe_2O_3 nanotube arrays. Chem. Mater. 21, 3048–3055.

Muradov, N., 1993. How to produce hydrogen from fossil-fuels without CO_2 emission. Int. J. Hydrogen Energy 18, 211–215.

Murayama, T., Ono, Y., Kawai, Y., 1977. Step-wise reduction of hematite pellets with CO-CO_2 gas mixtures. Tetsu-to-Hagané 63, 1099–1107.

Nath, K., Das, D., 2004. Improvement of fermentative hydrogen production: Various approaches. Appl. Microbiol. Biot. 65, 520–529.

NIST, 2010. National Institute of Standards and Technology. Chemistry WebBook. Online: http://webbook.nist.gov/chemistry/.

NOAA, 2009. Earth System Research Laboratory, Mauna Loa, Hawaii. Online: http://www.esrl.noaa.gov/gmd/ccgg/trends.

Omori, Y., 1987. Blast Furnace Phenomena and Modelling. London: Elsevier.

Otsuka, K., Kaburagi, T., Yamada, C., Takenaka, S., 2003. Chemical storage of hydrogen by modified iron oxides. J. Power Sources 122, 111–121.

Patil, C., van Sint Annaland, M., Kuipers, J., 2007. Fluidised bed membrane reactor for ultrapure hydrogen production *via* methane steam reforming: Experimental demonstration and model validation. Chem. Eng. Sci. 62, 2989–3007.

Perez-Alonso, F., Melián-Cabrera, I., Granados, M. L., Kapteijn, F., Fierro, J., 2006. Synergy of $Fe_xCe_{1-x}O_2$ mixed oxides for N_2O decomposition. J. Catal. 239, 340–346.

Popović, S., Ristić, M., Musić, S., 1995. Formation of solid solutions in the system Al_2O_3-Fe_2O_3. Mater. Lett. 23, 139–142.

Pozdnyakov, O., Teschner, D., Wootsch, A., Kröhnert, J., Steinhauer, B., Sauer, H., Toth, L., Jentoft, F., Knop-Gericke, A., Paál, Z., Schlögl, R., 2006. Preferential CO oxidation in hydrogen (PROX) on ceria-supported catalysts. Part I: Oxidation state and surface species on Pt/CeO_2 under reaction conditions. J. Catal. 237, 1–16.

Premnath, K., Abraham, J., 2007. Three-dimensional multi-relaxation time (MRT) lattice-Boltzmann models for incompressible flow. J. Comp. Phys. 224, 539–559.

Raiskinmäki, P., Koponen, A., Merikoski, J., Timonen, J., 2000. Spreading dynamics of three-dimensional droplets by the lattice-Boltzmann method. Comp. Mat. Sci. 18, 7–12.

Ramage, M., 2004. The Hydrogen Economy: Opportunities, Costs, Barriers, and Needs. Washington D.C.: National Academies Press, Ch. G, p. 199.

Ranz, W., Marshall, W., 1952. Evaporation from drops: Part I. Chem. Eng. Prog. 48, 141–146.

Reimer, L., 1998. Scanning Electron Microscopy: Physics of Image Formation and Microanalysis. London: Springer-Verlag.

Rostrup-Nielsen, T., 2005. Manufacture of hydrogen. Catal. Today 106, 293–296.

Satterfield, C., 1980. Heterogeneous Catalysis in Practice. London: McGraw-Hill, Ch. 4, pp. 86–94.

Smith, N., Amundson, N., 1951. Intraparticle diffusion in catalytic heterogeneous systems. Ind. Eng. Chem. Res. 43, 2156–2167.

Spitzer, R., Manning, F., Philbrook, W., 1966. Mixed-control reaction kinetics in the gaseous reduction of hematite. Trans. Metall. Soc. AIME 236, 726–741.

Steinfeld, A., 2005. Solar thermochemical production of hydrogen - a review. Sol. Energy 78, 603–615.

Steinfeld, A., Meier, A., 2004. Encyclopedia of Energy: Solar Fuels and Materials. Vol. 5. Cambridge: Cambridge University Press, pp. 623–637.

Sterling, J., Chen, S., 1996. Stability analysis of lattice Boltzmann methods. J. Comp. Phys. 123, 196–206.

Succi, S., 2001. The Lattice Boltzmann Equation for Fluid Dynamics and Beyond. Oxford: Oxford University Press.

Sukop, M., Thorne, D., 2006. Lattice Boltzmann Modeling: An Introduction for Geoscientists and Engineers. Netherlands: Springer-Verlag.

Sullivan, S., 2006. Lattice Boltzmann development for chemical engineering applications. PhD Thesis. Department of Chemical Engineering, University of Cambridge.

Sullivan, S., Sederman, A., Johns, M., Gladden, L., 2007. Verification of shear-thinning LB simulations in complex geometries. J. Non-Newton. Fluid 143, 59–63.

Szekely, J., Evans, J., 1970. A structural model for gas-solid reactions with a moving boundary. Chem. Eng. Sci. 25, 1091–1107.

Szekely, J., Evans, J., Sohn, H., 1976. Gas-Solid Reactions. London: Academic Press.

Takegoshi, E., Hirasawa, Y., Imura, S., Shimazaki, T., 1984. Measurement of thermal properties of iron oxide pellets. Int. J. Thermophys. 5, 219–228.

Taylor, H., 1921. Industrial Hydrogen. New York: J.J. Little and Ives Company, Ch. 10, p. 172.

Teixeira, C., 1998. Incorporating turbulence models into the lattice-Boltzmann method. Int. J. Mod. Phys. C 9, 1159–1175.

Thiele, E., 1939. Relation between catalytic activity and size of particle. Ind. Eng. Chem. Res. 31, 916–920.

Third, J., Scott, D., Scott, S., Müller, C., 2010. Tangential velocity profiles of granular material within horizontal rotating cylinders modelled using the DEM. Granul. Matter., (submitted).

Topsøe, H., Dumesic, J., Boudart, M., 1973. Alumina as a textural promoter of iron synthetic ammonia catalysts. J. Catal. 28, 477–488.

Toschi, F., Succi, S., 2005. Lattice Boltzmann method at finite Knudsen numbers. Europhys. Lett. 69, 549–555.

Towhidi, N., Szekely, J., 1983. The influence of carbon deposition on the reduction kinetics of commercial grade hematite pellets with CO, H_2, and N_2. Metall. Trans. B. 134 (14B), 359–367.

Trushenski, S., Li, K., Philbrook, W., 1974. Non-topochemical reduction of iron oxides. Metall. Trans. 5, 1149–1158.

Turner, J., Sverdrup, G., Mann, M., Maness, P., Kroposki, B., Ghirardi, M., Evans, R., Blake, D., 2008. Renewable hydrogen production. Int. J. Energ. Res. 32, 379–407.

v. Bogdandy, L., Engell, H.-J., 1971. The Reduction of Iron Ores. Berlin: Springer-Verlag, Ch. 1, pp. 19–30.

Valipour, M., Saboohi, Y., 2007. Modeling of multiple noncatalytic gas-solid reactions in a moving bed of porous pellets based on finite volume method. Heat Mass Transfer 43, 881–894.

Wakao, N., Funazkri, T., 1978. Effect of fluid dispersion coefficients on particle-to-fluid mass transfer coefficients in packed beds. Chem. Eng. Sci., 1375–1384.

Wang, H., Wang, G., Wang, X., Bai, J., 2008. Hydrogen production by redox of cation-modified iron oxide. J. Phys. Chem. C 112, 5679–5688.

Ward, D., Ko, E., 1995. Preparing catalytic materials by the sol-gel method. Ind. Eng. Chem. Res. 34, 421–433.

Washburn, E., 1921. The dynamics of capillary flow. Phys. Rev. 17, 273–283.

WebofKnowledge, 2009. A search for ”lattice Boltzmann” yielded 91 hits in 1999 and 785 hits in 2009. Online: http://apps.isiknowledge.com.

Wen, C., Yu, Y., 1966. A generalized method for predicting minimum fluidization velocity. AICHE J. 12, 610–612.

Whitaker, S., 1972. Forced convection heat transfer correlations for flow in pipes, past flat plates, single cylinders, single spheres, and for flow in packed beds and tube bundles. AIChE J. 18, 361–371.

Wolf-Gladrow, D., 2000. Lattice Gas Cellular Automata and Lattice Boltzmann Models. London: Springer-Verlag.

Wolfram, S., 1986. Cellular automaton fluids: Basic theory. J. Stat. Phys. 45, 471–526.

Yoldas, B., 1975. Alumina gels that form porous transparent Al_2O_3. J. Mat. Sci. 10, 1856–1860.

Young, J., 2006. Lecture notes on molecular thermodynamics: Kinetic theory. Department of Engineering, University of Cambridge.

Yu, D., Mei, R., Luo, L., Shyy, W., 2003. Viscous flow computations with the method of lattice Boltzmann equation. Prog. Aerosp. Sci. 39, 329–367.

Yu, H., Zhao, K., 2000. Lattice Boltzmann method for compressible flows with high Mach numbers. Phys. Rev. E 61, 3867–3870.

Zeiser, T., 2007. Investigations of flow and species transport in packed beds by lattice Boltzmann simulations: High performance computing in science and engineering 2006. Berlin: Springer-Verlag, Ch. 8, Part 4, pp. 343–354.

Zeiser, T., 2008. Simulation und Analyse von durchströmten Kugelschüttungen in engen Rohren under Verwendung von Hochleistungsrechnern. PhD Dissertation. University of Erlangen-Nürnberg.

Zhang, C., Wan, H., Yang, Y., Xiang, H., Li, Y., 2006. Study on the iron-silica interaction of a co-precipitated Fe/SiO_2 Fischer-Tropsch catalyst. Catal. Commun. 7, 733–738.

Zhao, H., Liu, L., Wang, B., Xu, W., Jiang, L., Zheng, C., 2008. Sol-gel-derived $NiO/NiAl_2O_4$ oxygen carriers for chemical-looping combustion by coal char. Energy Fuels 22, 898–905.

Zhavoronkov, N., Aerov, M., Umnik, N., 1949. Hydraulic resistance and packing density of a layer of grains. Zhurnal Fizicheskos Khimii 23, 342–360 (original text in Russian).

Zou, Q., He, X., 1997. On pressure and velocity boundary conditions for the lattice Boltzmann BGK model. Phys. Fluids 9, 1591–1598.